THE UNIVERSITY *of* EDINBURGH

Exploring ruthenium dye synthesis and TiO_2-dye-I^-/I_3^- electron transfer reactions in a Dye-Sensitised Solar Cell.

Nina Chadwick

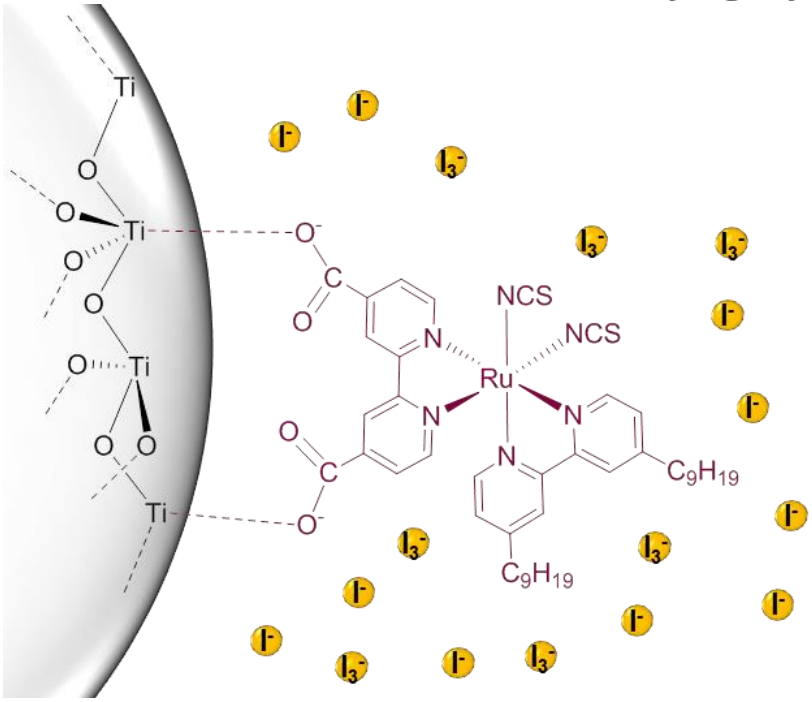

Thesis submitted for the degree of Ph.D

The University of Edinburgh

Own work declaration

I hereby declare that the following thesis is entirely my own work unless otherwise indicated in the references, acknowledgements or text. This work has not been submitted for any other degree or professional qualification.

Nina Chadwick.
September 2013.

Acknowledgements

Neil; thank you for the opportunity to complete this Ph.D and for teaching me so much about solar cells, physics, dyes etc. etc! I certainly have a much better understanding of scientific research and this experience will definitely make me a better teacher! Thanks for allowing Tracy and I to go to lots of conferences, I really learned a lot from those experiences. Lastly, thanks for letting me run riot with The Solar Spark! I enjoyed every second (except for some of the tidying!) and can only hope the project grows and improves. If you want any help during school holidays then let me know!

Lesley; such a busy (and successful!) lady and yet you always found time for me when I needed it! I can't thank you enough.

Tracy; partner in solar fun times! Thanks for the conferences, the holidays, the laughs, for keeping the lab tidy, and for showing me how to do various solar related things! It's been fun – now we get to share lesson plans instead!

Maddy; I loved having someone to share The Solar Spark with! I'll never forget sitting in that dingy basement painting, organising and messing around with solar toys – so much fun!! Thanks in particular for being amazing at the job so I could let it go and actually finish this thesis!

Solar girls: Charlotte; you made the first year immense! Martina; bella chica, it's been a pleasure working with you. Emily; thanks for keeping the lab tidy while Tracy was away! It's been good getting to know you.

Rest of the Robertson crew: Miquel; Thanks for the help, advice, and for chasing the shadows in Athens! Luca, Max, Alex; It's been fun! Good luck for the future. Yue, Sara, Ioanna; I'm sad I couldn't really get to know you properly, good luck for your Ph.Ds.

The rest of the corridor: Matt; I'm going to miss your moaning! Looking forward to some proper fun again in August! And Paul, Mike, Oleg, Top; It's been great getting to know you better this year – I hope you find someone else to be mean to Mike / Paul!!!

The homies, the flatties, the CHVers; your support has meant everything. Thanks for being so understanding at times when the Ph.D really did take over. I can't wait to spend more time with you all.

My family; Thanks for always being on the end of the phone and for not making it all about the academic stuff. You've kept me sane!! Love you all!

And Dave…you've done so much for me. I like to think I could have done this without all of your help, but I'm overwhelmingly grateful to you, because I didn't have to try. Now it's my turn ☺!

Abstract

Octahedral, six co-ordinate ruthenium complexes containing acid substituted polypyridyl ligands have proved particularly successful as dyes for Dye-Sensitised Solar Cells (DSSCs); thus there have been hundreds, if not thousands of these types of complexes synthesised and studied. Ruthenium dyes are now incorporated into commercial DSSCs; yet there is limited understanding of the interactions between the dye and the liquid I^-/I_3^- electrolyte, which can both facilitate and hinder the generation of current and voltage within the cell.

Monodentate $^-$NCS ligands incorporated into ruthenium dyes appear to interact strongly with I^- and I_2 within the electrolyte. The analogous $^-$NCO containing dye has therefore been synthesised to study the effect of the chalcogen atom on these interactions. Substituting $^-$NCS for $^-$NCO resulted in a significant change in the spectroscopic and electronic properties of the molecular dye, with destabilisation of the HOMO of the dye causing a red shift in dye absorption. Possibly due to this change in properties, the nature of the chalcogen atom was shown to have a significant impact on the performance of the dye in a DSSC.

The effect of the nature of substituents on ancillary ligands of Ru(H_2-dcbpy)(4,4`-Y_2-bpy)$(NCS)_2$ dyes on recombination across the TiO_2 – electrolyte interface within the cell has been proven significant due to changes in the strength of binding of I_2 to the substituent groups. However, few substituent groups have been investigated; therefore a series of halogenated dyes, where Y = Cl, Br, were synthesised. The effect of the nature of the halogen on dye recombination was significant, although the trends observed were not consistent with the reported data for iodine binding. Similar trends were observed for the analogous series, Ru(H_2-dcbpy)(5,5'-Y_2-bpy)$(NCS)_2$ where Y = F, Cl, Br. By comparison of this series of dyes with the 4,4` dyes, it was discovered that the position of the substituent had a significant effect on the rate of recombination within the solar cell, as well as the electrochemical and spectroscopic properties of the dyes themselves. Such isomeric effects have not been previously reported.

In the synthesis of these dyes, and in attempting the synthesis of five other ruthenium dyes, many barriers to efficient dye synthesis were discovered. Therefore, an investigation into the synthesis of ruthenium dyes has been conducted. By analysis of the breakdown products formed a number of avoidable side reactions, including decarboxylation and ruthenium catalysed nucleophilic substitution of the bpy ligands, were shown to occur. Problems associated with the high lability of the ruthenium centre at high temperatures have also been explored, and the use of UV/vis monitoring to aid optimisation of the reaction conditions was implemented. Thus, the development of two novel synthetic procedures allowed the synthesis of the dyes investigated during the course of this thesis.

Contents

Abbreviations

Pertaining to analytical techniques:

NMR	Nuclear magnetic resonance spectroscopy
TMS	Trimethylsilane
ESI-MS	Electrospray ionisation mass spectrometry
IR	Infrared
ATR-FTIR	Attenuated total reflectance-fourier transform IR spectroscopy
CHN	Elemental analysis
EA	Elemental analysis
UV/vis	Ultraviolet/visible spectroscopy
CV	Cyclic voltammetry
DPV	Differential pulse voltammetry
RE	Reference electrode
CE	Counter electrode
WE	Working electrode
NHE	Normal hydrogen electrode
DFT	Density functional theory
TD-DFT	Time-dependent density functional theory
PCM	Polarisable continuum model
J_{MP}	Current at maximum power
V_{MP}	Voltage at maximum power
J_{SC}	Short circuit current
V_{OC}	Open circuit voltage
FF	Fill factor
EIS	Electrochemical impedance spectroscopy
TAS	Transient absorption spectroscopy

Chemicals:

bpy	2,2`-bipyridine
dcbpy	4,4`-$(CO_2^-)_2$-2,2`-bipyridine
H_2-dcbpy	4,4`-$(CO_2H)_2$-2,2`-bipyridine

decbpy	4,4`-$(CO_2CH_2CH_3)_2$-2,2`-bipyridine
dmbpy	4,4`-$(CH_3)_2$-2,2`-bipyridine
dnbpy	4,4`$(C_9H_{19})_2$-2,2`-bipyridine
bbzt	2,2`-bibenzothiazole
DMF	Dimethyl formamide
DMSO	Dimethyl sulfoxide
MeOH	Methanol
EtOH	Ethanol
MeCN	Acetonitrile
d^6-DMSO	Deuterated dimethylsulfoxide
MeOD	Deuterated methanol
OAc	Acetate
TBA	Tetrabutylammonium
BMII	1-butyl-3-methylimidazolium iodide
TBP	4-*tert*-butylpyridine
Gnd.NCS	Guanidinioum thiocyanate

Miscellaneous:

DSSC(s)	Dye-sensitised solar cell(s)
CB	Conduction band
FTO	Fluorine doped tin oxide
AM	Air mass
HOMO	Highest occupied molecular orbital
LUMO	Lowest unoccupied molecular orbital
MLCT	Metal to ligand charge transfer
LLCT	¯NCX ligand to bpy ligand charge transfer
RT	Room temperature
ppm	Parts per million
TW	Terawatts
thexi	Thermally equilibrated excited state

Chapter 1: Introduction

1.1 The Energy Problem

Since the beginning of the first industrial revolution in the late 18th century, the world's population and its energy demands have increased dramatically; mostly fuelled by coal, oil and natural gas. It is now feared that supplies of fossil fuels may become insufficient within this generation's lifetime. Also, the use of such fuels causes the release of debris and ash into the environment. In particular, oil spillages, including the 2010 disaster in the Gulf of Mexico, are causing people to look to alternative energy supplies to prevent the detrimental environmental effects that have been all too common in recent years.

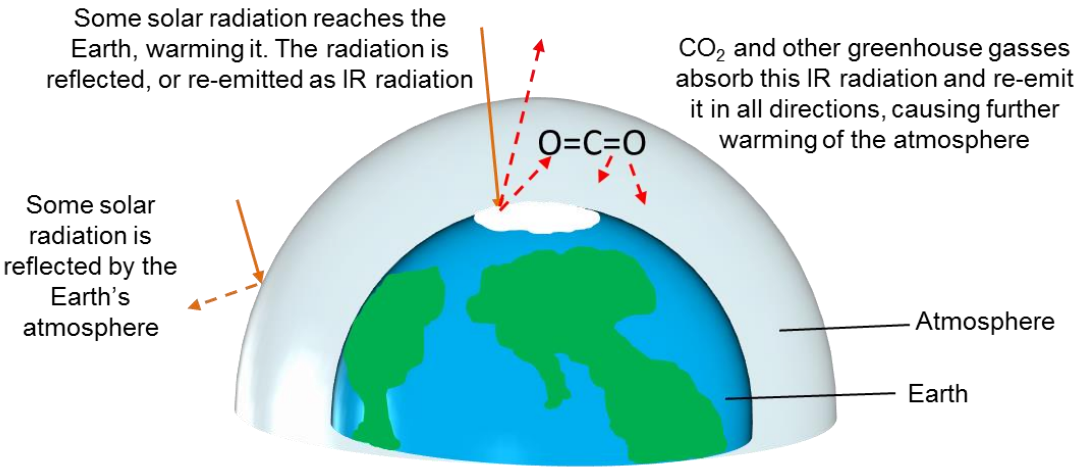

Fig. 1.1: *The greenhouse effect*

Along with soot and toxic gasses such as CO, the combustion of fossil fuels produces CO_2. In the late 19th century Svante Arrhenius quantified the contribution of CO_2 to the greenhouse effect (Fig. 1.1), and calculated that with increasing CO_2 levels, warming of the Earth would occur[1]. CO_2 levels at the beginning of the industrial revolution have been estimated as 280 ppm[2]. In late 1957 Keeling began measuring atmospheric CO_2 levels, providing incontrovertible evidence for a continuous

increase in the average annual CO_2 levels – from 316 ppm in 1957[2] to 393 ppm in 2012[3]. This proved that the extensive combustion of coal, oil and gas causes the volume of CO_2 produced to be too high to be counteracted by CO_2 absorption into oceans, and use of CO_2 for photosynthesis. Due to the greenhouse effect, the resulting increase in atmospheric carbon dioxide is causing global warming, an effect which is believed to be having catastrophic consequences on the Earth's climate.

According to the 2012 World Energy Outlook compiled by the International Energy Agency (IEA), energy demands are likely to continue increasing, causing a rise in CO_2 emissions from 31.2 Gigatonnes (Gt) in 2011 to 37.0 Gt in 2035[4]. This is due to a continued reliance on fossil fuels for energy production (Fig. 1.2). It is predicted that by 2050 global energy demands will reach 27.6 Terawatts (TW)[5]. Therefore, to meet future energy demands, and prevent significant environmental consequences, alternative energy resources must be utilised.

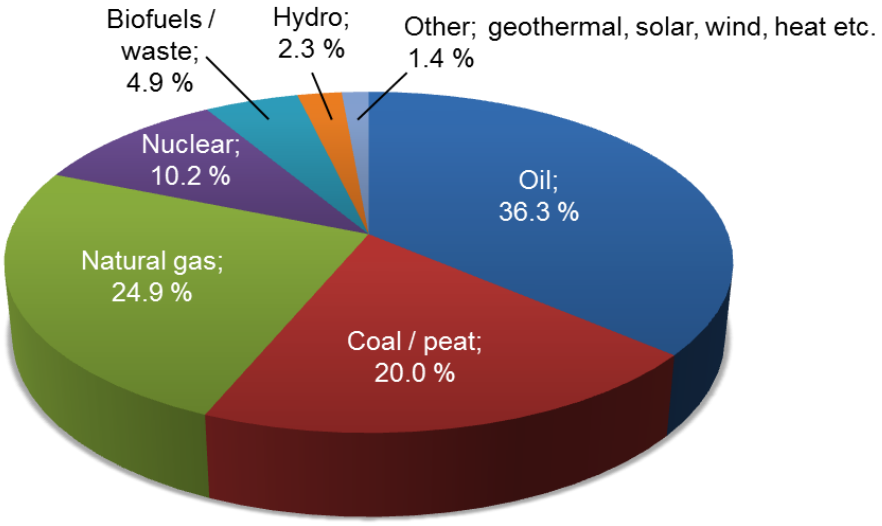

Fig. 1.2: *Primary energy supplies in 2011*[6]

Of the non-CO_2 emitting energy resources available, nuclear power has been the most widely developed. However, uranium is not yet being extracted from nuclear waste; thus under the current levels of consumption uranium will run out in 80 years[7]. Safety considerations after the Fukushima disaster in 2011 have also

prompted some countries to pledge to terminate nuclear energy production[8,9]. Therefore, using renewable sources of energy is likely to be the safest and most environmentally friendly method of fulfilling the world's long term energy demands. By comparing the maximum theoretical power that could be generated from different renewable energy resources (Fig 1.3)[5], it is clear that solar power has the most potential to fulfil our energy requirements. Therefore, solar technologies must be developed to capture and harvest this energy efficiently and cheaply.

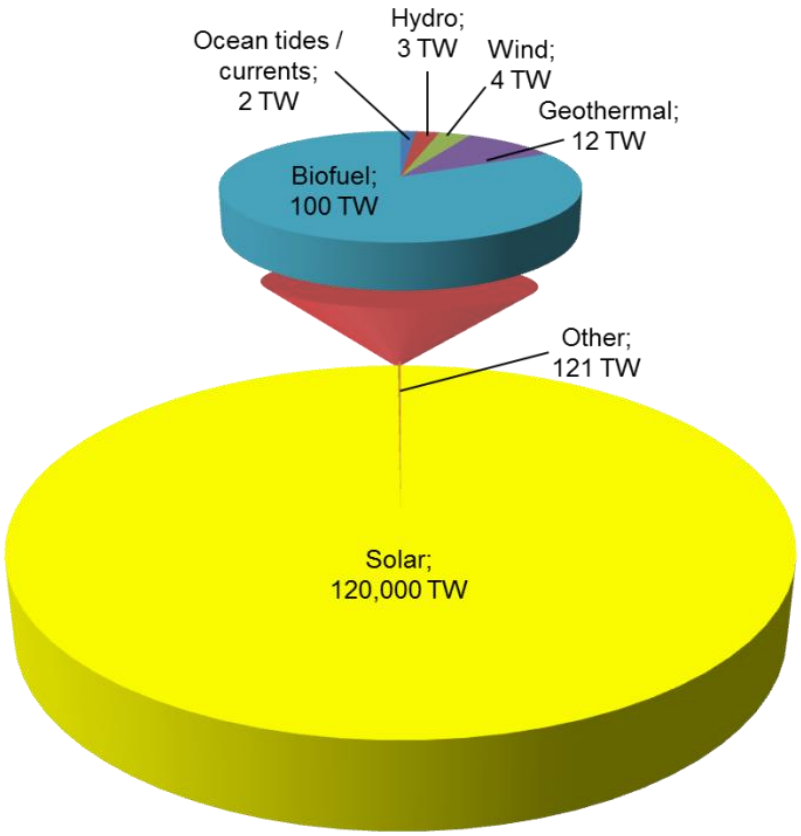

Fig. 1.3: *Maximum theoretical energy production from renewable energy resources*[5]

1.2 Solar technologies

As well as heating and lighting, solar power can be used in photocatalytic water splitting to produce hydrogen[10], and solar electricity production using photovoltaic

technologies. The photovoltaic effect (the generation of a voltage or current by exposure of a material to sunlight) was first discovered by Becquerel[11] in 1839 and was subsequently exploited in 1883 by Fritts[12] who is credited with making the first solar cell. Subsequently, advances in solar technology were driven by the development of new photovoltaic modules for space exploration. However, widespread commercialisation of solar cells in the late 1990s has caused the incidence of solar panel installation to rise exponentially, causing the volume of research into solar technologies to increase. Thus, by the end of 2012, worldwide installations of photovoltaic module surpassed 100 GW[13].

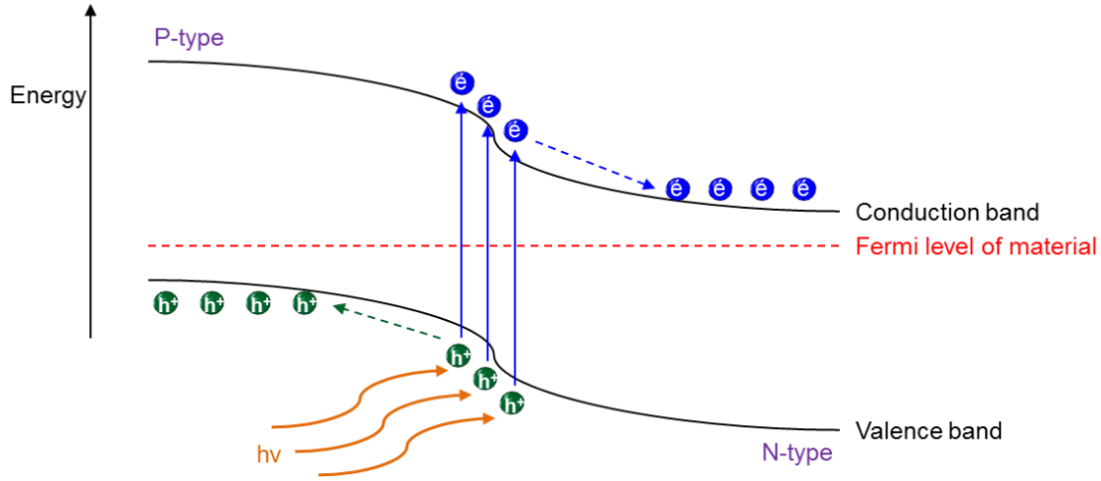

Fig. 1.4: *Charge separation across a p-n junction*

Since the first solar cell was discovered, many different types of solar cell have been devised. With all photovoltaic devices, separation of negative electrons and positive holes is essential to ensure electrical power is generated. The majority of cells achieve charge separation by generating an internal electric field across a p-n junction (Fig. 1.4). Such systems have been developed to reach high efficiencies (Table 1.1), but the environmental and economic costs of manufacture are large. Therefore, novel technologies, such as the Dye-Sensitised Solar Cell (DSSC), are being developed.

Solar cell type	Highest recorded efficiency / %	Year
Multi-junction cell	44.4	2013
Single-junction GaAs	29.1	2012
Single crystal Si cell	27.6	2005
Multicrystalline Si cell	20.4	2004
Thin film Cu(In,Ga)Se_2 cell	20.4	2013
Thin film CdTe cell	19.6	2013
Thin film amorphous Si	13.4	2013
Dye-sensitised Solar Cells	11.4	2011
Organic cells	11.1	2011
Quantum dot cells	7.0	2012

Table 1.1: *The highest recorded efficiencies of different types of solar cell at 1 sun (AM 1.5) in 2013*[14].

1.3 The Dye-Sensitised Solar Cell (DSSC)

1.3.1 The DSSC; an overview

DSSCs (Fig. 1.5) function by using a dye (generally a ruthenium polypyridyl complex) which absorbs solar radiation in the visible region of the electromagnetic spectrum. The resulting MLCT (step 1, Fig. 1.5) forms an excited state complex which injects an electron into the nanocrystalline TiO_2 (k_2, Fig.1.5); to which the dye is bound through carboxylic acid substituted polypyridyl ligands[15]. The dye is thus oxidised; but it is subsequently reduced by I^- ions (k_5, Fig. 1.5) regenerating the ground state of the dye. The injected electron diffuses through the TiO_2 (k_3, Fig. 1.5), is transferred into the FTO electrode and propagated around the external circuit to the platinum counter electrode. At this electrode, I_3^- ions are reduced (k_4, Fig. 1.5), forming the I^- ions used to regenerate the dye. Hence, the electrolyte completes the electrical circuit of the cell.

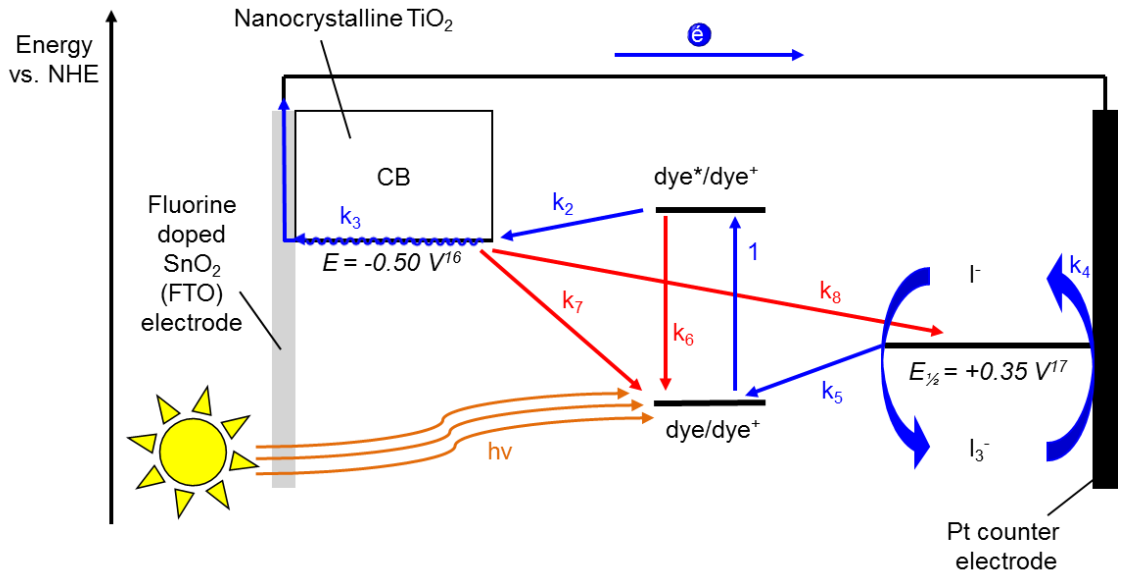

Fig. 1.5: *The possible electron transfer mechanisms in a DSSC*[16,17]

Loss mechanisms within a DSSC are radiative or non-radiative decay of the excited state dye (k_6, Fig. 1.5), recombination of the injected electron with the dye (k_7, Fig. 1.5) and recombination of the injected electron with the I^-/I_3^- redox couple (k_8, Fig. 1.5). These processes essentially short circuit the cell and prevent generation of electricity. The outcome of the kinetic competition between the forward and short circuit processes (Table 1.2) determines the efficiency of electron transfer within the solar cell.

Forward electron transfer		Competing loss mechanisms	
Process	Rate / s^{-1}	Process	Rate / s^{-1}
1; Dye excitation	-	-	-
k_2; Injection	$6.7 \times 10^9 – 2 \times 10^{13}$ [17]	k_6; Dye* decay	$2\text{-}6 \times 10^7$ [18,19]
k_3; Electron diffusion	$1.0\text{-}10 \times 10^5$ [20]	k_8; TiO_2 to electrolyte	$\approx 1 \times 10^3$ [17]
k_4; I_3 reduction	-	-	-
k_5; Dye regeneration	$1.6 \times 10^5 – 1.4 \times 10^8$ [21]	k_7; TiO_2 to dye	$2.9\text{-}5.6 \times 10^3$ [22,23]

Table 1.2: *The rates of electron transfer in an optimised TiO_2-Ru complex-I^-/I_3^- DSSC.*

1.3.2 The development of the DSSC

1.3.2.1 The invention of the DSSC

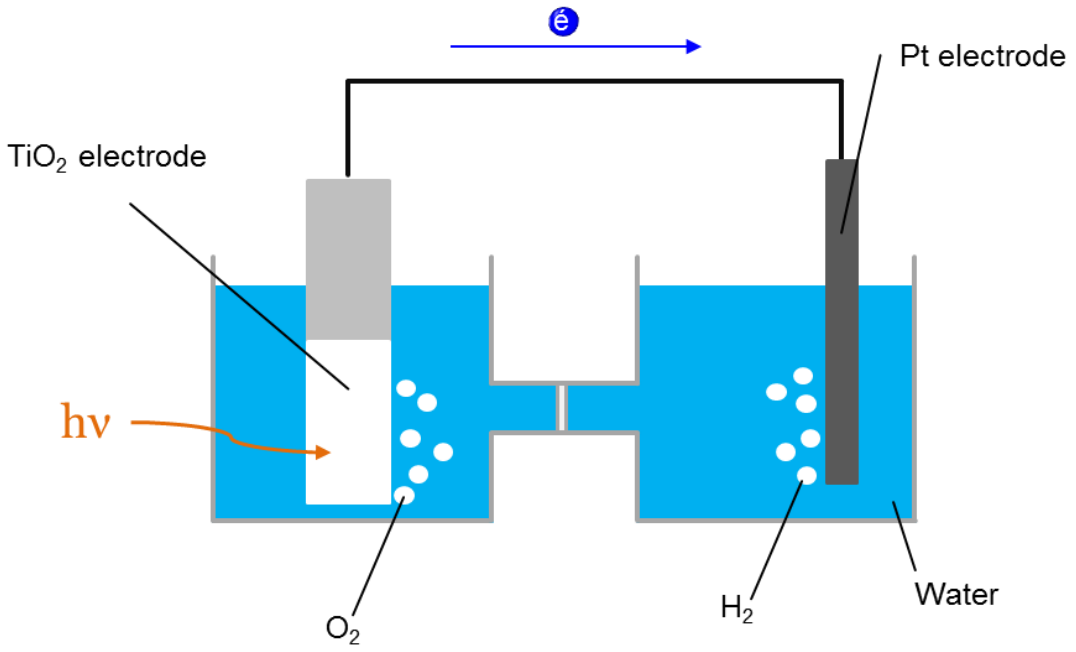

Fig. 1.6: *Generation of electricity by TiO_2*

In the early 1970s, the photolysis of water without the application of an external current was achieved by irradiation of a titanium dioxide semiconductor (Fig. 1.6). As well as splitting of water, this reaction induced a flow of current[24]. At a similar time, investigations into the mechanisms of photosynthesis showed the generation of an electrical current using a similar system (Fig. 1.7) but with added chlorophyll in the electrolyte solution to absorb sunlight[25].

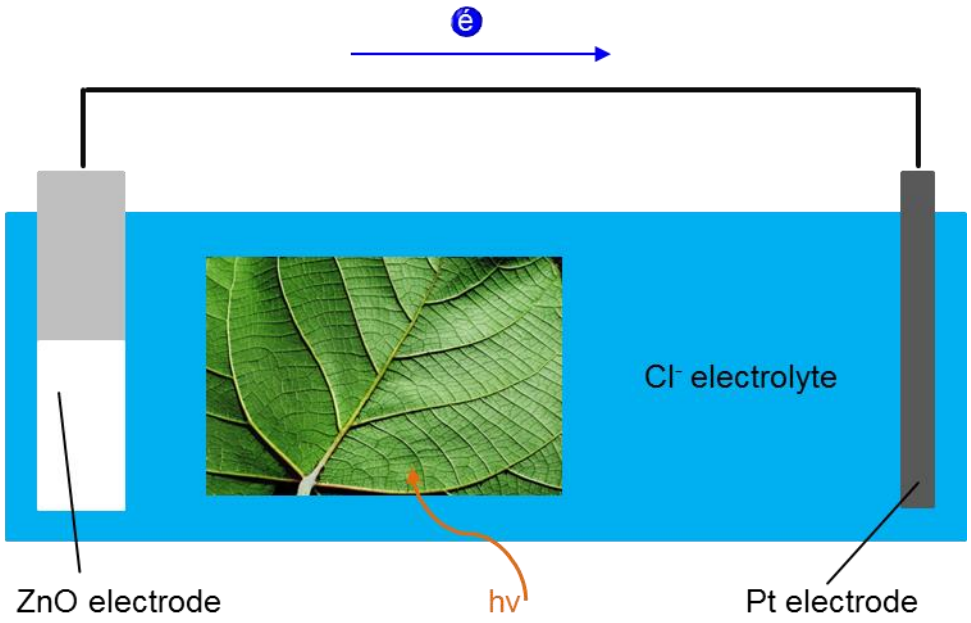

Fig. 1.7: *Investigations into the mechanism of photosynthesis*

Mimicking this process, dyes were used to overcome the poor absorption of solar radiation by wide band gap semiconductors (the band gap of TiO_2 is 3.2 eV[26]). The dye molecule was bound to a semiconductor surface to absorb sunlight in the visible region of the electromagnetic spectrum[27,28]. However, light harvesting by dying a smooth semiconductor surface was poor[26]. By preparation of colloidal polycrystalline TiO_2 films[29], more dye molecules were able to bind to the semiconductor surface (Fig. 1.8), causing a substantial increase in the light harvesting properties of the electrode.

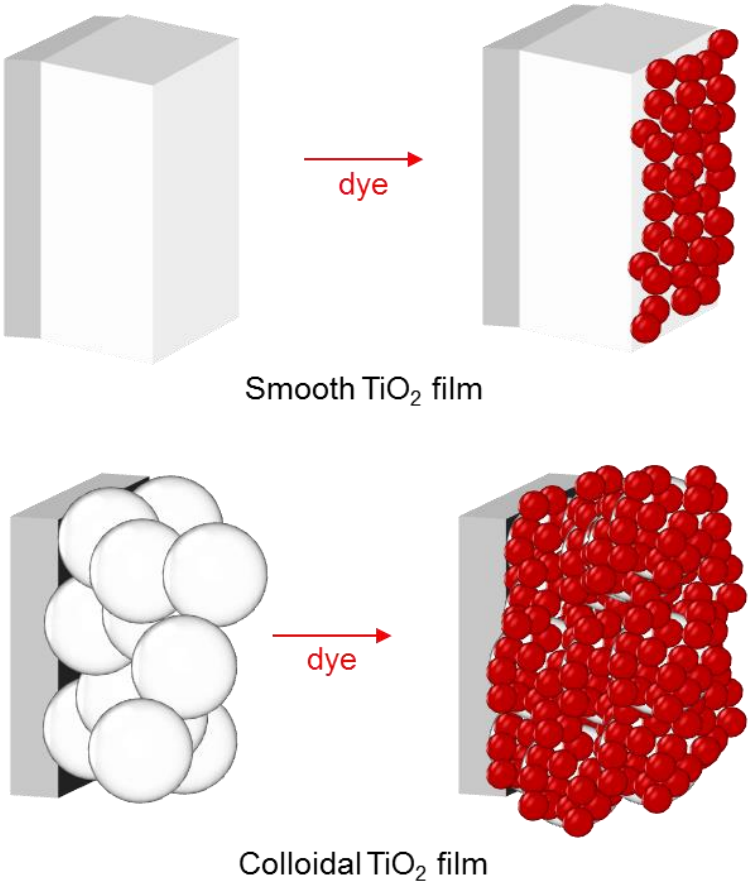

Fig. 1.8: *Increasing the surface area of the semiconductor. Within a solar cell the TiO_2 layer is hundreds of nanoparticles thick.*

To this point, symmetrical $[Ru(H_2\text{-dcbpy})_3]^{2+}$ dyes (Fig. 1.9a) were used for sensitisation of the semiconductor. By using this dye on a colloidal TiO_2 film, a solar cell with 1.2% efficiency at 1 sun (AM 1.5) was produced[29]. However, development of a novel asymmetric dye (Fig. 1.9b), in which the excited state electrons were 'funnelled' to the $Ru(H_2\text{-dcbpy})_2$ fragment which was bound to the TiO_2 layer, increased the efficiency of electron transfer into the semi-conductor[30]. This dye was the first example of a dye with intramolecular charge separation to prevent recombination of the electron hole pair generated by solar irradiation. By combining the use of this dye with the use of a high surface area TiO_2 electrode and an I^-/I_3^- electrolyte dissolved in an organic medium, the production of a solar cell with 7.0% efficiency at 1 sun was achieved[26]. This is regarded as the point at which the invention of the DSSC was realised.

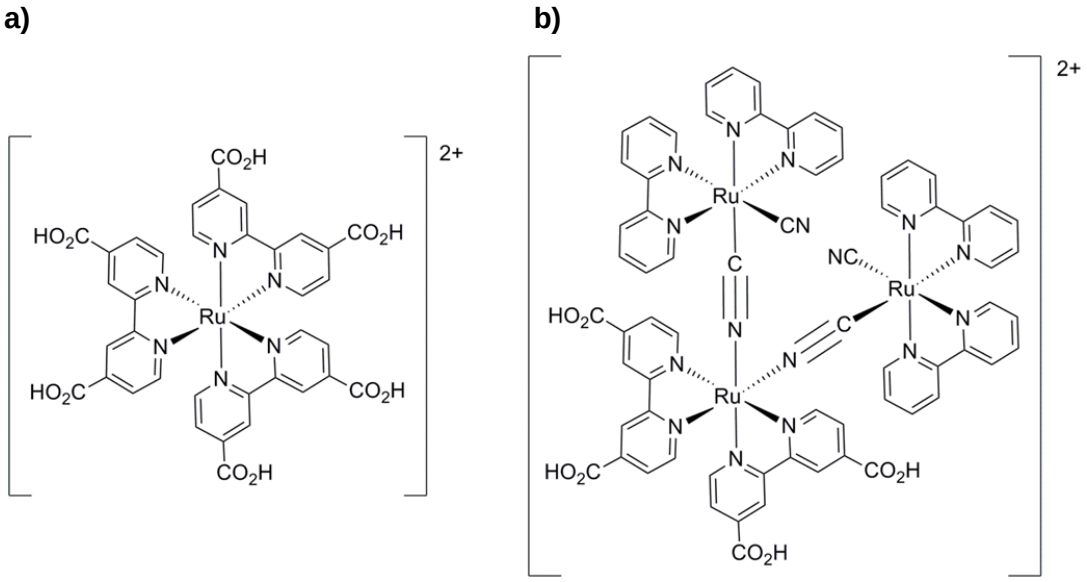

Fig. 1.9: *The first dyes used in DSSCs:* ***a)*** *symmetrical* $[Ru(H_2\text{-}dcbpy)_3]^{2+}$ *dye;* ***b)*** *asymmetric* $[Ru(H_2\text{-}dcbpy)_2(\mu\text{-}CN)_2(Ru(bpy)_2CN)_2]^{2+}$ *dye.*

1.3.2.2 From discovery to commercialisation of the DSSC

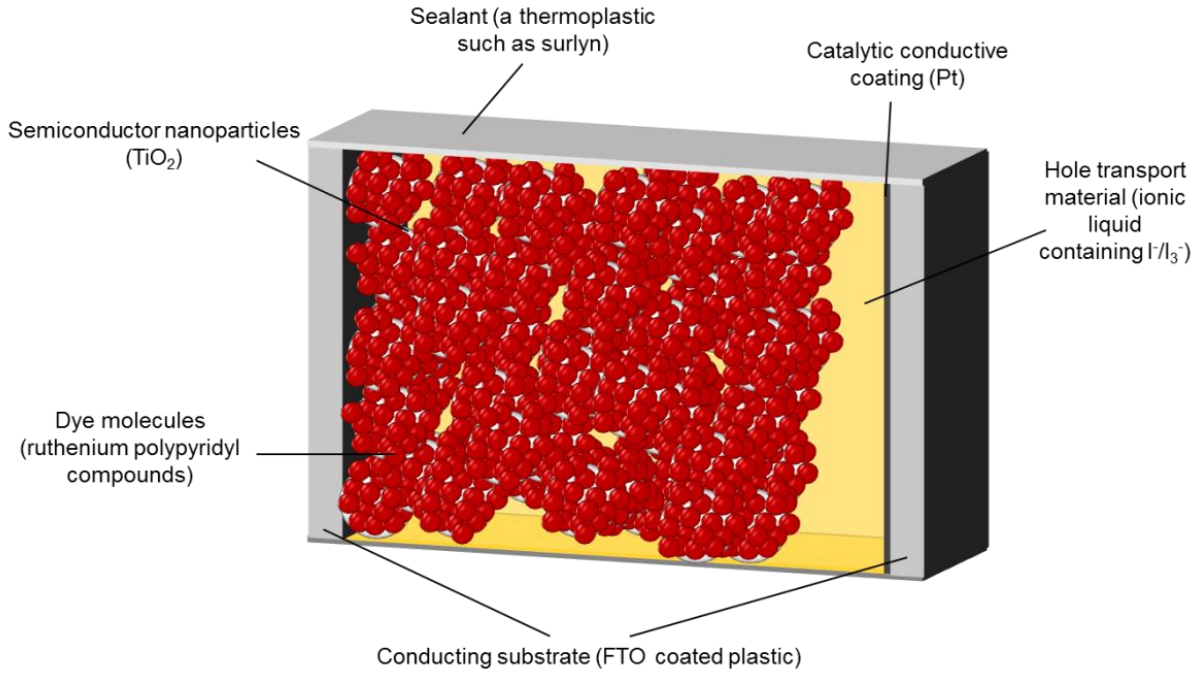

Fig. 1.10: *Components of a commercial DSSC*

Since 1991, the fundamental structure of the DSSC has changed little (Fig. 1.10), but the volume of research into the DSSC has increased exponentially. A lot of this research has focused on modifying the structure of the dye to improve cell efficiency. Formation of a bond between the dye and TiO_2 has been proved imperative for promotion of electron transfer between the dye and the semiconductor[31]; hence some research has explored the use of phosphonic acid groups ($PO(OH)_2$) instead of carboxylic acid groups (CO_2H) to link the dye to the TiO_2 nanoparticles. Although the phosphonic acid group binds more strongly to TiO_2[32], cells have been shown to be less efficient using this linker[33]. Therefore, ruthenium dyes containing carboxylic acid substituted bpy ligands (H_2-dcbpy) have been the most widely explored dyes for DSSCs.

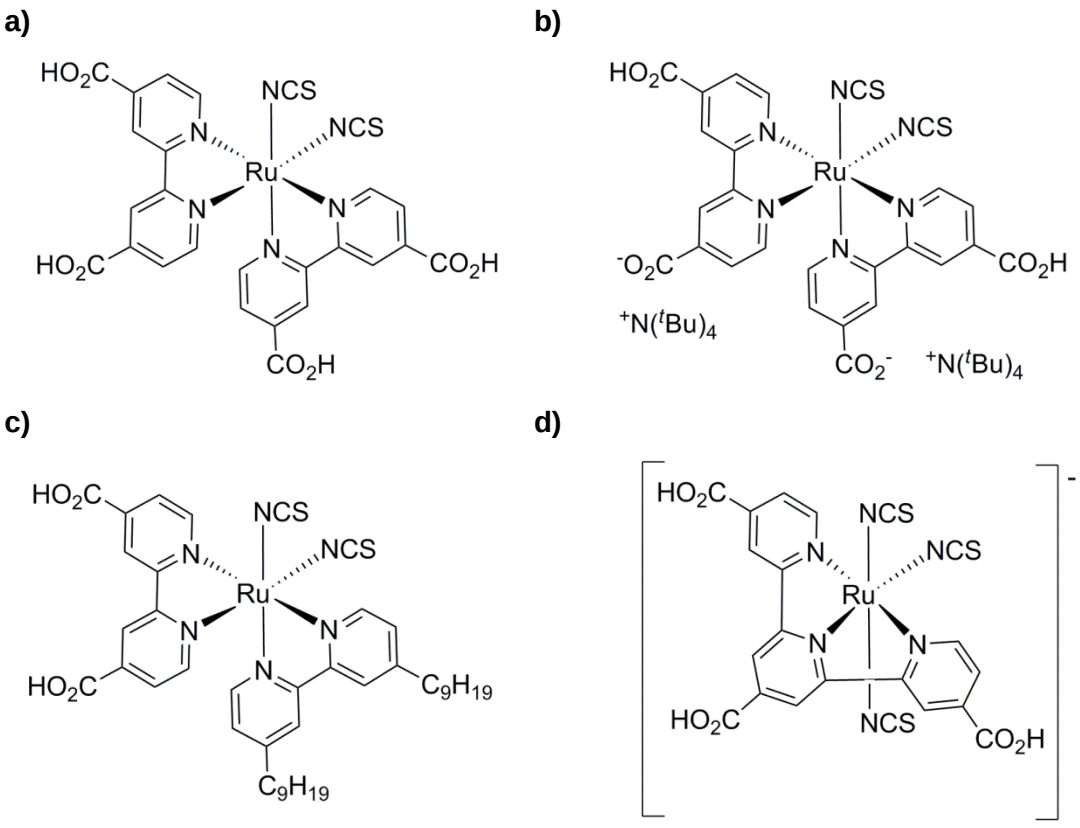

Fig. 1.11: a) *N3 dye;* ***b)*** *N719 dye;* ***c)*** *Z907 dye;* ***d)*** *black dye.*

A breakthrough in dye design was achieved when it was shown that in a series of $Ru(H_2\text{-dcbpy})_2X_2$ dyes where X = Cl^-, Br^-, I^-, CN^- and SCN^-, the cell efficiency was

considerably improved by use of the X = SCN^- analogue[18]. This research marked the discovery of the N3 dye (Fig. 1.11a). A subsequent investigation into the effect of the extent of protonation of the N3 dye on cell efficiency showed that the partially deprotonated N719 dye (Fig. 1.11b) produced the highest efficiency in a DSSC[34]. This dye is now the standard against which novel dyes are measured in a DSSC.

The black dye (Fig. 1.11d) was subsequently synthesised, and was shown to have significantly improved absorption in the red region of the solar spectrum compared to N719[35]. This dye currently holds the record for the highest externally verified efficiency in a solar cell[36]. However, poor cell stabilities led to investigations into asymmetric dyes such as Z907 (Fig. 1.11c). Z907 contains long alkyl chains to prevent interactions between the dye molecule and water; enhancing the stability of the dye on the TiO_2 surface[23]. Modifications of this type of asymmetric dye have generally involved the incorporation of chromophoric groups, such as thiophenes, into the long alkyl chains on the ancillary bpy ligand to increase the light harvesting properties of the dye[37,38].

Along with changes to dye structure, modification of each of the other components of the cell have been made resulting in a rise in the highest verified efficiency of the system from 7.0% in 1991[26] to 11.4% in 2012[36]. Although the cell efficiency is not as high as the efficiency of p-n junction cells (Table 1.1), manufacture of DSSCs can be performed using printing techniques, thereby reducing both the environmental and economic costs. The cells can be printed onto plastics to make flexible solar cells which can be incorporated into bags and clothing. DSSCs can also be recycled, further reducing their environmental impact. Unlike most p-n junction cells, DSSCs perform at a similar efficiency at low light intensities as in bright sunlight; so the cells will generate electrical power under indoor lighting. Therefore, the development of indoor electronics and bags incorporating DSSCs allowed commercialisation of the DSSC to be realised in 2009.

1.3.3 Dissecting an optimised DSSC: Desired electron transfer processes

1.3.3.1 Step 1: Dye excitation

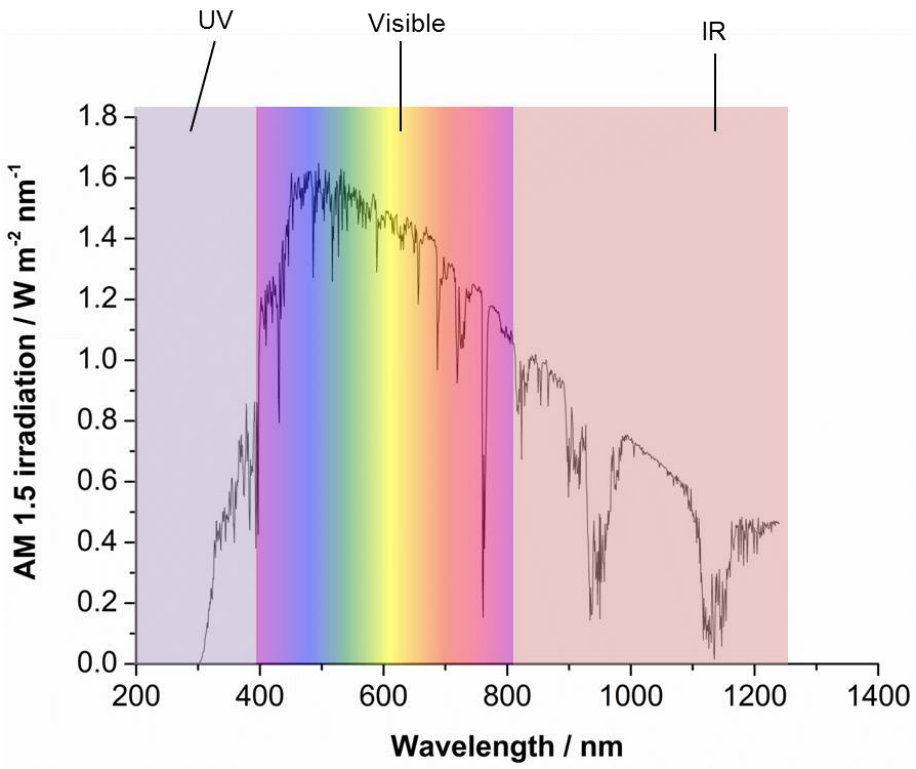

Fig. 1.12: *AM1.5 solar spectrum*[39]

Absorption of solar radiation by the dye in the solar cell induces electronic excitation of the dye. Solar radiation which reaches the Earth's surface is composed of light which is mostly in the visible region of the electromagnetic spectrum (Fig. 1.12). Therefore, it is essential that the electronic excitation of the dye is stimulated by light in the visible region. Irradiation of a ruthenium dye causes electronic excitation in the form of metal ligand charge transfers (MLCT), metal-centred transitions (d-d) and intra-ligand transitions (π-π*). The high energy π-π* transitions are in the UV region of the electromagnetic spectrum so they contribute little to electron transfer in a DSSC as there is very little solar radiation in the UV (Fig. 1.12). MLCT transitions dominate the absorption spectrum of ruthenium polypyridyl complexes in the visible

region of the electromagnetic spectrum[40]. And if the crystal field splitting of the ligands is high, these transitions are also the lowest energy transitions (Fig. 1.13) as the σ_M^* orbital will be higher in energy than the low-lying π_L^* orbital.

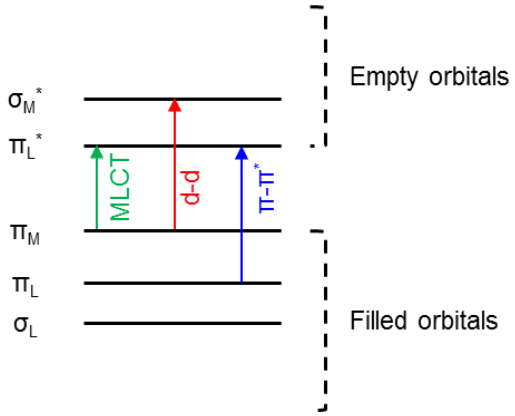

Fig. 1.13: *The electronic excitations observed in* $[Ru(bpy)_3]^{2+}$ [40]

MLCT excited states are a mixture of singlet and triplet states. For most ruthenium (II) polypyridyl complexes, the lowest energy MLCT excited state is a cluster of triplet states (^{3}MLCT)[40]. Transitions into this state are spin forbidden, although spin orbit coupling due to the heavy ruthenium atom does allow some singlet-triplet transitions to take place[41]. However, spin allowed excitations into singlet MLCT excited states (^{1}MLCT) dominate electronic excitation spectra[41,42]. These transitions are observed at slightly higher energies than transitions into ^{3}MLCT states, so transitions into the ^{3}MLCT excited state can be observed by a small increase in intensity of the red wing of the absorption spectrum[41]. π_M to π_L^* MLCT transitions are generally observed in ruthenium bis bipyridyl bis isothiocyanato complexes at 500-550nm[18,23,37,38]; within the visible region of the electromagnetic spectrum. The molar extinction co-efficients of these dyes are 7,000 to 14,000 $M^{-1}cm^{-1}$; hence they are effective light absorbers. However, the dyes do not absorb in the near IR and IR regions of the electromagnetic spectrum, so a large proportion of solar radiation is not absorbed by the DSSC.

The location of the excited electron within the dye is also important when considering dye excitation in DSSCs. In accordance with literature precedence[43], the LUMO of the ground state dye has been used to represent the excited state dye throughout this thesis. Within a solar cell dye, the HOMO and LUMO orbitals of the dye are discretely located (Fig. 1.14)[44]; thus the movement of electrons caused by electronic excitation is directed towards the H_2-dcbpy ligand which is bound to the TiO_2 nanocrystal. This directionality of electronic excitation is essential to promote electron injection into TiO_2.

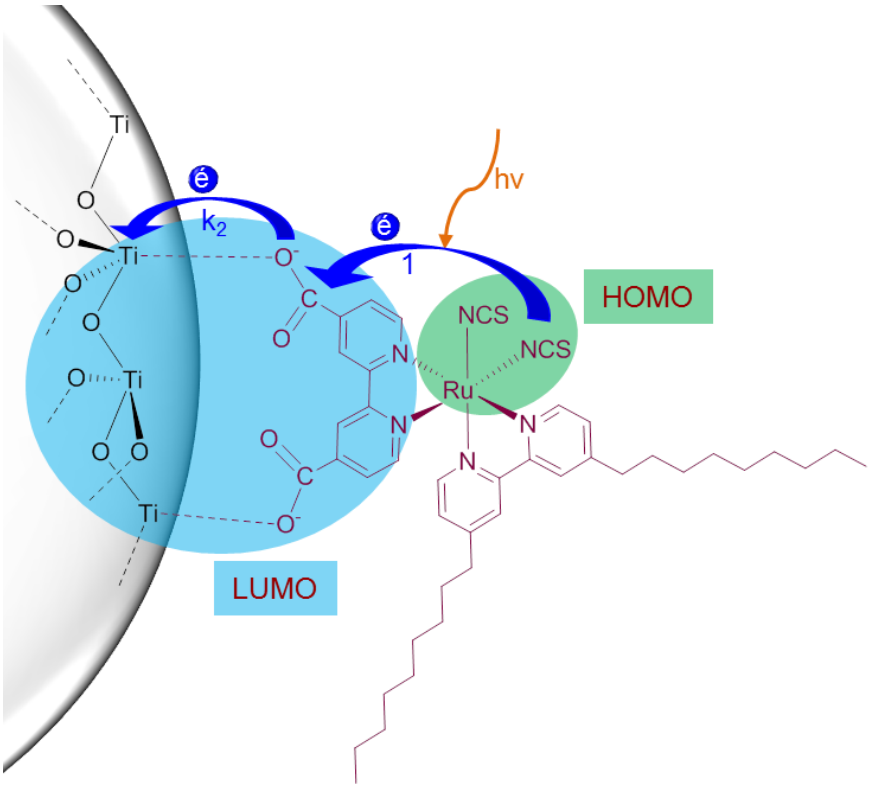

Fig. 1.14: *Electronic excitation and electron injection in a DSSC*

1.3.3.2 Step k_2: Injection into TiO_2

After absorption of light and electronic excitation, electron injection into the TiO_2 conductance band is necessary to begin the process of electron transfer around the circuit. Electron injection takes place from the MLCT excited state of the dye[45].

However, injection could occur before thermal equilibration of the excited state dye - from the Frank-Condon state (Fig. 1.15a) - or from the thermally equilibrated excited (thexi) state of the dye (Fig. 1.15b). Studies on electron transfer from dye sensitised TiO_2 into acceptor materials with a higher energy than the thexi state of the dye have shown that such electron transfer is feasible[46]. This verified previous studies, suggesting that electron transfer to the TiO_2 can take place before thermal relaxation of the excited state dye[47,48]. However, the efficiency of electron injection from the Frank-Condon state is poor[46], whereas electron injection within a DSSC is close to 100% efficient[17]. This suggests that within a DSSC injection occurs from both the Frank-Condon and thexi states of the dye.

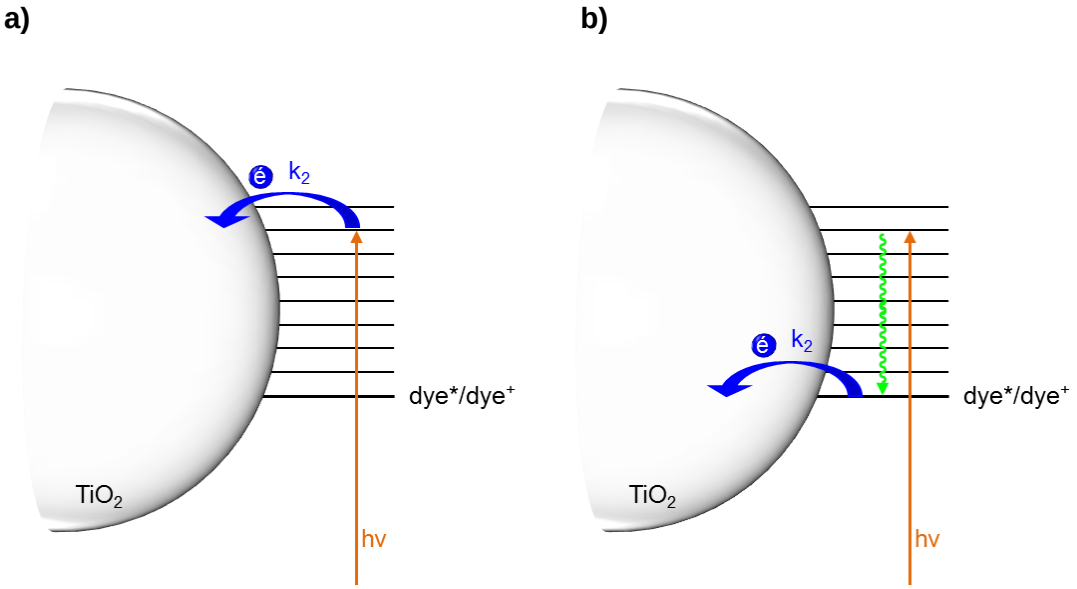

Fig. 1.15: *Electron injection from* ***a)*** *the Frank-Condon state of the dye;* ***b)*** *the thexi state of the dye*

Therefore, for efficient electron injection, the energy of the thexi state of the dye must be higher than the energy of the TiO_2 conductance band (0.5 V vs. NHE[16]). Electrochemical[18] and TD-DFT[44] studies have shown that the thexi states of ruthenium bipyridyl isothiocyanato complexes bound through a H_2-dcbpy ligand satisfy this criterion. To promote electron injection, the dye must also form a covalent bond with the TiO_2 surface (Fig. 1.14)[31]. Computational studies have shown

that on binding to TiO_2, the LUMO of ruthenium bis bipyridyl isothiocyanato dyes is delocalised into unoccupied states in the TiO_2 surface[49], which explains the experimental observations that electron injection into the TiO_2 conductance band occurs on a sub-picosecond time scale[50]. The rate of injection can vary depending on the TiO_2 conformation[51]; nonetheless electron injection within an optimised DSSC is a highly efficient process.

1.3.3.3 Step k_3: Diffusion through the TiO_2 nanoparticles

After injection into the TiO_2, diffusion of the injected electrons through the film to the FTO electrode is necessary. To ensure electron diffusion through the entire film can occur, the titania nanoparticles are annealed at high temperatures to form crystalline anatase, thus ensuring that the TiO_2 nanoparticles are electronically interconnected[20]. Electrons injected into the TiO_2 are shielded by cations in the electrolyte[52,53], so the diffusion of electrons through the electrode is not influenced by an internal electric field. Electron diffusion is therefore random; hence the transport of electrons through TiO_2 has been defined computationally using a random walk model (Fig. 1.16)[20].

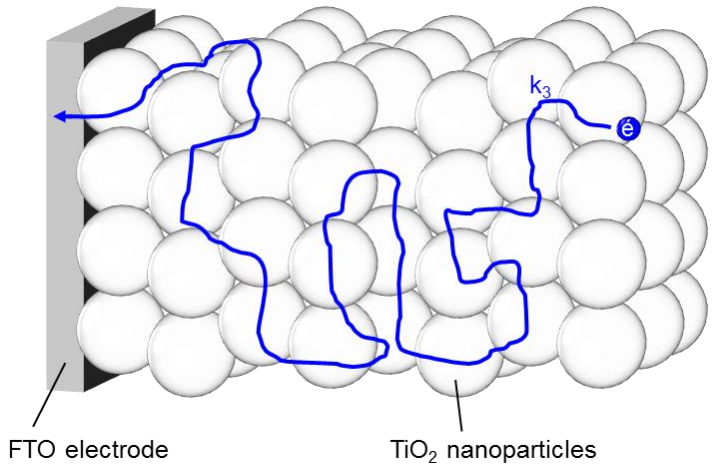

Fig. 1.16: *Random walk model for electron diffusion in TiO_2 nanoparticles*

Electron diffusion is, however, complicated by charge trapping[53], as electrons in the TiO_2 film can be trapped on picosecond to nanosecond timescales and the electron normally takes a few microseconds to reach the anode[20]. Thus, electron trapping is only prevented when all of the traps are filled – hence when the Fermi energy of the electron is close to the energy of the conductance band. This is demonstrated as the diffusion co-efficient increases at higher light intensities when more electrons are present in the TiO_2 film[52]. Therefore, at low light intensities, electron trapping can reduce the rate at which the electron reaches the FTO electrode.

1.3.3.4 Step k_4: I_3^- reduction and electrolyte diffusion

$$I_3^- + 2\acute{e} = 3I^- \qquad \text{Reaction 1.1}$$

$$D = \frac{kT}{6\pi\eta r} \qquad \text{Equation 1.1}$$

After propagation of the electron around the circuit, electrolyte reduction is necessary for electron transfer. The reduction of I_3^- to form I^- (Reaction 1.1) is facilitated by the platinum layer on the counter electrode[54]. Chemisorption of I_2 or I_3^- onto the platinum surface causes the I-I bond to break[55], thus the reduction becomes a rapid one-electron process[17]. By applying a platinum layer containing nano-sized platinum metal clusters to the counter electrode, the reduction of I_3^- is achieved rapidly; which reduces losses in electrochemical potential within the DSSC[54].

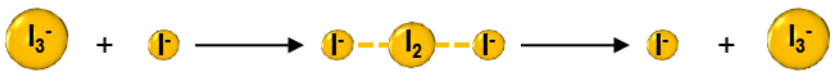

Fig. 1.17: *Grotthus mechanism of ion diffusion*

At low concentrations, transport of iodide and tri-iodide is mostly driven by diffusion[17], the rate of which is described by the diffusion coefficient (D) which is dependent on Boltzmann's constant (k), the temperature (T), the viscosity of the solution (η), and the radius of the ion (r) (Equation 1.1). When high concentrations of

iodine are added to the electrolyte, the rate of tri-iodide diffusion increases beyond what would be predicted by the Stokes-Einstein equation (Equation 1.1) which is likely to be due to a Grotthus mechanism of diffusion[56] (Fig. 1.17). However, increasing the concentration of iodine added into the electrolyte can also lead to an increase in photochemical reactions which cause electrolyte decomposition[17]. Fast diffusion of iodide is required for efficient dye regeneration, and fast diffusion of tri-iodide / iodine is necessary to prevent depletion of tri-iodide at the counter electrode causing a loss in cell voltage[17]. Therefore, the electrolyte composition has been heavily optimised in order to reduce the effects of electrolyte decomposition, while preventing the diffusion of the electrolyte from becoming a rate limiting process in the DSSC.

1.3.3.5 Step k_5: Dye regeneration

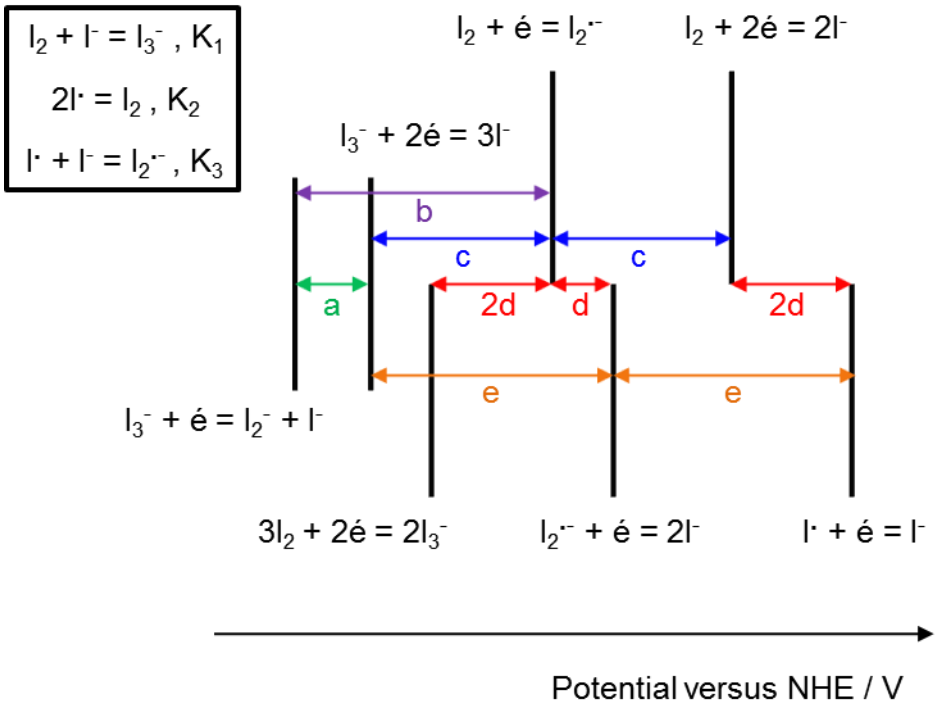

Fig. 1.18: *Redox reactions of the iodine – iodide system[17]. The differences in the formal potentials are a = (RT/F)ln(K_3); b = (RT/(2F))ln(K_2); c = b - a; d = (RT/(2F))ln(K_1); e = c + d.*

Due to the complicated nature of the I^-/I_3^- redox couple (Fig. 1.18), the mechanism of dye regeneration is not fully understood. The $E_{½}$ of the I^-/I_3^- redox couple is about 0.35 V versus NHE in acetonitrile[17], although the potential does vary by ± 0.05 V depending on the concentration of the redox species according to the Nernst equation (Equation 1.2); where E^θ is the formal potential of the couple in volts, R is the gas constant in J K^{-1} mol^{-1}, T is the temperature in K, and F is the Faraday constant in C mol^{-1}. A potential energy drive is required for dye regeneration to be successful. However, to determine the required potential of the oxidised dye, the mechanism of dye regeneration must be understood to reduce any overpotential in the cell whilst ensuring the energetics of the process remain favourable.

$$E_{redox} = E^\theta + \frac{RT}{2F} \ln \frac{[I_3^-]}{[I^-]^3} \qquad \text{Equation 1.2}$$

$$2dye^+ + 4I^- \longrightarrow 2dye^0 + I_3^- + I^- \qquad \text{Reaction 1.2}$$

The overall reaction for dye regeneration is a two electron transfer reaction[57] involving two dye molecules and four I^- ions (Reaction 1.2). Transient absorption studies have provided evidence for the generation of the I_2^- radical intermediate during the dye regeneration reaction[58]. This radical disproportionates to complete the regeneration process forming I^- and I_3^- (Step 2, Fig. 1.19); a reaction which occurs at a rate of 3 x 10^9 s^{-1} [59]. The considerably slower rate of dye regeneration (7.8 x 10^5 s^{-1} [21]), shows that disproportionation of the I_2^- radical is not the rate determining step of the reaction; thus the formation of the I_2^- radical determines the reaction rate.

Studies have shown that the regeneration reaction is first order with respect to the iodide concentration[21,58] suggesting that the formation of ion pairs to generate the I_2^- radical involves more than one step. The influence of the surface charge of the TiO_2 semi-conductor on the rate of regeneration led to suggestions that I^- ion pair formation on the TiO_2 surface aided the regeneration process[57]. However, more recent experimental[22,37,60], and computational[61-63] studies have showed that the regeneration rate is dependent on the ruthenium sensitiser, and this dependence does

not correlate with the potential driving force for regeneration[22]; suggesting that the dye structure is important. A mechanism for dye regeneration incorporating a dye-I^- intermediate was therefore postulated (Mechanism 1, Fig. 1.19), and this is the most widely accepted mechanism of dye regeneration[17].

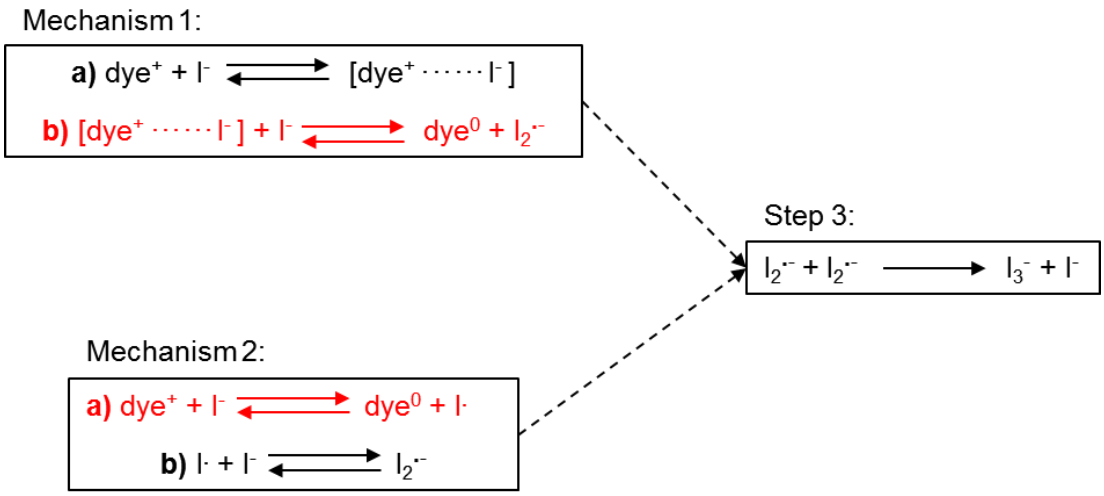

Fig. 1.19: *Possible mechanisms of dye regeneration. The rate determining step is highlighted in red.*

However, transient absorption studies showed that the rate of formation of the I_2^- radical was too slow for this radical species to be a direct product of dye regeneration. Instead, the rate was entirely consistent with the formation of this species by the reaction of an iodine atom with I^- (Mechanism 2b, Fig. 1.19)[64]. This observation is consistent with a mechanism for dye regeneration (Mechanism 2, Fig. 1.19) which has long been disregarded[21,57] because the oxidation of I^- to the iodine atom (Mechanism 2a, Fig. 1.19) has a potential which is 0.13 V higher than the reduction potential of the standard ruthenium bis bipyridyl bis isothiocyanato dye (Fig. 1.20)[65]. However, a recent computational study has explored an inner sphere electron transfer process whereby an interaction between the $^-$NCS ligand and the iodide ion leads to partial desolvation of I^-, causing a reduction in the oxidation potential of I^- [65]. This reduction in potential was calculated to be sufficient to allow oxidation of I^- by the dye; hence this mechanism of dye regeneration could be energetically feasible. If such a mechanism for dye regeneration were possible, it

would be consistent with the reaction being first order with respect to the concentration of I⁻. This mechanism of dye regeneration could also explain the considerable dependence of the DSSC efficiency on the solvent used in the electrolyte[66]. However, considerably more research would be necessary to determine the implications of this mechanism of dye regeneration on the possibility of reducing potential losses in the cell during the dye regeneration process.

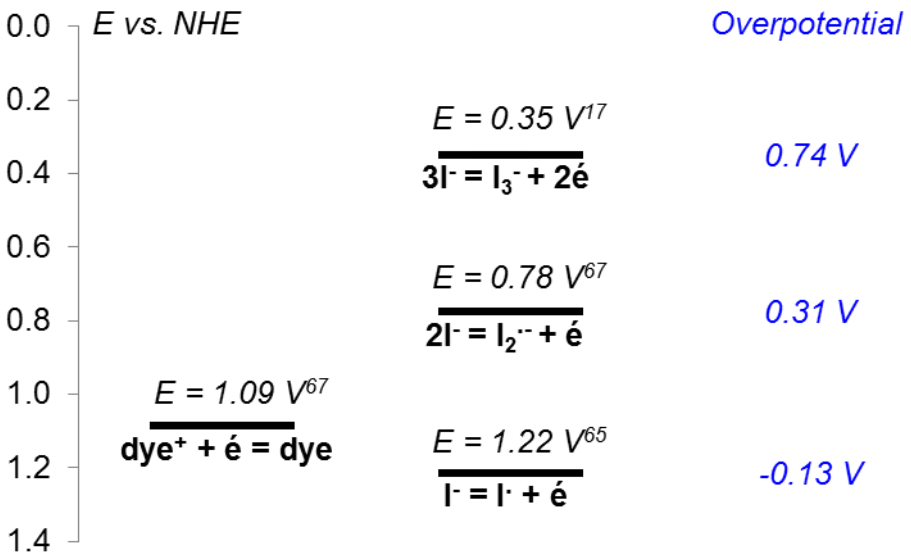

Fig. 1.20: *The energetics of dye regeneration[17,65,67].*

The range in the potentials of the possible intermediate electron transfer processes involved in dye regeneration is significant. By comparing the reduction potential of the dye to the standard electrochemical potential of the I^-/I_3^- couple (Fig. 1.20), it is clear that this is the origin of what is seen by many researchers as a large overpotential in dye regeneration in an optimised cell. To ensure that dye regeneration will be energetically favourable, the dye regeneration mechanism must be understood. Thus, this system could be further optimised by comparison of the reduction potential of the oxidised dye with the standard potentials of the reaction intermediates described.

As discussed, it is widely accepted that formation of a dye-I$^-$ intermediate is the rate-determining step of dye regeneration, and vibrational spectroscopy studies have provided evidence for this interaction[61]. The presence of $^-$NCS ligands in the dye appears to facilitate dye regeneration[22], as even dyes which don't contain $^-$NCS but produce high efficiency DSSCs have slower regeneration rates than $^-$NCS containing dyes[37,60]. Gas phase computational studies have shown favourable energetics for the formation of an NCS-I$^-$ interaction[62], and as the HOMO of the dye is delocalised across the ruthenium atom and the $^-$NCS ligands[44], the positive hole is partially located on this part of the dye after electron injection. Therefore, whatever the mechanism of dye regeneration, it is likely that an interaction between the $^-$NCS ligands and I$^-$ facilitates dye regeneration in an optimised DSSC (Fig. 1.21).

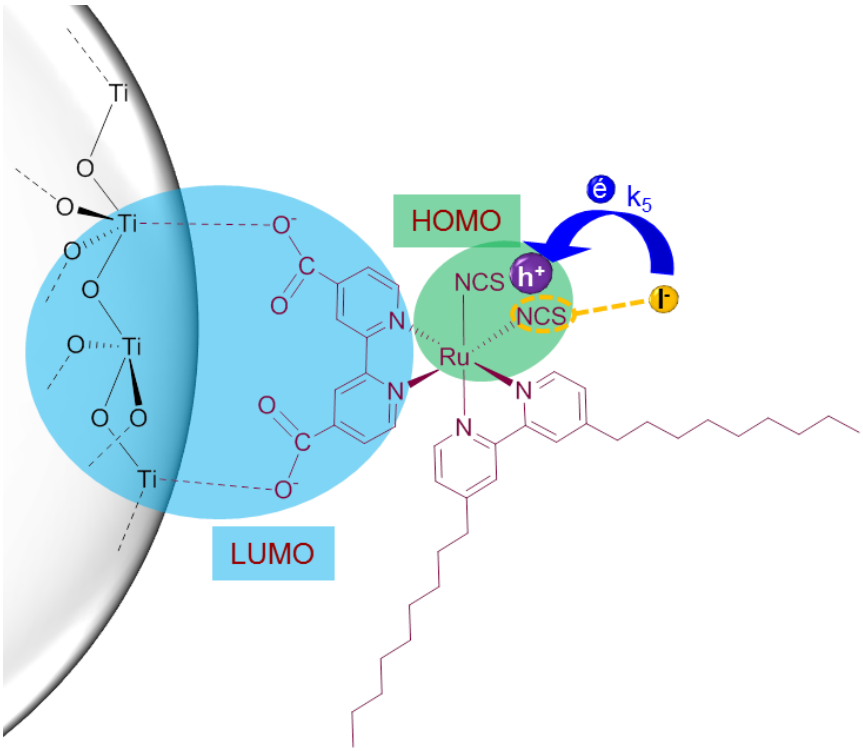

Fig. 1.21: *Dye-electrolyte interactions in the DSSC.*

1.3.4 Dissecting an optimised DSSC: Loss mechanisms

1.3.4.1 Step k_6: Decay of the dye excited state

Within a DSSC, decay of the dye excited state competes with, and can therefore prevent, electron injection into the TiO_2 film. In solution, after excitation of an electron to an excited state, a number of relaxation processes can occur which cause the electron to return to the ground state (2.2.2.2). The most common decay mechanism for ruthenium dyes results in phosphorescence; thus the excited state lifetime of ruthenium bis bipyridyl bis isothiocyanato dyes in solution is fairly long; about 15-50 ns[18,19]. The luminescence properties of ruthenium dyes are affected by binding to TiO_2[45], but rapid injection also prevents observation of excited state decay on a TiO_2 surface, so solution measurements are often used as approximations for excited state decay in the solid state. As injection into TiO_2 occurs on a picosecond timescale and can take place from the Frank-Condon state, the dye does not need to have a very long lived excited state for electron injection. The excited state decay of the dye in solution is at least two orders of magnitude slower than injection into the TiO_2 surface (Table 1.2, 1.3.1); thus this process is rarely observed as a loss mechanism in an optimised DSSC.

1.3.4.2 Step k_7: Electron recombination to the dye

At very high light intensities, when the TiO_2 surface has a high electron concentration, recombination of the injected electron with the hole which is localised on the dye can compete with dye regeneration[68]. As dye regeneration is deemed the rate determining step of the DSSC, it is imperative that this recombination mechanism is slow to prevent the DSSC from short circuiting. In an optimised DSSC, electron transfer from the TiO_2 to the dye is slower than dye regeneration as the lifetime of oxidised ruthenium bis bipyridyl bis isothiocyanato dyes bound to TiO_2 is in the order of milliseconds[22]. This long lifetime is contrary to the large driving force for this backwards electron transfer process; *ca.* 1.59 V (determined

from the difference between the potential of the TiO_2 conductance band[16] and the reduction potential of the oxidised dye[67] vs. NHE).

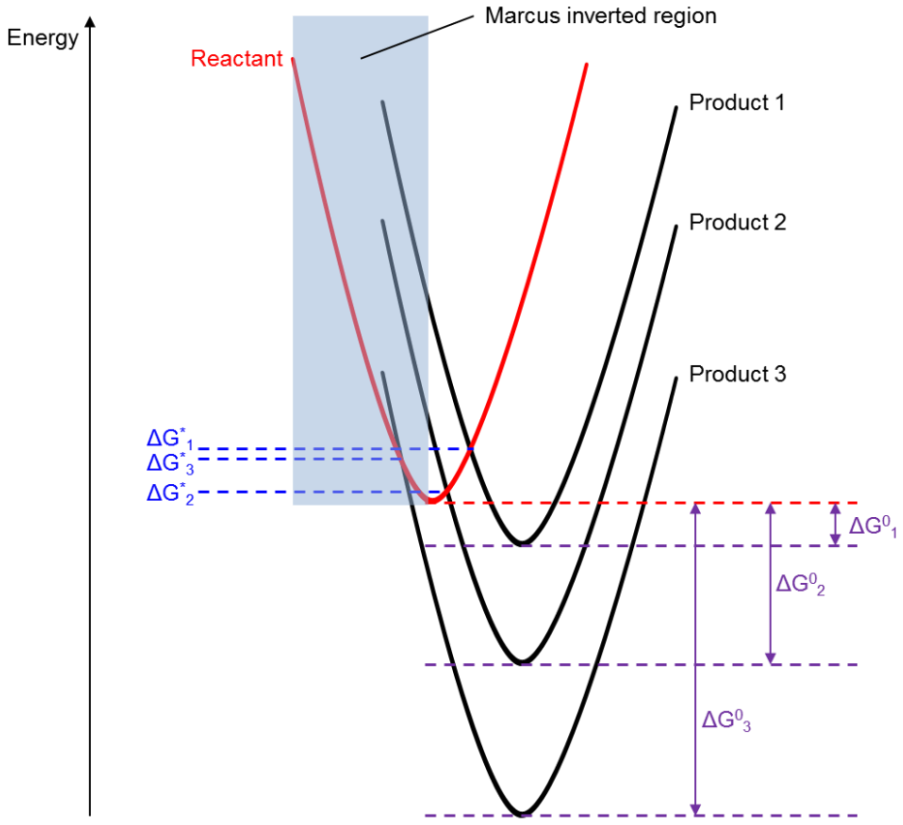

Fig. 1.24: *An illustration of Marcus theory[69]. In this case $\Delta G^0_3 > \Delta G^0_2 > \Delta G^0_1$; whereas $\Delta G^*_1 > \Delta G^*_3 > \Delta G^*_2$.*

$$\Delta G^* = \frac{\lambda}{4}\left(1 + \frac{\Delta G^0}{\lambda}\right)^2 \qquad \text{Equation 1.3}$$

However, Marcus theory[70,71], which describes the relationship between the free energy of activation (ΔG^*) and the free energy of an electron transfer process (ΔG^0), suggests a parabolic relationship between the two parameters (Equation 1.3); the effect of which is dependent on the reorganisation energy (λ). Thus, when $\Delta G^0 > \lambda$; $\Delta G^* > 0$, the electron transfer process is in the Marcus inverted region; implying that with a higher free energy, the activation energy of an electron transfer process will increase (Fig. 1.24). In DSSCs, recombination of the injected electron with the

oxidised dye has been shown to be in the Marcus inverted region, as the lifetime of the dye cation on TiO_2 increases as the driving force for recombination increases[72-75].

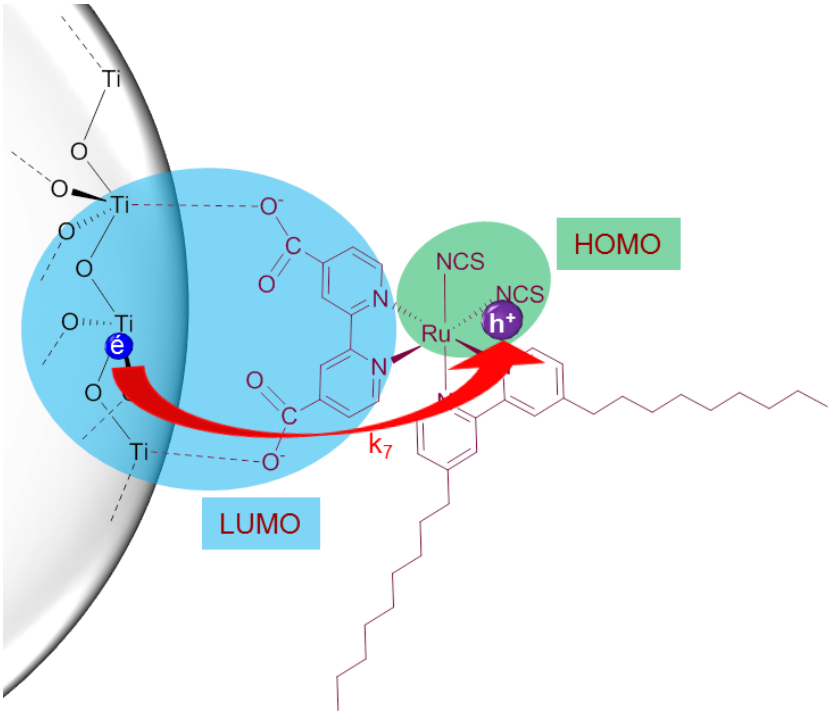

Fig. 1.25: *TiO_2-dye$^+$ recombination in a DSSC.*

Yet, the experimental data for the rate of recombination of a series of ruthenium dyes, $Ru(H_2\text{-dcbpy})_2XX$ dyes where XX = $(CN)_2$, Cl_2, $(NCS)_2$, DTC (dithiocarbamate), bound to TiO_2 does not follow Marcus theory. In each of the dyes, the HOMO is localised on the Ru atom and the XX ligand(s), but the decrease in dye lifetime was found to be directly proportional to the proportion of electron density localised on the ruthenium metal of the dye – with more HOMO electron density localised on the ruthenium metal centre, the rate of dye recombination increased[76]. Therefore, it is clear that significant spatial separation between the hole and the injected electron (Fig. 1.25) is important to prevent recombination of the injected electron and the dye cation. In this respect, ruthenium bis polypyridyl bis isothiocyanato dyes have proved highly successful dyes for DSSCs, as a large proportion of the HOMO is localised on the sulfur atoms of the $^-$NCS ligands[44]. Charge recombination to these dyes is also in the Marcus inverted region[75]; therefore,

there are both physical and energetic barriers to charge recombination in optimised DSSCs incorporating ruthenium bis bipyridyl bis isothiocyanato dyes.

1.3.4.3 Step k_8: Electron recombination to the electrolyte

Possibly the most common loss mechanism in the DSSC is the reduction of the redox electrolyte by the electrons injected into the TiO_2 surface (Fig. 1.26)[20]. This reaction occurs at only a slightly slower rate than electron diffusion away from the surface (Table 1.2, 1.3.1); so can have a significant impact on the performance of the solar cell. In the case of the one-electron Fc^+/Fc redox couple, electron recombination was the dominant process observed[17] as the rate of Fc^+ reduction at the TiO_2 surface competed with the electron transfer rate. However, the reduction of the I^-/I_3^- redox couple is a slow two-electron process[68] which is catalysed at the platinum counter electrode; thus promoting forward electron transfer in an optimised cell.

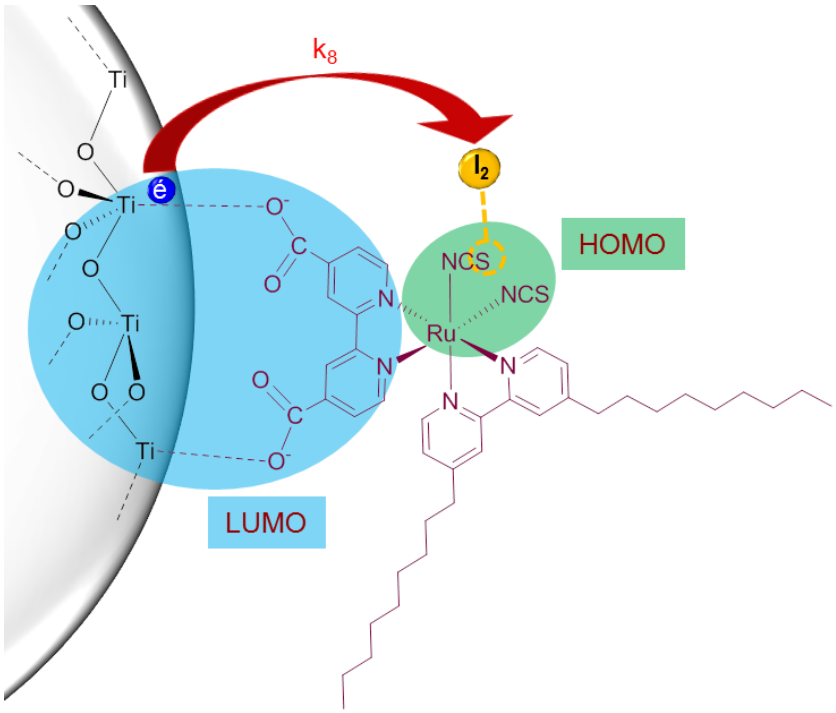

Fig. 1.26: *TiO_2-electrolyte recombination in a DSSC.*

Prevention of recombination across the TiO_2 interface has been achieved by addition of species such as 4-tert-butylpyridine[17], and guanadinium thiocyanate[77,78], to the electrolyte. Blocking layers such as citric acid[79], and more commonly chenodeoxycholic acid[80] are often added as a physical barrier to prevent recombination across this interface. A physical barrier to this recombination process can also be introduced by use of dyes with long alkyl chains[37,81]; hence the success of the Z907 dye[23].

By measuring the electron lifetime in the TiO_2 film using photovoltage decay methods, it has been shown that it is the reduction of iodine which causes this recombination process in a DSSC[79], not I_3^- as might be expected. Light induced photovoltage measurements[82,83] and impedance studies[84,85] on dye series which have similar physical barriers to recombination have also shown that the rate of recombination across the TiO_2 / electrolyte interface is affected by the dye structure. Binding between I_2 and the bpy ligands is weak[83], and growth of a crystal of an N3-I_2 adduct[86] showed that I_2 binds to the sulfur atoms of the $^-$NCS ligands (Fig. 1.26). Further studies have shown that I_2 can also bind to substituent groups such as NH_2 on ancillary ligands[87,88] which results in poorer cell efficiencies. This therefore suggests that interactions between the iodine molecule and the dye cause an increase in the I_2 concentration near to the TiO_2 surface, which can lead to an increase in recombination across the TiO_2 - electrolyte interface. Further understanding of this process of recombination, and the effect of the dye structure on the prevalence of this electron transfer mechanism, may enable engineering of more suitable sensitisers for DSSCs.

1.3.5 Recent breakthroughs in the DSSC

Up to 2010, little success had been achieved in increasing the efficiency of the DSSC by using different components (ie. different electrolytes or types of dye) to make up the cell. However, replacement of the electrochemically complex and corrosive I^-/I_3^- redox electrolyte has been an important area of research[89]. Particular focus has been placed on the use of cobalt polypyridyl complexes as electrolytes, but little success

was achieved combining this electrolyte with ruthenium sensitisers[90]. In 2010 a breakthrough was achieved when a DSSC utilising an organic sensitiser and a cobalt electrolyte was reported with 6.7% efficiency[91]. Significant research thus begun into such systems, and, by 2012, a DSSC utilising two zinc porphyrin dyes to co-sensitise the TiO_2 surface with a cobalt tris (bpy) tetracyanoborate electrolyte, was produced. This cell achieved an efficiency of 12.3%[92], and is currently the world record holder for the highest efficiency of a DSSC; although this value hasn't been externally verified.

Another large area of research has focused on the use of solid state hole transport materials to replace liquid electrolytes, thus circumventing any issues regarding leakage of electrolytes. Solid state hole transport materials such as spiro-OMeTAD and polymers including PEDOT or P3HT have been used, and due to a reduction in the overpotential required for dye regeneration such systems have produced a cell with the highest recorded V_{OC}[93]; and efficiencies have reached 7.1%[94]. By combining a TiO_2 layer, sensitised by a perovskite based dye on an inert Al_2O_3 scaffold, with the spiro-OMeTAD hole conductor, a solid state device was recently produced with an efficiency of 15.0%[95]. This device functions by electron transport through the perovskite layer; thus this development marks the invention of a novel type of hybrid solar cell which has evolved from the solid state DSSC.

1.3.6 Scope for research into ruthenium dyes for DSSCs

Despite the recent breakthroughs which have caused a shift in the focus of research into DSSCs, it is still solar cells with ruthenium based sensitisers that have produced solar cells with the highest externally verified efficiency[36]. The TiO_2-ruthenium dye-I^-/I_3^- system is used in commercial DSSCs, and until the reproducibility, manufacturability, and stability of novel types of DSSC can be proven, research into ruthenium dyes must continue.

1.3.6.1 Increasing the stability of the DSSC

a) **b)**

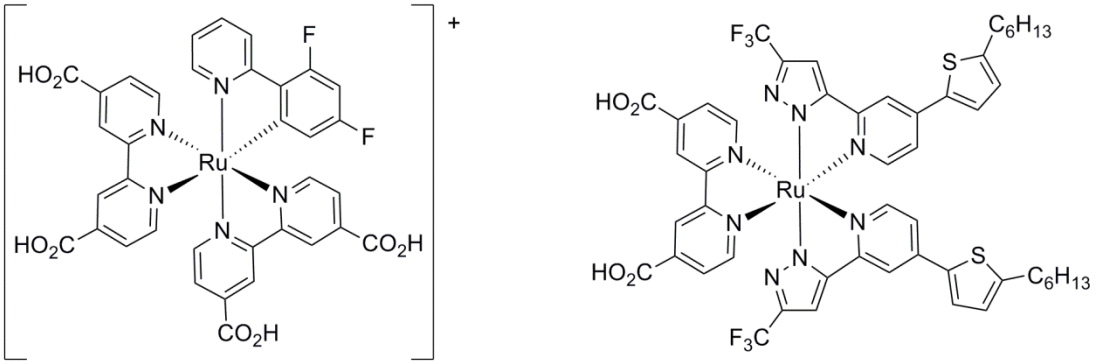

Fig. 1.27: *Fully conjugated, high efficiency ruthenium dyes for DSSCs:* ***a)*** *YE05 gives 10.1% efficiency[96];* ***b)*** *TFRS-2 gives 9.5% efficiency[84].*

To date ruthenium metal complexes containing carboxylic acid substituted polypyridyl ligands and NCS^- ligands have not been surpassed in terms of performance within an externally verified DSSC[36]. However, the dye is the main cause of degradation of the DSSC; for example, exchange of the monodentate ^-NCS ligands with I^-, OH^-, OH_2, and TBP has been observed in a DSSC over time[97-99]. Oxidation of the ^-NCS ligand to CN^- following electronic excitation is another significant breakdown mechanism in the DSSC[100]. Therefore the monodentate ^-NCS ligand is widely regarded as the weak point of the complex, thus the cell, in terms of stability. Replacement of the ^-NCS ligands with a bi-dentate ligand has therefore become a significant area of research, resulting in the successful synthesis of a number of fully chelating, high efficiency, dyes (Fig. 1.27)[84,96,101].

1.3.6.2 Increasing light harvesting

According to the physicists Shockley and Quiesser, the efficiency of a p-n junction solar cell is dependent on the band gap, as photons will lose any energy in excess of the band gap energy[102]. To optimise TiO_2 sensitisation it has also been shown that all photons with wavelengths below 920 nm should be absorbed[103]; hence a lot of

research is focusing on synthesising dyes with absorption into the near IR to increase the efficiency of dye excitation. This has been achieved by incorporating aromatic groups which extend light absorption towards the near IR region of the electromagnetic spectrum (Fig. 1.28a)[37,38,101], and σ-donor, π-acceptor ligands such as ($(CO_2H)_3$-trpy)[35], and CO_2H substituted 2,6-bis(quinolone-2-yl)pyridyl ligands (Fig. 1.28b)[104] to extend π- conjugation within the dye, thus increasing light harvesting. Some research is also focused on destabilising the Ru t_{2g}-orbitals to increase the energy of the HOMO of the dye[105], which would lead to a shift in dye absorption to the near IR. This has been attempted by incorporating strongly electron donating ligand in the dye, such as strongly electron donating cyclometallated ligands[96,101,106], and bidentate sulfur donor ligands[107]. However, significant increases in the HOMO energy level of the dye while maintaining cell efficiency have not yet been achieved, and considering the potential mechanisms of dye regeneration (1.3.3.5) this may not be possible with the I^-/I_3^- electrolyte.

a) **b)**

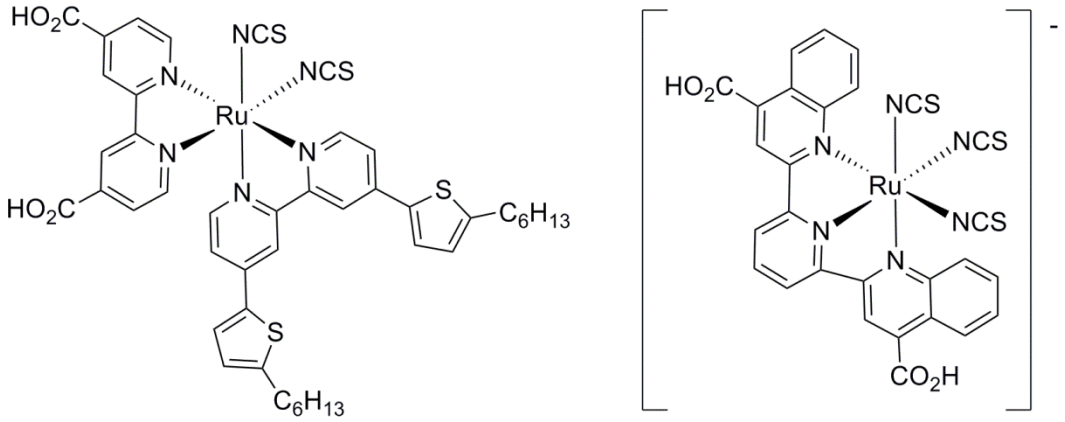

Fig. 1.28: *Enhancing the light absorption properties of ruthenium dyes by incorporation of* ***a)*** *light absorbing aromatic groups (C101 dye);* ***b)*** *ligands with extended π-conjugation.*

1.3.6.3 Studying electron transfer mechanisms in the DSSC

Herein, the effect of dye structure on the rate of dye regeneration and recombination across the TiO_2 - dye - electrolyte interface has been explored. With improved knowledge of the dye-electrolyte interactions, dye development could be carried out more logically to produce novel, high efficiency, dyes. The synthesis and characterisation of series of dyes with small changes in structure can improve understanding of the interactions between the dye and the electrolyte. Such dyes are the focus of this thesis.

1.3.6.4 The synthesis of ruthenium dyes

Despite the huge volume of research on ruthenium dyes for DSSCs, there have been few systematic studies into dye synthesis. Commercial ruthenium dyes are expensive, and the majority of the cost is attributed to the synthetic procedure. Dye synthesis can also be a bottle neck to the development of novel dyes for DSSCs. Therefore, a substantial investigation into the problems that can hinder the synthesis of novel dyes, and how to overcome such problems, has been undertaken during the course of this research.

Chapter 2: Experimental Methods

2.1 Elucidating the dye structure

To confirm the structural identity of each novel ruthenium dye synthesised, a variety of techniques was required. NMR spectroscopy, ESI-MS, CHN analysis and IR spectroscopy were used in combination to enable the geometry of the ruthenium centre, the binding mode of the ligands, and the structure of the ligands around the ruthenium centre to be determined. X-ray crystallography would have conclusively verified the dye structure, however ruthenium dyes are poorly soluble and they are often unstable in solution. Crystals of the N3[108] and N749[109] dyes have been grown, but slow evaporation of DMSO was required. As X-ray crystallography does not provide additional information on the dye characteristics with a DSSC, the analytical techniques described were deemed sufficient to provide proof of the structures of the dyes synthesised.

2.1.1 Nuclear magnetic resonance (NMR) spectroscopy

2.1.1.1 The technique

$$\text{Chemical shift } (\delta) = \frac{\nu_{\text{signal}} - \nu_{\text{reference}}}{\nu_{\text{spectrometer}}} \text{ x } 10^6 \qquad \text{Equation 2.1}$$

By applying a magnetic field to a sample, the electronic environments of the nuclei within a molecule can be differentiated due to shielding or deshielding of the magnetic field by the electrons surrounding each nucleus (Fig. 2.1). Radio frequency radiation (ν) causes an increase in the population of excited spin states. The energy thus absorbed (ΔE, Fig. 2.1) is measured and plotted against the applied magnetic field. Relaxation causes the population of the ground and excited states to return to equilibrium. The signals observed are calibrated to the signals from a standard sample (usually trimethylsilane, TMS, for ^{1}H NMR). The difference between the

standard and each nucleus under investigation is termed the chemical shift (Equation 2.1) and is measured in parts per million (ppm). Along with splitting patterns for each peak, which arise from coupling between magnetic nuclei, the chemical shift can provide a fingerprint for a molecule.

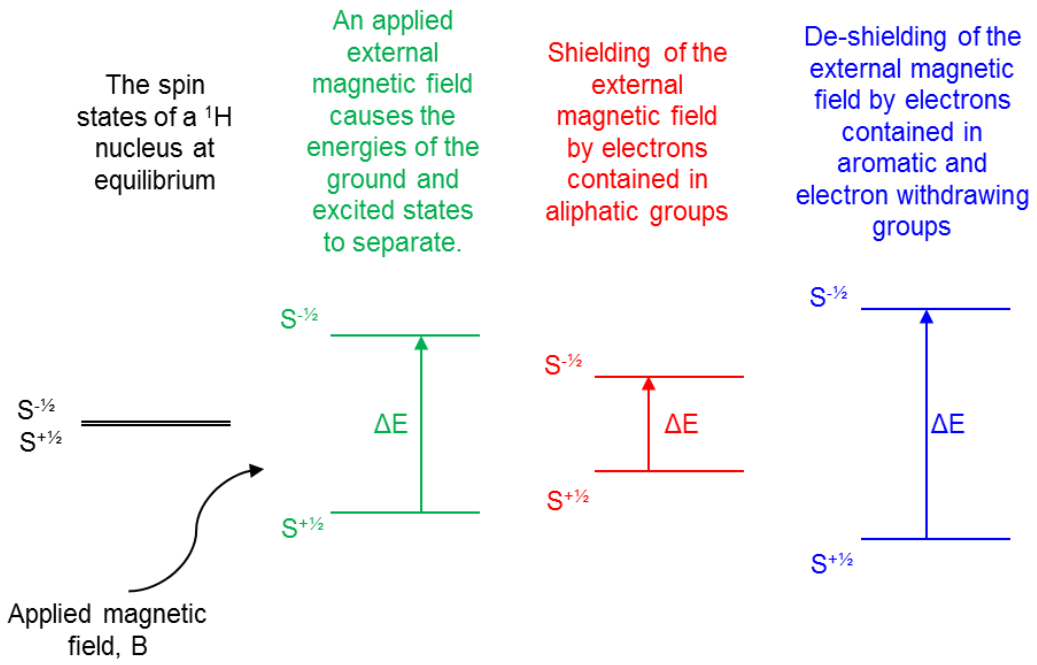

Fig. 2.1: *The effect of an applied magnetic field on the energies of spin +½ and spin –½ states in the nucleus of a proton.*

2.1.1.2 Relevance to ruthenium dyes

In the progress of this thesis, NMR spectroscopy was used universally to ensure the successful synthesis of starting materials and novel dyes. Where possible, comparison of the observed chemical shifts with literature values was carried out to confirm a successful synthesis. NMR analysis was also particularly useful to detect impurities containing the nucleus being measured by NMR. As an impurity within a sample can have a different solubility to the product, when feasible NMR analysis was performed in multiple solvents to increase the possibility of detecting any impurities.

a) **b)**

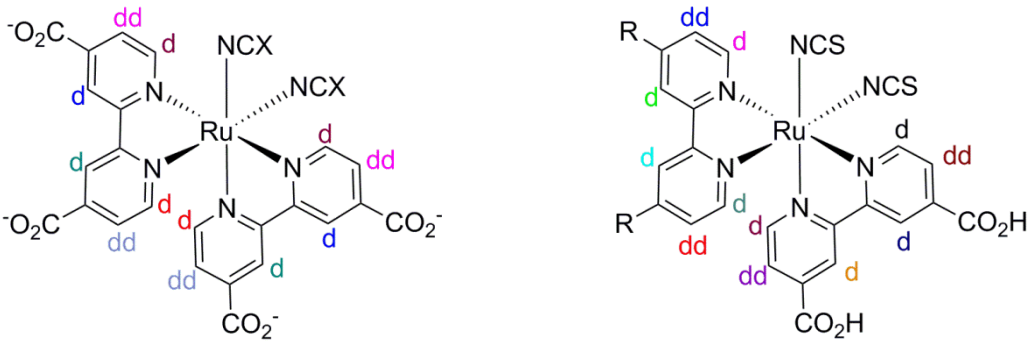

Fig. 2.2: *Expected splitting patterns of ^{1}H NMR peaks for* ***a)*** *$[Ru(dcbpy)_2(NCX)_2]^{4-}$ dyes;* ***b)*** *$[Ru(H_2\text{-}dcbpy)(R_2\text{-}bpy)(NCS)_2]$ dyes. Equivalent protons within a dye have the same colour and the splitting patterns are d – doublet; dd – doublet of doublets.*

The co-ordination geometry of the ruthenium dyes synthesised was also confirmed by ^{1}H NMR spectrometry. Ruthenium polypyridyl isothiocyanato complexes are known to have a *cis* conformation[110]. This conformation causes one pyridine ring of a bpy ligand to be *trans* to an $^{-}$NCS ligand, whereas the other pyridine ring is *trans* to another pyridine ring (Fig. 2.2). The chemical shifts of the protons on a pyridyl ring *trans* to $^{-}$NCS are more shielded than those *trans* to another pyridyl ring[111]. Hence, the *cis* symmetry of each of the dyes can be confirmed by analysing the aromatic region of the ^{1}H NMR spectrum, as the protons bound to the two pyridine rings of a bpy ligand will not be equivalent (Fig. 2.2). Comparison of the splitting patterns and the chemical shifts of the pyridyl protons therefore enables the assignment of the peaks observed by ^{1}H NMR.

2.1.1.3 Experimental details

^{1}H and ^{13}C NMR spectra were obtained using a 500 MHz Bruker Avance III spectrometer equipped with carbon optimised dual ^{1}H/^{13}C DCH ATMA cryo-probe. ^{19}F NMR spectra, both coupled and decoupled to the ^{1}H atom, were obtained using a 400 MHz Bruker Avance III spectrometer equipped with carbon optimised dual ^{1}H/^{13}C DCH ATMA cryo-probe. All spectra were analysed using MestReNova software version 8.1.1 and calibrated to the residual solvent signal[112,113].

2.1.2 Electrospray ionisation mass spectrometry (ESI-MS)

2.1.2.1 The technique and relevance to ruthenium dyes

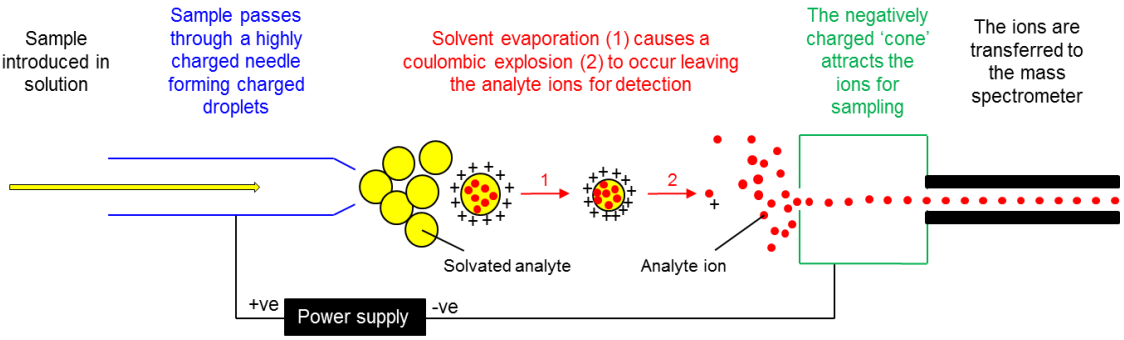

Fig. 2.3: *Schematic of positive mode electrospray ionisation mass spectrometry.*

Mass spectrometry allowed confirmation of the overall mass of the molecule synthesised. The presence of Ru, Cl, and Br could also be confirmed by analysis of the isotopic pattern of a peak. As a mass spectrometer analyses charged particles and the majority of the compounds synthesised were neutral, ionisation was required to detect the molecules. To prevent breaking of comparatively weak metal to ligand bonds, soft ionisation techniques were used. ESI-MS (Fig. 2.4) is the most common technique used in the analysis of ruthenium dyes and has been used solely to characterise the products formed during the breakdown of ruthenium dyes[114-116]. In ruthenium dyes, ionisation normally occurs at the CO_2H group producing singly and doubly deprotonated ruthenium-dcbpy dyes[117]. The analysis of compounds without the CO_2H group was achieved by detection of the positive ions which can form due to association with cations such as sodium[118]. Thus, ESI-MS analysis was performed for analysis of the compounds synthesised during the progress of this thesis, and for the analysis of breakdown products formed during reactions.

2.1.2.2 Experimental details

ESI-MS was performed at Edinburgh University by Alan Taylor using the Finnigan LCQ Ion Trap mass spectrometer.

2.1.3 Attenuated total reflectance fourier transform infra-red (ATR-FTIR) spectroscopy

2.1.3.1 Relevance to ruthenium dyes

The techniques described thus far allow determination of the co-ordination geometry of the ligands and confirmation that the desired product has formed. However, chalcogenocyanato ligands such as ⁻NCO and ⁻NCS are ambidentate ligands. Therefore, determination of the binding mode of the chalcogenocyanate ligands was required. Whether the ⁻NCX ligand is bound through the N atom or the X atom has a large effect on the energy of the C-N stretch of the ligand. IR spectroscopy was therefore used to observe the C-N stretching vibration of the ⁻NCS and ⁻NCO ligands within the dye. Comparison of the obtained vibrational frequencies with literature values (Table 2.1) allowed determination of the binding mode of the ligand.

Compound type	ν_{C-N} / cm^{-1}
⁻NCS	2053
M-NCS	2100-2050
M-SCN	2130-2085
M-NCS-M	2165-2065
⁻NCO	2165
M-NCO	2240-2170
M-OCN	2240-2200
M_2-NCO	2210-2150

Table 2.1: *Vibrational frequencies of the ⁻NCO and ⁻NCS ligands[119].*

2.1.3.2 The technique

The most common method for measuring IR spectra is transmission IR, where IR radiation is passed through a sample, and the transmittance of the radiation is measured by a detector. However, in the solid state, consistency in sample

preparation can be difficult to achieve which can result in poor reproducibility of the spectra obtained. Attenuated total reflectance (ATR) methods use total internal reflection of the IR radiation within a crystal to produce a wave which penetrates into the sample and allows the detection of bond vibrations within a solid (Fig. 2.4). This technique can therefore be used to directly analyse solid state samples without the need for further preparation. Thus ATR-FTIR was used in the analysis of the novel products synthesised.

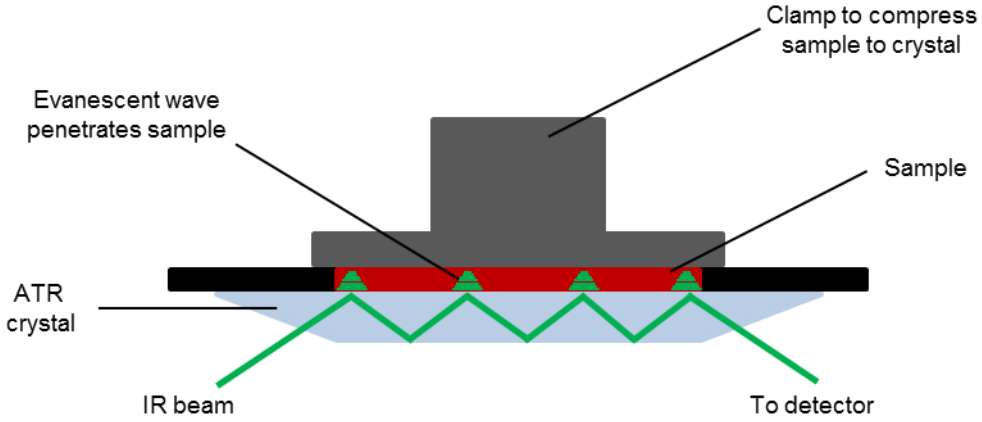

Fig. 2.4: *Schematic of an ATR-FTIR spectrometer.*

2.1.3.3 Experimental details

ATR-FTIR was performed using a PerkinElmer Spectrum 65 FT-IR spectrometer controlled by PerkinElmer Spectrum software. The results were analysed using Origin software, version 8.5.1.

2.1.4 Elemental analysis

2.1.4.1 The technique and relevance to ruthenium dyes

Synthesising a pure dye is essential to ensure that any change in the function of the dye within the DSSC is due to the structure of the dye and not any impurities. By NMR, ESI-MS and ATR-FTIR, salts or $Ru^{(III)}$ compounds will not necessarily be

observed. By elemental analysis, the sample is combusted and analysis of the masses of the combustion products (CO_2, H_2O and NO_2) allows the determination of the percentage content of C, H, and N within the sample. As combustion of the entire solid is performed, any impurities due to salts can be observed as a difference between the experimental and the predicted CHN values. Thus good agreement between the experimental and predicted CHN results was deemed important to ensure the dyes were synthesised to a high level of purity.

2.1.4.2 Experimental details

Elemental analysis was performed at London Metropolitan University by Stephen Boyer using the Carlo Erba Flash 2000 Elemental Analyser.

2.2 Dye characterisation

2.2.1 UV/vis spectroscopy

2.2.1.1 The technique

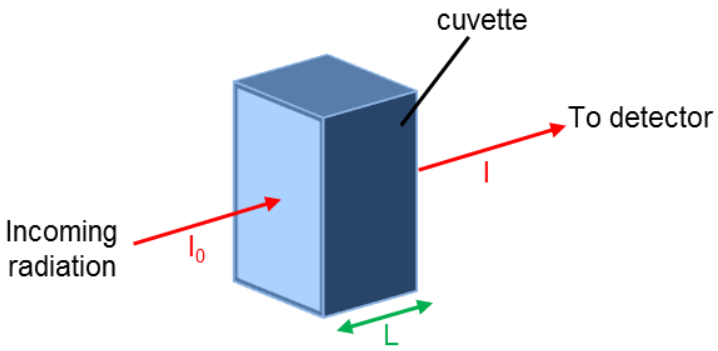

Fig. 2.5: *Light passing through a cuvette within a UV/vis spectrometer. I_0 – incident light; I – light transmitted through sample; L – path length in cm.*

UV/vis spectroscopy is the measurement of the energy of electronic excitations within a molecule. Determination of the UV/vis spectrum of a dye in solution is performed by passing a beam of light through a sample (Fig. 2.5). The light which is transmitted through the sample (I) is detected by the spectrometer, and the transmittance (T) of the sample is calculated (Equation 2.2). Thus the absorbance (A) of light by the sample at each wavelength can be calculated (Equation 2.3). By plotting the absorbance against the wavelength of light absorbed, a UV/vis spectrum is produced.

$$T = \frac{I}{I_0} \qquad \text{Equation 2.2}$$

$$A = -\log_{10} T \qquad \text{Equation 2.3}$$

2.2.1.2 Absorption properties of ruthenium dyes

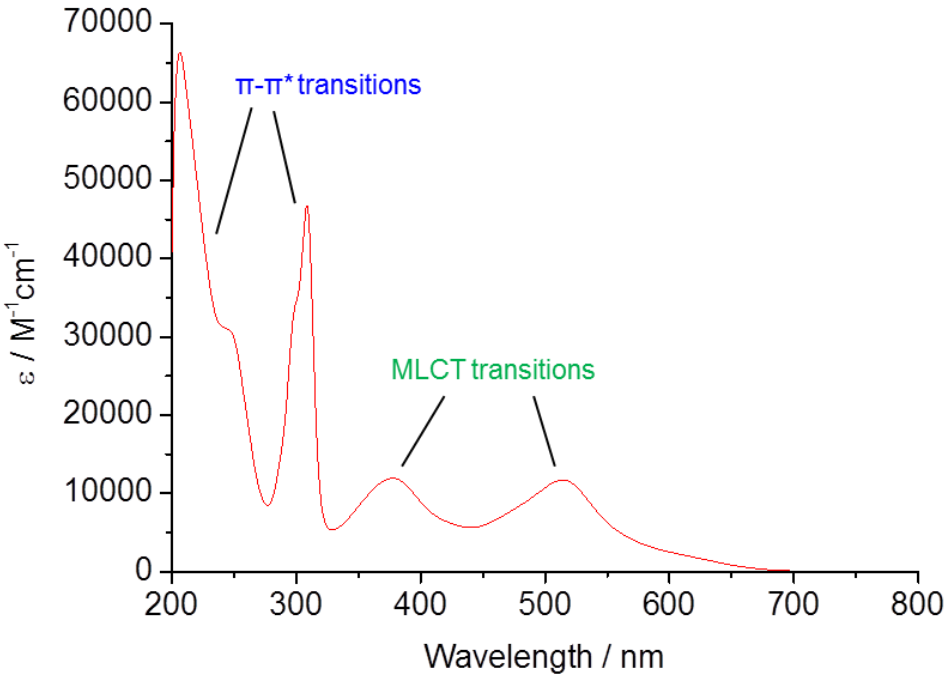

Fig. 2.6: *The UV/vis spectrum of a ruthenium dye*

There are numerous types of electronic transitions that can occur within a molecule. In ruthenium complexes, metal-centred excitations (d-d), ligand centred transitions

(π-π^*) and metal to ligand charge transfer transitions (MLCT) are commonly observed[40]. Which of these transitions is prominent depends on the co-ordination environment of the metal centre, but due to the low lying π^* orbitals of the bpy ligands in bis polypyridyl bis ruthenium dyes, and the inherent weakness of d-d transitions, only MLCT and π-π^* transitions are usually observed (Fig. 2.6)[40]. As the solar radiation which reaches the Earth's surface is mostly in the visible and IR regions of the electromagnetic spectrum (Fig. 1.12, 1.3.3.1), the wavelengths of the MLCT transitions of ruthenium dyes are significant as they give an indication of the quantity of solar radiation that will be absorbed by the dye.

$$A = \varepsilon Lc \qquad \text{Equation 2.4}$$

Determination of the probability of an electronic transition occurring is also extremely important when considering dyes for solar cells, as this quantifies how well a species absorbs light at a particular wavelength. This parameter is represented by the molar extinction co-efficient (ε / $M^{-1}cm^{-1}$) and is directly proportional to the absorbance of the sample. The absorbance also depends on the sample concentration (c / $moldm^{-3}$) and the path length (L / cm) as described by the Beer-Lambert law (Equation 2.4). Therefore, by measuring the UV/vis spectrum of solutions of know concentrations, and plotting the concentration against the absorbance, the molar extinction co-efficient was calculated by determining the gradient of the resulting straight line (2.2.1.3).

2.2.1.3 Experimental details

Three samples of each dye were made up and five dilutions of each sample, over a total concentration range of 1×10^{-5} to 1×10^{-4} mol dm^{-3}, were measured. Absorption spectroscopy was performed using a JASCO V-670 spectrophotometer controlled by Spekwin32 version 1.71.6. The results were analysed using Origin software, version 8.5.1 and a Beer-Lambert plot was used to calculate ε.

2.2.2 Luminescence spectroscopy

2.2.2.1 The technique

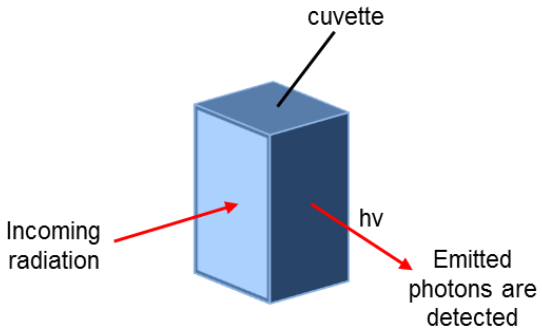

Fig. 2.7: *Measuring emission within a fluorimeter*

After an electronic excitation process has taken place, the electron must return to its ground state. In doing so, the electron loses energy which can be emitted as heat energy (non-radiative decay), or it can be emitted as light energy in the form of a photon (radiative decay or luminescence). Within a fluorimeter, radiative decay is measured by determining the energy of an emitted photon (Fig. 2.7). The energy of this photon directly correlates to the difference in the energies of the ground and excited states; thus allowing information about the energy levels within a molecule to be extracted. Therefore, when measuring emission from a triplet state, the wavelength of the high energy onset of emission can be used as an approximation of the 0-0 transition energy of the dye – the energy difference between the ground state and the lowest energy excited state of the dye.

A fluorimeter uses a monochromator to stimulate electronic excitation at a particular wavelength, and the detector analyses the photons emitted across a range of wavelengths to produce an emission spectrum. Conversely, the fluorimeter can be set to stimulate excitation across a range of wavelengths, and only measure the emission of photons at a particular energy. The excitation spectrum thus produced should be similar to the absorption spectrum seen by UV/vis spectroscopy. When measuring both emission and excitation of a dye within a fluorimeter, the wavelength at which

the observed peak is most intense is determined, allowing the excitation and emission energies to be coupled.

2.2.2.2 Luminescence properties of ruthenium dyes

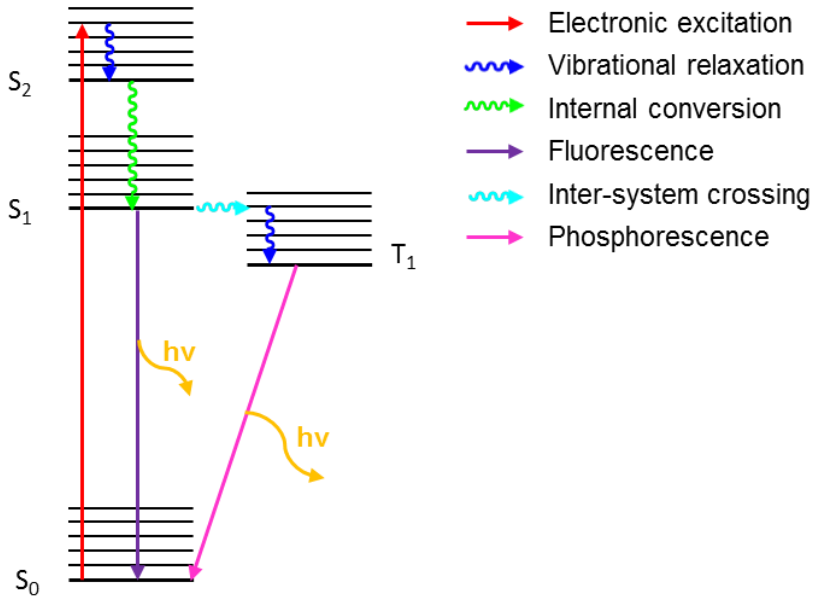

Fig. 2.8: *A Jablonski diagram*

After promotion of an electron to an excited state, a number of relaxation processes can occur which result in the electron returning to the ground state (Fig. 2.8). The rate of non-radiative decay in ruthenium polypyridyl complexes is determined by the energy gap law for radiationless decay[42,120]; thus it decreases with an increasing energy gap[121]. As π-π^* and MLCT excited states are not strongly displaced along the metal-ligand vibrational co-ordination geometry[40] (Fig. 2.9), the energy gap between these states is large thus non-radiative decay is slow. Hence, appreciable radiative decay of ruthenium dyes is usually observed. Due to significant mixing of singlet and triplet excited states in ruthenium (II) polypyridyl compounds[40], inter-system crossing followed by phosphorescence of the excited state is the most common decay pathway in ruthenium dyes. As phosphorescence results in the emission of a photon, this process should be easily observed in a fluorimeter. However, quenching of emission from triplet states by oxygen can prevent observation of phosphorescence,

therefore measurement of frozen dye solutions can be required for phosphorescence to be observed.

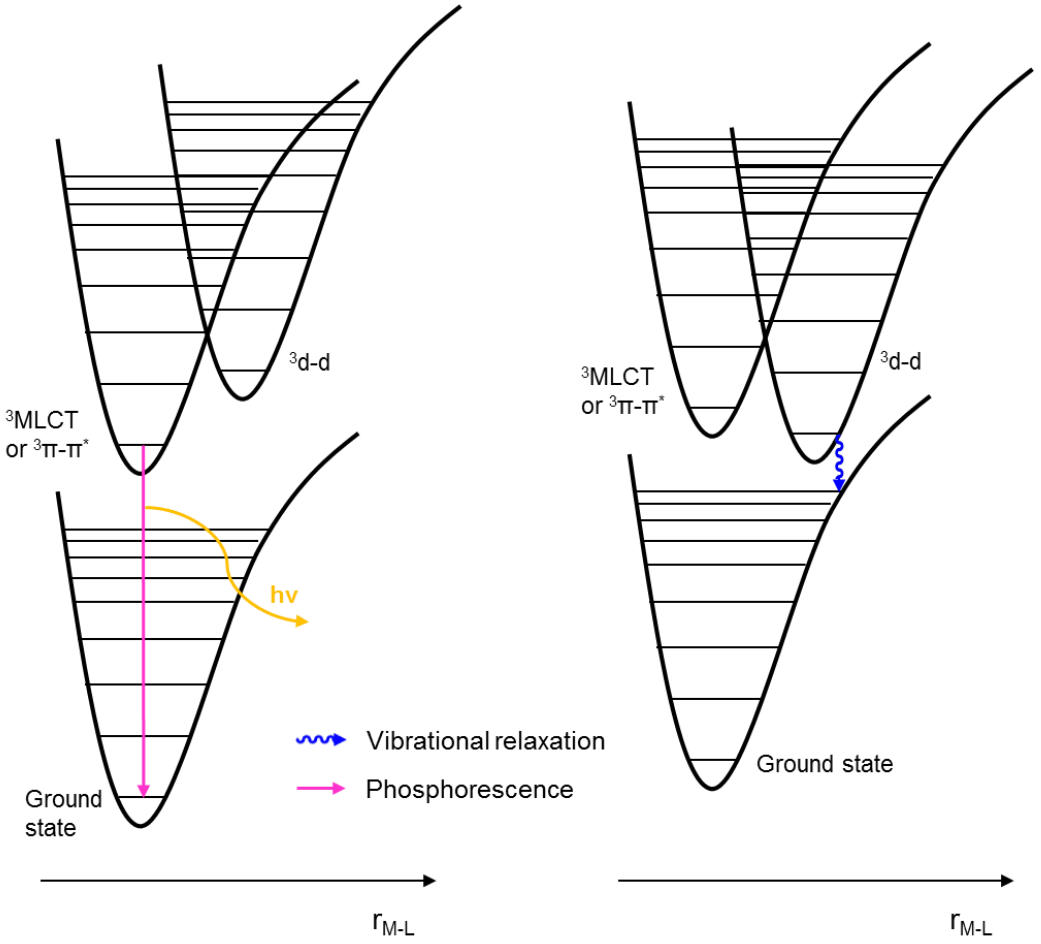

Fig. 2.9: *Dependence of the mechanism of decay of the ^{3}MLCT or ^{3}π-π* excited states on the relative energies of the ^{3}MLCT, ^{3}π-π* and metal centred ^{3}d-d excited states[40].*

Thermal population of low-lying ^{3}d-d excited states has also been observed in ruthenium polypyridyl complexes[42,45]. In octahedral ruthenium complexes, ^{3}d-d excited states are strongly displaced with respect to the ground state geometry along the metal-ligand vibration co-ordinates[40] (Fig. 2.9); thus the energy gap between low-lying ^{3}d-d excited states and the ground state is small. Consequently, decay from a low lying ^{3}d-d excited state is normally non-radiative (Fig. 2.9) and is unlikely to be detected in a fluorimeter. The extent of thermal population of ^{3}d-d excited states is

dependent on the relative energies of the ^{3}MLCT and ^{3}d-d excited states (Fig. 2.9); which are determined by the co-ordination environment of the ruthenium metal centre. Therefore, both the solvent used[120], and the nature of the ligands bound to the ruthenium centre[42] can have a large effect on the decay mechanism of a ruthenium dye. As the population of ^{3}d-d states has been shown to result in ligand-loss photochemistry[42,45,122], low lying ^{3}d-d excited states can cause ruthenium dyes to be unstable.

In ruthenium bipyridyl isothiocyanato dyes, the bpy ligands have an effect on the energies of ^{3}MLCT excited states, and the isothiocyanato ligands affect the energies of the metal based d-orbitals[44]. Therefore, changes in the luminescence properties of a dye can provide information about the effect of a ligand on the energies of the molecular orbitals. As injection into the TiO_2 conductance band occurs on a nano to picosecond timescale[51], observation of radiative decay implies that the excited state lifetime of the dye is long enough for injection to occur at a high yield. Therefore the likelihood of efficient injection can also be determined using luminescence spectroscopy.

2.2.2.3 Experimental details

Samples were measured in N_2 purged, dry MeOH and DMF; both in solution, and frozen using liquid nitrogen. Luminescence measurements were taken using the Fluoromax2 fluorimeter controlled by ISAMain software. The results were analysed using Origin software, version 8.5.1.

2.2.3 Electrochemistry

2.2.3.1 Relevance to dyes for DSSCs

In order to ensure that a dye has the right energy levels for injection into the TiO_2 conductance band (energy of TiO_2 conductance band is -0.50 V vs. NHE[16]) and regeneration by I^- (energy of I^-/I_3^- redox couple is 0.35 V vs. NHE[17]),

electrochemistry of the dye is performed. During injection, the excited state dye is oxidised; and reduction of the oxidised dye is performed by I^-. The reduction potential of the oxidised dye can be observed using cyclic voltammetry (2.2.3.3). Conversion of the 0-0 transition energy (determined by luminescence spectroscopy, 2.2.2) to electron volts (Equation 2.5) and subtraction of this value from the oxidation potential of the dye, allows approximation of the oxidation potential of the excited state dye. Therefore, electrochemical measurements coupled with luminescence spectroscopy allow calculation of the energy levels of novel dyes, ensuring that the dye has the right energy levels to function efficiently in a solar cell.

$$E\ (eV) = \frac{1240\ (eV\ nm)}{\lambda\ (nm)} \qquad \text{Equation 2.5}$$

2.2.3.2 The three electrode system

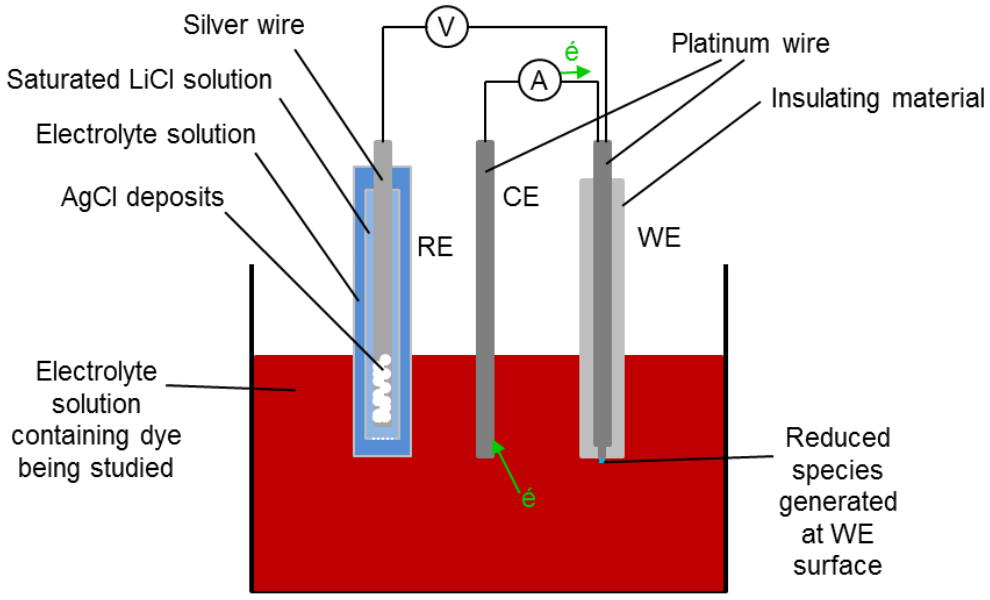

Fig. 2.10: *The three electrode system*

Electrochemical measurements were performed using the three-electrode system (Fig. 2.10). Within this system, the reference electrode (RE) has a known potential; therefore the potential is applied across the reference and working electrodes to allow

calculation of the potential at the working electrode (WE). Redox reactions of the molecule being studied take place on the surface of the working electrode. To allow accurate analysis of these processes, the working electrode has a small surface area, and it must be able to apply a constant charge. Therefore, an electrode must be connected which can balance the charge at the working electrode as redox processes take place. In doing so, a constant potential cannot be maintained, so the reference electrode cannot perform this function. Therefore, a third, high surface area, counter electrode (CE) is used to modulate the charge at the working electrode. The current is therefore measured across the counter and working electrodes. The electrodes are all connected by the solution, to which is added an electrolyte such as $[NBu_4]^+[BF_4]^-$ to increase the conductivity.

2.2.3.3 Cyclic voltammetry (CV)

$$E_{½} = \frac{E_{pa} + E_{pc}}{2} \qquad \text{Equation 2.6}$$

In cyclic voltammetry, an electric potential is applied to cause oxidation (more positive voltage) or reduction (more negative voltage) of a species. When a redox process occurs the movement of electrons takes place, thus a current is produced. Therefore, a plot of current against applied voltage allows a redox process to be observed (Fig. 2.12). From this scan, the standard electrochemical potential for a process ($E_{½}$) can be calculated (Equation 2.6). To account for experimental variations, all scans were calibrated to reported $E_{½}$ values for Ferrocene (Fc^+/Fc^0)[123].

$$Ox + né \underset{k_r}{\overset{k_f}{\rightleftharpoons}} Red \xrightarrow{k_c} Z \qquad \text{Equation 2.7}$$

$$1 = \frac{i_{pc}}{i_{pa}} \qquad \text{Equation 2.8}$$

Depending on the species being analysed, reduction or oxidation processes can be chemically and / or electrochemically reversible. Chemical reversibility of a

reduction process depends on the magnitude of the rate constant k_c compared to the rate constant k_r (Equation 2.7). If k_c is large, the process is likely to be chemically irreversible. The rate of the experiment can also influence the reversibility, as at high scan rates (v) the reverse process can be initiated before a chemical reaction takes place. In such cases a reaction is said to have limited chemical reversibility. If the redox process is chemically reversible (Fig. 2.11), the forward and backwards peaks have a similar shape and the peak heights will have the same amplitude even at low scan rates (Equation 2.8).

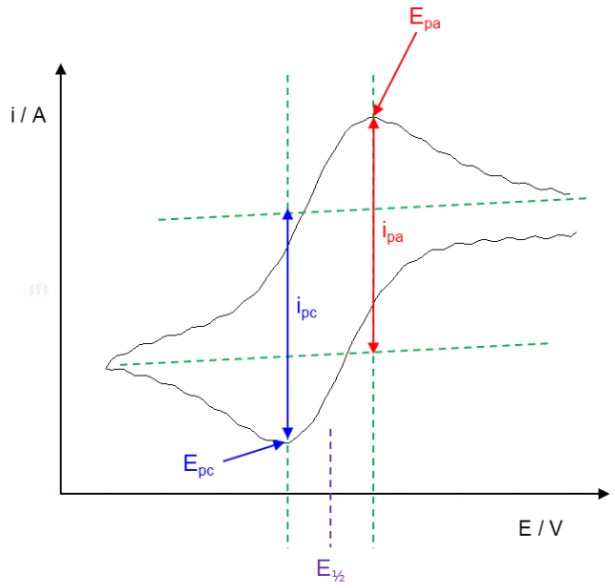

Fig. 2.11: *A chemically reversible cyclic voltammagram.*

The electrochemical reversibility of a system considers the factors which limit the rate of electron transfer at the working electrode. If electron transfer at the surface is limited by a slow kinetic process at the electrode surface, such as a change in geometry of a species, a process is electrochemically irreversible. In such situations, the rates of change of k_r and k_f (Equation 2.7) are slower than the scan rate (v), resulting in a change in the peak potential with scan rate. Therefore, by performing scan rate studies (Fig. 2.12) on each redox process observed, the E_{pa} and E_{pc} at each scan rate can be determined. That these values don't change with scan rate is one of the features of an electrochemically reversible reaction.

$$E_{pa} - E_{pc} = 59\ mV \qquad \text{Equation 2.9}$$

If a reaction is electrochemically irreversible, the change in E_{pa} or E_{pc} with scan rate will affect the difference in the oxidation and reduction peak potentials. The difference in oxidation and reduction peak potentials for a one-electron process is well-defined (Equation 2.9). However, to account for possible variations within the system, the $E_{pa} - E_{pc}$ for the processes studied were compared to that of Ferrocene.

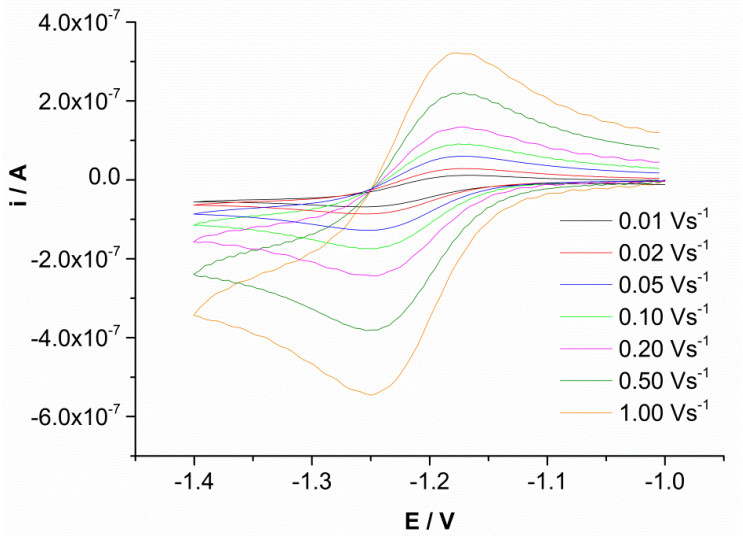

Fig. 2.12: *An electrochemically reversible cyclic voltammagram.*

Thus, the invariable value of E_{pc} and E_{pa} with scan rate, that i_{pc} is equivalent to i_{pa} and that $E_{pa} - E_{pc}$ is the same as the value for Ferrocene (for a one-electron process), proves that a process is fully chemically and electrochemically reversible. Also, if the rate of electron transfer at the electrode surface is fast, the factor which limits the amplitude of the current produced at the working electrode will be diffusion to the working electrode. This can be proved by a linear plot of i_{pc} against $v^{½}$.

2.2.3.4 Differential pulse voltammetry (DPV)

In CV measurements, the charging current can mask electrochemical processes. As opposed to CV, where the change in voltage is linear, DPV uses a stepwise change in

potential. The current is sampled just before each change in potential, decreasing the effect of the charging current. Hence this technique has a higher sensitivity than CV. As well as assuring that no electrochemical processes were masked by the charging current in the CV, DPV was used to verify chemical reversibility of redox processes, as the oxidation and reduction peaks should have equivalent amplitudes when the process is chemically reversible (Fig. 2.13).

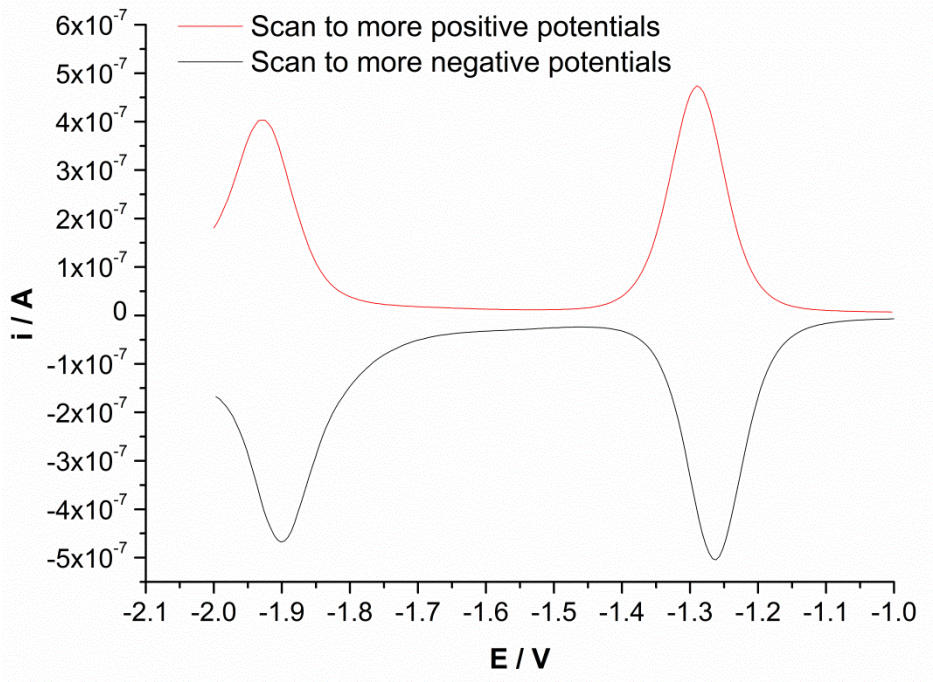

Fig. 2.13: *Differential pulse voltammagram of two chemically reversible reduction processes.*

2.2.3.5 Electrochemical properties of ruthenium dyes

Both the reduction[124] and oxidation[111] of a ruthenium dye are one-electron processes – although more than one reduction is normally observed. In ruthenium dyes, reduction of the bpy ligands is normally observed at negative potentials. These reductions are usually chemically and electrochemically reversible[111,124], unless the bpy ligand has a CO_2H substituent in which case loss of protons from the ligand causes the process to be chemically irreversible[125]. Oxidation of the dye is observed at positive potentials. However, if the complex contains ¯NCS ligands the oxidation

is rarely chemically reversible as the $^-$NCS ligands degrade to form $^-$CN[111,116]. Therefore, an irreversible oxidation is normally observed. Within a solar cell, this reaction is reduced by rapid dye regeneration. However, this process is one of the main degradation mechanisms within a solar cell[97] so improved electrochemical stability of the oxidised dye would be likely to increase the lifetime of a solar cell.

2.2.3.6 Experimental details

Electrochemical studies were performed using a μAUTOLAB type III controlled by GPES version 4.9.007. Platinum working and counter electrodes were used and the potentials were recorded in 0.3 M $TBABF_4$ in methanol or 0.1M $TBABF_4$ in DMF versus Ag/AgCl (saturated LiCl in EtOH) and calibrated against the Fc/Fc^+ couple ($E_{½}$ = 0.448 V in MeOH, $E_{½}$ = 0.578 V in DMF[123]). Differential pulse voltammetry was performed using the same apparatus applying a step potential of 0.01V and modulation amplitude of 0.025 V. The results were analysed using Origin software, version 8.5.1. Voltages recorded versus Ag/AgCl were converted to versus NHE by addition of 0.22 V[126].

2.2.4 Computational studies

2.2.4.1 Relevance to ruthenium dyes

Computational studies performed on ruthenium polypyridyl dyes, using density functional theory (DFT) to optimise the geometry of the dye and calculate molecular orbitals, have shown that the LUMO is localised on the bpy ligands and the HOMO is localised across the Ru metal centre and the $^-$NCS ligands[44]. This distinct distribution of molecular orbitals results in good charge separation upon excitation of the dye molecule, reducing the likelihood of recombination from electrons in the TiO_2 surface to the dye cation. To ensure similar charge separation, geometry optimisation and calculation of the location of the HOMO and LUMO of the dyes synthesised in this study was performed. Time-dependent (TD) DFT calculations add the parameter of time to the calculation, allowing electronic excitation processes to

be observed *in silica*. Such calculations have also been performed on ruthenium dyes and have been shown to predict solvatochromic effects which have been observed experimentally[127]. TD-DFT was therefore used in this study to calculate UV/vis spectra, and allow assignment of the nature of each electronic transition observed experimentally.

2.2.4.2 The approximations used

$$\hat{H}\psi = E\psi \qquad \text{Equation 2.10}$$

The principal aim of *ab initio* computational calculations is to solve the Schrödinger equation (Equation 2.10); thus enabling calculation of the wavefunctions (ψ) and energies (E) of the orbitals within an atom or a compound. However, the Schrödinger equation cannot be solved for a system with more than one electron, therefore approximations have to be made to find a solution. The 'level of theory' used in DFT describes the interaction of electrons with each other; modelling the effects of both electron exchange (pertaining to Pauli's exclusion principle; that electrons of the same spin cannot occupy the same orbital) and electron correlation (that the movement of one electron affects the movement of other electrons because of coulombic repulsion between electrons). Which level of theory should be used depends on how suitable the approximations made are for the molecules being studied. As B3LYP[128-130] has proven to successfully calculate the properties of molecular ruthenium dyes[16,44,127,131,132] and has been recently shown to give the best approximation of their excitation properties[133], the B3LYP level of theory was used for calculations on the dyes synthesised in this thesis.

As well as calculating the effects of electronic interactions, the energies and nature of the orbitals in the dye must be calculated. The orbitals are described by the 'basis set' used for the calculation, which uses the linear combination of a series of functions (basis functions) to create wavefunctions (ψ) for molecular orbitals. The basis set exchange (https://bse.pnl.gov/bse/portal[134,135]), which contains a catalogue of basis sets for calculations involving different atoms, was used to ensure appropriate basis

sets were used for each of the atoms within the dyes studied. LANLD2Z[136], which has been previously used to successfully model ruthenium atoms within a dye[41,123,127,128], was used as the basis set for ruthenium. This basis set applies a core potential to the non-valence electrons to reduce the computational cost of the experiment.

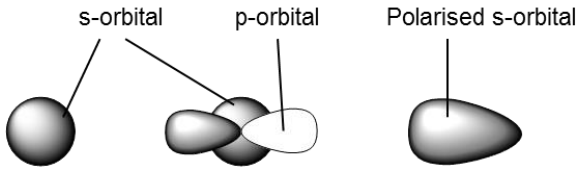

Fig. 2.14: *The effect of a p-orbital polarisation functional on an s-orbital.*

6-31G basis sets with (d,p) polarisation functions have been used to successfully model the atoms other than ruthenium in ruthenium dyes for DSSCs[41,123,127,128]. The polarisation function, (d,p), allows modelling of any asymmetry in the p-orbitals by addition of d-orbital symmetry to the calculation. Similarly, potential polarisation of s-orbitals is accounted for by addition of p-orbital symmetry to the calculation (Fig. 2.14). Therefore, any polarisation of bonds due to the highly electronegative atoms within the ruthenium dye can be accounted for.

Split basis sets such as 6-31G use multiple Gaussian functions to represent valence orbitals. 6-31G is a double zeta basis set; however a triple zeta function was required for modelling of the selenium and bromine atoms[130,131]. A triple zeta basis set uses more Gaussian functions to model the valence orbitals than a double zeta basis set, and is therefore more computationally expensive. However, as the triple zeta functional was required for the selenium and bromine containing dyes 6-311G[137-139] was used instead of 6-31G to model all of the dyes to ensure consistency in the calculations.

In performing TD-DFT calculations, the effects of solvent must be considered. Explicit solvation of the dye – placing solvent molecules in appropriate positions around the dye - can be carried out to investigate the nature of the interactions

between the solvent and the molecule being studied[140]. However, this method does not include the effects of solvent – solvent interactions. The polarisable continuum model (PCM)[141,142] treats the solvent as a long range continuum with a dielectric constant, ε. Therefore, it is the dielectric constant of the solvent which determines the effect of the solvent on the molecule being studied *in silico*. Using the polarisable continuum model, the pH dependence of the UV/vis spectrum of $Ru(H_2\text{-}dcbpy)_2(NCS)_2$ has been successfully reproduced[132]. This model was therefore used to describe the effects of solvation on the dyes studied in the course of this investigation. To perform TD-DFT calculations, the geometry of the solvated dye was optimised, and time dependent calculations were subsequently performed.

2.2.4.3 Experimental details

Starting structures were built using Avagadro software and calculations were performed using Gaussian 09. The DFT level of theory B3LYP[128-130] was used, and the Ru centre was modelled using a LANDL2DZ[136] pseudopotential. The remaining atoms were modelled using the 6-311G(d,p)[137-139] basis set. Geometry optimisation of each dye was performed *in vacuo* and subsequently including solvent effects via a self-consistent reaction field method using the polarisable continuum model. Explicit solvation[140] of some of the dyes was performed by placing six water molecules in appropriate positions around the dye. All calculations were checked to ensure that no imaginary frequencies were calculated. Isosurface maps were generated by Avagadro using an iso value of 0.03. TD-DFT calculations were performed on the optimised solvated structures with the first 50 singlet states calculated.

2.3 Studying the dyes in DSSCs

2.3.1 Solar cell fabrication

2.3.1.1 General procedures

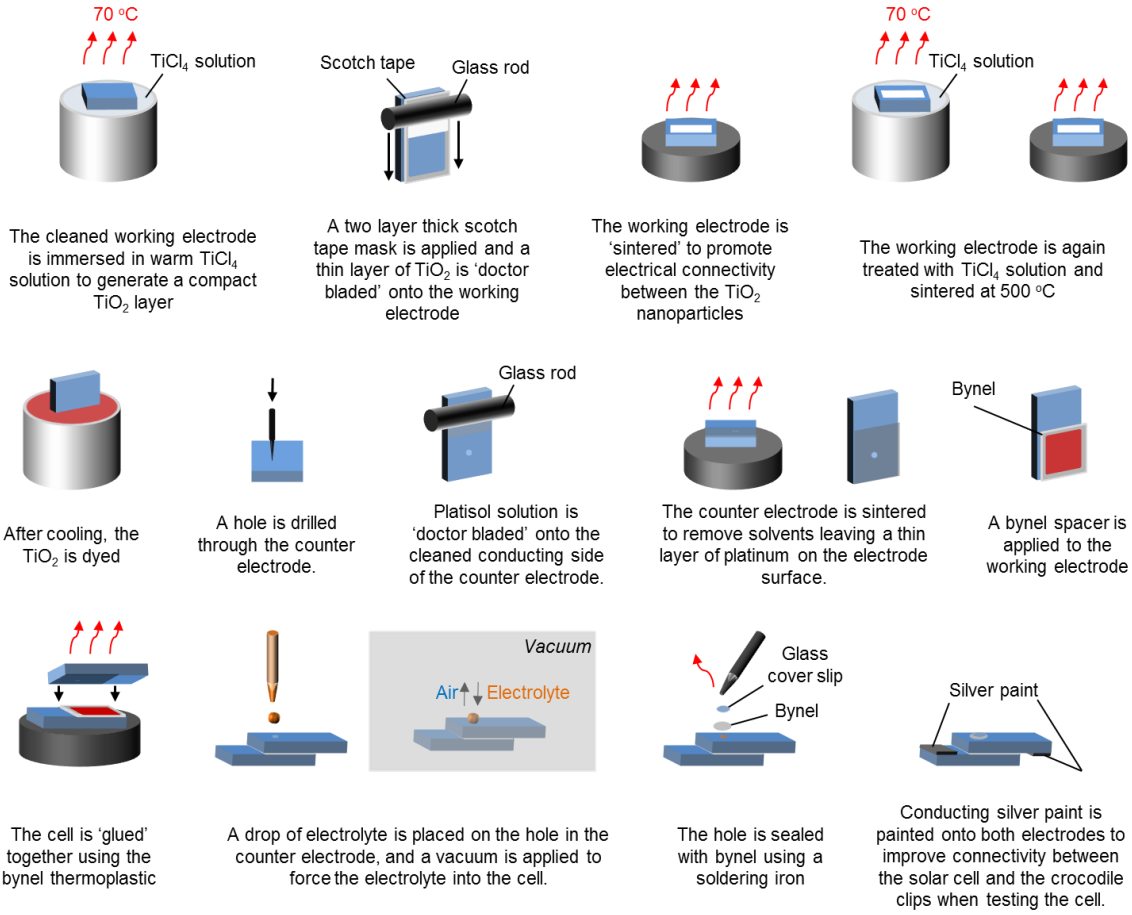

Fig. 2.15: *Fabrication of a dye-sensitised solar cell*[143].

Test DSSC were initially fabricated (Fig. 2.15) using different dye bath solutions and UV/vis spectroscopy of the working electrodes was performed to ensure the electrodes had dyed properly. The cells were tested to determine the optimal dye bath solution for each of the dyes. Cells sensitised by N719 were used as a reference (Appendix, Table A1.1), and solar cells were made in sextuplet to ensure consistency

of the results. These cells were then tested (2.3.2.2) to determine the effect of the change in dye structure on the performance of the dye in a solar cell.

Dye	Dye bath solution	Dying time / hr
N719	1:1 MeCN:^{t}BuOH	20
$K_4[Ru(dcbpy)_2(NCO)_2]$	2:1 MeOH:^{t}BuOH	20
$K_4[Ru(dcbpy)_2(NCO)_2]$	1:1 MeOH:^{t}BuOH	20
$Ru(dcbpy)(5,5'\text{-}F_2\text{-}bpy)(NCS)_2$	9:1 MeCN:DMSO	20
$Ru(dcbpy)(4,4'\text{-}Cl_2\text{-}bpy)(NCS)_2$	9:1 MeCN:DMSO	20
$Ru(dcbpy)(5,5'\text{-}Cl_2\text{-}bpy)(NCS)_2$	4:1 MeCN:DMSO	20
$Ru(dcbpy)(4,4'\text{-}Br_2\text{-}bpy)(NCS)_2$	9:1 MeCN:DMSO	20
$Ru(dcbpy)(5,5'\text{-}Br_2\text{-}bpy)(NCS)_2$	4:1 MeCN:DMSO	20

Table 2.2: *The dye bath solutions used to dye the TiO_2 working electrode.*

2.3.1.2 Experimental details

Solar cells were fabricated using TECH-8 FTO glass from Pilkington. The working electrodes were cleaned with isopropanol, and pre-treated with a 40 mM solution of $TiCl_4$ for 30 minutes at 70 ^oC. After rinsing with deionised water and ethanol, a 12 μm layer of TiO_2 paste (18 NR-T from Dyesol) was deposited using doctor blading methods. The working electrodes were sintered and then treated with 40 mM $TiCl_4$ solution as described previously. The electrodes were subsequently dyed for 20 hrs in 0.5 mM solutions of the dyes (Table 2.2). The drilled counter electrodes were cleaned with isopropanol and dried at 400 ^oC for 15 minutes. They were then treated with platisol solution (Platisol T from Solaronix) and heated for a further 15 minutes at 400 ^oC. The electrodes were assembled using a bynel melt and the electrolyte (0.6 M BMII, 0.03 M I_2, 0.5 M TBP, 0.01 M Gnd.NCS, 0.05 M LiI) was inserted using vacuum back filling methods. The cell was sealed with bynel and tested (2.3.2.2). High efficiency solar cells were constructed by Benjamin Grew from Loughborough University using similar procedures except that a 10 μm layer of TiO_2 paste (18 NR-T from Dyesol) followed by a 6 μm scattering layer (18NR-AO from Dyesol), were deposited using screen printing methods.

2.3.2 Determining the efficiency of the solar cell

2.3.2.1 Parameters used to calculate solar cell efficiency

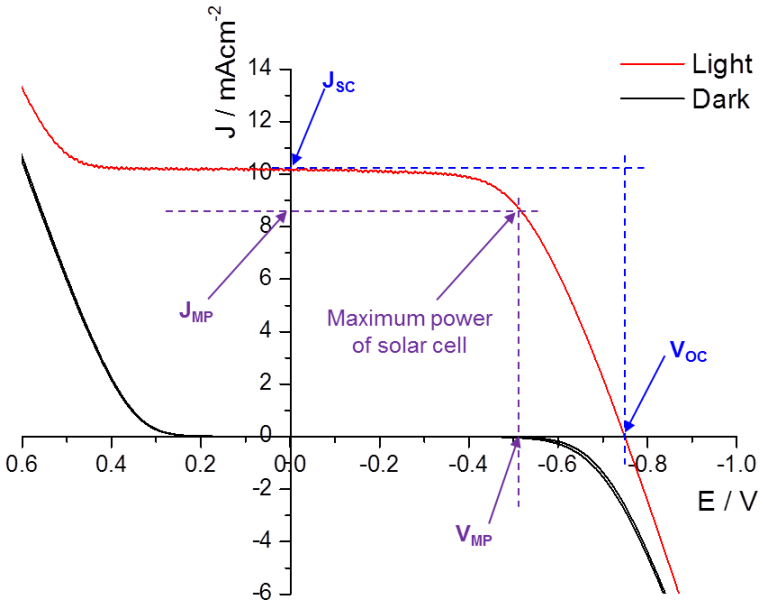

Fig. 2.16: *A J-V curve.*

After assembly, the solar cells were tested to determine their efficiency. The efficiency (η) of a solar cell is determined by measuring the power put into the cell and the power generated by the cell (Equation 2.11). The power input is determined by the light intensity of the lamp used for testing; standard solar cells are tested at AM1.5 (1000 Wm^{-2}). In a solar cell, the power output in watts (W) is calculated (Equation 2.12) by applying a load voltage (V) and measuring the current (I) produced. To account for the surface area of the cell, the current density (J / A cm^{-2}) is calculated and plotted against the voltage to produce a JV curve (Fig. 2.16). From the J and V values, the maximum power point of the solar cell can be determined from the current density at maximum power (J_{MP}) and the voltage at maximum power (V_{MP}).

$$\eta\ (\%) = \frac{\text{power out}}{\text{power in}} \times 100 \qquad \text{Equation 2.11}$$

$$\text{Power} = JV \qquad \text{Equation 2.12}$$

Although determination of the maximum power point allows the efficiency to be calculated, calculation of other parameters is useful to further explore the solar cell function. The short circuit current (J_{SC}, Fig. 2.16) is the maximum current produced within the cell and it can indicate how well the dye is absorbing light and how efficiently that light is being converted to electrical energy. The maximum voltage produced within the cell is called the open circuit voltage (V_{OC}, Fig. 2.16), and it indicates the level of charge build up in the TiO_2 conductance band which can provide information on recombination processes within the cell. By calculating the maximum theoretical power of the cell (J_{SC} x V_{OC}) and comparing it to the actual maximum power of the cell (J_{MP} x V_{MP}), the fill factor (FF) is calculated (Equation 2.13) which allows exploration of loss processes due to the resistance within the cell. Thus the efficiency of a DSSC is calculated by measurement of the J_{SC} (mA cm^{-2}), V_{OC} (mV) and the FF (Equation 2.14).

$$\text{Fill factor (FF)} = \frac{J_{MP} \text{ x } V_{MP}}{J_{SC} \text{ x } V_{OC}} \qquad \text{Equation 2.13}$$

$$\eta\ (\%) = \frac{J_{SC}\ (\text{mAcm}^{-2}) \text{ x } V_{OC}\ (\text{mV}) \text{ x FF}}{1000\ (\text{Wm}^{-2})} \qquad \text{Equation 2.14}$$

2.3.2.2 Experimental details

The working area of the cells was masked to 0.64 cm^2, and the IV characteristics in the dark and in the light were tested using the AUTOLAB PGSTAT30 potentiostat controlled by GPES version 4.9.007. AM 1.5 solar illumination (1000 Wm^{-2}) was provided by a Sciencetech Inc. solar simulator (Model SF150, 1kW Xe lamp) with an AM 1.5 filter (Müller). The power output was calibrated by a silicon diode; itself calibrated at 1000 Wm^{-2} by GBSOL.

2.3.3 Electrochemical Impedance Spectroscopy (EIS)

2.3.3.1 The technique

Electrochemical impedance spectroscopy[144] measures the frequency response of a system – the rate at which the current responds to a small perturbation in the applied voltage. The rate of perturbation (frequency, ω) is varied, which can lead to differentiation of the different electron transfer processes within a system. The data are expressed using either Nyquist (Fig. 2.17) or Bode plots, although the former is more commonly utilised when measuring EIS of Dye-Sensitised Solar cells.

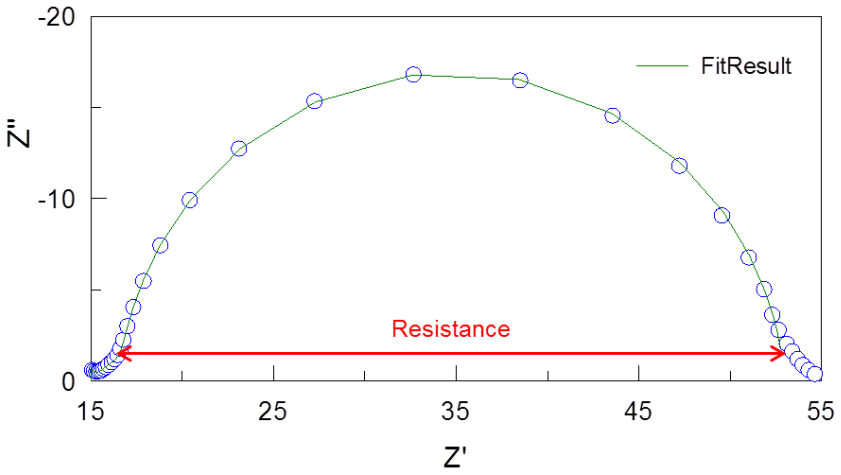

Fig. 2.17: *A Nyquist plot*

From a Nyquist plot, the resistance to an electron transfer process can be determined by measuring the diameter of the semi-circle relating to that electron transfer process (Fig. 2.17). The capacitance of a system is related to the height of the semi-circle in the Bode plot, although as the Z`` axis is an imaginary axis the capacitance cannot be directly calculated from the Bode plot. Therefore, modelling using equivalent electrical circuits is required to fit the data and determine the capacitance and resistance of each electron transfer process.

2.3.3.2 Electrochemical impedance spectroscopy of a DSSC

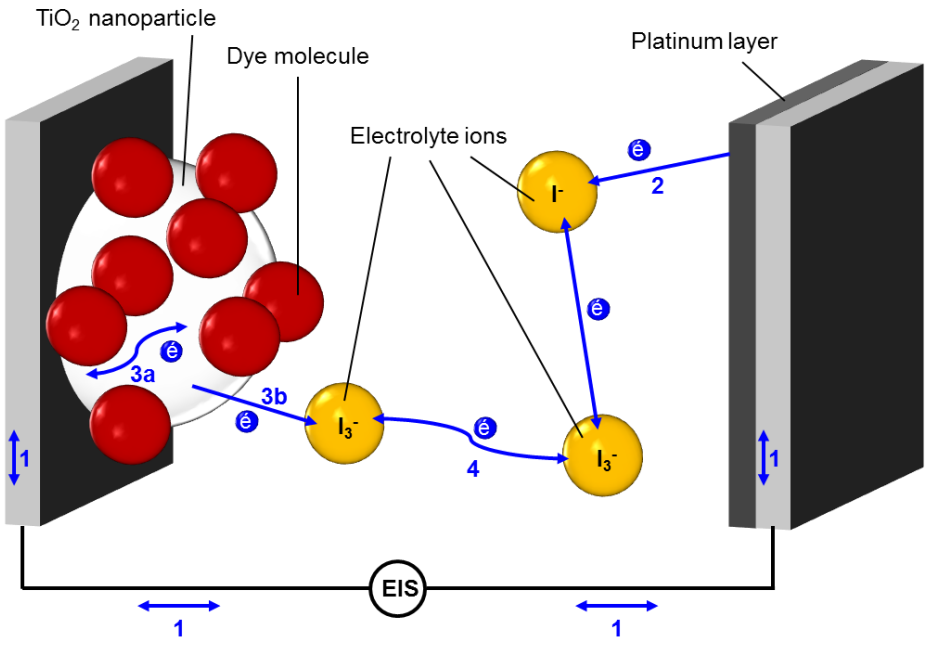

Fig. 2.18: *Recombination processes in a DSSC.*

Impedance measurements on a DSSC are carried out with an applied forward bias. The resulting build-up of electrons in the TiO_2 nanoparticles induces recombination across the TiO_2-dye-I^-/I_3^- interface (Step 3b, Fig. 2.18); a process which is one of the loss mechanisms within a DSSC. A high resistance across this interface is therefore desirable, as it indicates a reduction in the likelihood of this recombination mechanism. By applying voltages around the V_{OC} of the cell, recombination across this interface can be probed using EIS. Recombination to the dye cannot be directly observed by EIS, but the dye has been shown to affect recombination across the TiO_2-dye-I^-/I_3^- interface[84,85]; thus impedance studies were carried out.

The electron transfer processes within the DSSC (Fig. 2.18; processes 1, 2, 3, 4) which can be probed by EIS have been assigned to low, medium, and high frequency regions of the Nyquist plot (Fig. 2.19)[145,146]. Therefore, the effect of changing one component of the solar cell on each recombination process within the cell can be determined using EIS. However, the centre semi-circle of a Nyquist plot of a DSSC

relates to two electron transfer processes (Fig. 2.19) which must be independently calculated. A complete equivalent circuit for the DSSC has been developed by Biqsquert[147-150] (Fig. 2.20) and was used as a basis to model the impedance spectra.

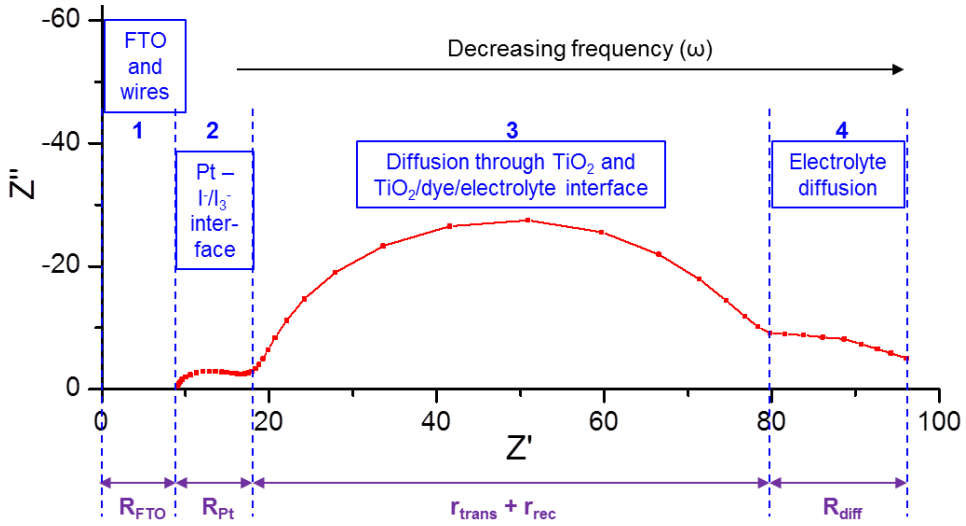

Fig. 2.19: *A Nyquist plot of a DSSC produced by performing electrochemical impedance spectroscopy at V_{OC}.R = resistance.*

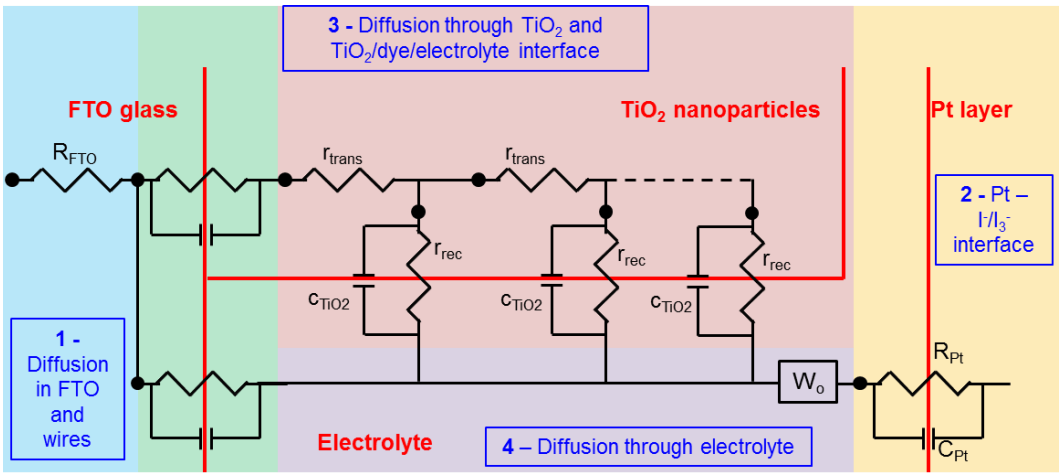

Fig. 2.20: *The complete equivalent circuit to model a DSSC. r_{trans} – resistance to the transport of electrons in TiO_2; r_{rec} – resistance to recombination across the TiO_2-dye-I^-/I_3^- interface; c_{TiO2} – double layer capacitance; W_o – Warburg impedance of electrolyte diffusion; R_{Pt} – resistance across Pt-I^-/I_3^- interface; C_{Pt} – capacitance at the Pt-I^-/I_3^- interface. A constant phase element (CPE) was used to model all capacitive processes.*

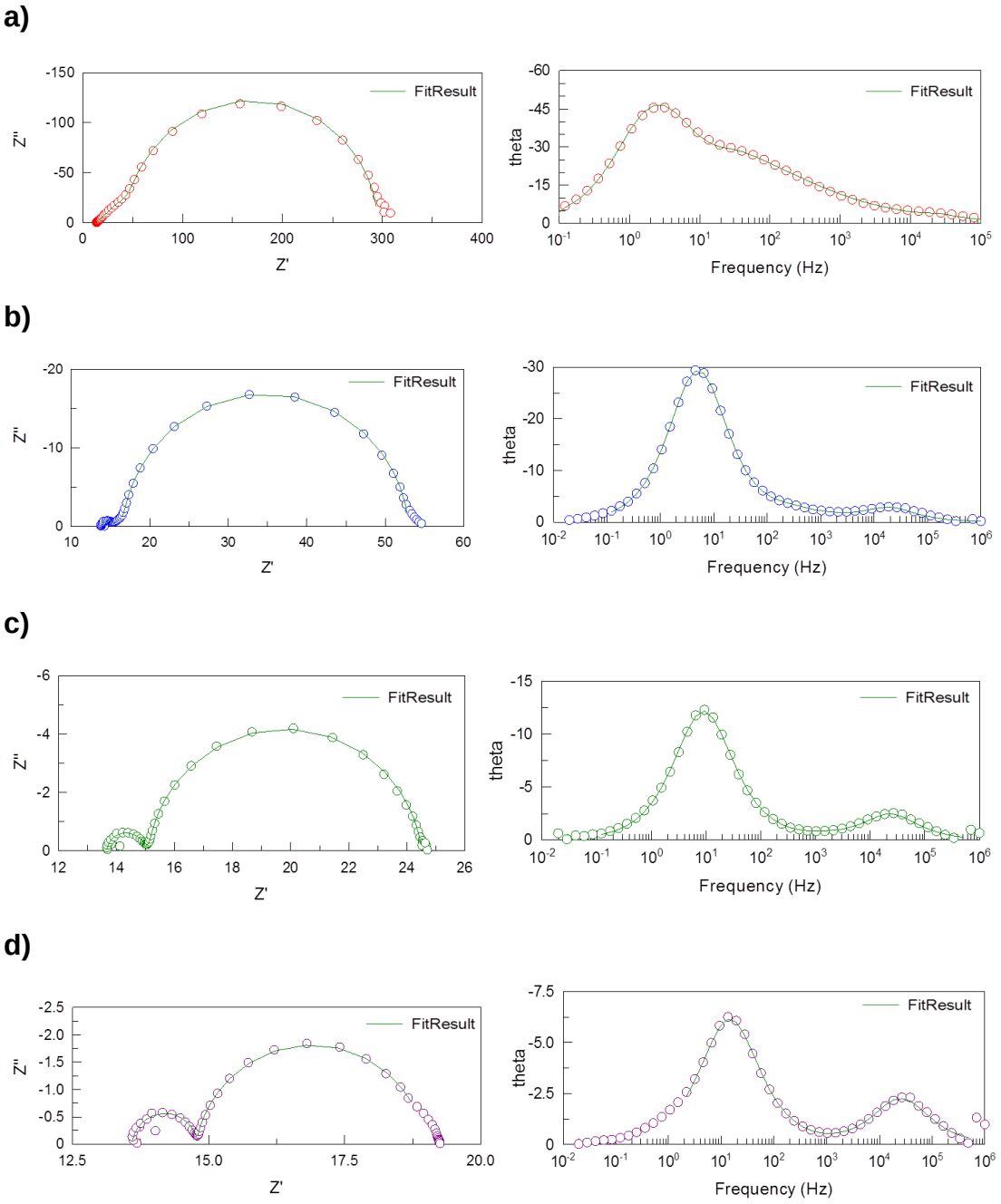

Fig. 2.21: *The Nyquist and Bode plots for a DSSC sensitised by N719 at* ***a)*** *0.5 V;* ***b)*** *0.6 V;* ***c)*** *0.7 V;* ***d)*** *0.8 V.*

However, the applied bias under which analysis is performed can have a large effect on the impedance characteristics of a DSSC (Fig. 2.21). With different applied biases, the model used must be altered to account for this change in properties. For example, at high voltages (greater than the V_{OC} of the cell), the charge traps are filled

so TiO_2 film becomes conducting[151]; thus the resistance to transport through the TiO_2 film is deemed negligible[143]. At lower potentials, less than the V_{OC} of the cell, contribution of R_{trans} in the TiO_2 can be seen by a straight line at the high frequency end of the second semi-circle (Fig. 2.21a)[151]; thus all spectra were analysed to ensure the model used was appropriate for the spectra produced. The FTO - TiO_2 and FTO - electrolyte interfaces are rarely observed in an impedance spectrum, so were not included in the model used. As the electrolyte diffusion processes were not always well defined in the impedance spectra and this parameter is not affected by the dye, fits were only obtained for the data relating to the two high frequency semi-circles[146]. Therefore, the model used for the impedance data obtained during this thesis was simplified (Fig. 2.22), and the contribution of transport through the TiO_2 film (r_{trans}) was only included if the straight line at the high frequency end of the spectrum was observed. The fits obtained for all of the spectra analysed were of similar quality to those displayed herein (Fig. 2.21).

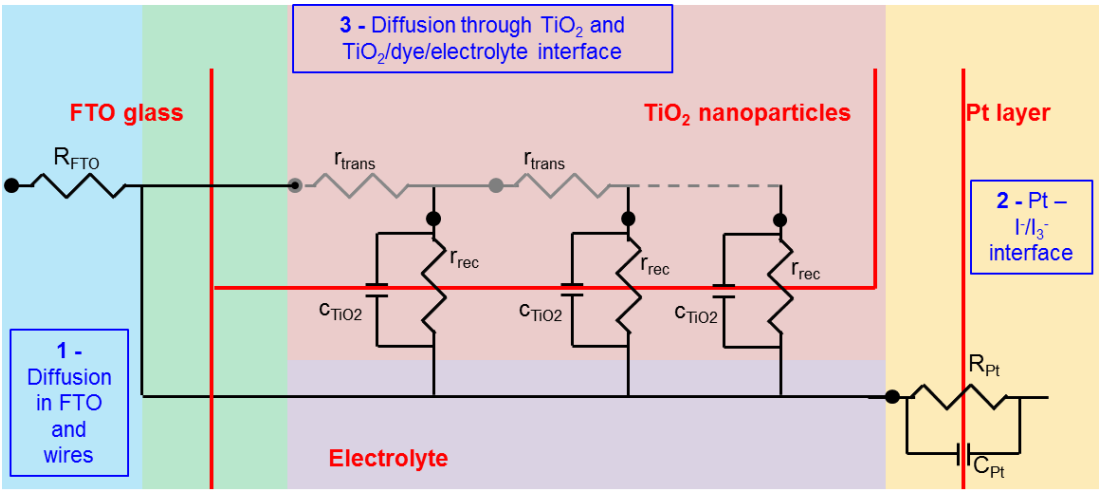

Fig. 2.22: *The equivalent circuit used to model the impedance data obtained for the DSSCs tested in this thesis. r_{trans} – resistance to the transport of electrons in TiO_2; r_{rec} – resistance to recombination across the TiO_2-dye-I^-/I_3^- interface; c_{TiO2} – double layer capacitance; R_{Pt} – resistance across Pt-I^-/I_3^- interface; C_{Pt} – capacitance at the Pt-I^-/I_3^- interface. A constant phase element (CPE) was used to model all capacitive processes. The r_{trans} parameter was only included when a straight line at the high frequency region of the spectrum was observed.*

$$R_{rec} = \frac{r_{rec}}{d}$$ Equation 2.15

$$C_{TiO2} = c_{TiO2}\, d$$ Equation 2.16

$$R_{trans} = r_{trans} d$$ Equation 2.17

It is important to note that the thickness of the TiO_2 layer (d / cm) is an important parameter when considering electron transfer within the cell. The values calculated by application of the transmission line model refer to the element per unit length, as the elements are distributed through the transmission line model in a repetitive manner[147]. The distributed elements (r_{rec}, c_{TiO2}, r_{trans}) and the film thickness can therefore be used to calculate the resistive and capacitive parameters of the cell - R_{rec}, R_{trans} and C_{TiO2} (Equations 2.15-2.17[151,152]). In order to determine the thickness of the TiO_2 layer, four doctor bladed working electrodes were measured at Loughborough University using a profilometer, and calculated to have an average film thickness of 11.7 µm ± 0.5. However, for each cell the thickness of the film across the working area varied from 10 to 15 µm. The cells were also individually doctor bladed, but not individually tested. Therefore, due to the significant error in calculations utilising the cell thickness, calculation of R_{rec}, C_{TiO2} and R_{trans} was not carried out and the distributed elements were compared.

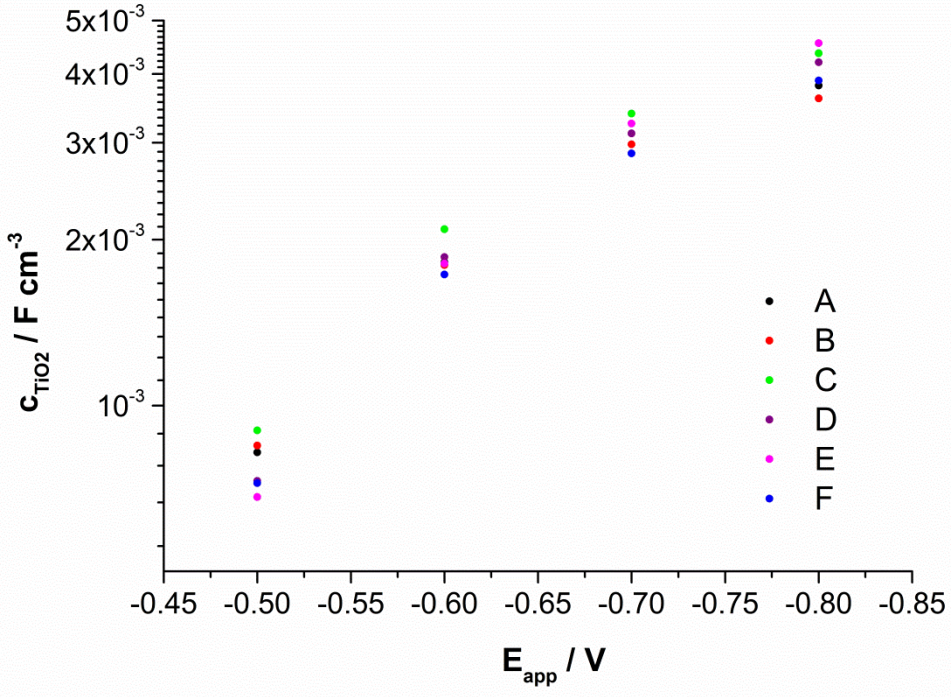

Fig. 2.23: *Capacitance versus applied voltage for six DSSC sensitised by N719*

By plotting the logarithmic capacitance of the TiO_2 surface (c_{TiO2}) against the applied voltage (E_{app}), the effect of the dye on the chemical capacitance of the TiO_2 surface was determined (Fig. 2.23). By comparison of six different cells sensitised by N719, it can be seen that there is variation in the distributed capacitance for the different cells, which could be due to differences in cell thickness or changes in the TiO_2 surface structure. That the logarithmic capacitance is not linearly related to the applied voltage (Fig. 2.23), suggests that at higher potentials there may also be some contribution of Helmholtz capacitance at the surface which is causing the capacitance to saturate[143]. This factor must be considered when analysing the data.

$$\tau_n = R_{rec}C_{TiO2} \qquad \text{Equation 2.18}$$

To compare recombination across the TiO_2-dye-I^-/I_3^- interface for each dye the electron lifetime at this interface was calculated (Equation 2.18[143,152]). Use of this parameter accounted for any changes in the capacitance of the TiO_2 surface, which could affect recombination within the cell. Also, this calculation results in

cancellation of the cell thickness parameter; thus errors due to potential variations in cell thickness were irrelevant with respect to the lifetime. The lifetime at the TiO_2-dye-I^-/I_3^- interface (τ_n) has a logarithmic relationship with the voltage applied to the cell[152] (E_{app}); therefore $\log\tau_n$ against E_{app} was plotted for each cell (Fig. 2.24) to ascertain the effects of the dye on recombination across this interface. However, if the dye structure had a significant effect on the capacitance of the TiO_2 film, $\log\tau_n$ was plotted against c_{TiO2} to ensure that the lifetimes across this interface were compared when the electronic properties of the TiO_2 are similar[143].

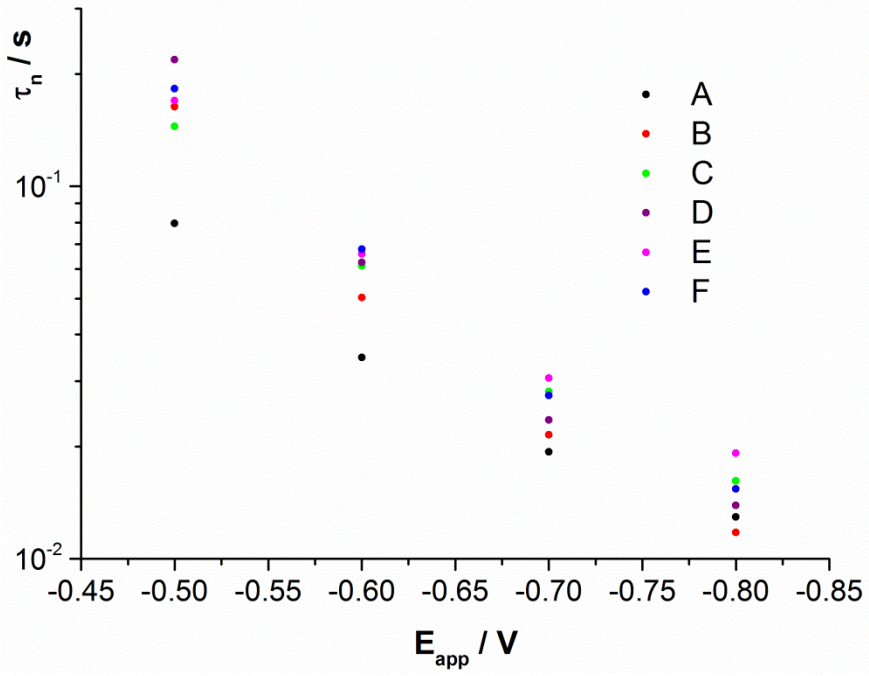

Fig. 2.24: *The effect of the applied voltage on the electron lifetime at the TiO_2-dye-I^-/I_3^- interface for six DSSCs sensitised by N719.*

Experimentally, impedance analysis was performed according to literature methods[153,154] using the same applied biases for each cell. As the light intensity can have a large effect on the impedance of a solar cell[155], all cells were measured under the same lighting conditions; under artificial, low level, room lighting. Multiple cells were constructed for each dye, thus multiple impedance measurements were performed for each dye allowing any variations due to cell construction to be accounted for. To ensure the impedance measurements were not effecting large

changes within the cell, the JV curve of each cell was taken before and after impedance measurements (Appendix 1, J-V data).

2.3.3.3 Experimental details

Electrochemical impedance measurements were performed using the AUTOLAB PGSTAT30 potentiostat controlled by FRA software, version 4.9.007. The cells were measured under low level artificial room lighting, with an oscillation amplitude of 10 mV applied at 50 frequencies distributed logarithmically in the range 1,000,000 to 0.02 Hz. Analysis was performed on complete DSSCs with applied forward biases of 0.5, 0.6, 0.7, and 0.8 V. The Nyquist and Bode plots obtained were fit according to the model developed by Bisquert et. al[147-150] using Z-view software version 3.3a.

2.3.4 Transient Absorption Spectroscopy (TAS)

2.3.4.1 The technique and its application to DSSCs

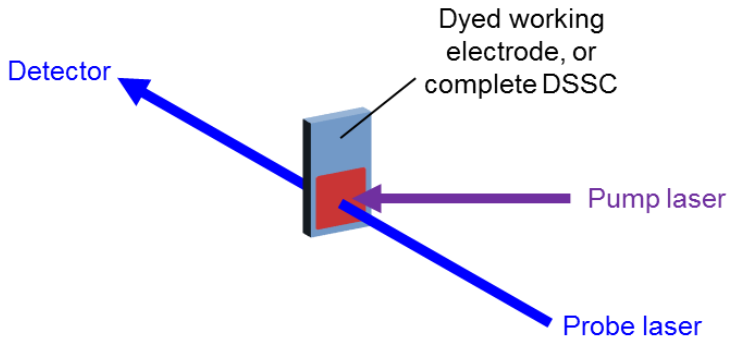

Fig. 2.25: *Transient absorption spectroscopy of a DSSC.*

Transient absorption spectroscopy of DSSCs is used to measure the lifetime of the oxidised dye on the TiO_2 surface. To do so, a laser (the probe laser) is passed through the sample which measures the optical density of the sample at a particular probe wavelength. Exciting the dye with a second laser (the pump laser) allows the signal for the oxidised dye to be measured by the probe laser (Fig. 2.25). By measuring the

optical density at the wavelength at which the excited state dye absorbs, and plotting the change in the optical density (ΔO.D) as a function of time (Fig. 2.26), the decay of the oxidised dye can be monitored.

The titanium working electrode sensitised with the dye species was initially measured by varying the probe wavelength to determine the wavelength at which the signal had the highest intensity; thus the wavelength of the oxidised dye. At that wavelength, the decay of the dye cation on TiO_2 was determined using an inert electrolyte to determine the rate of electron transfer from the TiO_2 to the oxidised dye. Measurements were then performed at the same probe wavelength on a complete cell to measure the lifetime of the dye cation in a DSSC; which should decrease due to regeneration of the dye by the electrolyte[60]. Thus comparison of the rate of decay of the dye on TiO_2 using an inert electrolyte, and the dye in a full cell allowed exploration of dye regeneration.

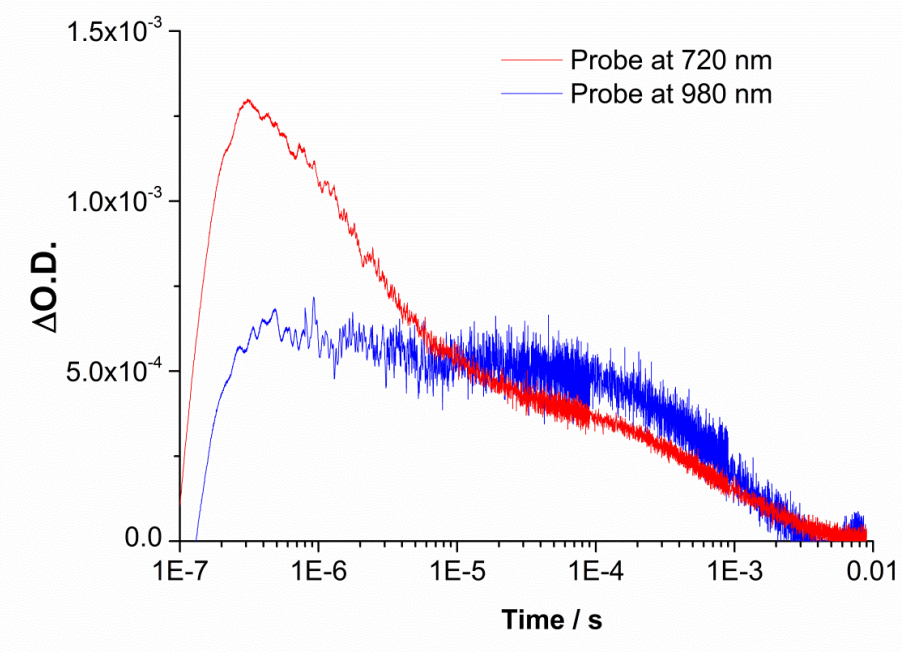

Fig. 2.26: *The TAS spectrum for a complete DSSC sensitised with $K_4[Ru(dcbpy)_2(NCS)_2]$.*

In a complete DSSC, biphasic decay of the signal is observed which is attributed to the decay of the excited state of the dye, and the decay of excited state electrons in the TiO_2 working electrode[58]. Decay of the electrons injected into TiO_2 have been shown to display a signal at 980 nm[59]. By comparison of the signal at 980 nm and the signal from the excited state dye (Fig. 2.26), it is clear that the initial decay observed is due to decay of the oxidised dye. Therefore, only the data for the first phase of decay were fit to determine the lifetime of the oxidised dye in a complete cell. The data were fit using a stretched exponential function (Equation 2.15; ΔO.D = change in optical density, A = initial absorption, t = time (s), τ_{ww} = relaxation time (s), β = stretching parameter); thus allowing the lifetime of the excited state dye to be calculated (Equation 2.19)[21].

$$\Delta O.D. = A \cdot e^{-\left[\frac{t}{\tau_{ww}}\right]^{\beta}} \qquad \text{Equation 2.19}$$

As dye regeneration is deemed the rate determining step of electron transfer in the solar cell[21], it is important to explore the mechanisms of the regeneration process. By determining the lifetime of the oxidised dye in a DSSC, the rate of dye regeneration can be explored. To probe the mechanism of regeneration, TAS studies have been used on numerous occasions to characterise the effect of dye structure on the rate of dye regeneration[22,37,60]. Such studies were thus implemented in this thesis.

2.3.4.2 Experimental details

TAS studies were performed by John Clifford at ISIQ. An 8 μm thick TiO_2 film was sensitised over 20 hours, and the cell was completed with a I^-/I_3^- electrolyte or an inert electrolyte made up of a solution of 0.5 M TBP / 0.01 M Gnd. NCS in acetonitrile. Dye excitation was achieved using a pump laser at 580 nm, and a probe laser at 800 nm measured the decay of the oxidised dye. The cells were measured at short circuit under low light levels.

Chapter 3: Lessons learnt in dye synthesis

3.1 Introduction

Although hundreds of ruthenium dyes for DSSCs have been synthesised, only the successful synthetic route to a new ruthenium dye is generally reported. The possible synthetic routes to fully chelated tris (bidentate), bis-heteroleptic, tris-heteroleptic and bis (tridentate) ruthenium-polypyridyl dyes have been comprehensively reviewed[156] although the conditions for the syntheses of these dyes were not detailed. Otherwise, there is little emphasis on dye synthesis in the literature and as yet there is no research which focusses on problems which can hinder or prevent the synthesis of novel ruthenium dyes. As ruthenium dyes are still the basis of commercial DSSCs; such studies are important to ensure that difficulties in the synthesis of new dyes do not continue to be a bottle neck in the development of more stable, highly efficient dyes for DSSCs.

3.1.1 General considerations

The starting material for the synthesis of all ruthenium dyes is $RuCl_3.xH_2O$[156]. However, $RuCl_3.xH_2O$ is highly hygroscopic[157] which can cause difficulties in the measurement of accurate stoichiometries for a reaction. It also contains ruthenium species in oxidation states ranging from +2 to +4[157]; thus reducing solvents such as DMSO, DMF, alcohols and water are used to reduce the ruthenium centre to the +2 oxidation state. DMF is the most commonly used solvent as it has a high boiling temperature (153 ^{o}C) and a high polarity for dissolution of the poorly soluble H_2-dcbpy ligand and Ru-H_2-dcbpy dyes. Ruthenium species under multiple oxidation states can be seen under similar conditions[158]; therefore an oxygen free environment is used to prevent oxidation of the Ru (II) centre. Reduced light can also be used to prevent photodegradation of the ruthenium dyes formed[100,159], although this is less common.

3.1.2 Synthesis of $Ru(H_2\text{-dcbpy})_2(ZZ`)$ dyes

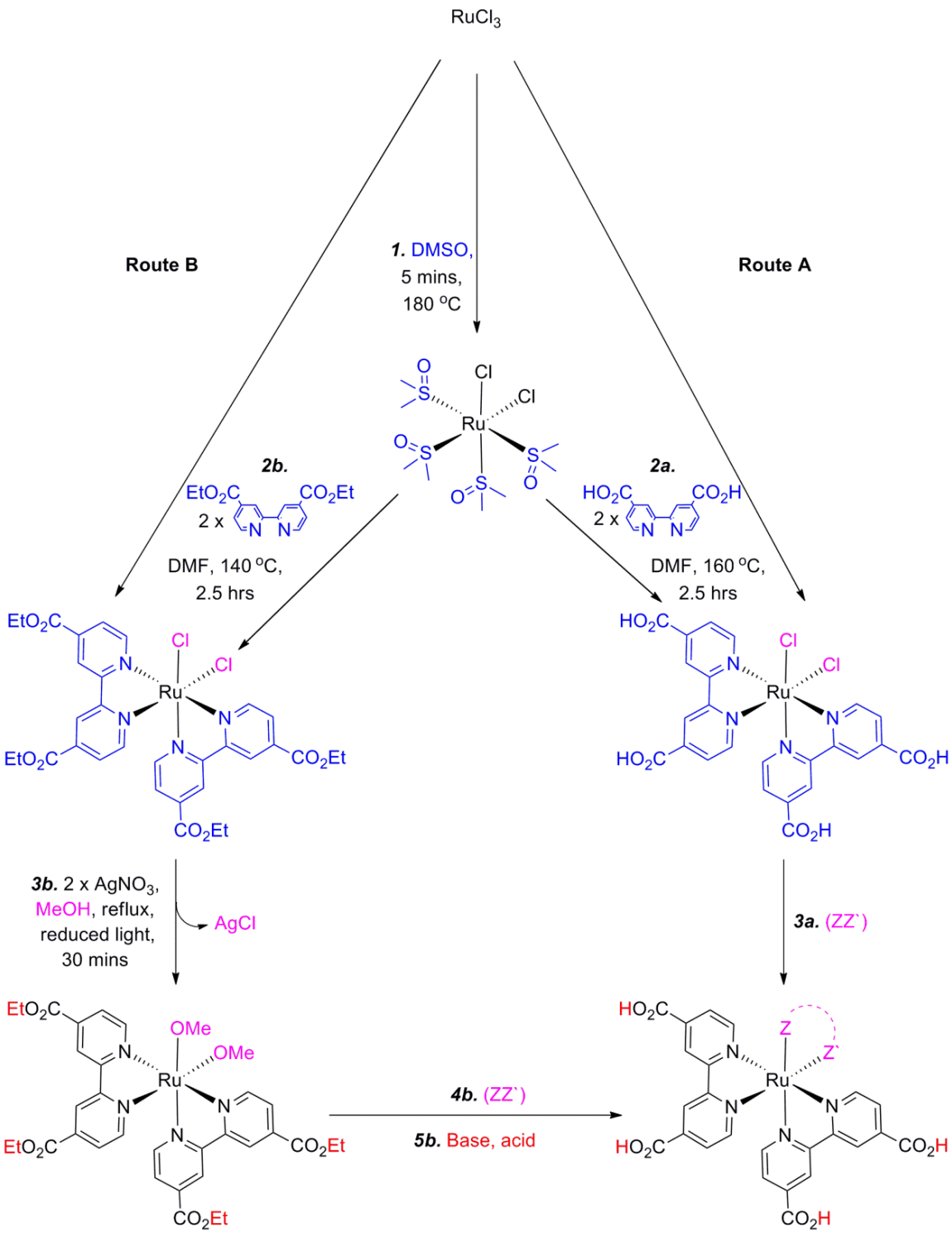

Fig. 3.1: *Procedures for the synthesis of $Ru(H_2\text{-dcbpy})_2(ZZ`)$ dyes where (ZZ`) is a bidentate ligand or two equivalent monodentate ligands.*

$Ru(H_2\text{-}dcbpy)_2(ZZ`)$ dyes, where (ZZ`) is a bidentate ligand[96,160] or two equivalent monodentate ligands[18,31,111,124], are most commonly synthesised from $Ru(H_2\text{-}dcbpy)_2Cl_2$ (Route A, Fig 3.1). However, $Ru(decbpy)_2Cl_2$ can also be used as a starting material. The higher solubility of $Ru(decbpy)_2Cl_2$ compared to $Ru(H_2\text{-}dcbpy)_2Cl_2$ allows the removal of the chloride ions by silver salts which can be used to reduce the kinetic barrier to substitution of the (ZZ`) (Route B, Fig. 3.1). This method has been shown to increase the yield and purity of the products formed[107]. However, the hydrolysis of the ester group and subsequent acidification of the carboxylic acid groups can be problematic if (ZZ`) is sensitive to acidic or basic conditions.

Starting Ru complex	Solvent	Heating	Time	Reference
$RuCl_3.xH_2O$	DMF	Thermal, reflux	1 hr	[161]
$RuCl_3.xH_2O$	DMF	Thermal, reflux	12 hrs	[162]
$RuCl_3.xH_2O$	DMF, LiCl	Thermal, reflux	2 days	[163]
$RuCl_3.xH_2O$	DMF	Thermal, 140 ^oC	2.5 hrs	[111]
$[Ru(p\text{-}cymene)Cl_2]_2$	1:1 HCl:H_2O	Microwave, 170 ^oC	1 hr	[164]
$Ru(DMSO)_4Cl_2$	DMF	Thermal, 140 ^oC	2.5 hrs	This work
$Ru(DMSO)_4Cl_2$	2:3 $CHCl_3$:EtOH	Thermal, reflux	24 hrs	[165]

Table 3.1: *Possible conditions for the synthesis of $Ru(H_2\text{-}dcbpy)_2Cl_2$.*

The synthesis of $Ru(H_2\text{-}dcbpy)_2Cl_2$ must be carried out stoichiometrically to prevent the formation of $[Ru(H_2\text{-}dcbpy)_3]^{2+}$. The difficulty of ruthenium dye synthesis can be demonstrated by the wide variety of conditions that can be used to synthesise a simple compound such as $Ru(H_2\text{-}dcbpy)_2Cl_2$ (Table 1.1). Despite the large number of procedures for the synthesis of this compound, during the progress of this thesis difficulties in the synthesis of both $Ru(H_2\text{-}dcbpy)_2Cl_2$ and $Ru(decbpy)_2Cl_2$ were encountered as the stoichiometry of the reactions could not be assured due to the use of highly hygroscopic $RuCl_3$ (3.1.1). This problem was overcome by using $Ru(DMSO)_4Cl_2$ as a starting material (Fig. 3.1); a complex which is easily synthesised from $RuCl_3.xH_2O$ to a high level of purity[166].

The synthesis of $Ru(H_2\text{-}dcbpy)_2(ZZ`)$ dyes from $Ru(DMSO)_4Cl_2$ via the $Ru(H_2\text{-}dcbpy)_2Cl_2$ intermediate can be performed in a one-pot reaction once the substitution

of Cl_2 by (ZZ`) has been optimised. For example, substitution of the Cl^- ligands in $Ru(H_2\text{-dcbpy})_2Cl_2$ by ^-NCS to form the N3 dye has been extensively studied. As substitution of ^-Cl by ^-NCS can lead to the formation of both the N- and S-bound isomers of the dye[167], either high reaction temperatures or long reaction times are required to ensure that only the thermodynamically favourable N-bound isomer of the dye is synthesised. To ensure complete substitution of the Cl^- ligands, excess ^-NCS is added, but again there are many different reaction conditions which allow the successful synthesis of this compound (Table 3.2, 3.2.1). Despite the range of possible reaction conditions for the overall synthesis of the N3 dye, the correct combination of reaction conditions and reaction time is essential to ensure that the reaction goes to completion without the formation of any impurities or side products such as $[Ru(H_2\text{-dcbpy})_3]^{2+}$ [111,161]. Determining the optimal reaction conditions for the synthesis of novel dyes can therefore be difficult.

3.1.3 Synthesis of $Ru(H_2\text{-dcbpy})(Y_2\text{-bpy})(NCS)_2$ dyes

Asymmetric complexes are normally synthesised using the $[Ru(p\text{-cymene})Cl_2]_2$ dimer as a starting material. This dimer is easily synthesised (3.8.1.2[168]) and it provides control for the reaction as substitution of the p-cymene ligand requires a significantly higher energy than substitution of the bridging Cl^- ligands. Therefore, the $[Ru(Y_2\text{-bpy})(p\text{-cymene})Cl]^+$ intermediate is formed at low temperatures with the p-cymene ligand preventing over substitution of the Y_2-bpy ligand[169]. Substitution of the p-cymene ligand by H_2-dcbpy can then be performed at a higher temperature, followed by substitution of the two Cl^- ligands by ^-NCS. Thus the synthesis of $Ru(dcbpy)(Y_2\text{-bpy})(NCS)_2$ dyes can be performed in a highly controlled one-pot reaction (Fig. 3.2). To date, many dyes of this type have been synthesised, often with long alkyl chains incorporating different chromophoric aromatic groups as the Y group[23,37,38]. Unlike the synthesis of the N3 dye, synthetic procedures which utilise this method are usually performed in a very similar manner, with only small variations in the temperature used for the reaction.

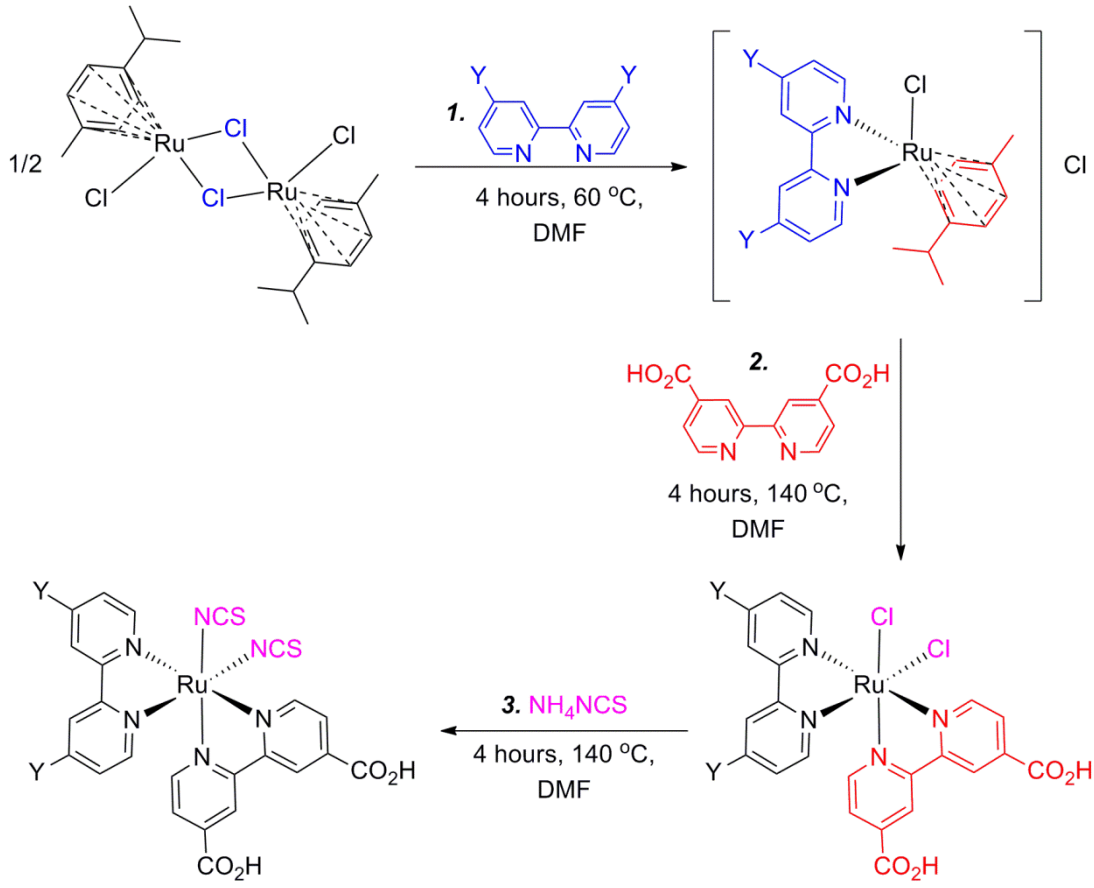

Fig. 3.2: *The synthesis of Ru(H_2-dcbpy)(Y_2-bpy)$(NCS)_2$ dyes*

3.1.4 Dye purification

Dye purification by recrystallisation is rarely achieved[167] as dyes are often poorly soluble and unstable in solution[100,159]. Purification of dyes by deprotonation and re-precipitation from water has been successful[18,161,162,165], but producing a pure dye often requires the use of sephadex column chromatography. This is a type of size exclusion chromatography[170] which has been widely used in the purification of ruthenium dyes where the product and the impurities are significantly different in size. However, up to four columns can be required to purify a dye[38]. Silica gel chromatography cannot be used to purify Ru-H_2-dcbpy compounds due to the strong interactions between the silica gel and the carboxylic acid group on the H_2-dcbpy ligand. An ethyl ester protecting group can allow the use of silica gel

chromatography for dye purification[84]. However, the procedure for removal of the protecting group must be considered.

3.1.5 Microwave synthesis

Considering the commercial nature of ruthenium dyes for DSSCs, product synthesis without the use of complex or lengthy purification procedures is desirable to reduce the cost of dye manufacture. The majority of commercial dyes require significant purification, and purification free synthesis is rarely achieved using thermal methods[171]. The use of microwave reactions in the synthesis of pure ruthenium dyes leads to a significant reduction in the reaction time and an increase in the yield and purity of the product formed[164,172,173]. However, using a closed microwave system decarboxylation of the H_2-dcbpy and decbpy ligands can occur[173,174]. This can be prevented by using a microwave reactor with an external reflux condenser[175], which reduces the pressure within the reactor thus preventing decarboxylation[173]. Therefore, although microwave reactions are extremely promising, the availability of such apparatus may limit their use.

3.1.6 Lessons learnt in dye synthesis

During the course of this investigation, the synthesis of twelve new dyes (Fig. 3.3) was attempted, and in each case the standard synthetic procedures described herein proved unsuccessful. Identification of the breakdown products and impurities formed proved that the synthesis of $K_4[Ru(H_2\text{-dcbpy})_2(NCSe)_2]$, $[Ru(H_2\text{-dcbpy})_2(bbzt)]^{2+}$, $Ru(H_2\text{-dcbpy})_2(NCS)Cl$, $Ru(3,3`\text{-}(CO_2H)_2\text{-bpy})(dnbpy)(NCS)_2$ and $Ru(H_2\text{-dcbpy})(4,4`\text{-}F_2\text{-bpy})(NCS)_2$ to a high level of purity would be improbable. However, for the rest of the dyes, exploration of the products of each synthesis allowed the development of new methods to prevent the formation of breakdown products and develop novel procedures to achieve a pure product. It is hoped that this work will promote the use of more systematic and controlled synthetic procedures, as well as widening the scope of ligands that could be used in ruthenium dyes.

$K_4[Ru(dcbpy)_2(NCX)_2]$

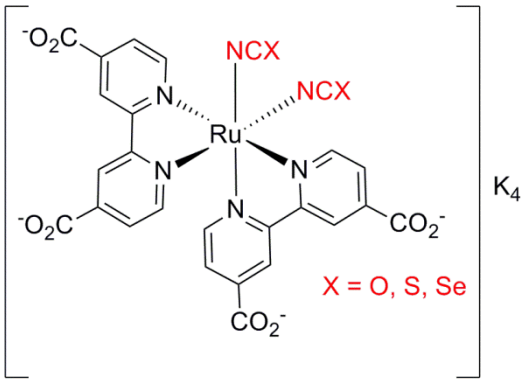

$[Ru(H_2\text{-}dcbpy)_2(bbzt)]^{2+}$

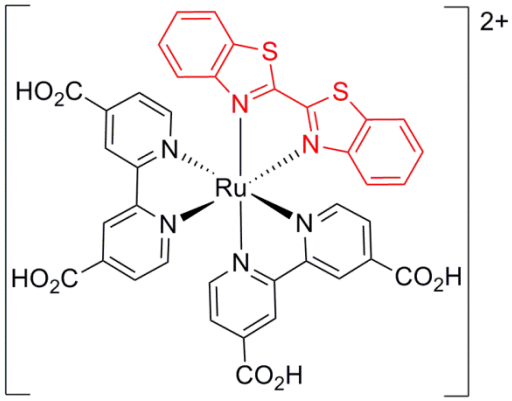

$Ru(H_2\text{-}dcbpy)_2(NCS)Cl$

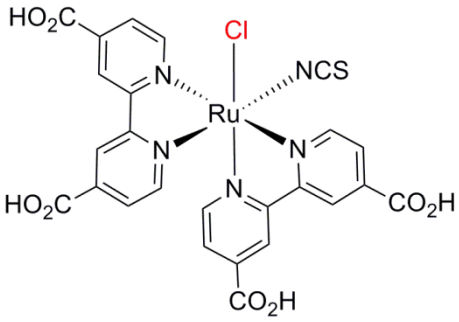

$Ru(3,3'\text{-}(CO_2H)_2\text{-}bpy)(dnbpy)(NCS)_2$

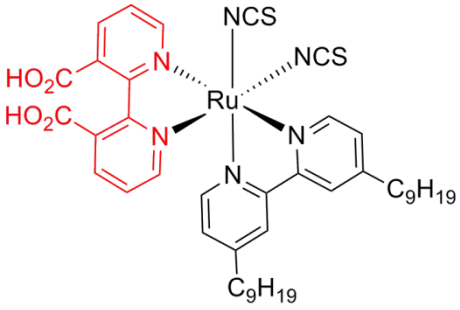

$Ru(H_2\text{-}dcbpy)(4,4'\text{-}Y_2\text{-}bpy)(NCS)_2$ and $Ru(H_2\text{-}dcbpy)(5,5'\text{-}Y_2\text{-}bpy)(NCS)_2$

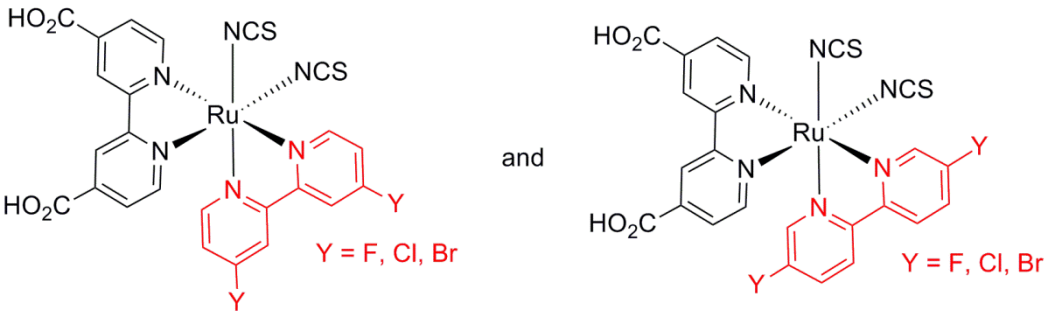

Fig. 3.3: *Synthetic procedures for the formation of a number of dyes were studied.*

3.2 $Ru(H_2\text{-dcbpy})_2(NCX)_2$ synthesis where X = O, S, Se

3.2.1 The acid-base chemistry of H_2-dcbpy

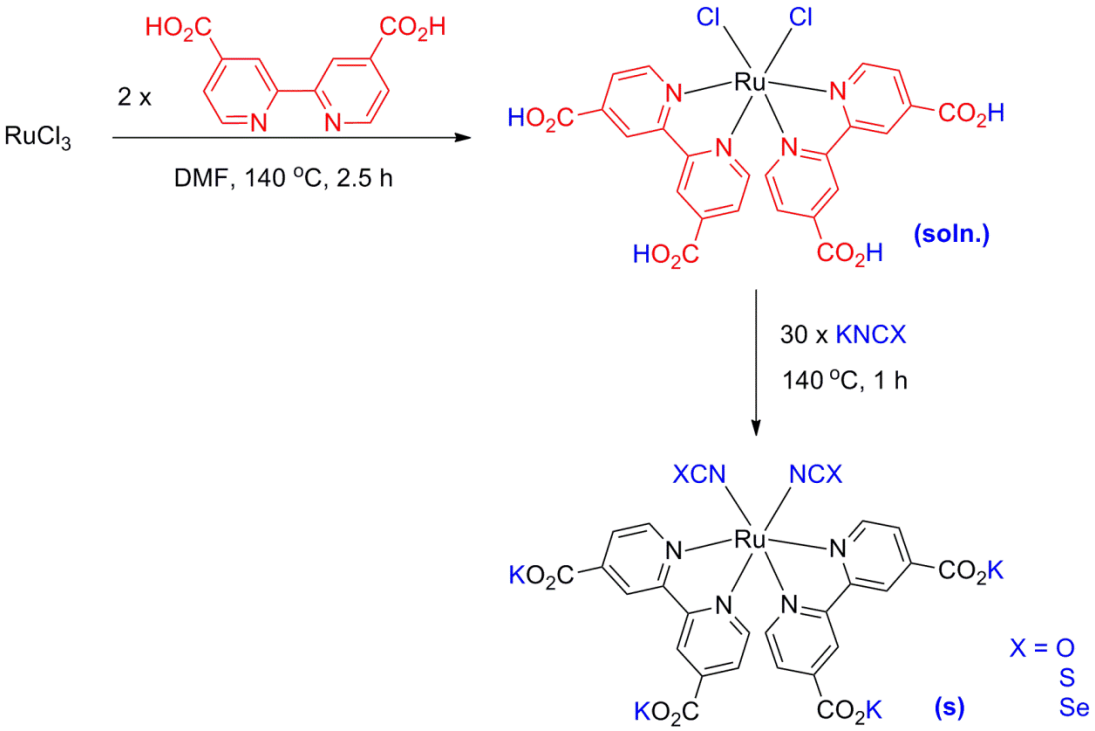

Fig. 3.4: *Attempted synthesis of $Ru(H_2\text{-dcbpy})_2(NCX)_2$.*

The synthesis of $Ru(H_2\text{-dcbpy})_2(NCX)_2$ was initially attempted using the standard one pot synthesis for the N3 dye, $Ru(H_2\text{-dcbpy})_2(NCS)_2$ (Fig 3.4). Due to the availability of the ^-NCX salts, KNCX was utilised for introduction of the ^-NCO and ^-NCSe ligands. However, a water soluble product precipitated from DMF after addition of KNCX (Fig. 3.3), suggesting that the potassium salt of the dye had formed. Use of the $[NBu_4][NCO]$ salt caused an acetone soluble product to form, suggesting that the fully deprotonated product with $[NBu_4]^+$ counter ions was produced. Thus *in situ* dissociation of the carboxylic acid group of the H_2-dcbpy ligand was observed.

In neutral or alkaline solutions, the H_2-dcbpy ligand is not fully protonated[176]. Therefore, in the synthesis of the series of dyes $Ru(H_2\text{-dcbpy})_2(NCX)_2$, precipitation of the potassium salt of the dye from DMF drives the reaction towards formation of the fully deprotonated complex. Considering literature procedures for the synthesis of $Ru(H_2\text{-dcbpy})_2(NCS)_2$ from $Ru(H_2\text{-dcbpy})_2Cl_2$ (Table 3.2), the product formed when using potassium or sodium $^-$NCS salts required precipitation from water, suggesting that deprotonation of the H_2-dcbpy ligand also occurred during these syntheses. Use of the slightly acidic ammonium salt of $^-$NCS[111] prevented the deprotonation of H_2-dcbpy. However, ammonium salts of $^-$NCO and $^-$NCSe were not commercially available and attempts to synthesise these salts were unsuccessful. Therefore, ammonium salts could not be used in the synthesis of $Ru(H_2\text{-dcbpy})_2(NCX)_2$ dyes.

$^-$NCS salt	Solvent	Heating	Time	Product precipitation from water?	Reference
NaNCS	22:30 0.1M NaOH:DMF	Thermal, reflux	6 hrs	$HClO_4$ (aq), CF_3SO_3H (aq)	18
NaNCS	1:19 H_2O:DMF	Thermal, reflux	12 hrs	$HClO_4$ (aq)	162
NH_4NCS	DMF	Thermal, 80 ^oC	1 hr	Not required	111
NH_4NCS	DMF	Thermal, 140 ^oC	1 hr	Not required	This work
KNCS	H_2O	Microwave, 170 ^oC	30 mins	Not required	164
NaNCS	22:25 0.1M NaOH:EtOH	Thermal, reflux	6 hrs	$HClO_4$ (aq)	165

Table 3.2: *Possible conditions for the synthesis of $Ru(H_2\text{-dcbpy})_2(NCS)_2$ from $Ru(H_2\text{-dcbpy})_2Cl_2$.*

3.2.2 Acid sensitivity of $^-$NCO

The synthesis of $Ru(H_2\text{-dcbpy})_2(NCO)_2$ was therefore attempted by precipitation of $K_4[Ru(dcbpy)_2(NCO)_2]$ from water using weak acid. This reaction resulted in a rapid colour change from dark purple to bright red, but no precipitate formed. This colour change was likely to be due to the hydrolysis of $^-$NCO to CO_3 and NH_4^+ which is catalysed by acids[177,178]. Precipitation of the product was therefore attempted from methanol using methanolic acid, but a colour change was again observed suggesting

that enough water remained to hydrolyse ¯NCO. Therefore, the ¯NCO ligand was too sensitive to acidic conditions for the synthesis of $Ru(H_2\text{-dcbpy})_2(NCO)_2$ to be achieved, and protection of the ¯NCO ligand from the acidic protons was necessary to prevent hydrolysis from occurring.

3.2.3 Protection and deprotection of the carboxylic acid group

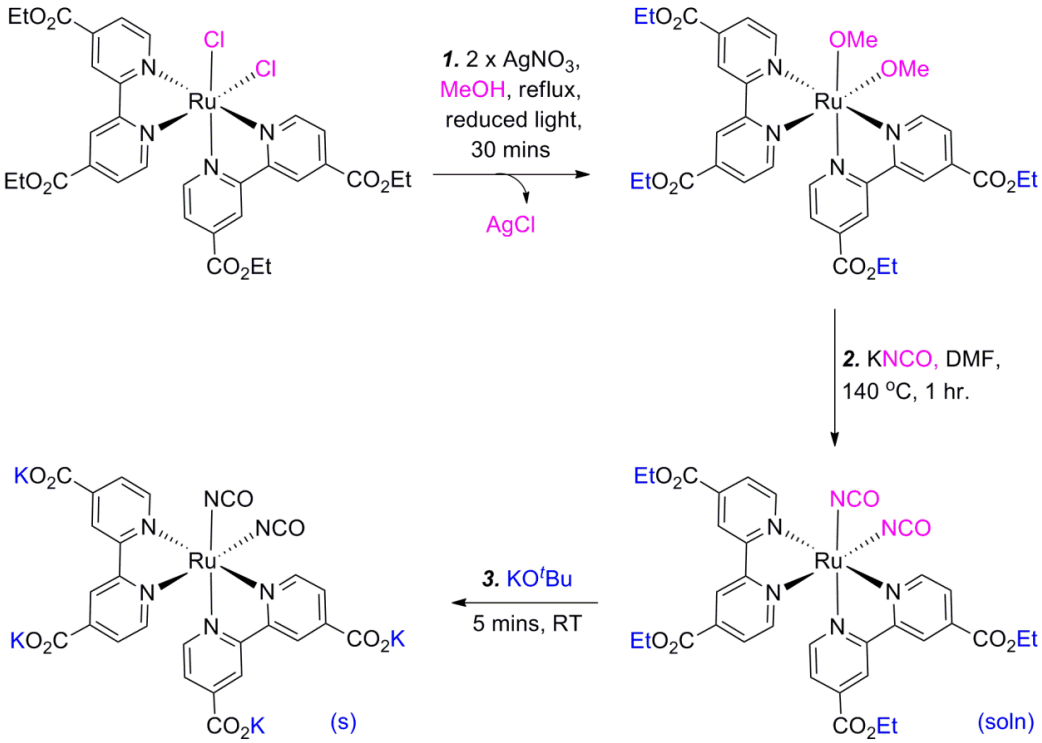

Fig. 3.5: *The synthesis of $K_4[Ru(dcbpy)_2(NCO)_2]$*

The effects of the acid-base chemistry of the H_2-dcbpy ligand and the sensitivity of the ¯NCO ligand to acid were circumvented by using $Ru(decbpy)_2Cl_2$ as a starting material. Removal of the chloride ligands by silver nitrate (3.1.2) was utilised in the synthesis of this dye to ensure complete substitution of the ¯NCO ligand as KNCO is only sparingly soluble in DMF[179]. After substitution, the resulting solution was filtered to remove insoluble impurities (mostly KNCO) and then a strong DMF soluble potassium containing base (KO^tBu[180]) was added to remove the ester groups, causing precipitation of the potassium salt of the dye (Fig. 3.5).

Although the potassium salt of the dye was initially synthesised by the reflux of $Ru(H_2\text{-dcbpy})_2Cl_2$ and KNCO in DMF (3.2.1), this procedure was preferred as it provided complete protection for the $^-$NCO ligand from the acidic protons. Insoluble impurities formed were removed by filtration of the DMF soluble ester complex, and precipitation of the product from the filtrate isolated the product from any soluble impurities. Use of potassium salts throughout the reaction ensured the exclusive formation of the potassium salt of the complex, and precipitation of this salt also avoided the low pressure evaporation of DMF[161] which is often necessary in the synthesis of ruthenium dyes. Thus the synthesis of $K_4[Ru(dcbpy)_2(NCO)_2]$ was successfully achieved to a high level of purity.

3.2.4 Promotion of $^-$NCSe breakdown by ruthenium

The synthesis of $K_4[Ru(dcbpy)_2(NCSe)_2]$ was initially performed as described for the $^-$NCO analogue (3.2.3), but breakdown of the $^-$NCSe ligand to $^-$CN was observed; thus $K_4[Ru(dcbpy)_2(CN)_2]$ was synthesised. Breakdown of the $^-$NCSe ligand to $^-$CN on binding to ruthenium has been shown to occur particularly rapidly when the ligand is bound to ruthenium through the nitrogen atom[167]. However, the study was not executed under an inert atmosphere, and the free $^-$NCSe ligand is prone to oxidation, as well as decomposition above 100 ^oC[181]. Therefore, the synthesis of $K_4[Ru(dcbpy)_2(NCSe)_2]$ from $Ru(decbpy)_2Cl_2$ was attempted under an inert atmosphere in ethanol by removal of the chloride ions, substitution of $^-$NCSe by reflux in ethanol for half an hour, and precipitation of the product with KO^{t}Bu (3.2.3). Although some peaks were present which could show product formation, comparison with the ^{1}H NMR for $K_4[Ru(dcbpy)_2(CN)_2]$ showed that breakdown of the $^-$NCSe ligand to $^-$CN had again occurred (Fig. 3.6a). ^{1}H NMR analysis of the reaction mixture before the addition of KO^{t}Bu showed similar ligand breakdown, confirming that this breakdown was not due to the reaction of $^-$NCSe with this base. The synthesis was repeated by stirring dechloridated $Ru(decbpy)_2Cl_2$ with KNCSe at room temperature for 12 hours. Despite the mild conditions used, formation of $K_4[Ru(dcbpy)_2(CN)_2]$ was still observed (Fig. 3.6b). Therefore the $^-$NCSe ligand is

highly prone to breakdown to $^{-}$CN when bound to ruthenium, and neither the synthesis of $K_4[Ru(dcbpy)_2(NCSe)_2]$ nor $Ru(H_2dcbpy)_2(NCSe)_2$ could be achieved.

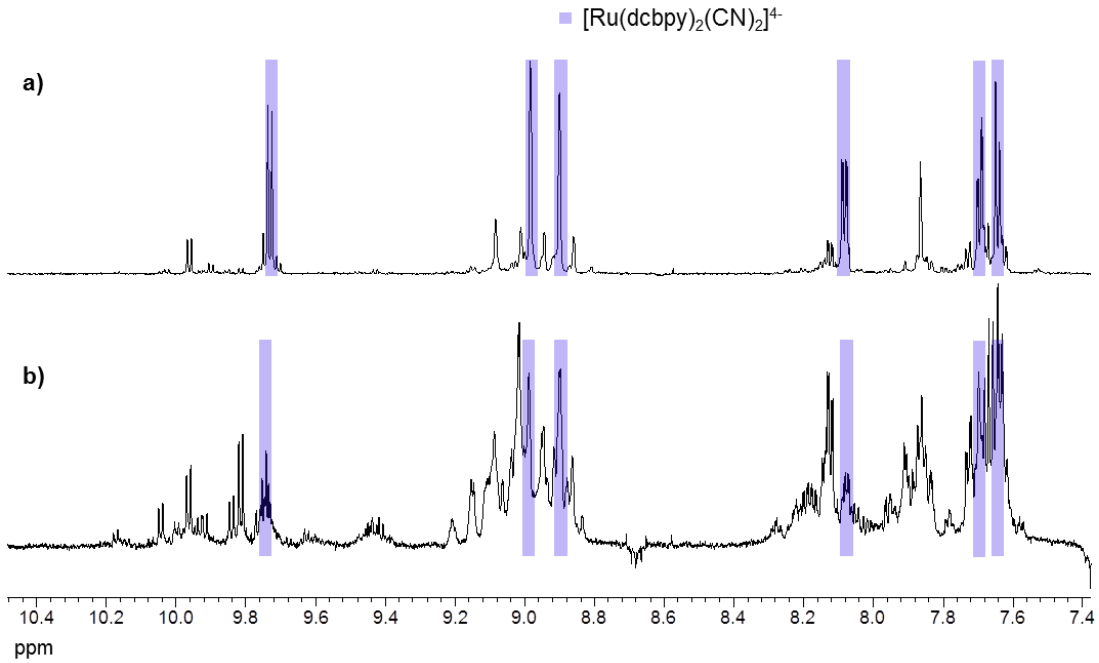

Fig. 3.6: *^{1}H NMR in MeOD of the products formed when binding $^{-}$NCSe to ruthenium at **a)** 78 ^{o}C for 30 mins; **b)** room temperature for 12 hours.*

3.2.5 Novel procedure for $Ru(H_2\text{-dcbpy})(ZZ`)$ and $K_4[Ru(H_2\text{-dcbpy})(ZZ`)]$ dyes

The syntheses of both $K_4[Ru(dcbpy)_2(NCO)_2]$ and $K_4[Ru(dcbpy)_2(NCS)_2]$, using the methods described in 3.2.3, have been repeated more than five times; producing yields consistently in the range of 70-80% after purification by sephadex column chromatography. The ^{1}H NMR, ^{13}C NMR, ESI-MS and elemental analysis results have also been of consistently high quality (3.8.4.1, 3.8.4.2), which suggests the discovery of a highly reproducible synthetic procedure. Purification by sephadex column chromatography was solely required for removal of any $[Ru(dcbpy)_3]^{4-}$ which had formed during the reaction. Therefore, if precipitation of the product from water with acid were possible, it is likely that purification of the product by sephadex column chromatography would not be required as $[Ru(H_2\text{-dcbpy})_3]^{2+}$ is soluble in

water. As well as overcoming problems associated with the use of acid sensitive ligands, this procedure could be extremely useful in the synthesis of $Ru(H_2\text{-}dcbpy)_2(ZZ`)$ dyes containing (ZZ`) ligands which are heat sensitive; as substitution of the (ZZ`) ligand(s), precipitation of the potassium salt of the product from ethanol or DMF, and precipitation of the protonated product from water can be carried out at room temperature (3.2.4). The procedure does, however, rely on the poor solubility of the potassium salt of the dye in those solvents.

3.3 $[Ru(H_2\text{-}dcbpy)_2(bbzt)]^{2+}$ synthesis

3.3.1 The breakdown of DMF

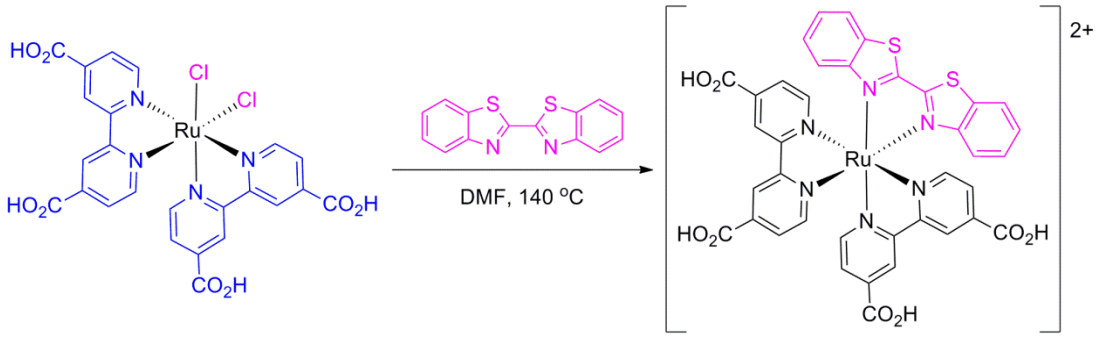

Fig. 3.7: *Attempted synthesis of* $[Ru(H_2\text{-}dcbpy)_2(bbzt)]^{2+}$

The synthesis of $[Ru(H_2\text{-}dcbpy)_2(bbzt)]^{2+}$ was initially attempted by refluxing $Ru(H_2\text{-}dcbpy)_2Cl_2$ with one molar equivalent of bbzt (Fig. 3.7) for up to 24 hours in DMF. It was clear by ^1H NMR that no reaction had occurred, so reflux was carried out in DMF for three days resulting in a crude material which was seen to contain a large number of different products by ^1H NMR analysis. ESI-$MS^{(+)}$ analysis of the crude product showed peaks at m/z = 652.71, 323.13; which are consistent with the formation of $[Ru(H_2\text{-}dcbpy)_2(Cl)(CO)]^+$ and $[Ru(H_2\text{-}dcbpy)_2(CO)_2]^{2+}$. The isotopic patterns were also consistent with the assigned molecules. With prolonged heating, DMF can breakdown into CO and $HNMe_2$ thus allowing the CO ligand to bind to

ruthenium[172]; which is most likely what occurred during this synthesis. Therefore, when using DMF as the solvent for dye synthesis, use of prolonged reaction times should be avoided to prevent the formation of CO.

3.3.2 The anti-chelate effect

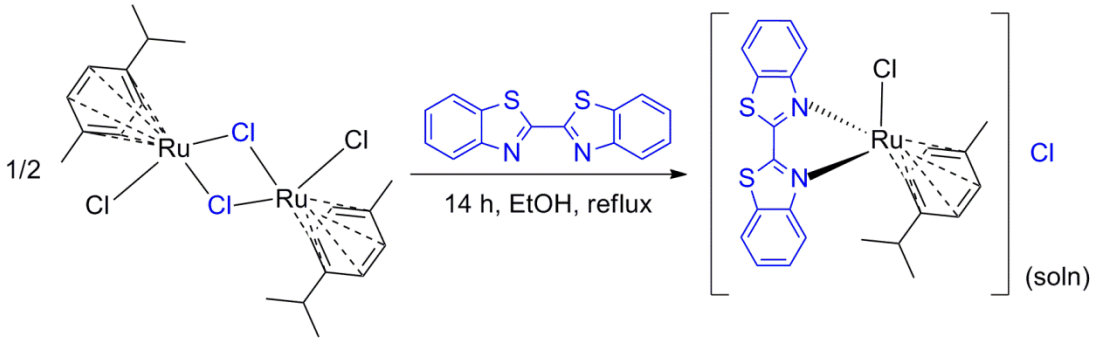

Fig. 3.8: *The attempted synthesis of [Ru(bbzt)(p-cymene)Cl]$^+$.*

Many dyes have been synthesised in order to increase the stability of ruthenium complexes by substitution of the monodentate $^-$NCS ligands with bidentate ligands[84,96,160]; and the synthesis of $[Ru(H_2\text{-dcbpy})_2(bbzt)]^{2+}$ was attempted for a similar purpose. The synthesis of this dye was attempted by dechloridation of the $Ru(decbpy)_2Cl_2$ starting material (3.1.2) and using microwave procedures (3.1.5) but no product formation was observed. Therefore, in order to investigate the binding of bbzt to ruthenium, the synthesis of $[Ru(p\text{-cymene})(bbzt)Cl]^+$ was attempted (Fig. 3.8). ^{1}H NMR and ESI-MS$^{(+)}$ analysis of the resulting crude material confirmed the presence of $Ru(bbzt)_2Cl_2$ in the product (Fig. 3.9a; peak observed at 730.84 consistent with $[NaRu(bbzt)_2Cl_2]^+$). A second product was also present which contained the bbzt ligand bound to ruthenium, but could not be identified by ^{1}H NMR or ESI-MS$^{(+/-)}$. After two days at room temperature the colour of the solution in the NMR tube changed from green to blue, and by ^{1}H NMR analysis it became clear that this second product had broken down to re-form the $[Ru(p\text{-cymene})Cl_2]_2$ dimer (Fig. 3.9b). The implication that the bbzt ligand was easily displaced from ruthenium was confirmed when the attempted substitution of the chloride ligands in $Ru(bbzt)_2Cl_2$ for H_2-dcbpy resulted in the substitution of the bbzt ligands. Therefore,

in this case the bidentate ligands were less stable when bound to ruthenium than the monodentate ligands. Weak binding of chelating ligands has been observed in lanthanide tripods and is attributed to limited intramolecular cyclisation[182]; as intermolecular interactions are more favourable than the formation of the intramolecular metal-bidentate ligand ring[183]. Testing the binding of a ligand to ruthenium, and studying the stability of the resulting complex can therefore be useful to screen novel ligands before incorporating them into ruthenium dyes.

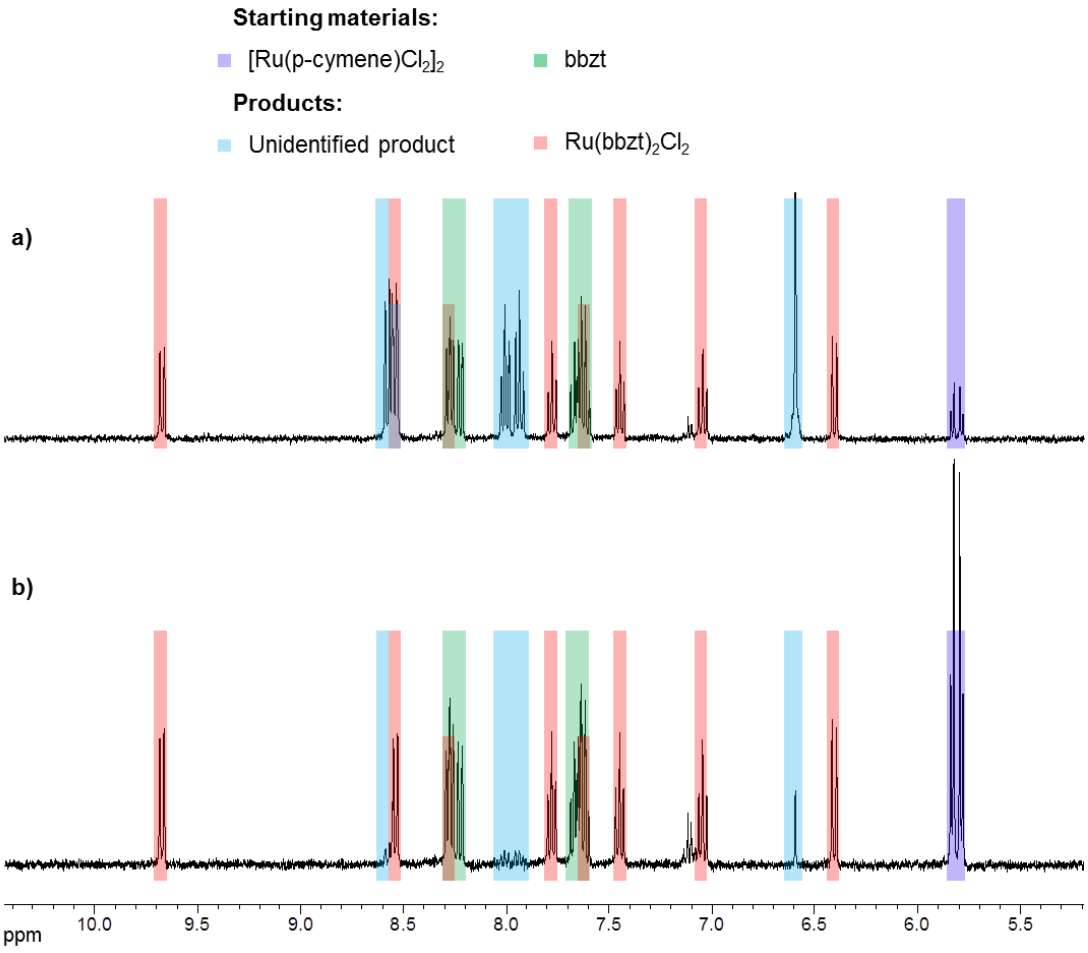

Fig. 3.9: a) *^{1}H NMR in d^{6}-DMSO of the products of the attempted synthesis of [Ru(bbzt)(p-cymene)Cl]$^{+}$* ***b)*** *Products after two days in solution at room temperature*

3.4 Ru(H_2-dcbpy)$_2$(NCS)Cl synthesis

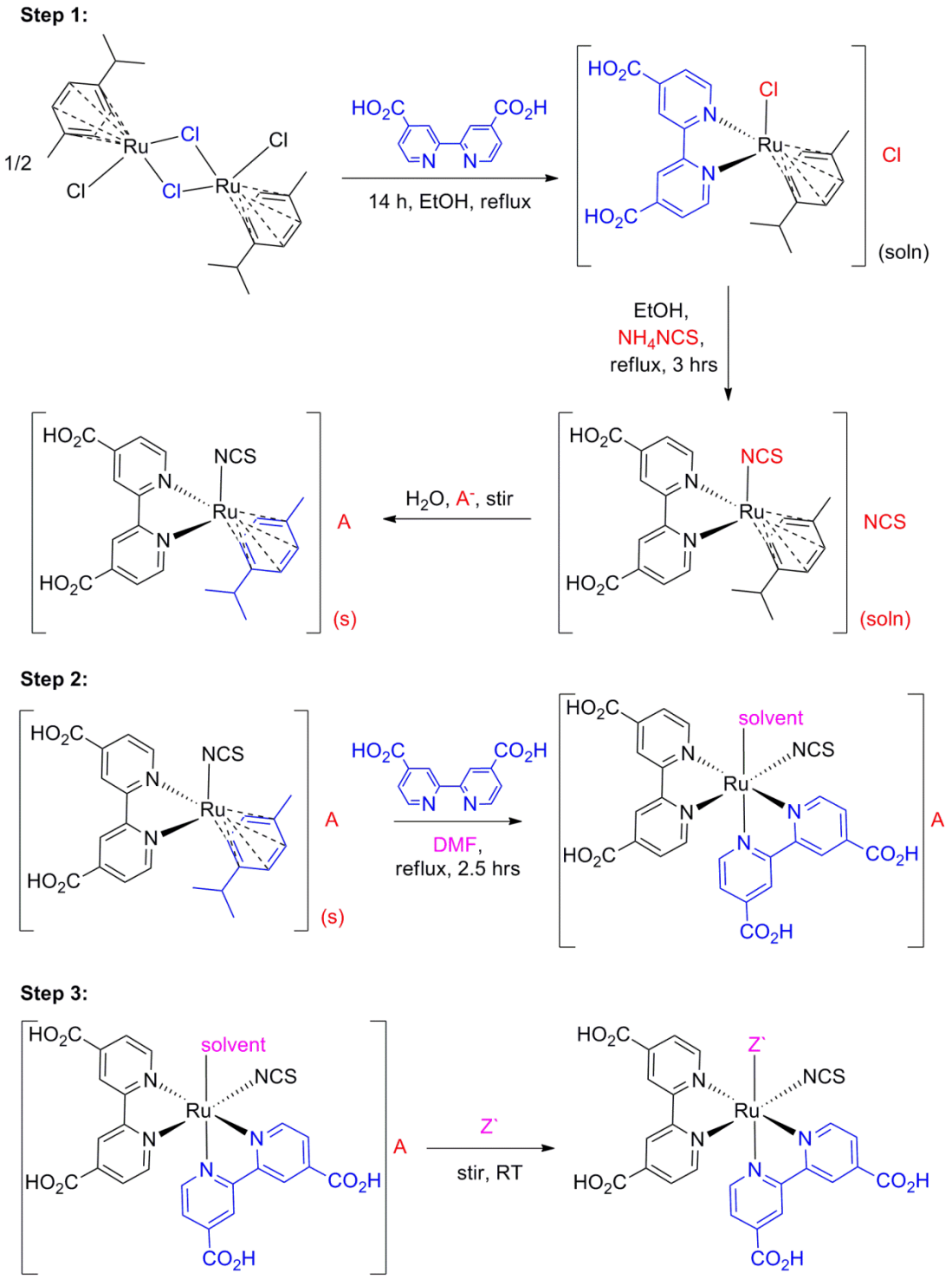

Fig. 3.10: *Proposed synthetic scheme for Ru(H_2-dcbpy)$_2$(NCS)Z` dyes where A$^-$ is a non-co-ordinating anion and Z` is a monodentate ligand*

As the $^{-}$NCS ligand has been proved important for effective dye regeneration (1.3.2.2), the synthesis of a series of Ru(H_2-dcbpy)(NCS)Z` dyes where Z` is a monodentate ligand would allow tuning of the HOMO of the ruthenium dye while maintaining efficient dye regeneration through the $^{-}$NCS ligand. The proposed synthetic procedure (Fig. 3.10) involved the isolation of [Ru(H_2-dcbpy)(p-cymene)(NCS)][A], where A is a non-coordinating counter ion. The substitution of H_2-dcbpy for p-cymene would lead to the formation of the intermediate [Ru(H_2-dcbpy)$_2$(NCS)(solvent)][A] which could again be isolated. From this intermediate it was postulated that substitution of the weakly bound solvent molecule for a monodentate ligand could be easily undertaken, allowing the systematic formation of a series of Ru(H_2-dcbpy)$_2$(NCS)Z` dyes. The synthesis of Ru(H_2-dcbpy)$_2$(NCS)Cl was initially attempted to test the synthetic procedure.

3.4.1 The acid-base chemistry of H_2-dcbpy

The formation of the [Ru(H_2-dcbpy)(p-cymene)NCS)][A] was attempted by precipitation of the [Ru(H_2-dcbpy)(p-cymene)(NCS)][NCS] salt by addition of PF_6 and BF_4 salts. However, the [Ru(H_2-dcbpy)(p-cymene)(NCS)][NCS] salt was only sparingly soluble in water, so precipitation of the desired product from water could not be achieved. The precipitation of [Ru(H_2-dcbpy)(p-cymene)(NCS)][NCS] from methanol or ethanol with PF_6 and BF_4 salts was also unsuccessful.

Use of silver nitrate to introduce the non-coordinating NO_3^- counter ion at different stages of the procedure (Fig. 3.11) was therefore attempted. This resulted in the formation of a product which was shown by ^{1}H NMR to contain bound H_2-dcbpy and p-cymene ligands. However, the product was extremely water soluble suggesting that either the zwitterion [Ru(H-dcbpy)(p-cymene) (NCS)], or [Ru(dcbpy)(p-cymene) (NCS)]$^-$ had formed (Fig. 3.11). Precipitation of [Ru(H_2-dcbpy)(p-cymene)Cl][NO_3] has been achieved by addition of 0.01M HNO_3 to [Ru(H_2-dcbpy)(p-cymene)Cl]$^+$ [169], but addition of acid (0.01 to 1.0 M HNO_3) to an aqueous solution of [Ru (H_2-dcbpy)(p-cymene)(NCS)]$^+$ did not result in the formation of a solid.

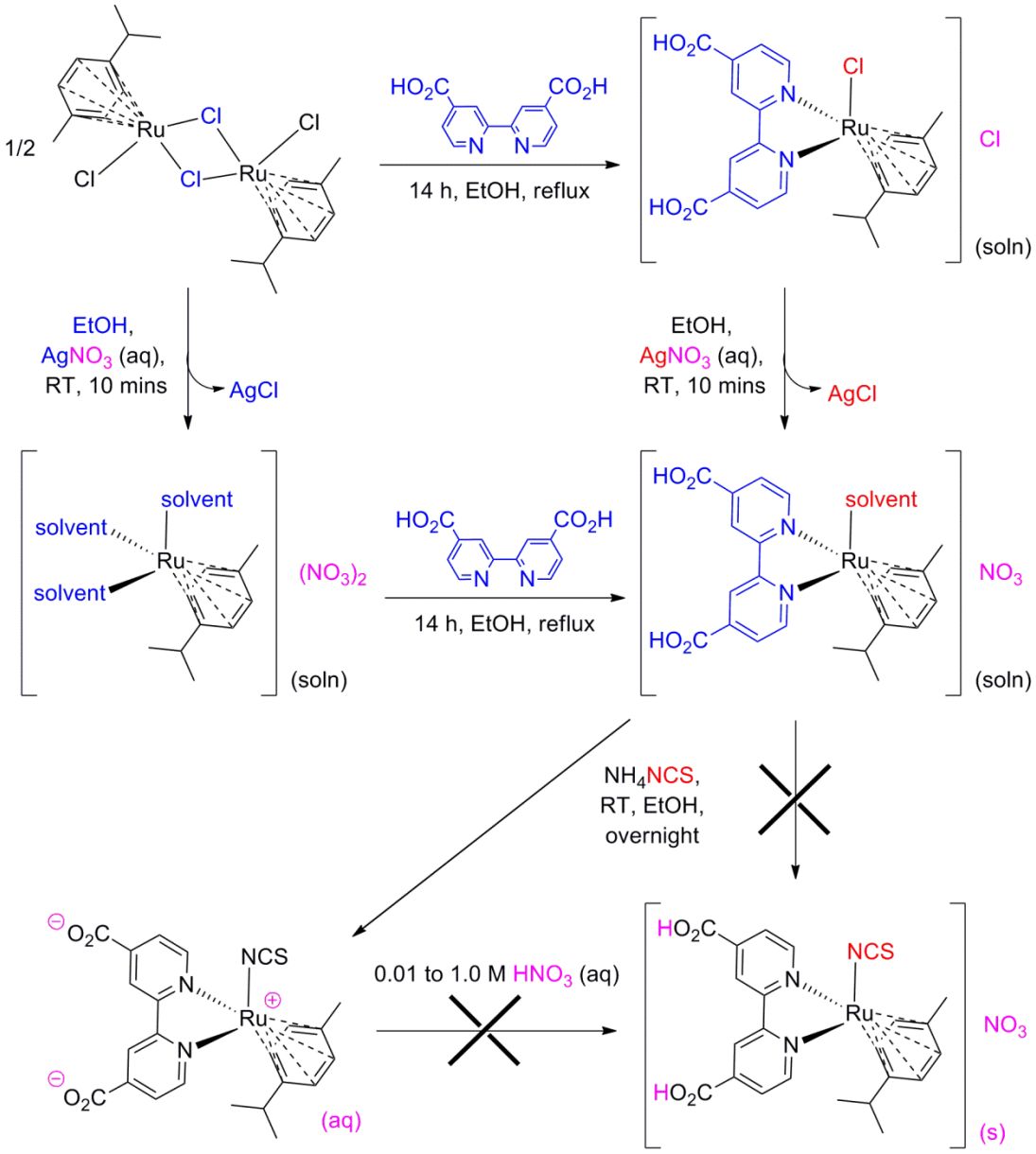

Fig. 3.11: *Formation of a highly water soluble complex during the attempted synthesis of [Ru(H_2-dcbpy)(p-cymene)(NCS)][NO_3].*

The effects of the acid-base chemistry of the H_2-dcbpy ligand have been previously discussed (3.2.1). It appears that in this case the addition of counter ions to the reaction mixture further complicates the acid-base behaviour of the H_2-dcbpy ligand. Hydrolysis of BF_4 and PF_6 counter ions can occur in acidic conditions[184], which could explain the difficulties with the attempted synthesis of [Ru(H_2-dcbpy)(p-cymene)(NCS)][BF_4] and [Ru(H_2-dcbpy)(p-cymene)(NCS)][PF_6]. The difference in

the behaviour of $[Ru(dcbpy)(p\text{-}cymene)Cl]^-$ and $[Ru(dcbpy)(p\text{-}cymene)(NCS)]^-$ with addition of HNO_3 is likely to be due to the change in the co-ordination environment, which can have a large effect on the pK_a of the H_2-dcbpy ligand (Table 3.3). Although the use of other non-coordinating counter ions or reaction mixtures with a lower pH could have allowed the synthesis of $[Ru(H_2\text{-}dcbpy)(p\text{-}cymene)(NCS)][A]$, it was decided to simplify the synthesis by protecting the H_2-dcbpy ligand with an ester group. In doing so, the synthesis of the $[Ru(decbpy)(p\text{-}cymene)(NCS)][PF_6]$ salt was easily achieved (3.8.2.1) by precipitation of $[Ru(decbpy)(p\text{-}cymene)(NCS)]^+$ from methanol.

Compound	pK_{a1}	pK_{a2}	pK_{a3}	pK_{a4}
H_2-dcbpy[185]	< 2.0[#]	3.70 (4.20[176])	-	-
$[Ru(H_2\text{-}dcbpy)(bpy)_2]^{2+}$ [176]	1.75	2.85	-	-
$Ru(H_2\text{-}dcbpy)_2(NCS)_2$ [127]	1.33	2.24	3.45	4.20
$Ru(H_2\text{-}dcbpy)_2(NCS)_2$ [*34]	1.50		3.0	
$Ru(H_2\text{-}dcbpy)_2(4\text{-}Clpcyd)_2$ [*186]	5.4		6.4	
$[Ru(H_2\text{-}dcbpy)_2(bpy)]^{2+}$ [*176]	1.80		2.50	

Table 3.3: *The pK_as of Ru-H_2-dcbpy complexes. pK_{a1} = [complex] to [complex]$^-$; pK_{a2} = [complex]$^-$ to [complex]$^{2-}$; pK_{a3} = [complex]$^{2-}$ to [complex]$^{3-}$; pK_{a4} = [complex]$^{3-}$ to [complex]$^{4-}$. $^*pK_{a1}$ and pK_{a2} = [complex] to [complex]$^{2-}$; pK_{a3} and pK_{a4} = [complex]$^{2-}$ to complex]$^{4-}$. $^\#$The pK_a could not be accurately determined due to precipitation of the neutral H_2-dcbpy ligand[176,185]. 4-Clpcyd is 4-chlorophenylcyanamide.*

3.4.2 Lability of the ruthenium centre at high temperatures

To maintain the symmetry of the dye with respect to the bpy ligands, the reaction to produce $Ru(H_2\text{-}dcbpy)_2(NCS)Cl$ was continued by substitution of the p-cymene ligand with a second decbpy ligand (Fig. 3.12). It was hoped that the synthesis of $[Ru(decbpy)_2(NCS)(solvent)]^+$ (Route 1, Fig. 3.12) as a starting material would allow easy substitution of any monodentate ligand to form a series of $Ru(decbpy)_2(NCS)Z`$ compounds. The ester group could then be hydrolysed, and precipitated from water with acid addition to form a series of dyes for DSSCs. Thermal methods were found to produce incomprehensible products by ^1H NMR; thus microwave synthesis (3.1.5)

was used to increase the selectivity of the reaction by reducing reaction times and preventing substitution of the ⁻NCS ligand.

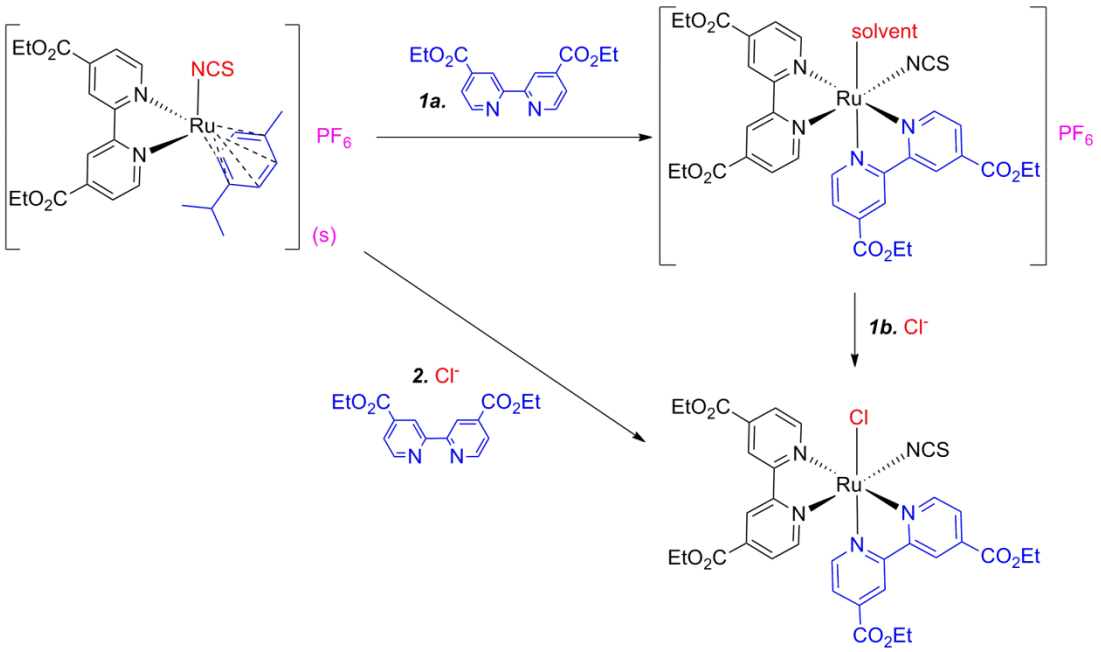

Fig. 3.12: *Routes to the synthesis of Ru(decbpy)$_2$(NCS)Cl*

Substitution of the p-cymene ligand with a second decbpy ligand resulted in a ^{1}H NMR which could not be assigned to a product (Fig. 3.13a). However, by ESI-MS$^{(+)}$ only one peak was observed at 760.16 m/z, which is consistent with [Ru(decbpy)$_2$(NCS)]$^+$. Therefore, a weakly co-ordinating molecule, for example a solvent molecule, could have been bound to the sixth co-ordination site. The high lability of such a molecule could explain the large number of peaks observed by ^{1}H NMR. Synthesis of Ru(decbpy)$_2$(NCS)Cl from this product was therefore attempted by stirring the product in methanol with excess [NMe$_4$][Cl] at room temperature. ^{1}H NMR analysis of the product showed that a reaction occurred (Fig. 3.12b) but a number of different products formed. Analysis by ESI-MS$^{(+/-)}$ showed no peaks which could be assigned to Ru(decbpy)$_2$(NCS)Cl. Similar results were achieved by heating the product with excess [NMe$_4$][Cl], and purification of the product by sephadex column chromatography was not achieved.

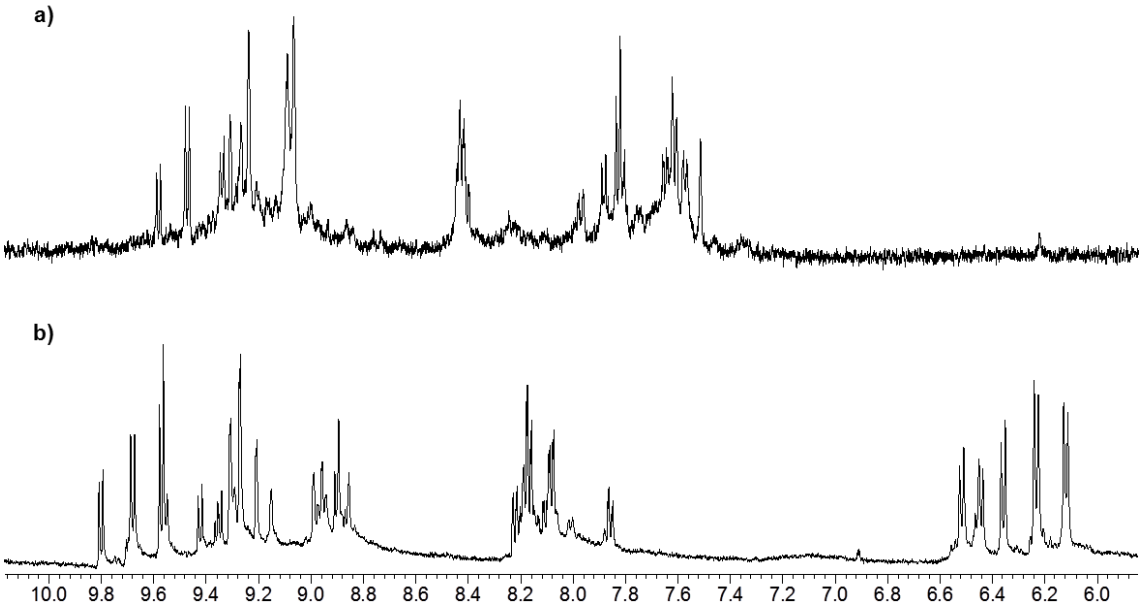

Fig. 3.13: *^{1}H NMR in d^{6}-DMSO of* ***a)*** *product after reaction of [Ru(decbpy)(p-cymene)(NCS)]PF$_6$] with decbpy* ***b)*** *product formed by reacting the product from a) with [NMe$_4$][Cl] in methanol.*

The substitution of p-cymene by decbpy was therefore performed with a stoichiometric quantity of *in situ* [NMe$_4$][Cl] (Route 2, Fig. 3.12), yielding a product which showed peaks consistent with a mixture of Ru(decbpy)$_2$(NCS)$_2$, Ru(decbpy)$_2$Cl$_2$ and a third product (Fig. 3.14a). The number of peaks, splitting patterns and integrals for the third product were entirely consistent with the expected ^{1}H NMR for Ru(decbpy)(NCS)Cl. The formation of this mixture of products was confirmed by the presence of peaks consistent with Na[Ru(decbpy)$_2$(Cl)$_2$]$^{+}$ (795.02), Na[Ru(decbpy)$_2$(NCS)$_2$]$^{+}$ (841.01) and Na[Ru(decbpy)$_2$(Cl)(NCS)]$^{+}$ (817.97) by ESI-MS$^{(+)}$ analysis. In each case, the isotopic patterning due to the ruthenium and chlorine atoms was also consistent with the assigned complex. Therefore, the synthesis of Ru(decbpy)$_2$(NCS)(Cl) was achieved, but the lability of the ruthenium centre at high temperatures caused unwanted substitution of the $^{-}$NCS ligand to occur.

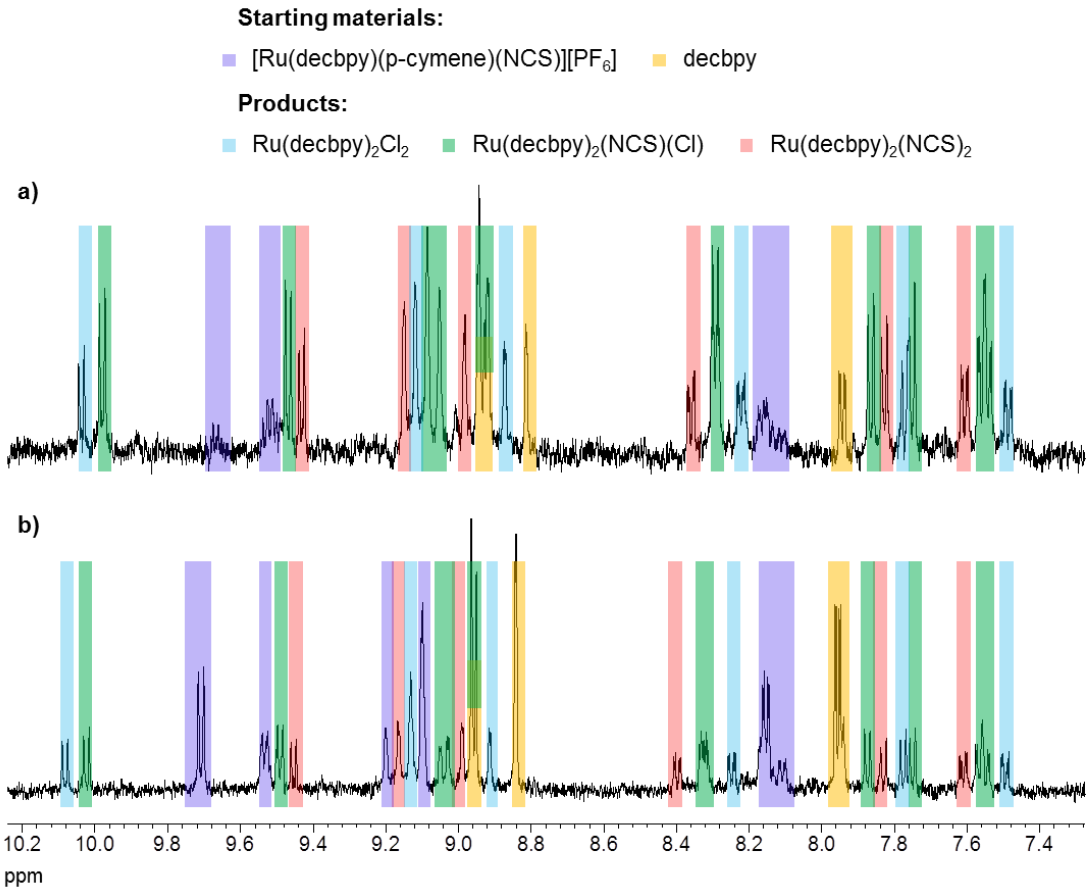

Fig. 3.14: *^{1}H NMR spectra in d_6-DMSO of the products of the microwave reaction of [Ru(decbpy)(p-cymene)(NCS)][PF_6] with decbpy and [NMe_4][Cl] for* ***a)*** *10 mins;* ***b)*** *2 mins.*

In an attempt to increase the selectivity of the synthesis of $Ru(decbpy)_2(NCS)(Cl)$, the reaction time was reduced. However, even performing the reaction for just two minutes resulted in the formation of a similar ratio of $Ru(decbpy)_2Cl_2$, $Ru(decbpy)_2(NCS)_2$ and $Ru(decbpy)_2(NCS)Cl$ (Fig. 3.14b); and a significant proportion of starting material remained. Therefore, the lability of the ruthenium centre at 140 ^oC caused almost immediate substitution of a proportion of the bound ^-NCS ligand. Because the ruthenium centre is kinetically inert, use of lower temperatures to prevent the substitution of ^-NCS would also prevent the substitution of p-cymene by decbpy. Therefore, that the ruthenium centre is kinetically inert, but highly labile once the kinetic barrier is overcome, prevented the selective synthesis of $Ru(H_2\text{-}dcbpy)_2(NCS)Cl$ and therefore the possible series of $Ru(H_2\text{-}$

dcbpy)$_2$(NCS)Z` dyes. That a similar mixture of products was obtained by refluxing one molar equivalent of ¯NCS with Ru(H$_2$-dcbpy)$_2$Cl$_2$ in DMF shows the poor selectivity of this procedure. The selective synthesis of Ru(H$_2$-dcbpy)$_2$(NCS)Z` dyes is therefore only likely to be achieved using a bulky Z` ligand, as steric hindrance to the formation of Ru(H$_2$-dcbpy)$_2$(Z`)$_2$ would provide selectivity for the reaction.

3.5 Synthesis of Ru(3,3`-(CO$_2$H)$_2$-bpy)(dnbpy)(NCS)$_2$

3.5.1 Decarboxylation; the effect of the position of the CO$_2$H group

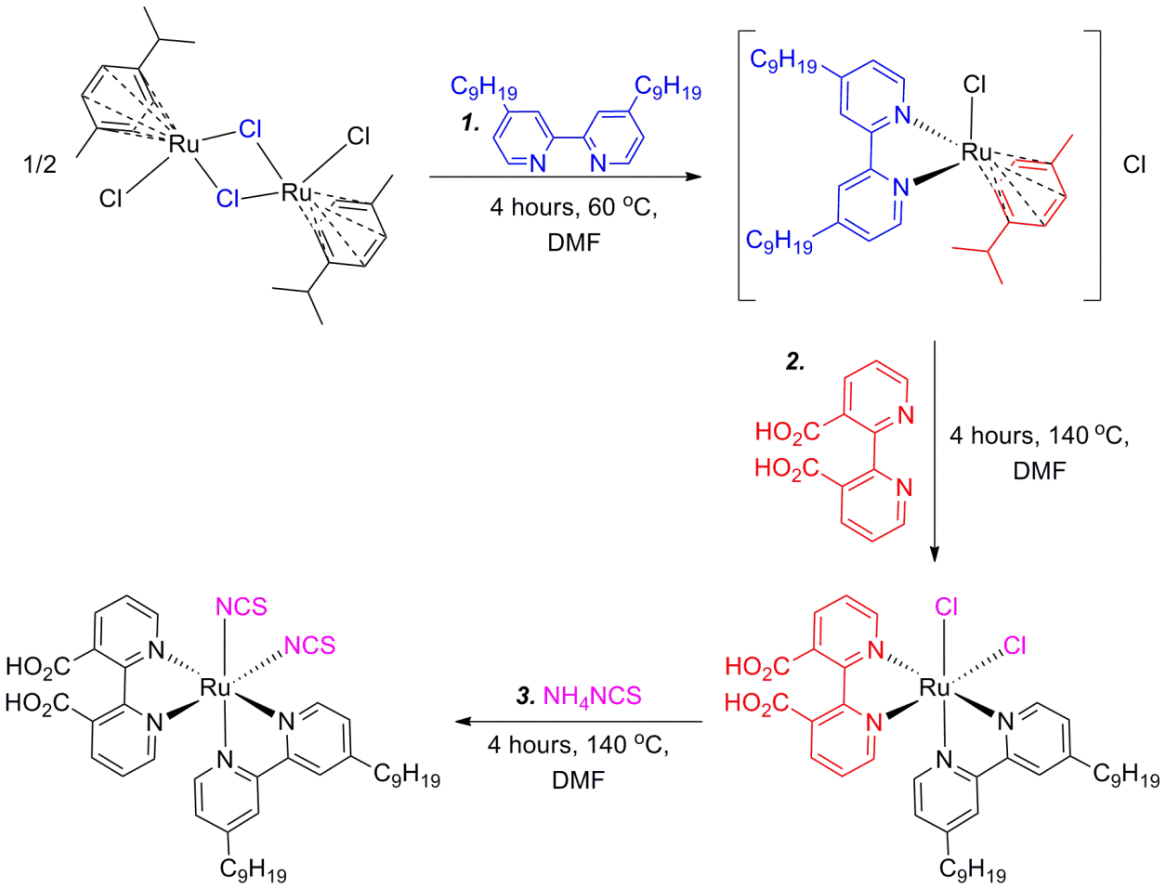

Fig. 3.15: *One-pot reaction scheme for the attempted synthesis of [Ru(3,3`-(CO$_2$H)$_2$-bpy)(dnbpy)(NCS)$_2$.*

The synthesis of the analogue of the commercially used Z907 dye (1.3.2.2), was attempted to explore the effect of the position of the carboxylic acid groups on the binding of the dye to TiO_2. The synthetic procedure for the Z907 dye[23] was initially attempted, but adding 3,3`-$(CO_2H)_2$-bpy (Fig. 3.15) instead of 4,4`-$(CO_2H)_2$-bpy. By comparison of the ^{1}H NMR of the crude product with the ^{1}H NMR of simultaneously synthesised Z907 (Fig. 3.16), it was clear that side reactions or breakdown of the product had occurred. ESI-MS$^{(-)}$ analysis showed a peak at 824.8 which is consistent with $[Ru((CO_2)\text{-bpy})(dnbpy)(NCS)_2]^-$; suggesting that decarboxylation of the 3,3`-$(CO_2H)_2$-bpy ligand had occurred.

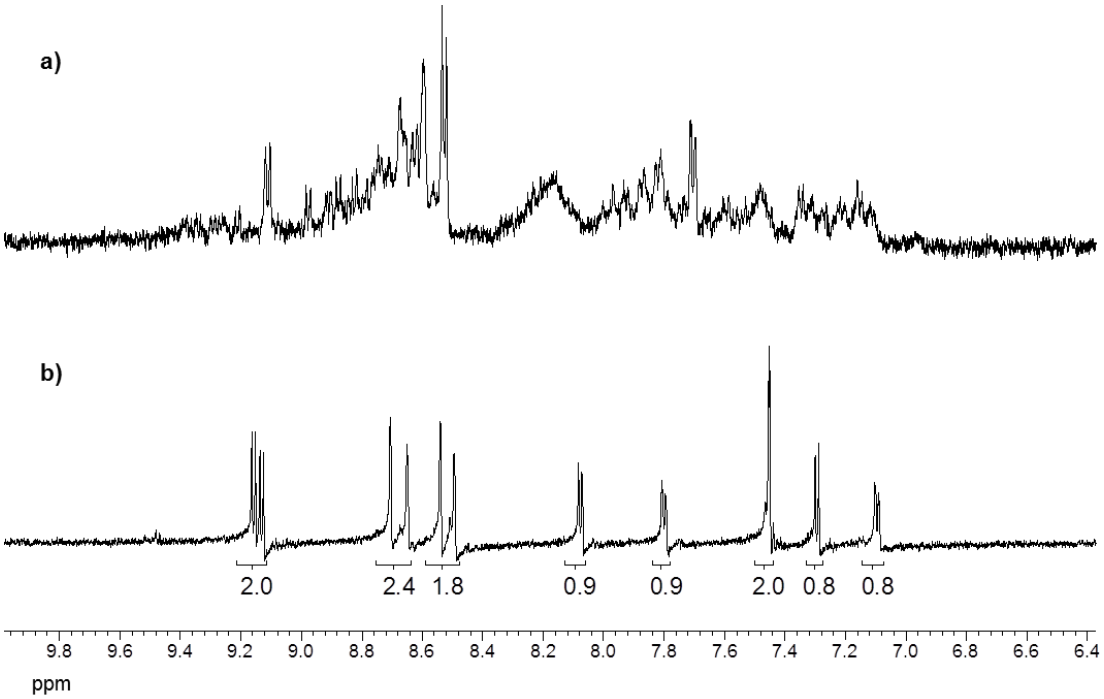

Fig. 3.16: *^{1}H NMR in d^6-DMSO of the crude products formed after the attempted synthesis of* ***a)*** *Ru(3,3`-$(CO_2H)_2$-dcbpy)(dnbpy)$(NCS)_2$;* ***b)*** *Ru(4,4`-$(CO_2H)_2$-dcbpy)(dnbpy)$(NCS)_2$*

Decarboxylation of ruthenium-3,3`-$(CO_2H)$-bpy compounds has been previously observed due to excessive heating at high temperatures (reflux in DMF and DMSO)[165]. On binding to ruthenium, a 30$^o$ twist in the plane of the ligand is observed due to steric hindrance of the bulky substituents at the 3 and 3` positions[187].

This steric clash probably drives the decarboxylation of the ligand. In the 4,4`-$(CO_2H)_2$-bpy ligand such steric effects need not be considered, thus decarboxylation only occurs at high temperatures (220-240 ^oC)[165]. The position of the CO_2H group on the bpy ligand therefore has a significant effect on the stability of the ligand when it binds to ruthenium.

3.5.2 Alternative procedure for the synthesis of asymmetric dyes

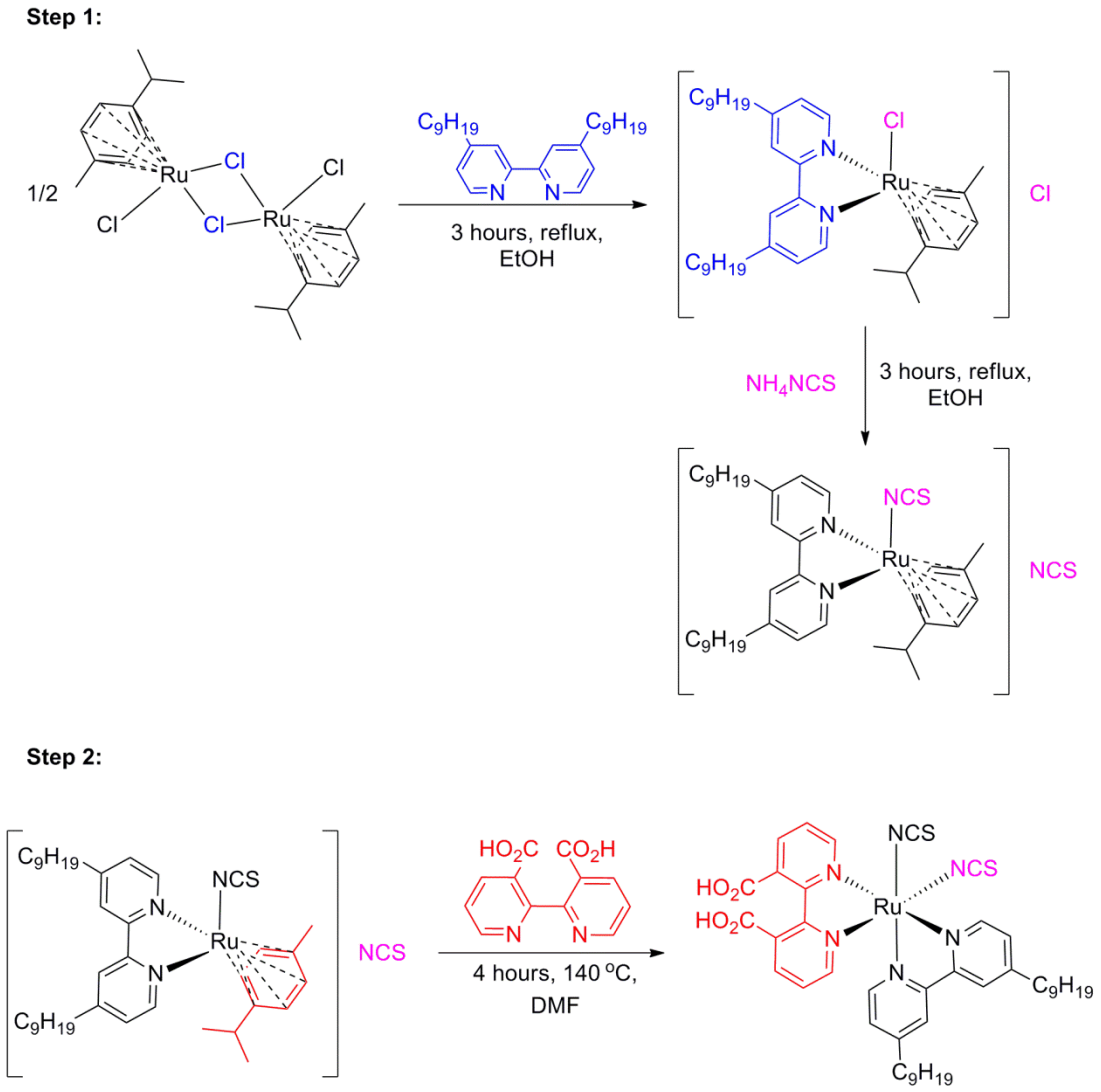

Fig. 3.17: *Novel two step reaction scheme for the attempted synthesis of Ru(3,3`-$(CO_2H)_2$-bpy)(dnbpy)$(NCS)_2$.*

In order to prevent the decarboxylation of 3,3`-$(CO_2H)_2$-bpy, a novel reaction scheme was developed (Fig. 3.17) which involved the synthesis of the [Ru(dnbpy)(p-cymene)(NCS][NCS] intermediate, and subsequent reaction of this compound with 3,3`-$(CO_2H)_2$-bpy. It was hoped that this method would reduce the time that the 3,3`-$(CO_2H)_2$-bpy ligand was bound to ruthenium while being heated at high temperatures, thus preventing decarboxylation of the ligand from occurring. Synthesis of [Ru(dnbpy)(p-cymene)(NCS][NCS] was achieved to a high degree of purity by ^{1}H and ^{13}C NMR and ESI-MS (3.8.2.2). A mixture of N-bound and S-bound isomers of the $^{-}$NCS ligand were observed by ^{1}H NMR, but the second step of the reaction, which involves the use of higher temperatures, would favour the formation of the thermodynamically favoured N-bound isomer of the dye. Elemental analysis of this product could not be achieved due to the oily nature of the solid formed, but the organic phase of the reaction was thoroughly washed with water to remove any salts, therefore the synthesis of a pure intermediate was assumed.

3.5.3 Using UV/vis spectroscopy to monitor and optimise the reaction

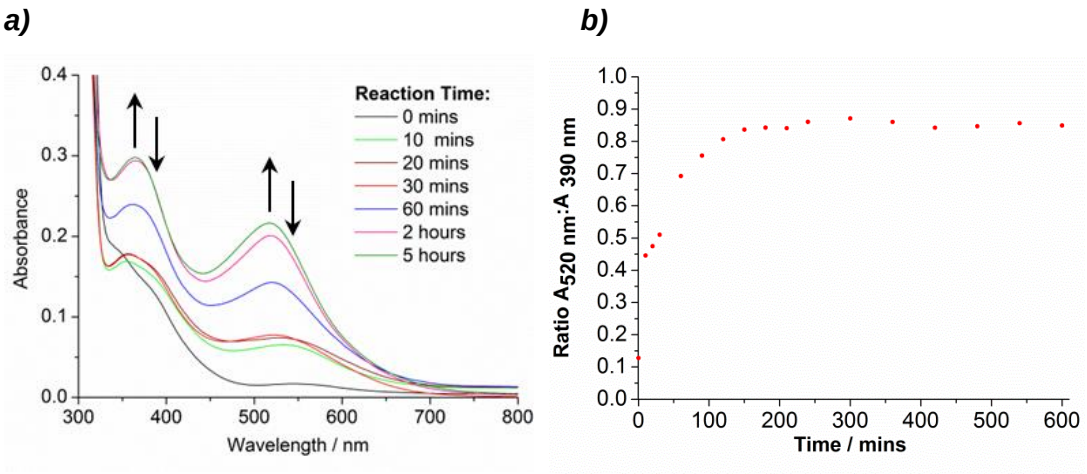

Fig. 3.18: *UV/vis monitoring of the synthesis of Ru(3,3`-$(CO_2H)_2$-bpy)(dnbpy)$(NCS)_2$ at 140 ^{o}C.*

The reaction was initially performed with UV/vis monitoring (3.8.3.1) at 140 ^{o}C. The progress of a reaction monitored by UV/vis can be quantified by taking the ratio of

the absorbance at the peak wavelength of the product and the absorbance of the peak wavelength of the starting material[188-191]. During this reaction, the shoulder at 390 nm and the peak at 550 nm in the starting material disappeared, and peaks at 360 nm and 520 nm grew as the reaction progressed (Fig. 3.18a). The ratio of the absorbance at 520 nm to 390 nm was therefore used to monitor the reaction. The point at which there was no considerable change was reached after just 2 hours (Fig. 3.18b), but at this point of the reaction the ^{1}H NMR still showed that considerable product breakdown had occurred.

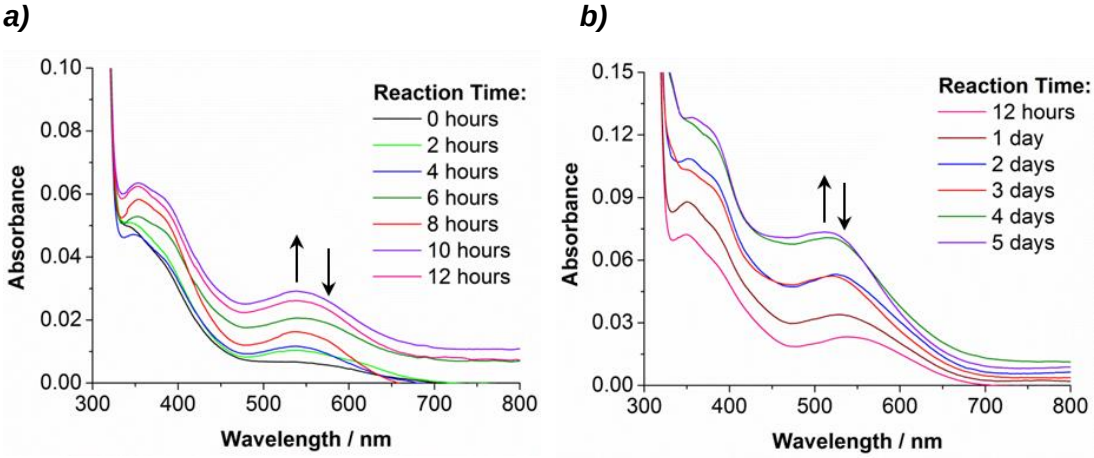

Fig. 3.19: *Monitoring the synthesis of Ru(3,3`-$(CO_2H)_2$-bpy)(dnbpy)$(NCS)_2$ at 80 ^{o}C.*

Ru-(3,3`-$(CO_2H)_2$-bpy) complexes have been synthesised without decarboxylation of the ligand at 80 $^{o}$C[165,187]; thus the synthesis of Ru(3,3`-$(CO_2H)_2$-bpy)(p-cymene)$(NCS)_2$ was attempted at 80 ^{o}C with UV/vis monitoring. Close analysis of the UV/vis spectra showed that up to a reaction time of 12 hours a peak at 540 nm was growing (Fig. 3.19a). However, as the reaction continued, the position of this peak shifted towards the blue region of the electromagnetic spectrum; with a peak wavelength of 510 nm after 5 days. That this change was indicative of product breakdown was confirmed by ^{1}H NMR of the reaction mixture at 12 hours and at 3 days. However, even after 3 days considerable starting material remained, showing that product breakdown occurred before the reaction reached completion. Thus, the high temperature or long reaction time required to remove the p-cymene ligand

prevented the synthesis of this dye. Removal of the p-cymene ligand in a photochemical reactor[192] before introduction of the 3,3`-$(CO_2H)_2$-bpy ligand would therefore be required for the synthesis of this dye to be achieved.

3.6 Synthesis of Ru(H_2-dcbpy)(N,N`-Y_2-bpy)$(NCS)_2$ dyes where N = 4, 5; Y = F, Cl, Br

3.6.1 The order of ligand addition

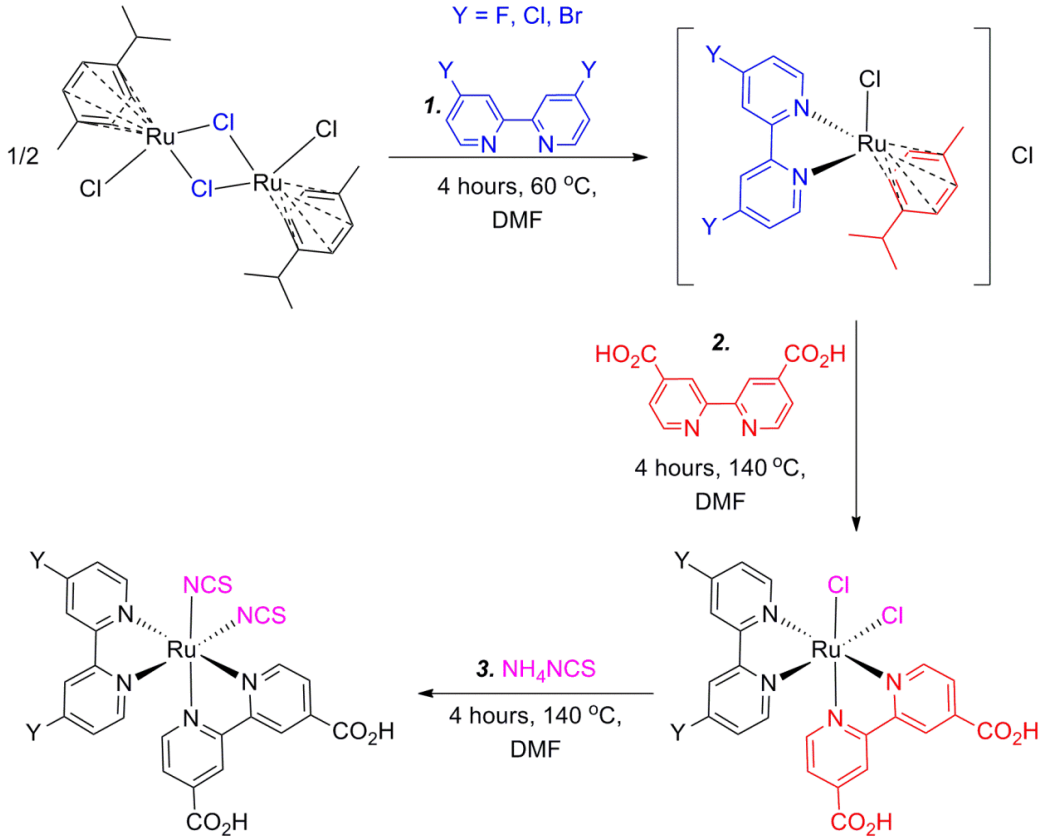

Fig. 3.20: *Synthesis of Ru(H_2-dcbpy)(Y_2-bpy)$(NCS)_2$ dyes*

The synthesis of Ru(H_2-dcbpy)(4,4`-Y_2-bpy)$(NCS)_2$ where Y = Cl, Br, was initially attempted using the standard procedure for the synthesis of asymmetric dyes (Fig. 3.20). ^{1}H NMR analysis of the products formed suggested that a mixture of the

desired product, $Ru(H_2\text{-dcbpy})_2(NCS)_2$, and a third product had formed (Fig. 3.21). Analysis of each reaction mixture by ESI-$MS^{(-)}$ showed a peak at 704.8 and 704.9, corresponding to $[Ru(H_2\text{-dcbpy})(H\text{-dcbpy})(NCS)_2]^-$. Peaks at 774.8 and 684.9 were assigned to the $[Ru(H\text{-dcbpy})(Y_2\text{-bpy})(NCS)_2]^-$ ion where Y = Br and Cl respectively. The isotopic patterns of these peaks were consistent with the presence of bromine and chlorine atoms. ESI-$MS^{(+)}$ showed a peak at 692.5 with isotopic patterning consistent with the presence of four Cl^- atoms; implying the formation of $Na[Ru(4,4`\text{-}Cl_2\text{-bpy})_2(NCS)_2]^+$. A similar peak was not observed for $Na[Ru(4,4`\text{-}Br_2\text{-bpy})_2(NCS)_2]^+$, possibly due to difficulties solubilising the product in methanol. However, it is likely that a mixture of $Ru(H_2\text{-dcbpy})_2(NCS)_2$, $Ru(4,4`\text{-}Y_2\text{-bpy})_2(NCS)_2$ and $Ru(H_2\text{-dcbpy})(4,4`\text{-}Y_2\text{-bpy})(NCS)_2$ formed during these reactions.

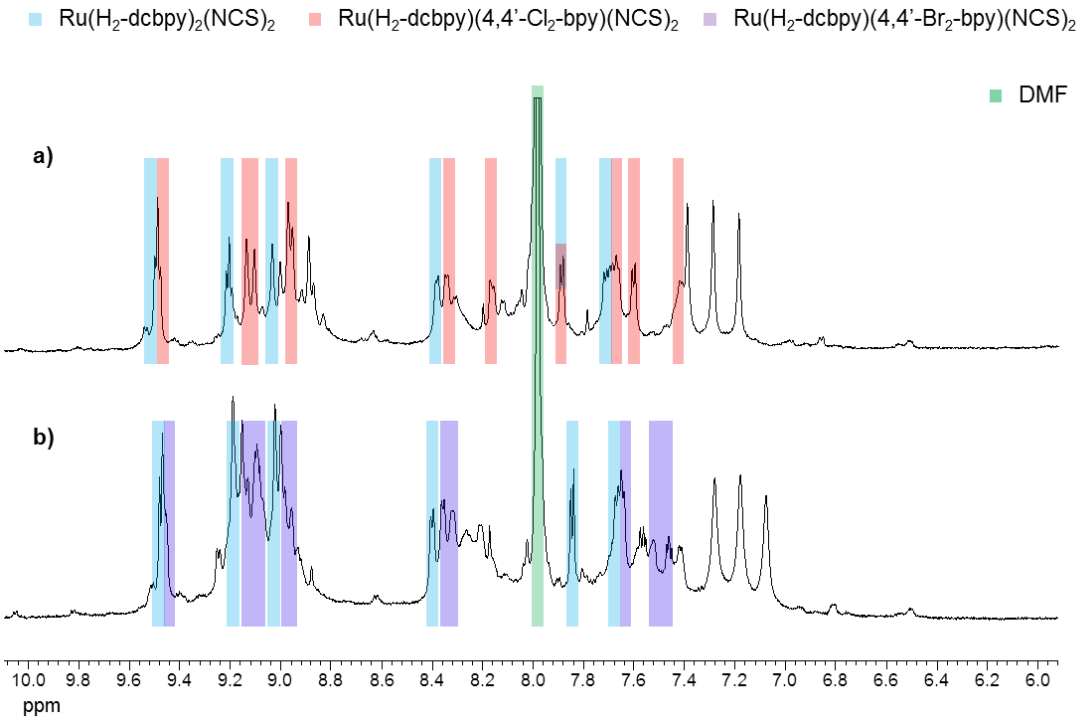

Fig. 3.21: *^1H NMR in d^6-DMSO of the products formed after the attempted one pot synthesis of* ***a)*** *Ru (H_2-dcbpy)(4,4`-$Cl_2$-bpy)$(NCS)_2$* ***b)*** *Ru($H_2$-dcbpy)(4,4`-Br_2-bpy)$(NCS)_2$*

The reaction was therefore repeated, allowing more time for the first step of the reaction to ensure complete substitution of the 4,4`-Y_2-bpy ligand. ^1H NMR analysis

of each of the reaction mixtures just before addition of the H_2-dcbpy ligand showed no free ligand or $[Ru(p\text{-cymene})Cl_2]_2$, and the peaks observed were entirely consistent with the formation of $[Ru(4,4`\text{-}Y_2\text{-bpy})(p\text{-cymene})Cl]^+$. The reaction was therefore continued, yet the same mixture of products was observed by ^1H NMR and ESI-MS. This shows that ligand scrambling must occur during the second step of the reaction. The formation of $Ru(H_2\text{-dcbpy})_2(NCS)_2$ was also observed when the reaction was attempted using $4,4`\text{-}Y_2$-bpy ligands where Y = F, CF_3, although the other products formed could not be characterised. Therefore, the nature of the substituent on the bpy ligand can have a significant impact on the reaction which takes place.

Substituent, Y	Field and inductive parameter (σ-effect)	Resonance parameter (π-effect)
$CH_2CH_2CH_3$	0.01	-0.14
CH_3	0.01	-0.18
H	0.03	0.00
COOH	0.34	0.11
CF_3	0.38	0.16
Br	0.45	-0.22
Cl	0.42	-0.19
F	0.45	-0.39

Table 3.4: *The parameters for the calculation of Hammett parameters for a number of different substituent groups. Field and inductive effects were calculated by comparison of the ionisation energies of 4-Y, 1-(CO_2H) bicyclooctanes. The resonance parameters were calculated by determining the acidities of para substituted benzoic acids, and taking away the field and inductive effects*[193]*.*

Bpy ligands are σ-donor, π-acceptor ligands. Considering the σ- and π- effects of the substituent groups on the bpy ligand (Table 3.4), it is clear that where Y is an alkyl group, Y is less electron withdrawing than the CO_2H group. In this case, the Y_2-bpy ligand will be a stronger σ-donor ligand than the CO_2H ligand, and will bind more strongly to ruthenium. To date, novel $Ru(H_2\text{-dcbpy})(Y_2\text{-bpy})(NCS)_2$ dyes have incorporated a Y group which is a long alkyl chain or is bound to the ruthenium by an alkyl chain[23,37,38]. Therefore, in such dyes, the stronger metal – ligand bond is formed first in the reaction, and this bond is not broken during the second and third

steps of the reaction; thus a pure product is formed. Where Y = CF_3, F, Cl, Br, the Y substituent is a stronger electron withdrawing group than CO_2H (Table 3.4). Therefore, the H_2-dcbpy ligand will be a stronger σ-donor than the Y_2-bpy ligand. Where Y = F, Cl, Br, π-donation from Y will also reduce the strength of π-acceptance by the Y_2-bpy ligand. Thus, H_2-dcbpy will bind more strongly to the ruthenium centre than the Y_2-bpy ligand, suggesting that ligand scrambling during the second stage of the reaction must occur when the weaker ruthenium-bpy bonds are formed first. Consequently, the correct order of ligand addition is vital in the synthesis of asymmetric ruthenium dyes.

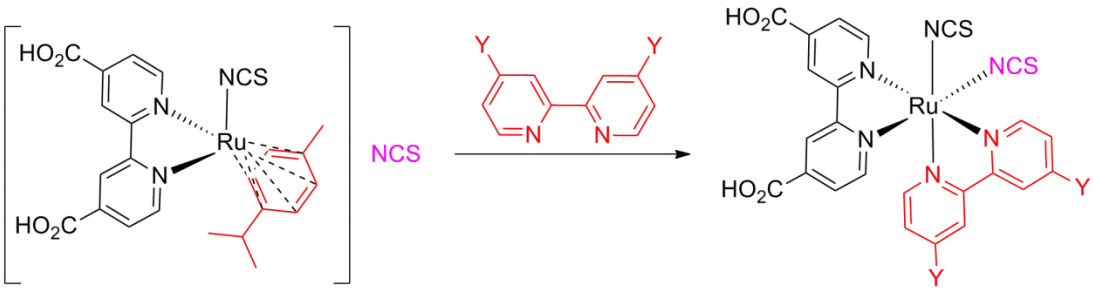

Fig. 3.22: *Synthesis of Ru(H_2-dcbpy)(Y_2-bpy)$(NCS)_2$ dyes*

The synthesis of the series of dyes E was therefore attempted by binding the H_2-dcbpy ligand to ruthenium before the Y_2-bpy ligand. To avoid independent optimisation of each of the three steps in the reaction, a synthetic procedure similar to that used in the attempted synthesis of Ru(3,3`-$(CO_2H)_2$-bpy)(dnbpy)$(NCS)_2$ (3.3.1.2) was developed; whereby a one-step synthesis of all of the dyes in series E from the intermediate [Ru(H_2-dcbpy)(p-cymene)(NCS)][NCS] could be performed (Fig. 3.22).

3.6.2 [Ru(H_2-dcbpy)(p-cymene)(NCS)][NCS] synthesis: Over-substitution of H_2-dcbpy.

The synthesis of the [Ru(H_2-dcbpy)(p-cymene)(NCS)][NCS] starting material was attempted in refluxing ethanol (Path 1, Fig. 3.23). However, this resulted in side

reactions causing both H_2-dcbpy and $[Ru(H_2\text{-dcbpy})_3]^{2+}$ to be present as impurities in the ^{1}H NMR spectrum (Fig. 3.24a, 3.8.2.3). Purification of this product by sephadex column chromatography in methanol was successful, but the resulting solid was extremely water soluble; again suggesting the formation of the zwitterion [Ru(H-dcbpy)(p-cymene)(NCS)], or $[Ru(dcbpy)(p\text{-cymene})(NCS)]^-$ (3.4.1).

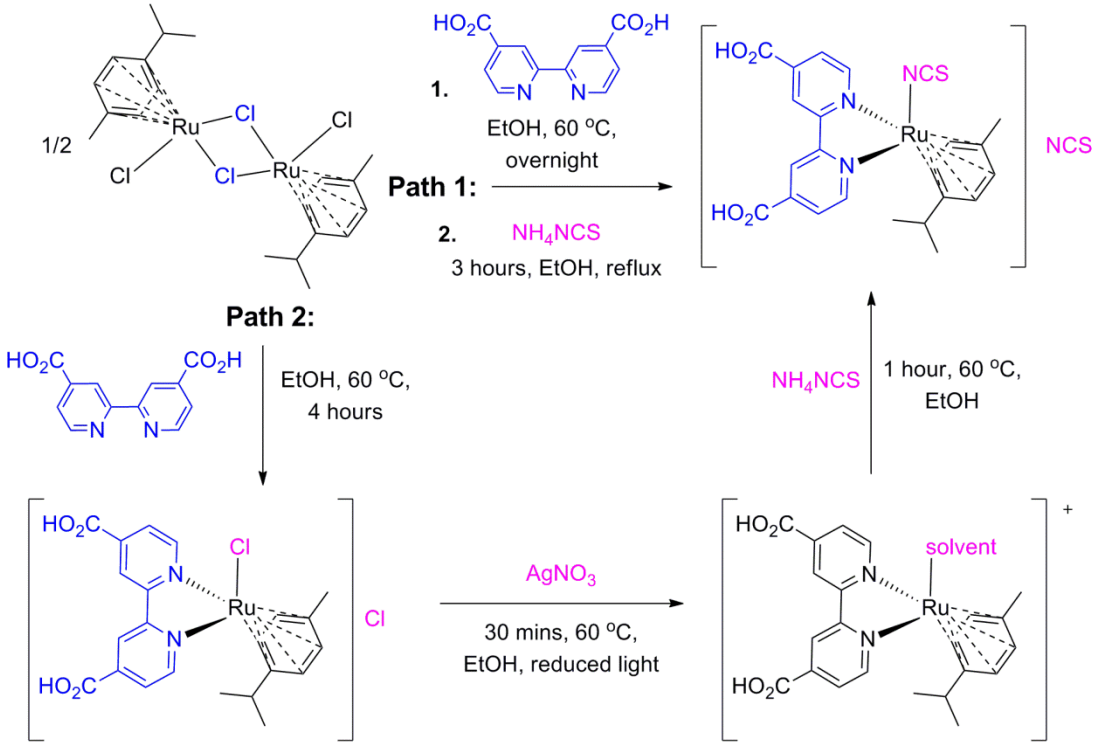

Fig. 3.23: *Initial attempts to synthesise [Ru(H_2-dcbpy)(p-cymene)(NCS)][NCS]*

Using a temperature of 60 °C prevented the substitution of the p-cymene ligand by H_2-dcbpy, but complete substitution of the Cl^- ligands for $^-$NCS could not be achieved, even after 36 hours. Removal of the Cl^- ligands using silver nitrate allowed complete substitution of the $^-$NCS ligand at a temperature of 60 °C (Path 2, Fig. 3.23). The resulting product did not require further purification, although mostly the S-bound isomer of the complex was observed by ^{1}H NMR (Fig. 3.24b). However, it was discovered by IR spectroscopy that the use of silver nitrate caused both $^-$NCS and NO_3^- counter ions (ν_{NO} = 1675 cm^{-1} [194]) to be present in the salt. The lack of $^-$NCS was overcome by addition of stoichiometric quantities of NH_4NCS to the

reaction of this material with Y_2-bpy. However, the purity of [Ru(H_2-dcbpy)(p-cymene)(NCS)][NCS] appeared to have little effect on the purity of the eventual product. The synthesis of this starting material was therefore performed using path 1, Fig. 3.23, due to the considerably higher yield of the reaction (79% compared to 56%).

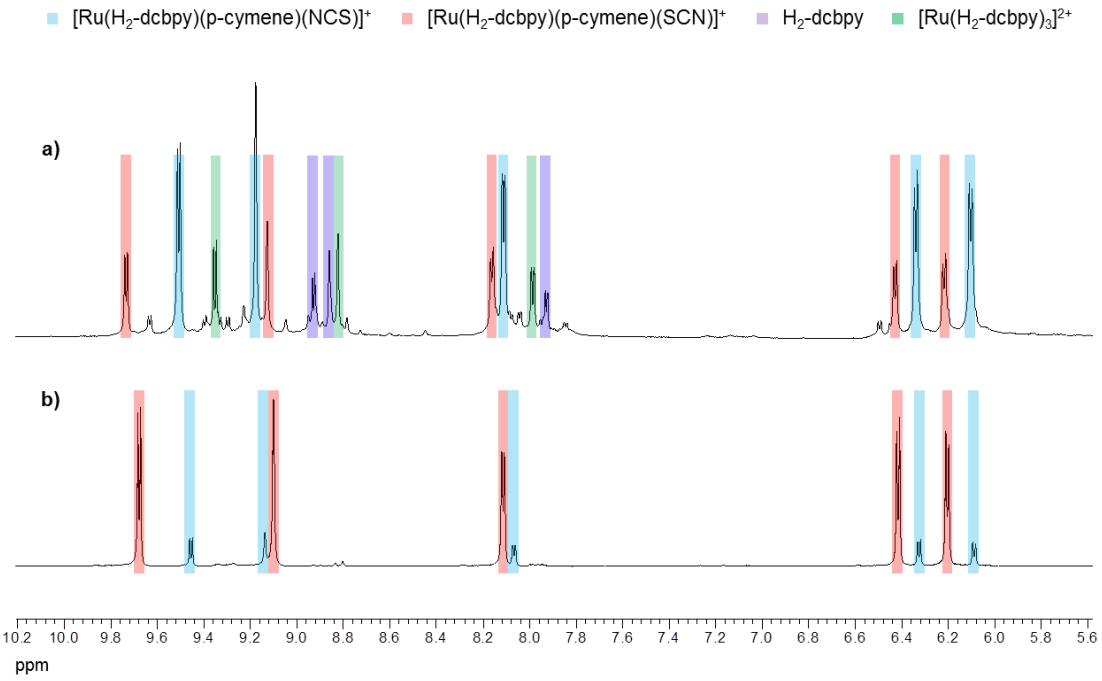

Fig. 3.24: *^{1}H NMR in d^6-DMSO of the product formed in the synthesis of [Ru(H_2-dcbpy)(p-cymene)(NCS)][NCS]* ***a)*** *in ethanol at 80 ^{o}C;* ***b)*** *in DMF at 60 ^{o}C.*

3.6.3 Catalysis of nucleophilic substitution reactions by ruthenium

By heating this starting material in DMF at 140 ^{o}C for four hours with the 4,4`-$Cl_2$-bpy and the 4,4`-Br_2-bpy ligands, product formation was observed and the ^{1}H NMR showed only small impurity peaks. However, in the synthesis of Ru(H_2-dcbpy)(4,4`-F_2-bpy)$(NCS)_2$, the ^{1}H NMR spectrum showed a large number of peaks which could not be identified. In an attempt to push the reaction to completion, the reaction was repeated for 24 hours in DMF, and a large mixture of products was again apparent (Fig. 3.25a i), but fewer than half of the peaks showed coupling to the fluorine atom,

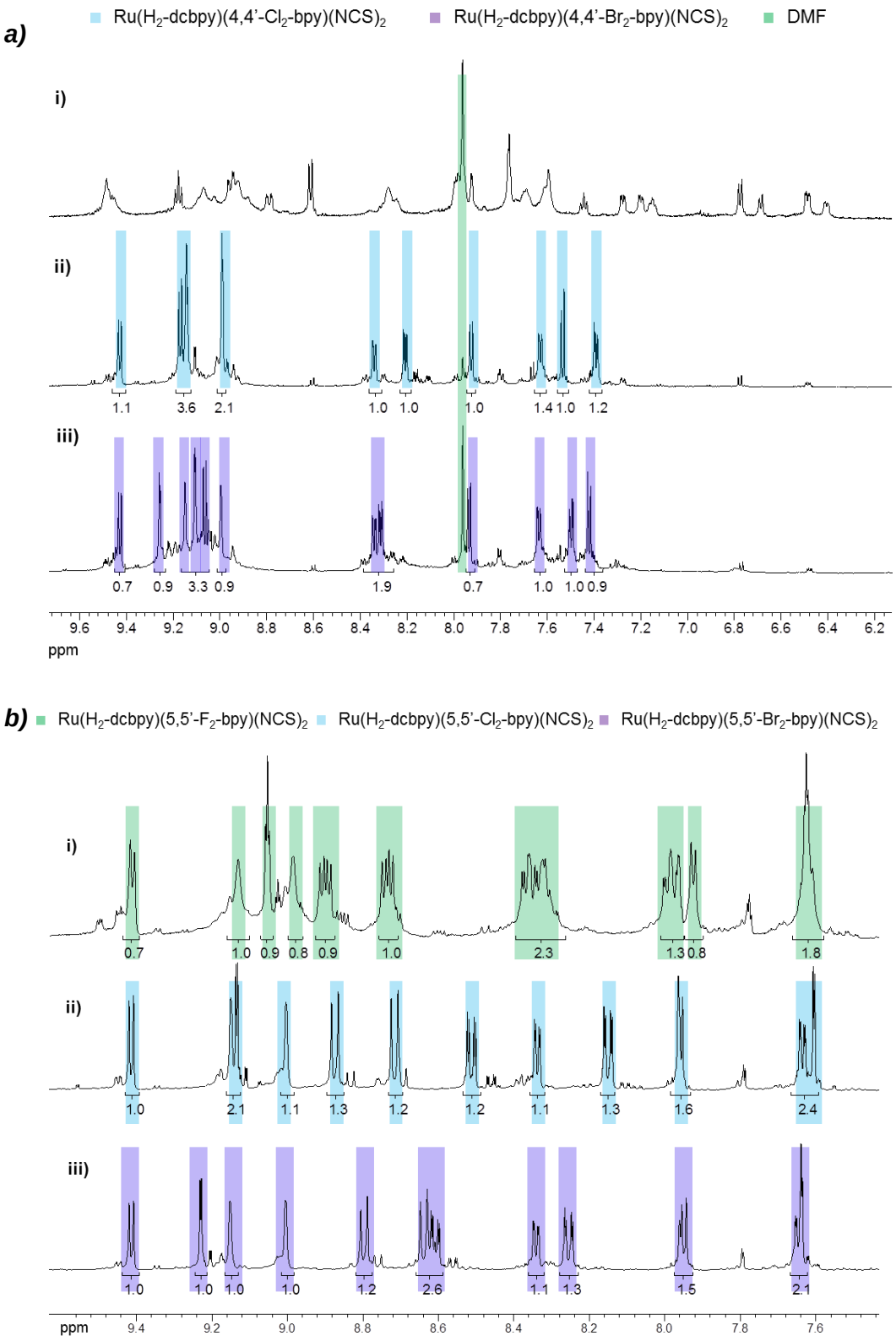

Fig. 3.25: *^{1}H NMR in d^{6}-DMSO of the product after heating N,N`-Y_2-bpy with [Ru(H_2-dcbpy)(p-cymene)(NCS)][NCS] in DMF at 140 ^{o}C for 24 hours.* ***a)*** *N = 4;* ***b)*** *N = 5;* ***i)*** *Y = F;* ***ii)*** *Y = Cl;* ***iii)*** *Y = Br,*

suggesting that loss of the fluorine atom(s) from the bpy ligand was occurring. Even by heating for 24 hours at 140 ^{o}C, very little product breakdown was seen for the reaction of [Ru(H_2-dcbpy)(p-cymene)(NCS)][NCS] with 4,4`-$Y_2$-bpy where Y = Cl, Br (Fig. 3.25a ii, iii). Reaction of the 5,5`-Y_2-bpy ligands where Y = F, Cl, Br under the same conditions also showed little breakdown (Fig. 3.25b).

ESI-MS$^{(-)}$ of the breakdown product showed a peak consistent with [Ru(H-dcbpy)(($NCS)_2$-bpy)$(NCS)_2]^-$ at m/z = 731.0, suggesting that substitution of the F^- for $^-$NCS ions was occurring. Performing the synthesis of Ru(H_2-dcbpy)(4,4`-F_2-bpy)$(NCS)_2$ with added $^-$NCS ions resulted in a product which had 12 peaks in the ^{1}H NMR spectrum with no coupling to the fluorine atom. Analysis of this product by ^{13}C NMR spectroscopy showed 26 carbon atoms to be present, and IR spectroscopy showed an extra peak in the $\nu_{C\text{-}N}$ stretch region of the spectrum (Table 3.5). Thus, the substitution of F^- by $^-$NCS, and therefore the formation of Ru(H_2-dcbpy)(4,4`-$(NCS)_2$-bpy)$(NCS)_2$ as a side product during this reaction was confirmed.

Compound	$\nu_{C\text{-}N}$ / cm^{-1}
KNCS	2040
K_4[Ru(dcbpy)$_2$$(NCS)_2$]	2109
Ru(H_2-dcbpy)(4,4'-$(NCS)_2$-bpy)$(NCS)_2$	2097; 1954
Ru(H_2-dcbpy)(5,5'-$(NCS)_2$-bpy)$(NCS)_2$	2098; 1982

Table 3.5: *The peaks observed in the ν_{CN} stretching frequency of the IR spectrum*

Although the Ru(H_2-dcbpy)(5,5`-$F_2$-bpy)$(NCS)_2$ dye was more resistant to nucleophilic substitution by $^-$NCS than Ru($H_2$-dcbpy)(4,4`-F_2-bpy)$(NCS)_2$; with addition of excess $^-$NCS, the formation of Ru(H_2-dcbpy)(5,5`-$(NCS)_2$-bpy)$(NCS)_2$ during the synthesis of Ru($H_2$-dcbpy)(5,5`-F_2-bpy)$(NCS)_2$ was confirmed by ^{1}H NMR, ESI-MS and IR spectroscopy (Table 3.5). Substitution of the halogen atoms for $^-$NCS was not observed for the other four dyes, although the use of more forcing conditions was not attempted.

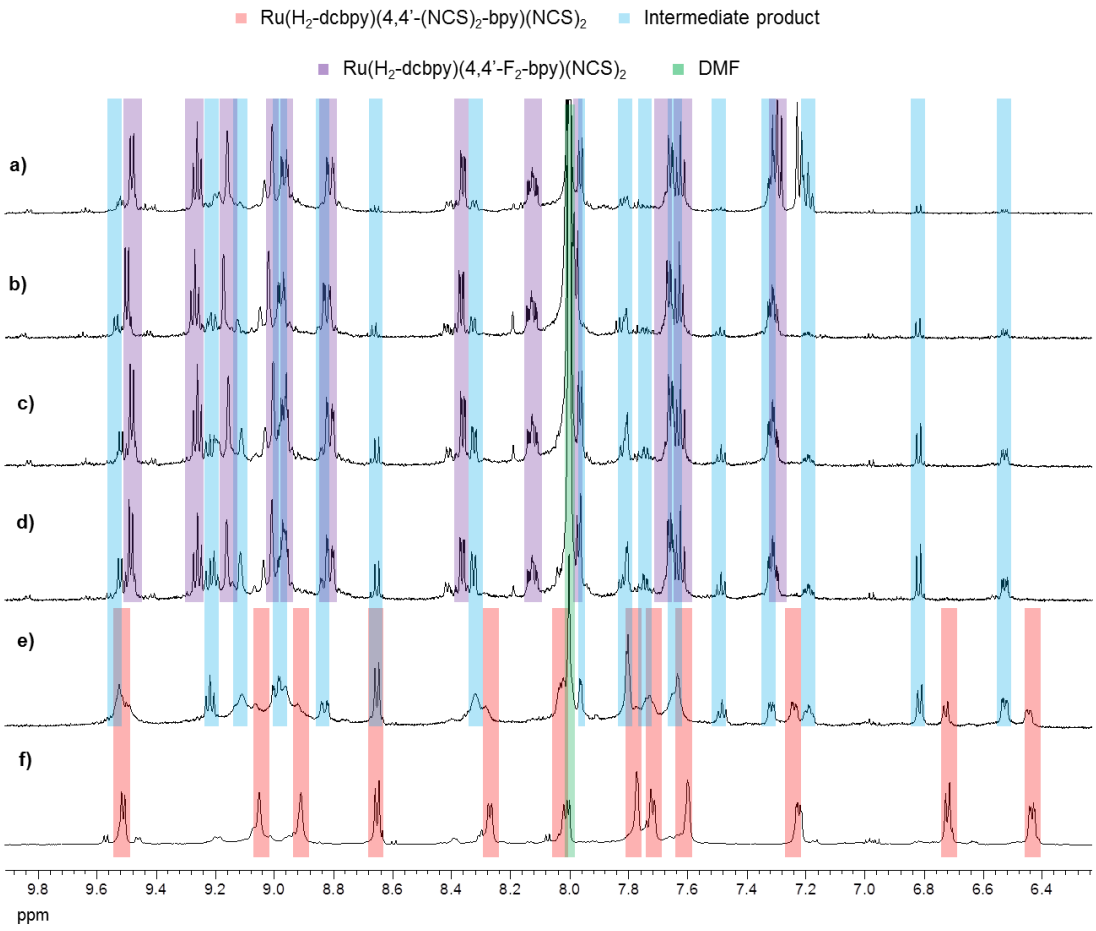

Fig. 3.26: *^{1}H NMR in d^{6}-DMSO of the product after heating 4,4`-F_2-bpy with [Ru(H_2-dcbpy)(p-cymene)(NCS)][NCS] in DMF at 140 ^{o}C for* ***a)*** *1 hour;* ***b)*** *2 hours;* ***c)*** *3 hours;* ***d)*** *4 hours;* ***e)*** *24 hours;* ***f)*** *24 hours with added $^{-}$NCS.*

The synthesis of 4,4`-$(NCS)_2$-bpy[195] and 5,5`-$(NCS)_2$-bpy[196] is performed using the corresponding diamino complex as a starting material. Substitution of fluoroaryl ligands by $^{-}$NCS has previously proved unsuccessful[197]. However, the reaction of the free 4,4'-F_2-bpy and 5,5`-F_2-bpy ligands with excess NH_4NCS was carried out for ten hours at 140 ^{o}C in DMF to ensure the ligands didn't react with $^{-}$NCS. No reactions were observed; therefore binding of the ligand to the ruthenium centre must have increased the susceptibility of the C-F bond to nucleophilic attack from $^{-}$NCS. ^{1}H NMR monitoring of the reaction of [Ru(H_2-dcbpy)(p-cymene)(NCS)][NCS] with 4,4`-$F_2$-bpy was performed (Fig. 3.26); and initial synthesis of [Ru($H_2$-dcbpy)(4,4`-F_2-bpy)$(NCS)_2$] followed by the formation of an intermediate product was apparent

before complete substitution of the F^- substituent by ^-NCS took place. The intermediate product still displayed the expected number of couplings between the aromatic H atoms on the bpy ligand, and fluorine, suggesting that both fluorine atoms are attached to the bpy ligand in this intermediate species.

Nucleophilic substitution reactions of electron rich fluoroarenes have been observed by activation of the C-F bond[198], or complexation of η^6-arenes to the metal centre[199]. C-F bond activation of fluoropyridines has also been reported[200,201]; and catalytic hydrodefluorination of fluorocarbons and fluoroarenes by ruthenium N-heterocyclic carbene complexes has been extensively studied[202-204]. In all cases, the nucleophilic substitution relies on initial nucleophilic attack of the nucleophile to stabilise the C-F bond breaking step. Although the reaction observed in this case is not catalytic, it is likely that nucleophilic attack by the ^-NCS ligand initiates the reaction, allowing the C-Y bond to break, causing de-halogenation of the bpy ligand.

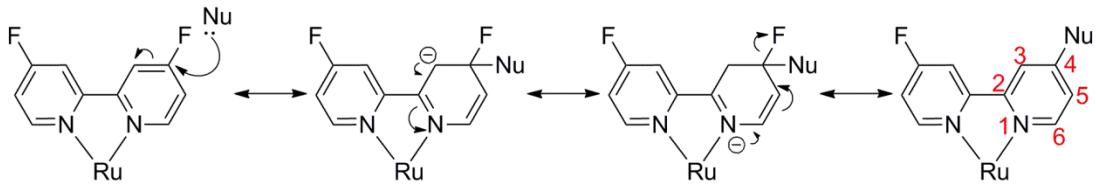

Fig. 3.27: *Resonance stabilisation of the nucleophilic attack of Ru-4,4`-F_2-bpy*

The C-F bond is more polar than the C-Cl and C-Br bonds; thus more susceptible to nucleophilic attack. The increased rate of substitution when Y = F than when Y = Cl, Br suggests that the rate-determining step for this S_{N2} reaction is the nucleophilic attack by ^-NCS. Stabilisation of the intermediate by resonance of the negative charge to the nitrogen atom when the C-F bond is in the 4 or 4` position (Fig. 3.27) explains the comparative ease of nucleophilic substitution of the 4,4`-F_2-bpy analogue compared to the 5,5`-F-bpy analogue.

3.6.4 Optimising the reaction using UV/vis spectroscopy (3.8.3.2)

In an attempt to prevent this nucleophilic substitution from occurring, the synthesis of Ru(H_2-dcbpy)(4,4`-F_2-bpy)$(NCS)_2$ was monitored by UV/vis spectroscopy. The initial progress of the reaction was indicated by a shift of both MLCT transitions to shorter wavelengths (Fig. 3.28a). But after two hours, the peak position of the higher energy MLCT transition shifted to a longer wavelength, and the amplitude of the trough of the spectrum between the two MLCT transitions decreased (Fig. 3.28b). By comparison of the results with the spectra obtained by NMR monitoring (Fig. 3.26), this change in the UV/vis spectrum was assigned to the initiation of the nucleophilic substitution of the F^- group by ^-NCS. The ratio of the absorbance at 537 nm (the λ_{max} of the lowest energy MLCT transition for the product) and the absorbance at 436 nm (the λ_{max} of the highest energy MLCT transition for the starting material) was used to monitor the reaction. As 436 nm lies between the two MLCT peaks of the fluorinated product, this analysis showed the effects of the flattening of the trough in the spectrum; thus monitoring nucleophilic substitution, as well as formation, of the product (Fig. 3.29).

a) ***b)***

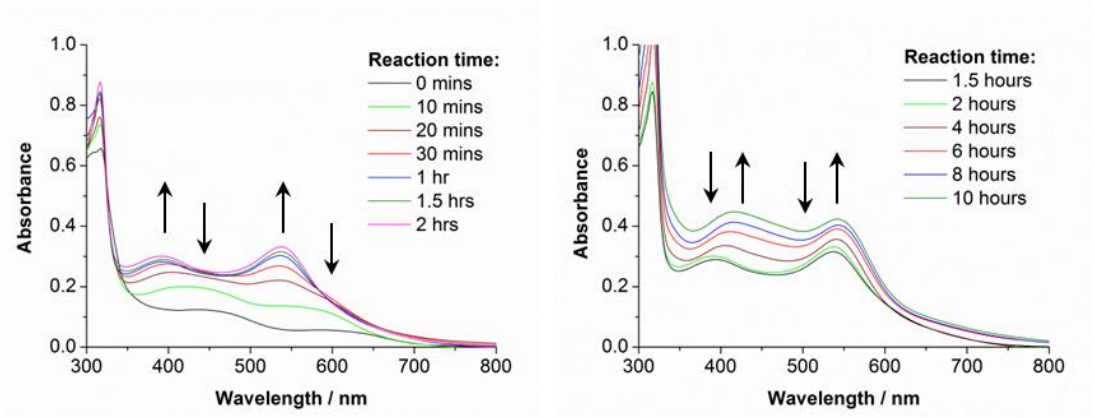

Fig. 3.28: *UV/vis monitoring of Ru(H_2-dcbpy)(4,4`-F_2-bpy)$(NCS)_2$ synthesis* ***a)*** *up to 2 hours;* ***b)*** *from 2 hours to 10 hours.*

The results (Fig 3.29) showed a large increase in the ratio of product to starting material over the first two hours, at which point a peak is apparent as the ratio slowly decreases from two to ten hours. This analysis suggests that the substitution reaction reaches completion after two hours, after which product breakdown begins to occur. This was verified by analysis of the ^{1}H NMR monitoring of the reaction performed previously (Fig. 3.26).

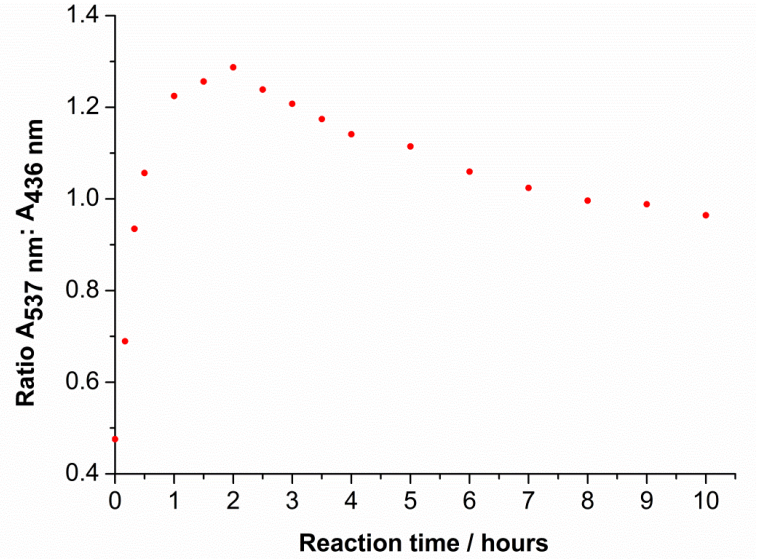

Fig. 3.29: *Monitoring the synthesis of Ru(H_2-dcbpy)(4,4`-F_2-bpy)(NCS)$_2$.*

Initially, UV/vis monitoring was carried out using [Ru(H_2-dcbpy)(p-cymene)(NCS)][NCS] which was shown to contain residual salts by elemental analysis (Expected: % C – 48.39, % H – 3.72, % N – 9.41; Obtained: % C – 44.85, % H – 3.27, % N – 8.96). The concentration of the reaction had a large effect on the synthesis of Ru(H_2-dcbpy)(4,4`-F_2-bpy)(NCS)$_2$ from this starting material, as the peak of the graph (the point at which product breakdown occurs more rapidly that product formation) was observed after just one hour at a higher concentration, compared to two hours at a lower concentration (Fig. 3.30). A lower peak ratio of desired product to breakdown product was also observed at a higher concentration, thus product breakdown occurred more rapidly. That this was due to an increase in the concentration of $^{-}$NCS ions in solution was proved by a reduction in the peak ratio in dilute solutions with addition of excess $^{-}$NCS (Fig. 3.30). Therefore, use of a

concentrated reaction mixture with excess salts in the starting material had a similar effect to the addition of extra $^{-}$NCS ions, suggesting that the synthesis of [Ru(H_2-dcbpy)(p-cymene)(NCS)][NCS] which is proved by CHN analysis to be pure, and contain no residual NH_4NCS, is extremely important to reduce the rate of product breakdown in this reaction.

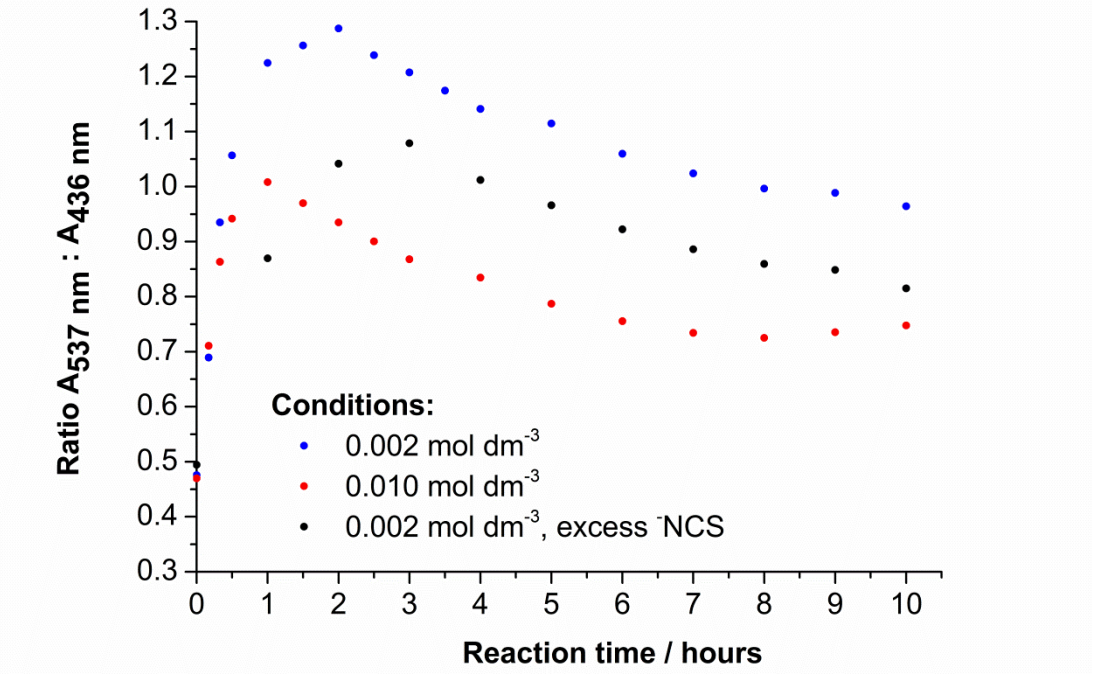

Fig. 3.30: *The effect of the concentration of $^{-}$NCS on the synthesis of Ru(H_2-dcbpy)(4,4`-F_2-bpy)$(NCS)_2$.*

The binding mode of the $^{-}$NCS ligand in the starting ruthenium complex also had a significant effect on the rate of dye breakdown, as using [Ru(H_2-dcbpy)(p-cymene)(NCS)][NCS] which contained mostly N-bound $^{-}$NCS proved vital in the prevention of product breakdown (Fig. 3.31). The reaction was also performed at various temperatures in an attempt to either increase the rate of product formation so that the product could be synthesised before breakdown could occur (reaction at 153 ^{o}C) or to decrease the rate of nucleophilic substitution of the dye (reaction at 120, 130 ^{o}C). The results showed a decrease in the rate of substitution of the p-cymene ligand at lower temperatures (Fig. 3.32), but there didn't appear to be a large effect of temperature on the relative rates of dye formation and dye breakdown.

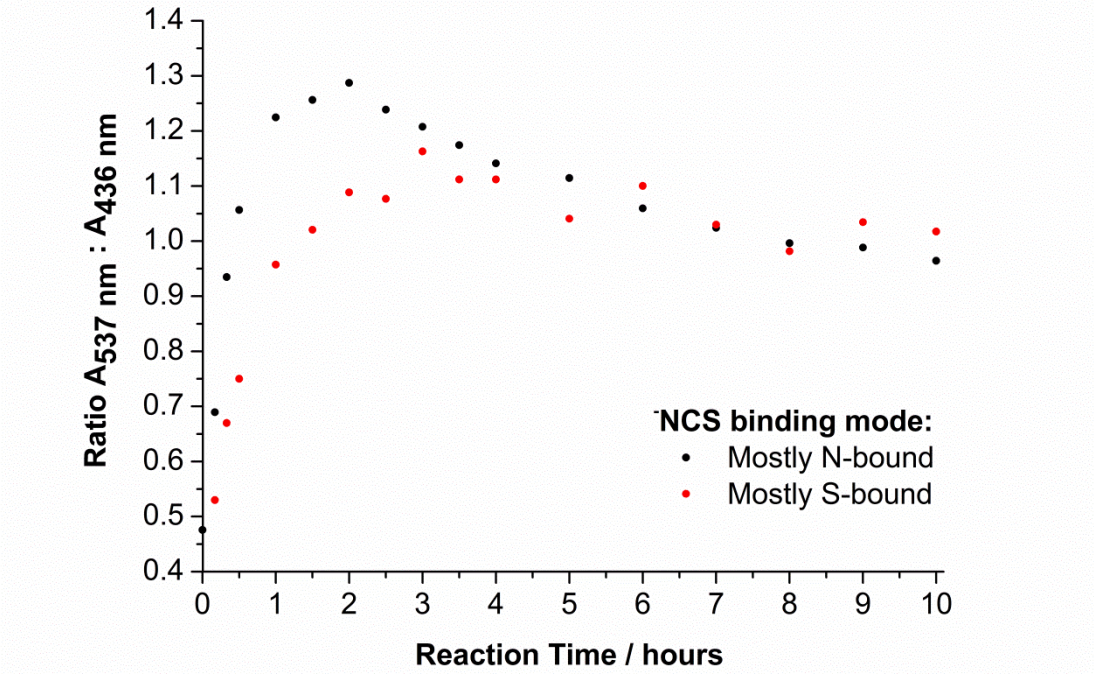

Fig. 3.31: *The effect of the ¯NCS binding mode in [Ru(H_2-dcbpy)(p-cymene)(NCS)][NCS] on the synthesis of Ru(H_2-dcbpy)(4,4`-F_2-bpy)(NCS)$_2$.*

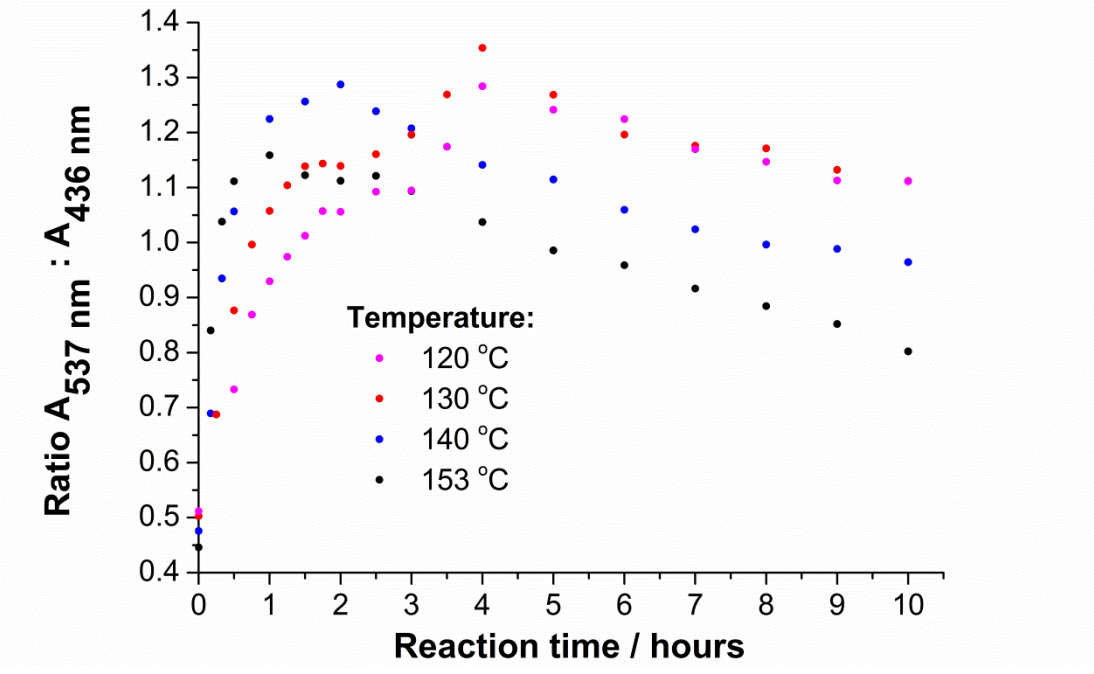

Fig. 3.32: *The effect of temperature on the synthesis of Ru(H_2-dcbpy)(4,4`-F_2-bpy)(NCS)$_2$.*

As nucleophilic substitution of Ru(H_2-dcbpy)(5,5`-$F_2$-bpy)$(NCS)_2$ was also observed, the synthesis of this dye was also performed with UV/vis monitoring. During the first two hours of the reaction of [Ru($H_2$-dcbpy)(p-cymene)(NCS)][NCS] with 5,5`-F_2-bpy, peaks appeared at 384 and 514 nm and the peaks representing the starting material at 436 and 590 nm reduced in size (Fig. 3.34a). It was confirmed by ^{1}H NMR that the reaction had reached completion by this point and little nucleophilic substitution of the fluorine atoms had occurred. From two hours, the positions of the main peaks did not change significantly, but the relative intensity of the peak at 514 nm decreased, and the amplitude of the trough at 436 nm also decreased (Fig. 3.34b). This change was assigned to nucleophilic substitution of the dye. Therefore, the ratio of the absorbance at 514nm and the absorbance at 436 nm was used to monitor the progress of the reaction.

a) **b)**

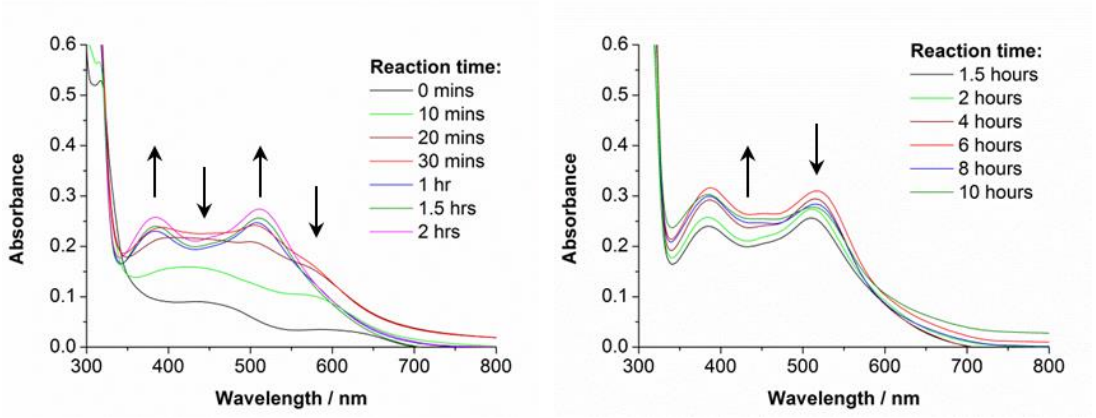

Fig. 3.34: *UV/vis monitoring of Ru(H_2-dcbpy)(5,5`-F_2-bpy)$(NCS)_2$ synthesis* ***a)*** *up to 2 hours;* ***b)*** *from 2 hours to 10 hours.*

As with the synthesis of Ru(H_2-dcbpy)(4,4`-F_2-bpy)$(NCS)_2$, temperature had little effect on the ratio of product to breakdown product. However, increasing the concentration of residual ¯NCS ions, and addition of excess NH_4NCS caused a small increase in the rate of product breakdown (Fig. 3.35); as did the use of a starting ruthenium complex containing mostly the S-bound ¯NCS isomer (Fig. 3.36).

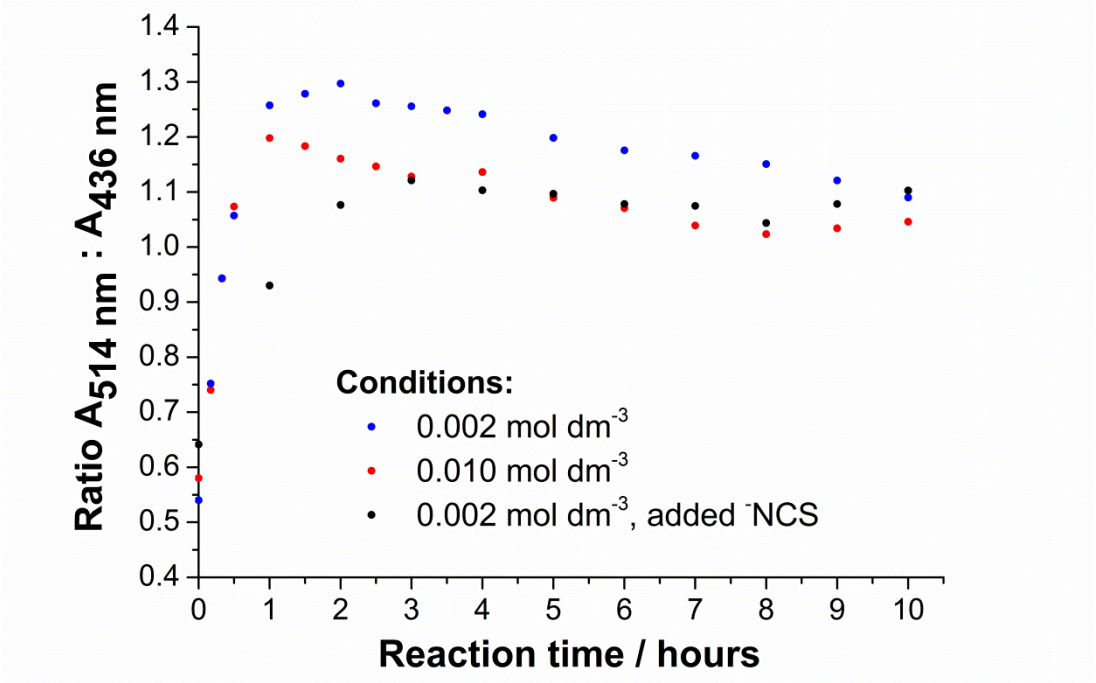

Fig. 3.35: *The effect of $^{-}$NCS concentration on the synthesis of Ru(H_2-dcbpy)(5,5`-F_2-bpy)$(NCS)_2$ at 140 ^{o}C.*

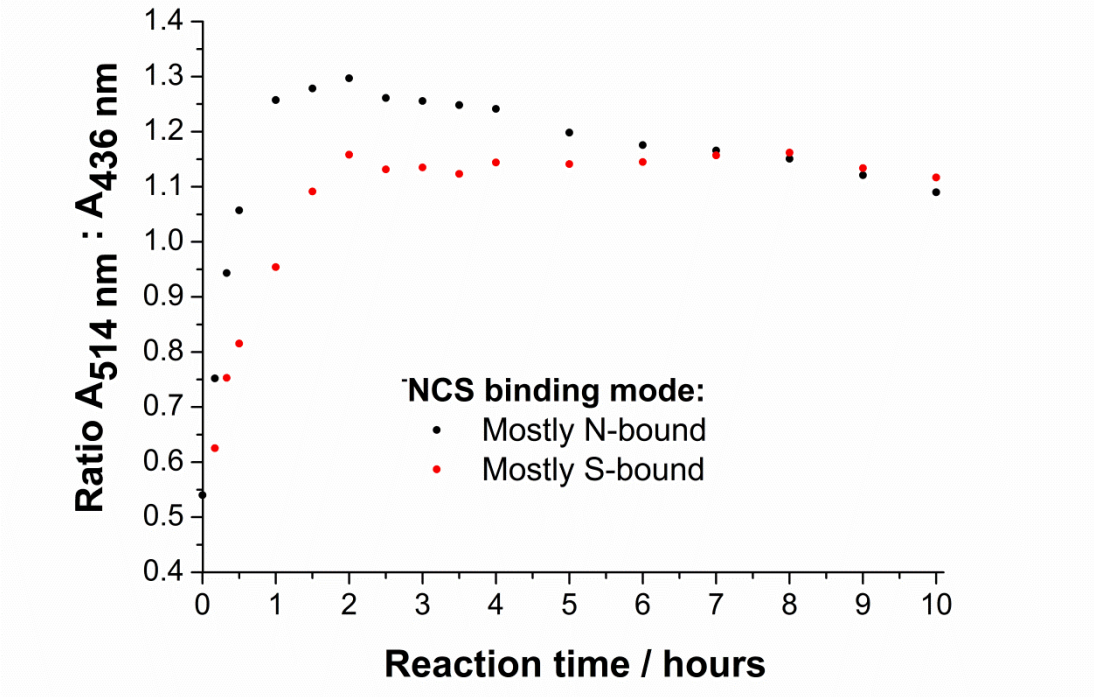

Fig. 3.36: *The effect of the binding mode of $^{-}$NCS on the synthesis of Ru(H_2-dcbpy)(5,5`-F_2-bpy)$(NCS)_2$ at 140 ^{o}C.*

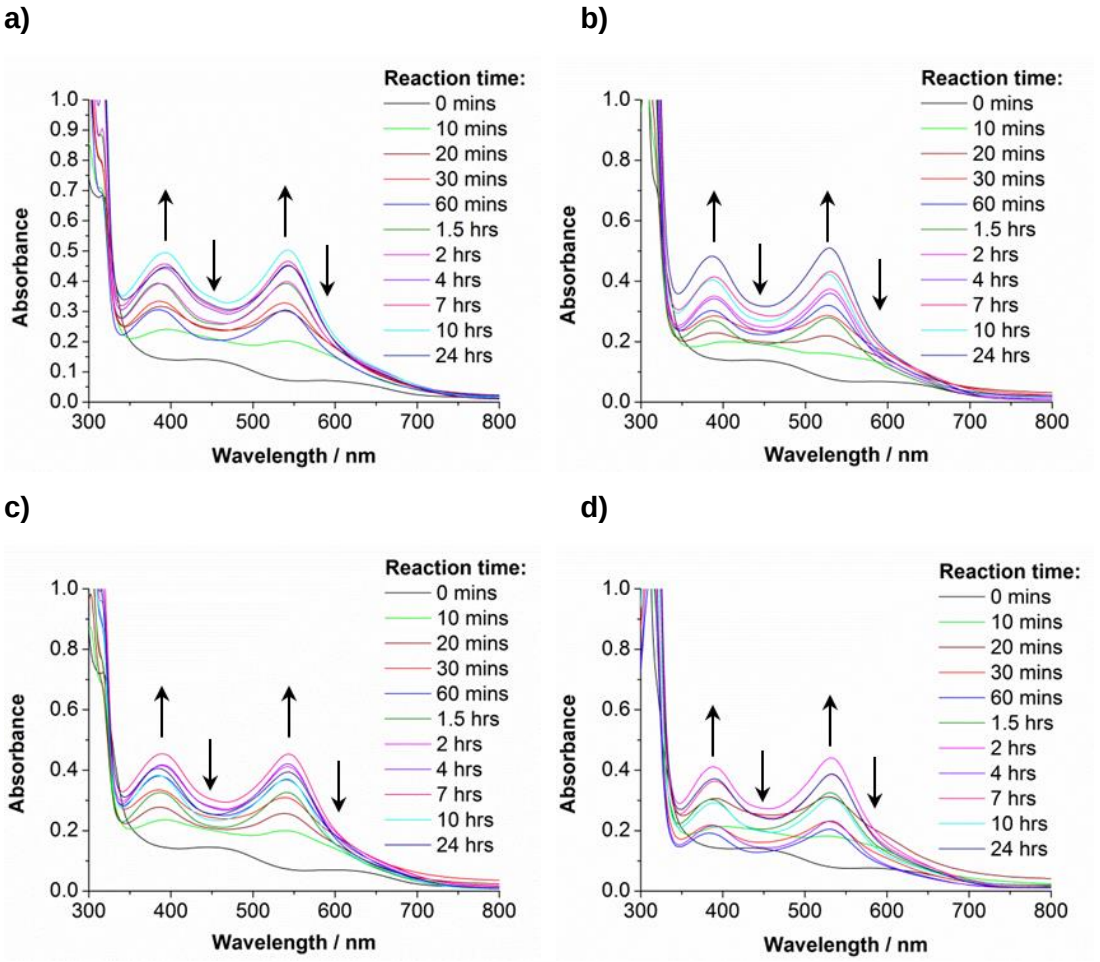

Fig. 3.37: *UV/vis monitoring of the synthesis of Ru(H_2-dcbpy)(Y_2-bpy)($NCS)_2$ where Y_2-bpy is* ***a)*** *4,4`-$Cl_2$-bpy;* ***b)*** *5,5`-Cl_2-bpy;* ***c)*** *4,4`-$Br_2$-bpy;* ***d)*** *5,5`-Br_2-bpy.*

In monitoring the synthesis of Ru(H_2-dcbpy)(N,N`-Y_2-bpy)($NCS)_2$ where N = 4,5 and Y = Cl, Br, there was no evidence of product breakdown in the UV/vis spectra (Fig. 3.37), which is consistent with the minimal product breakdown observed by ^{1}H NMR spectroscopy after 24 hours (3.6.2). Quantifying the results showed formation of the product to occur over the first 90 minutes; after which no considerable change was observed, suggesting that the reactions had reached completion (Fig. 3.38). This was confirmed by ^{1}H NMR analysis. Comparison of the UV/vis monitoring results for all six dyes in series E (Fig. 3.38) showed the breakdown of Ru(H_2-dcbpy)(4,4`-$F_2$-bpy)($NCS)_2$ and Ru($H_2$-dcbpy)(5,5`-F_2-bpy)($NCS)_2$; and the comparative stability of the other dyes.

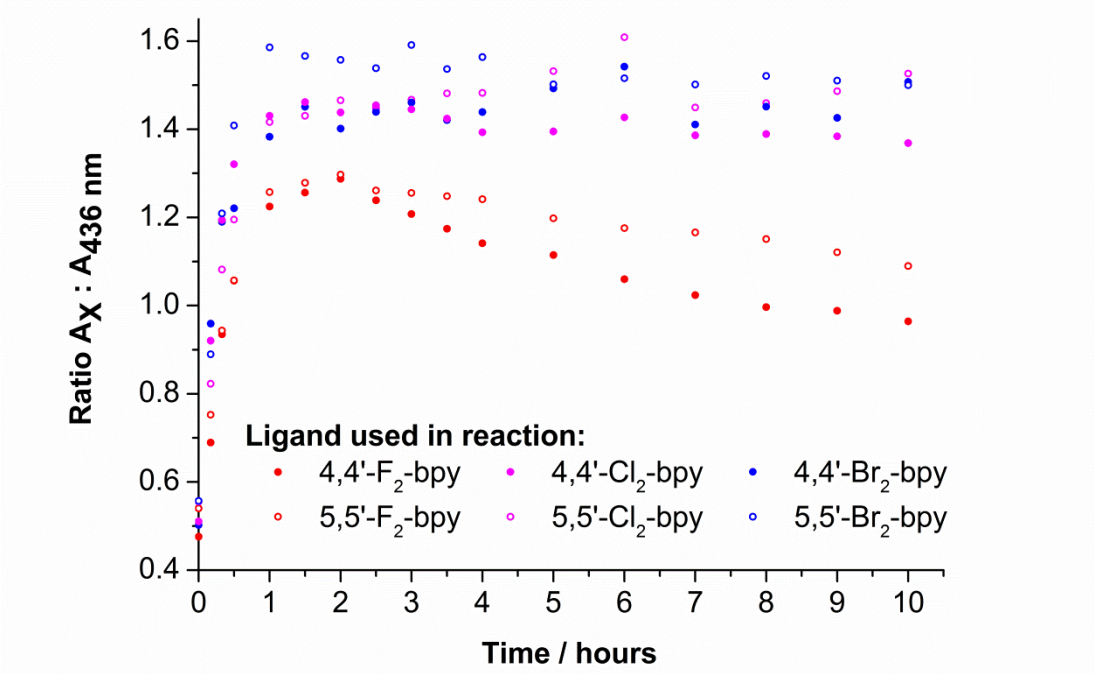

Fig. 3.38: *Monitoring of the reaction of [Ru(H_2-dcbpy)(p-cymene)(NCS)][NCS] with 4,4`-$F_2$-bpy (X = 537 nm); 5,5`-F_2-bpy (X = 514 nm); 4,4`-$Cl_2$-bpy (X = 541 nm); 5,5`-Cl_2-bpy (X = 529 nm); 4,4`-$Br_2$-bpy (X = 542 nm); 5,5`-Br_2-bpy (X = 532 nm).*

3.6.5 Novel procedures for Ru(H_2-dcbpy)(Y_2-bpy)$(NCS)_2$ dyes

Despite extensive optimisation of the reaction procedure, further reaction of the dye containing 4,4`-$F_2$-bpy could not be prevented. Purification of this dye was attempted by sephadex column chromatography, but the similar size of the breakdown products and the dye reduced the efficacy of the column. Therefore, the synthesis of Ru($H_2$-dcbpy)(4,4`-F_2-bpy)$(NCS)_2$ to an acceptable level of purity was not achieved. However, the rapid nucleophilic substitution of the F_2-bpy ligands when bound to ruthenium can be utilised to enable the synthesis of dyes containing a range of substituted Y_2-bpy ligands. Within our group, such a procedure has already been used in the synthesis of Ru(H_2-dcbpy)((4,4`-$(NCS)_2$-bpy)$(NCS)_2$ (Fig. 3.39)[205], and proved highly beneficial as the synthesis of the 4,4`-F_2-bpy ligand was considerably easier to achieve than the synthesis of the 4,4`-$(NCS)_2$-bpy ligand.

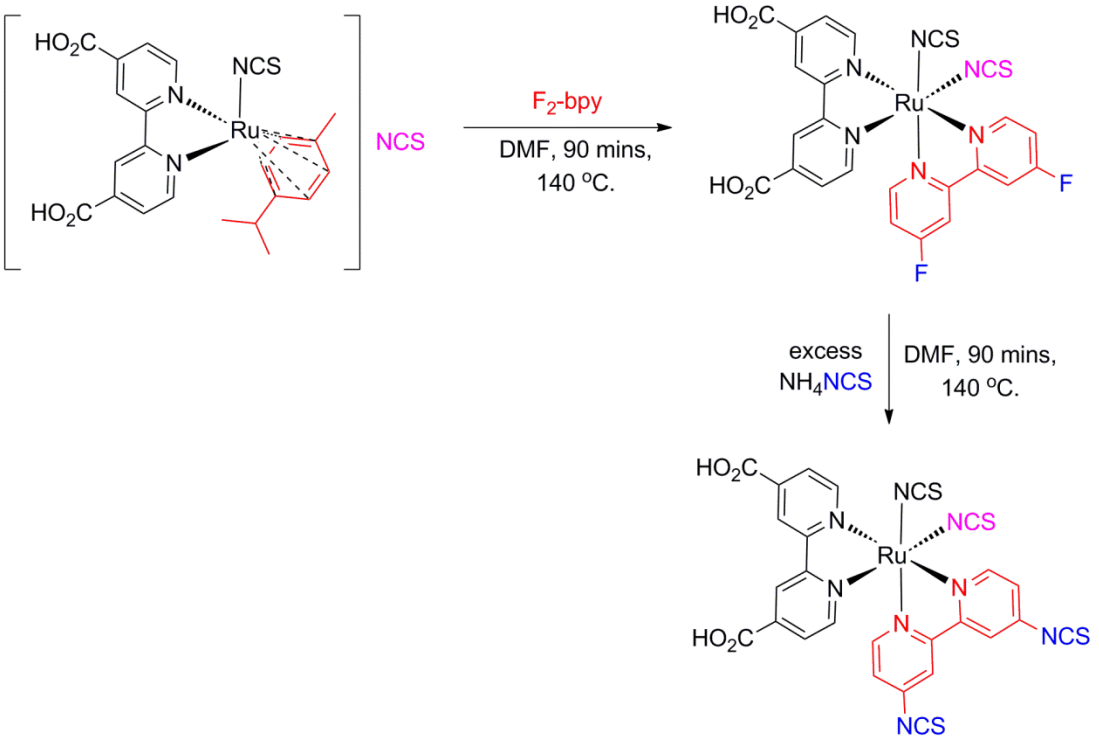

Fig. 3.39: *The synthesis of Ru(H_2-dcbpy)(4,4`-$(NCS)_2$-bpy)$(NCS)_2$.*

As the syntheses of all of the halogenated bpy dyes had been investigated at 140 ^oC and shown to reach completion after 90 minutes, the syntheses of the rest of the dyes were thus carried out (Fig 3.40), although it was found that addition of 0.25 molar ratio of NH_4NCS was required to prevent the formation of a highly insoluble black solid. Purification of the dyes by sephadex column chromatography using 0.1M solutions of [TBA][OH] in methanol resulted in rapid product breakdown for all of the dyes. ESI-$MS^{(-)}$ of the breakdown product contained a peak at m/z = 679.9, which only showed isotopic patterning for ruthenium. This peak is consistent with [Ru(H-dcbpy)(($H_3CO)_2$-bpy)$(NCS)_2]^-$, suggesting that nucleophilic substitution of the halogen by $^-OCH_3$ was occurring. Nucleophilic substitution by ^-NCS was only observed at high temperatures, but ^-NCS is a comparatively weak nucleophile[206]. Therefore these dyes are not stable in the presence of strong nucleophiles, even at room temperature.

Purification of the dyes was achieved by dissolution in aqueous 0.1 M NaOH solution, and careful reduction of the pH with addition of aqueous 0.1 M HNO_3 to precipitate the desired product from the solution. Thus, the dyes were synthesised with respectable yields (60-80%), to a high level of purity, without the need for further purification by sephadex column chromatography (3.8.4.3-3.8.4.7). This one step synthetic procedure, along with the synthesis and subsequent reaction of [Ru(dnbpy)(p-cymene)(NCS)][NCS] in the attempted synthesis of Ru(3,3`-$(CO_2H)_2$-bpy)$(NCS)_2$, therefore provided a route to novel asymmetric dyes with considerably shorter reaction times than the standard synthetic procedure. Although isolation of an intermediate product was required, this was achieved with high yields, and a single reaction intermediate was utilised to synthesise a whole series of novel dyes. This route to asymmetric dyes also allows optimisation of just one reaction step when a novel ligand is being used – a factor which has proved imperative in the synthesis of dyes containing halogenated bpy ligands.

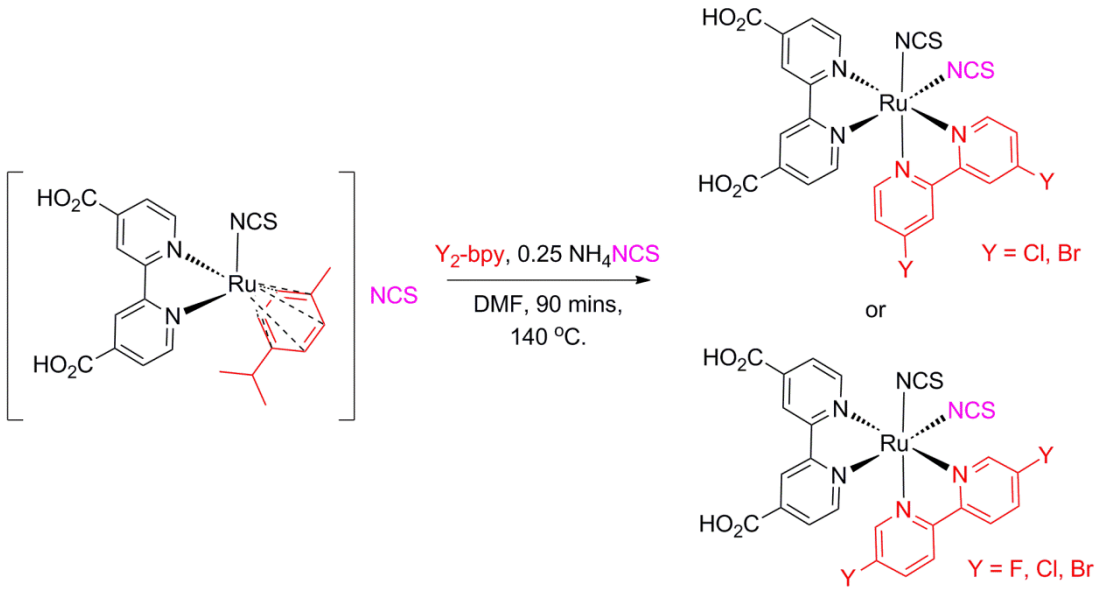

Fig. 3.40: *The synthesis of Ru(H_2-dcbpy)(N,N`-Y_2-bpy)$(NCS)_2$ where N = 4, Y = Cl, Br; N = 5, Y = F, Cl, Br.*

3.7 Conclusion

In ruthenium dyes, carboxylic acid substituted bpy ligands and the ruthenium metal centre are the most common structural features. However, the ruthenium metal centre is kinetically inert. Therefore, high temperatures are often required to initiate a reaction, and once those high temperatures are reached the ruthenium centre is highly labile so it can be difficult to have control over which products form. Even the use of microwave synthesis does not always allow complete kinetic control of a reaction. The low pK_a of the H_2-dcbpy ligand can lead to the formation of undesired salts, and decarboxylation of the ligand can occur. Therefore, even the essential components of a ruthenium dye can cause problems in dye synthesis.

DMF is commonly used in ruthenium dye synthesis; but prolonged heating times must be avoided to prevent the breakdown of DMF to CO and Me_2NH as CO can bind to the ruthenium centre causing the formation of a number of side products. A large number of side reactions and breakdown products have also been observed due to the nature of the novel ligands used. For example, the strength of binding of a novel ligand to ruthenium must be considered in the synthesis of $Ru(H_2\text{-dcbpy})(Y_2\text{-bpy})(NCS)_2$ dyes, as scrambling of the bpy ligands can occur if the more weakly binding ligand is bound to ruthenium first. Research into the stability of novel ligands and avoidance of prolonged reaction times and high temperatures can also avert the formation of impurities. However, the behaviour of a novel ligand when it is bound to ruthenium cannot always be pre-empted. Analysis of crude materials for deduction of the structure of breakdown products is therefore important to prevent their formation; thus allowing the creation of an appropriate synthetic procedure for a novel ruthenium dye.

Optimisation of the synthesis of a novel ruthenium dye can be systematically carried out by UV/vis monitoring of the reaction. The effects of different reaction conditions on dye formation and dye breakdown can be observed by a mixture of qualitative and quantitative analysis of the UV/vis spectra obtained. Initial analysis of the changes

observed must be supported by ^{1}H NMR, but UV/vis monitoring techniques use very little starting material; enabling subsequent exploration of a large variety of reaction conditions. UV/vis monitoring is therefore an extremely useful tool in the optimisation of a synthetic procedure for a novel ruthenium dye.

Two novel synthetic procedures have been developed which may widen the scope of ligands which could be used in novel dyes. The use of $KO^{t}Bu$ to de-esterify the decbpy ligand, thus precipitating the potassium salt of a dye from DMF or ethanol can allow the introduction of temperature sensitive ligands. This procedure also eliminates acidic protons from the synthetic procedure, allowing acid sensitive ligands to be used. In the synthesis of $Ru(H_2\text{-dcbpy})(Y_2\text{-bpy})(NCS)_2$ dyes, the use of $[Ru(Y_2\text{-bpy})(p\text{-cymene})(NCS)][NCS]$ or $[Ru(H_2\text{-dcbpy})(p\text{-cymene})(NCS)][NCS]$ as a starting material allows the optimisation of a single reaction step to produce a pure product. This procedure can prevent prolonged reactions which may produce side products, as well as allowing the one-step synthesis of a wide range of dyes from an easily synthesised starting material.

3.8 Experimental Methods

3,3`-$(CO_2H)_2$-bpy and 4,4`-Br_2-bpy were used as received from Keri L. McCall and Tracy Hewat respectively. All other materials and reagents were used as received from Sigma Aldrich or Fisher scientific.

3.8.1 - Synthesis and characterisation of starting materials

3.8.1.1 Ligand Synthesis

4,4`-$(CO_2H)_2$-2,2`-bipyridine[46] Dmbpy (5 g, 27.1 mmol) was dissolved in concentrated H_2SO_4 (130 ml) and was heated to 70 ^{o}C with stirring. $K_2Cr_2O_7$ (25 g, 85.0 mmol) was slowly (over two hours) added to the mixture which was

subsequently poured into ice/water (800 ml). The solution was filtered, and the solid washed with water. The product was re-crystallised by heating in 50% HNO_3 (130 ml) for four hours at 135 ^oC with stirring. This solution was poured into ice/water (800 ml) and filtered. The solid was washed with water, acetone and diethyl ether and dried in a dessicator yielding 6.32 g (95%). **^{1}H NMR (500.12 MHz, CD_3OD)** δ (ppm): 7.90 (dd, 2H, 5.01 Hz, 1.48 Hz); 8.77 (d, 2H, 5.01 Hz); 8.85 (s, 2H). **^{1}H NMR (500.12 MHz, d^6-DMSO)** δ (ppm): 7.91 (dd, 2H, 5.04 Hz, 1.73 Hz,); 8.85 (s, 2H); 8.91 (d, 2H, 5.04 Hz); 13.81 (broad s, 2H). **^{13}C NMR (125.76 MHz, d^6-DMSO)** δ (ppm): 120.03 (s, 2C); 123.97 (s, 2C); 140.03 (s, 2C); 151.17 (s, 2C); 156.01 (s, 2C); 166.50 (s, 2C). **ESI-MS$^{(-)}$:** [4-(CO_2H)-4`(CO_2)-bpy]$^-$ – 243.0 . **EA (expected):** % C – 59.02, % H – 3.30, % N – 11.47; **EA (obtained):** % C – 58.87, % H – 3.39, % N – 11.56.

4,4`-($CO_2Et)_2$-2,2`-bipyridine[111] H_2-dcbpy (3 g, 12.3 mmol) was added to a mixture of ethanol (180 ml) and concentrated H_2SO_4 (3 ml). The mixture was heated at reflux until the solution became clear (ca. 36 hours) and refrigerated overnight. The white needles thus formed were isolated by filtration and washed with cold ethanol and diethyl ether and dried in a desiccator overnight yielding 2.45 g (66%). **^{1}H NMR (500.12 MHz, CD_3OD)** δ (ppm): 1.47 (t, 6H, 7.09 Hz); 4.49 (q, 4H, 7.09 Hz); 7.99 (dd, 2H, 5.04 Hz, 1.58 Hz); 8.90 (d, 2H, 5.04 Hz); 8.96 (s, 2H). **^{13}C NMR (125.76 MHz, CD_3OD)** δ (ppm): 13.09 (s, 2C); 61.72 (s, 2C); 120.00 (s, 2C); 132.07 (s, 2C); 139.16 (s, 2C); 150.10 (s, 2C); 156.18 (s, 2C); 164.88 (s, 2C). **^{1}H NMR (500.12 MHz, d^6-DMSO)** δ (ppm): 1.38 (t, 6H, 6.94 Hz); 4.42 (q, 4H, 6.94 Hz); 7.97 (dd, 2H, 4.89 Hz, 1.58 Hz, 1.73 Hz,); 8.85 (s, 2H); 8.96 (d, 2H, 5.04 Hz). **^{13}C NMR (125.76 MHz, d^6-DMSO)** δ (ppm): 14.54 (s, 2C); 62.31 (s, 2C); 119.71 (s, 2C); 123.87 (s, 2C); 139.05 (s, 2C); 151.34 (s, 2C); 155.92 (s, 2C); 164.96 (s, 2C). **ESI-MS$^{(+)}$:** H^+[4,4'-($CO_2Et)_2$-bpy] – 301.12. **EA (expected):** % C - 63.99, % H - 5.37, % N - 9.33; **EA (obtained):** % C - 63.93, % H - 5.28, % N - 9.20.

2,2`-bibenzothiazole[207] Well-stirred polyphosphoric acid (25 ml) was heated to 70 ^oC in a three-necked flask under N_2. *o*-aminothiophenol (5.00 g, 0.04 mol) and oxalic acid (1.80 g, 0.02 mol) were mixed and added to the flask. The mixture was

subsequently heated at 140 ^{o}C for two hours. After cooling to room temperature the mixture was poured into ice cold water and the resulting precipitate was filtered, washed with dilute $NaHCO_3$ solution, and dried. The light yellow powder was subsequently recrystallised from chloroform yielding pale yellow crystals (1.47 g, 27%). **^{1}H NMR (500.12 MHz, d^{6}-DMSO)** δ (ppm): 7.64 (t, 2H, 7.60 Hz); 7.67 (t, 2H, 7.57 Hz); 8.22 (d, 2H, 8.19 Hz); 8.28 (d, 2H, 7.88 Hz). **EA (expected):** % C - 62.66, % H - 3.00, % N - 10.44.; **EA (obtained):** % C - 62.16, % H - 2.73, % N - 10.08.

4,4`-$F_2$-2,2`-bipyridine[208] 2-Br-4-F-pyridine (2 g, 11.36 mmol), $Pd(OAc)_2$ (64.2 mg, 0.284 mmol), Indium (582.4 mg, 5.67 mmol), LiCl (720.2 mg, 17.02 mmol) were stirred in dry DMF (22.8 ml) and the solution was N_2 purged for 15 minutes. The mixture was heated at 100 ^{o}C for 1 hour and the reaction was quenched by addition of saturated $NaHCO_3$ solution (300 ml). The product was extracted with ethyl acetate (300 ml, 2 x 100 ml) and the organic layers were washed with water (200 ml) and brine (100 ml) and dried over $MgSO_4$. The solvent was removed from the organic layers and the crude solid was recrystallised from methanol yielding pale yellow needle-like crystals (473.8 mg, 44%). **^{1}H NMR (500.12 MHz, CD_3OD)** δ (ppm): 7.72 (td, 2H, 8.67 Hz, 3.00 Hz); 8.41 (dd, 2H, 8.99 Hz, 4.41 Hz); 8.54 (d, 2H, 2.84 Hz). **^{13}C NMR (125.76 MHz, CD_3OD)** δ (ppm): 122.12 (d, 2C, 5.49 Hz); 123.68 (d, 2C, 18.95 Hz); 136.85 (d, 2C, 23.94 Hz); 151.50 (d, 2C, 3.99 Hz); 159.00 (s, 2C); 161.04 (s, 2C). **^{19}F NMR ^{1}H coupled (376.28 MHz, CD_3OD)** δ (ppm): -129.55 (dd, 2F, 8.51 Hz, 4.09 Hz). **^{19}F NMR ^{1}H decoupled (376.28 MHz, CD_3OD)** δ (ppm): -129.55 (s, 2F). **^{1}H NMR (500.12 MHz, d^{6}-DMSO)** δ (ppm): 7.50 (tdd, 2H, 5.67 Hz, 2.68 Hz, 2.84 Hz); 8.18 (dd, 2H, 10.40 Hz, 2.68 Hz); 8.77 (dd, 2H, 8.67 Hz, 5.67 Hz). **^{13}C NMR (125.76 MHz, d^{6}-DMSO)** δ (ppm): 108.75 (d, 2C, 18.95 Hz); 113.10 (d, 2C, 16.95 Hz); 152.98 (d, 2C, 7.48 Hz); 157.87 (dd, 2C, 7.48 Hz, 3.99 Hz); 168.52 (s, 2C); 170.58 (s, 2C). **^{19}F NMR ^{1}H coupled (376.28 MHz, d^{6}-DMSO)** δ (ppm): -101.97 (q, 2F, 9.20 Hz). **^{19}F NMR ^{1}H decoupled (376.28 MHz, CD_3OD)** δ (ppm): -101.97 (s, 2F). **ESI-MS$^{(+)}$**: H^{+}[4,4`-F_2-bpy] - 193. **EA (expected):** % C – 62.52, % H – 3.15, % N – 14.58; **EA (obtained):** % C - 62.40, % H – 3.06, % N - 14.49.

5,5`-$F_2$-2,2`-bipyridine[208] This reaction was performed as described for 4,4`-$F_2$-2,2`-bipyridine using 2-Br-5-F-pyridine (2 g, 11.36 mmol) instead of 2-Br-4-F-pyridine. The crude solid was recrystallised from methanol yielding white needle-like crystals (735.0 mg, 67%). **^{1}H NMR (500.12 MHz, CD_3OD)** δ (ppm): 7.29 (tdd, 2H, 5.52 Hz, 3.00 Hz, 2.84 Hz); 8.18 (dd, 2H, 10.40 Hz, 2.21 Hz); 8.70 (dd, 2H, 8.51 Hz, 5.52 Hz). **^{13}C NMR (125.76 MHz, CD_3OD)** δ (ppm): 108.55 (d, 2C, 19.45 Hz); 111.91 (d, 2C, 17.45 Hz); 151.83 (d, 2C, 7.98 Hz); 158.07 (dd, 2C, 7.48 Hz, 3.99 Hz); 168.76 (s, 2C); 170.83 (s, 2C). **^{19}F NMR ^{1}H coupled (376.28 MHz, CD_3OD)** δ (ppm): -103.60 (q, 2F, 10.22 Hz, 8.51 Hz). **^{19}F NMR ^{1}H decoupled (376.28 MHz, CD_3OD)** δ (ppm): -103.60 (s, 2F). **^{1}H NMR (500.12 MHz, d^6-DMSO)** δ (ppm): 7.90 (td, 2H, 8.83 Hz, 3.00 Hz); 8.40 (dd, 2H, 8.83 Hz, 4.41 Hz); 8.70 (d, 2H, 3.00 Hz). **^{13}C NMR (125.76 MHz, d^6-DMSO)** δ (ppm): 122.47 (d, 2C, 5.49 Hz); 124.94 (d, 2C, 18.95 Hz); 137.90 (d, 2C, 24.43 Hz); 151.43 (d, 2C, 3.99 Hz); 158.96 (s, 2C); 160.99 (s, 2C). **^{19}F NMR ^{1}H coupled (376.28 MHz, d^6-DMSO)** δ (ppm): -127.31 (t, 2F, 6.13 Hz). **^{19}F NMR ^{1}H decoupled (376.28 MHz, CD_3OD)** δ (ppm): -127.31 (s, 2F). **ESI-MS$^{(+)}$**: H^+[5,5`-F_2-bpy] - 193. **EA (expected):** % C – 62.52, % H – 3.15, % N – 14.58; **EA (obtained):** % C – 62.45, % H – 3.24, % N – 14.51.

4,4`-$Cl_2$-2,2`-bipyridine[209] 2-Br-4-Cl-pyridine (1.77 g, 9.20 mmol), $Pd(Ph_3)_4$ (0.285 g, 0.24 mmol), and η-Bu_6Sn_2 (2.87 g, 4.98 mmol) were added to toluene (45 mmol) and the solution was N_2-purged for 15 minutes. The mixture was heated at reflux for 43 hours. After cooling, diethyl ether (50 ml) and water (50 ml) were added to the solution and the mixture was stirred for 1 hour, filtered and separated. The organic layer was washed with water (2 x 100 ml) and brine (100 ml) and dried over $MgSO_4$. The solvent was removed from the organic phase by rotary evaporation and the resulting crude product was recrystallised from methanol twice yielding pale pink, needle-like crystals (0.323 g, 31%). **^{1}H NMR (500.12 MHz, CD_3OD)** δ (ppm): 7.54 (dd, 2H, 5.36 Hz, 2.21 Hz); 8.44 (s, 2H); 8.63 (d, 2H, 5.36 Hz). **^{13}C NMR (125.76 MHz, CD_3OD)** δ (ppm): 121.22 (s, 2C); 124.39 (s, 2C); 145.24 (s, 2C); 150.29 (s, 2C); 156.13 (s, 2C). **^{1}H NMR (500.12 MHz, d^6-DMSO)** δ (ppm): 7.73 (dd, 2H, 5.36 Hz, 2.05 Hz); 8.43 (d, 2H, 2.05 Hz); 8.75 (d, 2H, 5.36 Hz). **^{13}C NMR (125.76 MHz, d^6-DMSO)** δ (ppm): 121.20 (s, 2C); 125.30 (s, 2C); 144.82 (s, 2C); 151.51 (s, 4C);

156.05 (s, 2C). **ESI-MS$^{(+)}$**: H^+[4,4'-Cl_2-bpy] – 225.20. **EA (expected):** % C – 53.36, % H – 2.69, % N – 12.45; **EA (obtained):** % C – 53.44, % H – 2.76, % N – 12.38.

5,5`-$Cl_2$-2,2`-bipyridine[210] 2-Br-5-Cl-pyridine (1.6 g, 8.3 mmol), N,N`-diisopropylethylamine (1.074 g, 8.3 mmol), $Pd(OAc)_2$ (0.0935 g, 0.415 mmol) and [TBA][Br] (1.342 g, 4.15 mmol) were added to toluene (50 ml) and stirred under N_2 for 15 minutes. The mixture was heated to 105 ^oC and isopropanol (0.5 g, 8.3 mmol) was added. The mixture was held at 105 ^oC for 20 hours, and after cooling water (50 ml) and diethyl ether (50 ml) were added. The mixture was filtered and separated and the organic phase was washed with water (2 x 100 ml) and dried over $MgSO_4$. The solvent was removed by rotary evaporation and the resulting solid was recrystallised from methanol yielding pale yellow plate-like crystals (0.145 g, 15%). **^{1}H NMR (500.12 MHz, CD_3OD)** δ (ppm): 7.97 (dd, 2H, 8.67 Hz, 2.52 Hz); 8.40 (d, 2H, 8.51 Hz); 8.66 (d, 2H, 2.52 Hz). **^{13}C NMR (125.76 MHz, CD_3OD)** δ (ppm): (s, 2C); 121.73 (s, 2C); 132.45 (s, 2C); 136.82 (s, 2C); 147.77 (s, 2C Hz); 153.18 (s, 2C). **^{1}H NMR (500.12 MHz, d^6-DMSO)** δ (ppm): 8.15 (dd, 2H, 8.51 Hz, 2.52 Hz); 8.41 (d, 2H, 8.51 Hz); 8.81 (d, 2H, 2.52 Hz). **^{13}C NMR (125.76 MHz, d^6-DMSO)** δ (ppm): 122.28 (s, 2C); 132.36 (s, 2C); 137.87 (s, 2C); 148.51 (s, 2C); 153.15 (s, 2C). **ESI-MS$^{(+)}$**: Na^+[5,5`-Cl_2-bpy] - 247. **EA (expected):** % C – 53.36, % H – 2.69, % N – 12.45; **EA (obtained):** % C – 53.28, % H – 2.73, % N – 12.36.

5,5`-$Br_2$-2,2`-bipyridine[211] 5-Br-2-I-pyridine (2.2 g, 7.73 mmol), $Pd(Ph_3)_4$ (0.24 g, 0.21 mmol), and η-Bu_6Sn_2 (2.42 g, 4.17 mmol) were stirred in toluene (40 ml) with N_2 bubbling for 15 minutes. The mixture was heated at reflux for 3 days, and after cooling diethyl ether (50 ml) was added to the solution. The mixture was filtered and washed with distilled water and diethyl ether. The solid was dissolved in chloroform (*ca.* 100 ml) and washed with water (2 x 100 ml) and brine (100 ml). The organic phase was then dried over $MgSO_4$ and the solvent was removed by rotary evaporation. The solid formed was recrystallised from chloroform yielding pale yellow crystals (0.6325 g, 52%). **^{1}H NMR (500.12 MHz, CD_3OD)** δ (ppm): 8.12 (dd, 2H, 8.51 Hz, 2.36 Hz); 8.34 (d, 2H, 8.51 Hz); 8.76 (d, 2H, 2.36 Hz). **^{1}H NMR (500.12 MHz, d^6-DMSO)** δ (ppm): 8.26 (dd, 2H, 8.51 Hz, 2.36 Hz); 8.35 (d, 2H,

8.51 Hz); 8.88 (d, 2H, 2.36 Hz). **^{13}C NMR (125.76 MHz, d^6-DMSO)** δ (ppm): 121.72 (s, 2C); 122.67 (s, 2C); 140.68 (s, 2C); 150.66 (s, 2C); 153.54 (s, 2C). **ESI-MS$^{(+)}$:** H^+[5,5'-Br_2-bpy] – 314.9; H^+[5-Br-bpy] – 234.0. **EA (expected):** % C – 53.36, % H – 2.69, % N – 12.45; **EA (obtained):** % C – 53.28, % H – 2.73, % N – 12.36.

3.8.1.2 Synthesis of starting ruthenium complexes

Ru(DMSO)$_4$Cl$_2$[166] $RuCl_3.xH_2O$ (5.437 g, 24.11 mmol) was heated at reflux in DMSO (40 ml) for 10 minutes. The solution was cooled and acetone (300 ml) was added to precipitate the product. The bright yellow solid was filtered and washed with diethyl ether (6.57 g, 56%). **^{1}H NMR (500.12 MHz, d^6-DMSO)** δ (ppm): 2.59 (s, 24H). **^{13}C NMR (125.76 MHz, d^6-DMSO)** δ (ppm): 40.91 (s, 8C). **ESI-MS$^{(+)}$:** Na^+[$Ru(DMSO)_4Cl_2$] – 506.64. **EA (expected):** % C - 19.83, % H - 4.99; **EA (obtained):** % C – 19.95, % H – 1.89.

[Ru(p-cymene)Cl$_2$]$_2$[168] $RuCl_3.xH_2O$ (2.01 g, 9.67 mmol) was dissolved in ethanol (100 ml) and α-phellandrene (10 ml, 61.4 mmol) was added. The mixture was heated at reflux for four hours, and cooled. The solvent was evaporated to half volume and the mixture was refrigerated overnight and filtered yielding an orange brown solid (2.011g, 67%). **^{1}H NMR (500.12 MHz, CD$_3$OD)** δ (ppm): 1.33 (d, 12H, 6.94 Hz); 2.22 (s, 6H); 2.80 (sep, 2H, 6.94 Hz); 5.68 (d, 4H, 6.15 Hz); 5.90 (d, 4H, 6.15 Hz). **^{13}C NMR (125.76 MHz, CD$_3$OD)** δ (ppm): 17.54 (s, 2C); 20.91 (s, 4C); 31.25 (s, 2C); 77.92 (s, 4C); 78.99 (s, 4C); 97.10 (s, 2C); 101.32 (s, 2C). **^{1}H NMR (500.12 MHz, d^6-DMSO)** δ (ppm): 1.20 (d, 12H, 6.81 Hz); 2.10 (s, 6H); 2.84 (sep, 2H, 6.92 Hz); 5.80 (d, 4H, 17.40 Hz); 5.81 (d, 4H, 17.40 Hz). **^{13}C NMR (125.76 MHz, d^6-DMSO)** δ (ppm): 18.35 (s, 2C); 21.98 (s, 4C); 30.45 (s, 2C); 85.99 (s, 4C); 86.84 (s, 4C); 100.57 (s, 2C); 106.85 (s, 2C). **ESI-MS$^{(+)}$:** H^+[Ru(p-cymene)Cl_2]$_2$ – 613.7; [Ru_2(p-cymene)$_2Cl_3$]$^+$ - 576.7. **EA (expected):** % C - 39.23, % H - 4.41; **EA (obtained):** % C - 39.13, % H - 4.69.

$Ru(H_2\text{-}dcbpy)_2Cl_2$[111] H_2-dcbpy (1.00 g, 4.1 mmol) and $RuCl_3.H_2O$ (451 mg, 2.0 mmol) were dissolved in DMF (30 ml). The solution was bubbled with N_2 and then heated at 140 ^oC for 2 ½ hours with stirring under N_2. After cooling to room temperature, the solvent was removed by rotary evaporation. Methanol (100 ml) was added to the residue and the mixture was stirred overnight. A dark red precipitate (0.96 g, 72%) was collected by filtration and dried overnight. **^1H NMR (500.12 MHz, d^6-DMSO)** δ (ppm): 7.50 (dd, 2H, 5.99 Hz, 1.73 Hz); 7.76 (d, 2H, 5.99 Hz); 8.23 (dd, 2H, 5.92 Hz, 1.73 Hz); 8.89 (s, 2H); 9.07 (s, 2H); 10.10 (d, 2H, 5.99 Hz). **ESI-$MS^{(-)}$:** $[Ru(H\text{-}dcbpy)(H_2\text{-}dcbpy)Cl_2]^-$ - 660.48; $[Ru(H\text{-}dcbpy)(H\text{-}dcbpy)Cl_2]^{2-}$ - 328.54. **EA (expected):** % C - 43.63, % H - 2.42, % N - 8.48; **EA (obtained):** % C - 43.91, % H - 2.62, % N - 8.58.

$Ru(H_2\text{-}dcbpy)_2(NCS)_2$[111] $Ru(DMSO)_4Cl_2$ (42.2 mg, 0.087 mmol) and H_2-dcbpy (42.5 mg, 0.17 mmol) were stirred in DMF (10 ml) with N_2 bubbling for 15 minutes. The mixture was subsequently heated at reflux for 2.5 hours with N_2 bubbling. NH_4NCS (388.21 mg, 5.1 mmol) was added to the mixture and reflux was continued for a further hour. The mixture was cooled, and the solvent removed by rotary evaporation. The residue was stirred in water overnight, and the resulting suspension was filtered. The dark red solid was washed with methanol and diethyl ether (35.7 mg, 58%). **^1H NMR (500.12 MHz, CD_3OD)** δ (ppm): 7.68 (dd, 2H, 4.46 Hz, 1.56 Hz); 7.85 (d, 2H, 5.78 Hz); 8.37 (dd, 2H, 4.26 Hz, 1.57 Hz); 8.95 (s, 2H); 9.11 (s, 2H); 9.64 (d, 2H, 5.68 Hz). **^1H NMR (500.12 MHz, d^6-DMSO)** δ (ppm): 7.64 (dd, 2H, 5.92 Hz, 1.75 Hz); 7.83 (d, 2H, 5.94 Hz); 8.41 (dd, 2H, 4.15 Hz, 1.64 Hz); 9.05 (s, 2H); 9.21 (s, 2H); 9.47 (d, 2H, 5.78 Hz). **EA (expected):** % C – 44.25, % H – 2.29, % N – 11.91; **EA (obtained):** % C – 44.13, % H – 2.23, % N – 11.85.

$Ru(decbpy)_2Cl_2$[111] Decbpy (1.00 g, 3.33 mmol) and $Ru(DMSO)_4Cl_2$ (0.81 g, 1.66 mmol) were heated in DMF (50 ml) at 140 ^oC for 2 ½ hours. The solution was cooled; the solvent removed by rotary evaporation, and the residue was stirred in water overnight. The solution was filtered and the green solid was washed with water, methanol, diethyl ether and dried in a desiccator overnight (0.995 g, 77%). **^1H NMR (500.12 MHz, d^6-DMSO)** δ (ppm): 1.30 (t, 6H, 7.09 Hz); 1.44 (t, 6H, 7.09

Hz); 4.35 (q, 4H, 6.94 Hz); 4.52 (q, 4H, 6.94 Hz); 7.49 (dd, 2H, 6.15 Hz, 1.73 Hz); 7.77 (d, 2H, 5.99 Hz); 8.26 (dd, 2H, 5.99 Hz, 1.73 Hz); 8.94 (s, 2H); 9.12 (s, 2H); 10.11 (d, 2H, 5.83 Hz). **^{13}C NMR (125.76 MHz, d^6-DMSO)** δ (ppm): 14.68 (s, 2C); 14.50 (s, 2C); 31.17 (s, 2C); 62.53 (s, 2C); 122.53 (s, 2C); 122.61 (s, 2C); 124.68 (s, 2C); 124.98 (s, 2C); 135.01 (s, 2C); 136.20 (s, 2C); 153.61 (s, 2C); 134.54 (s, 2C); 158.63 (s, 2C); 160.53 (s, 2C); 164.21 (s, 2C); 164.70 (s, 2C). **^{1}H NMR (500.12 MHz, CD_3OD)** δ (ppm): 1.40 (t, 6H, 7.11 Hz); 1.54 (t, 6H, 7.11 Hz); 4.44 (q, 4H, 7.09 Hz); 4.60 (q, 4H, 7.09 Hz); 7.60 (dd, 2H, 6.03 Hz, 1.87 Hz); 7.87 (d, 2H, 6.09 Hz); 8.29 (dd, 2H, 5.96 Hz, 1.75 Hz); 8.90 (s, 2H); 9.08 (s, 2H); 10.19 (d, 2H, 5.81 Hz). **ESI-MS$^{(+)}$:** $Ru(decbpy)_2Cl_2$ – 771.8. **EA (expected):** % C - 49.75, % H - 4.17, % N - 7.25; **EA (obtained):** % C - 49.84, % H - 4.28, % N - 7.30.

3.8.2 The synthesis of novel ruthenium precursor complexes

3.8.2.1 [Ru(decbpy)(p-cymene)(NCS)][PF_6]

$[Ru(p\text{-cymene})Cl_2]_2$ (0.2814 g, 0.4598 mmol) and decbpy (0.2759 g, 0.9197 mmol) were dissolved in EtOH (50 ml). The solution was N_2 purged for 15 minutes and subsequently heated with stirring and N_2 bubbling, at reflux for 3 hours. NH_4NCS (2.63 g, 34.6 mmol) was added and reflux was continued for a further 3 hours. The solution was cooled to room temperature, and NH_4PF_6 (11.41 g, 70.0 mmol) dissolved in water was added to the mixture which was subsequently stirred overnight. The mixture was filtered and the resulting green solid was washed with copious quantities of methanol and diethyl ether (0.1822 g, 27%). A mixture of N-bound (^{N}) and S-bound isomers (^{S}) were shown to be present by NMR analysis. **^{1}H NMR (500.12 MHz, d^6-DMSO)** δ (ppm): 1.00^N (d, 6H, 6.97 Hz); 1.02^S (d, 6H, 6.97 Hz); 1.10^S (t, 6H, 7.10 Hz); 1.46^N (t, 6H, 7.10 Hz); 2.20^S (s, 3H); 2.24^N (s, 3H); 2.64^N (sep, 1H, 6.97 Hz); 2.78^S (sep, 1H, 6.97 Hz); 4.39^S (q, 4H, 7.10 Hz); 4.53^N (q, 4H, 7.10 Hz); 6.16^N (d, 2H, 6.42 Hz); 6.28^S (d, 2H 6.42 Hz); 6.40^N (d, 2H, 6.42 Hz); 6.49^S (d, 2H, 6.42 Hz); 8.20^N (dd, 2H, 5.87 Hz, 1.63 Hz); 8.26^S (dd, 2H, 5.87 Hz, 1.63 Hz); 9.26^S (d, 2H, 1.63 Hz); 9.32^N (d, 2H, 1.63 Hz); 9.61^N (d, 2H, 5.87 Hz); 9.84^S (d, 2H, 5.87 Hz). **^{13}C NMR (125.76 MHz, d^6-DMSO)** δ (ppm): 14.52^N (s, 2C);

18.19^{N} (s, 1C); 22.22^{N} (s, 2C); 30.84^{N} (s, 1C); 63.10^{N} (s, 2C); 86.86^{N} (s, 2C); 89.59^{N} (s, 2C); 106.10^{N} (s, 2C); 109.02^{N} (s, 2C); 117.40^{N} (s, 2C); 124.29^{N} (s, 2C); 126.99^{N} (s, 2C); 140.89^{N} (s, 1C); 155.39^{N} (s, 1C); 157.75^{N} (s, 2C); 163.59^{N} (s, 2C). **ESI-MS$^{(+)}$:** [Ru(decbpy)(p-cymene)(NCS)]$^{+}$ - 594.09. **EA (expected):** % C – 44.14, % H – 3.57, % N – 5.72; **EA (obtained):** % C – 44.02, % H – 3.50, % N – 5.62.

3.8.2.2 [Ru(dnbpy)(p-cymene)(NCS)][NCS]

[Ru(p-cymene)Cl_2]$_2$ (110.5 mg, 0.18 mmol) and dnbpy (147.48 mg, 0.36 mmol) were dissolved in ethanol (20 ml) and the solution was N_2 purged for 15 minutes. The mixture was heated at reflux for 3 hours, then NH_4NCS (0.822 g, 10.8 mmol) was added and reflux was continued for a further 3 hours. The mixture was cooled, the solvent was removed by rotary evaporation, and the residue was stirred in a 1:1 mixture of water and diethyl ether overnight. The organic phase was separated from the aqueous phase and washed three times with water. The organic phase was dried over $MgSO_4$, and the solvent was removed by rotary evaporation yielding a thick, red/brown oil (219.9 mg, 80%). ^{1}H NMR analysis in DMSO showed a mixture of N-bound (^{N}) and S-bound isomers (^{S}); although the N-bound isomer was prominent. IR and EA could not be performed due to the nature of the product. **^{1}H NMR (500.12 MHz, d^{6}-DMSO)** δ (ppm): 0.84^{N,S} (t, 12H, 6.47 Hz); 0.91^{N} (d, 6H, 6.90 Hz); 0.94^{S} (d, 6H, 6.91 Hz); 1.24^{N,S} (m, 18H); 1.31^{N,S} (m, 8H); 1.70^{N,S} (m, 6H); 2.14^{S} (s, 3H); 2.19^{N} (s, 3H); 2.55^{S} (sep, 1H, 6.94 Hz); 2.84^{N} (sep, 1H, 6.94 Hz); 5.99^{N} (d, 2H, 6.62 Hz); 6.12^{S} (d, 2H, 6.46 Hz); 6.23^{N} (d, 2H, 6.46 Hz); 6.34^{S} (d, 2H, 6.44 Hz); 7.66^{N} (dd, 2H, 5.89 Hz, 1.62 Hz); 7.72^{S} (dd, 2H, 5.86 Hz, 1.59 Hz); 8.62^{N,S} (s, 4H); 9.18^{N} (d, 2H, 5.89 Hz); 9.41^{S} (d, 2H, 5.85 Hz). **^{1}H NMR (500.12 MHz, CD_3OD)** δ (ppm): 0.91^{N,S} (t, 12H, 6.84 Hz); 1.06^{N} (d, 6H, 6.91 Hz); 1.09^{S} (d, 6H, 6.91 Hz); 1.32^{N,S} (m, 18H); 1.42^{N,S} (m, 8H); 1.80^{N,S} (m, 6H); 2.26^{S} (s, 3H); 2.30^{N} (s, 3H); 2.65^{S} (sep, 1H, 6.88 Hz); 2.93^{N} (sep, 1H, 6.88 Hz); 5.87^{N} (d, 2H, 6.34 Hz); 6.00^{S} (d, 2H, 6.34 Hz); 6.13^{N} (d, 2H, 6.36 Hz); 6.22^{S} (d, 2H, 6.36 Hz); 7.63^{N} (dd, 2H, 5.89 Hz, 1.62 Hz); 7.66^{S} (dd, 2H, 5.84 Hz, 1.54 Hz); 8.48^{S} (s, 2H) 8.51^{N} (s, 2H); 9.13^{N} (d, 2H, 5.88 Hz); 9.34^{S} (d, 2H, 5.83 Hz). **ESI-MS$^{(+)}$:** [Ru(dnbpy)(p-cymene)(NCS)]$^{+}$ - 702.3.

3.8.2.3 [Ru(H_2-dcbpy)(p-cymene)(NCS)][NCS]

[Ru(p-cymene)Cl_2]$_2$ (1.123 g, 1.83 mmol) and H_2-dcbpy (0.896 g, 6.53 mmol) were heated in ethanol (100 ml) at 60 ^oC overnight. NH_4NCS (8.38 g, 110.1 mmol) was added to the mixture, which was heated at reflux for 3 hours. After cooling, the solvent was removed from the solution and the crude product was stirred in water overnight. The suspension was filtered and the resulting green solid was washed with ethanol and diethyl ether (1.73 g, 79%). A mixture of N-bound (^{N}) and S-bound isomers (^{S}) were observed; although the N-bound isomer was the prominent isomer. **^{1}H NMR (500.12 MHz, d^6-DMSO)** δ (ppm): 1.00^N (d, 6H, 6.82 Hz); 1.01^S (d, 6H, 6.82 Hz); 2.20^S (s, 3H); 2.24^N (s, 3H); 2.64^N (sep, 1H, 6.82 Hz); 2.77^S (sep, 1H, 6.94 Hz); 6.14^N (d, 2H, 6.10 Hz); 6.26^S (d, 2H, 6.10 Hz); 6.38^N (d, 2H, 6.10 Hz); 6.47^S (d, 2H, 6.10 Hz); 8.15^N (d, 2H, 5.60 Hz); 8.19^S (d, 2H, 5.60 Hz); 9.17^S (s, 2H); 9.22^N (s, 2H); 9.55^N (d, 2H, 5.60 Hz); 9.61^S (d, 2H, 5.60 Hz). **^{13}C NMR (125.76 MHz, d^6-DMSO)** δ (ppm): 18.17^N (s, 1C); 22.13^N (s, 2C); 30.86^N (s, 1C); 86.61^N (s, 2C); 89.25^N (s, 2C); 105.64^N (s, 1C); 108.70^N (s, 1C); 117.90^N (s, 2C); 123.96^N (s, 2C); 127.19^N (s, 2C); 144.24^N (s, 1C); 146.20^N (s, 1C); 155.22^N (s, 2C); 157.23^N (s, 2C); 165.14^N (s, 2C). **^{1}H NMR (500.12 MHz, CD_3OD)** δ (ppm): 1.12^N (d, 6H, 6.94 Hz); 1.15^S (d, 6H, 6.94 Hz); 2.31^S (s, 3H); 2.33^N (s, 3H); 2.73^N (sep, 1H, 6.94 Hz); 2.84^S (sep, 1H, 6.94 Hz); 6.04^N (broad, 2H); 6.14^S (broad, 2H); 6.26^N (broad, 2H); 6.33^S (broad, 2H); 8.22^N (broad, 2H); 8.25^S (broad, 2H); 9.01^S (broad, 2H); 9.05^N (broad, 2H); 9.48^N (broad, 2H); 9.68^S (broad, 2H). **ESI-MS$^{(-)}$:** [Ru(dcbpy)(p-cymene)(NCS)]$^-$ - 535.87. **ATR-FTIR:** ν_{C-N} 2107 cm^{-1}. **EA (expected):** % C – 48.39, % H – 3.72, % N – 9.41; **EA (obtained):** % C – 48.26, % H – 3.76, % N – 9.52.

3.8.3 Monitoring of reactions by UV/vis spectroscopy

3.8.3.1 Monitoring the synthesis of Ru(3,3`-(CO_2H)$_2$-bpy)(dnbpy)(NCS)$_2$

In a typical reaction [Ru(dnbpy)(p-cymene)(NCS)][NCS] (7.6 mg, 0.01 mmol) and 3,3`-(CO_2H)$_2$-bpy (2.4 mg, 0.01 mmol) were dissolved in DMF (5 ml) and the

solution was N_2-purged for 15 minutes. The mixture was then placed in a pre-heated oil bath at the prescribed temperature and sampled by taking 0.1 ml of the solution and making it up to 5 ml. At 140 ^oC, samples were taken every 10 minutes for the first 30 minutes, then every 30 minutes to 4 hours, then every hour to 10 hours. At 80 ^oC, samples were taken every hour for 12 hours, then every 12 hours for 5 days. When appropriate, small portions of the mixture were removed and the solvent removed by rotary evaporation for analysis of the crude product by ^1H NMR.

3.8.3.2 Monitoring the synthesis of $Ru(H_2\text{-dcbpy})(N,N`\text{-}Y_2\text{-bpy})(NCS)_2$ dyes where N = 4, 5; Y = F, Cl, Br.

In a typical procedure, $[Ru(H_2\text{-dcbpy})(p\text{-cymene})(NCS)][NCS]$ (5.9 mg, 0.01 mmol) and Y_2-bpy (0.01 mmol) were dissolved in DMF (5 ml). When appropriate, NH_4NCS (1.5 mg, 0.02 mmol) was also added to the mixture, which was N_2-purged for 15 minutes. The mixture was then placed in a pre-heated oil bath at the prescribed temperature, and sampled by taking 0.1 ml of the solution and making it up to 5 ml. At 140 and 153 ^oC, samples were taken every 10 minutes for the first 30 minutes, then every 30 minutes to 4 hours, then every hour to 10 hours. At 120 and 130 ^oC, samples were taken every 15 minutes for the first 2 hours, then every 30 minutes to 4 hours, then every hour to 10 hours. If required, small portions of the mixture were removed and the solvent removed by rotary evaporation for analysis of the crude product by ^1H NMR.

3.8.4 The synthesis of novel ruthenium dyes

3.8.4.1 $K_4[Ru(dcbpy)_2(NCO)_2]$ synthesis

$[Ru(decbpy)_2Cl_2]$ (150 mg, 0.194 mmol) was dissolved in 20ml methanol and $AgNO_3$ (66 mg, 0.388 mmol) was added. The solution was heated at reflux under reduced light with N_2 bubbling for 30 mins and cooled. The white solid formed was separated by centrifugation and the solvent was removed from the supernatant solution by rotary evaporation. The resulting residue was dissolved in 20 ml DMF

and KNCO (945 mg, 11.6 mmol) was added. The solution was heated at 140^0C for one hour under reflux conditions, and under reduced light with N_2 bubbling. After cooling to room temperature, the mixture was filtered, and KO^{t}Bu (796 mg, 6.208 mmol) was added to the filtrate. The mixture was stirred for 5 minutes at room temperature and the precipitate was isolated by centrifugation. The solid was washed with THF three times and then purified by sephadex column chromatography in methanol once. Collection of the purple band yielded the desired product (0.122g, 76%). **^{1}H NMR (500.12 MHz, CD_3OD)** δ (ppm): 7.50 (dd, 2H, 5.91Hz, 1.71 Hz); 7.64 (d, 2H, 5.84 Hz); 8.15 (dd, 2H, 5.76 Hz, 1.66 Hz); 8.81 (s, 2H); 8.98 (s, 2H); 9.58 (d, 2H, 5.70 Hz). **^{13}C NMR (125.76 MHz, CD_3OD)** δ (ppm): 123.12 (2C); 123.19 (2C); 125.81 (2C); 126.37 (2C); 127.74 (s, 2C); 145.40 (2C); 146.44 (2C); 152.83 (2C); 153.86 (2C); 159.42 (2C); 161.04 (2C); 170.87 (2C); 171.23 (2C). **^{1}H NMR (500.12 MHz, D_2O)** δ (ppm): 7.40 (dd, 2H, 5.93 Hz, 1.72 Hz); 7.77 (d, 2H, 5.95 Hz); 8.11 (dd, 2H, 5.79 Hz, 1.67 Hz); 8.69 (s, 2H); 8.86 (s, 2H); 9.53 (d, 2H, 5.80 Hz). **^{13}C NMR (125.76 MHz, D_2O)** δ (ppm): 121.81 (2C); 121.89 (2C); 124.27 (2C); 125.26 (2C); 142.69 (2C); 143.74 (2C); 152.65 (2C); 152.97 (2C); 158.07 (2C); 159.55 (2C); 171.65 (2C); 172.00 (2C). **^{1}H NMR (500.12 MHz, d^6-DMSO)** δ (ppm): 7.34 (dd, 2H, 5.78 Hz, 1.71 Hz); 7.38 (d, 2H, 5.53 Hz); 8.00 (dd, 2H, 5.68 Hz, 1.60 Hz); 8.48 (s, 2H); 8.64 (s, 2H); 9.31 (d, 2H, 5.62 Hz). **ESI-MS$^{(-)}$:** [Ru(H_2-dcbpy)(H-dcbpy)$(NCO)_2$]$^-$ - 672.98. **ATR-FTIR:** ν_{C-N} 2234 cm^{-1}. **EA (expected):** % C - 37.81, % H - 1.46, % N - 10.18; **EA (obtained):** % C 37.65, % H - 1.54, % N - 10.32.

3.8.4.2 $K_4[Ru(dcbpy)_2(NCS)_2]$ synthesis

This reaction was performed as for NCO but adding KNCS (1.132 g, 11.6 mmol) instead of KNCO. Collection of the red band from the column yielded the desired product (0.131g, 79%). **^{1}H NMR (500.12 MHz, CD_3OD)** δ (ppm): 7.55 (dd, 2H, 5.85 Hz, 1.60 Hz); 7.63 (d, 2H, 5.87 Hz); 8.22 (dd, 2H 5.72 Hz, 1.58 Hz); 8.84 (s, 2H); 9.00 (s, 2H); 9.49 (d, 2H, 5.73 Hz). **^{13}C NMR (125.76 MHz, CD_3OD)** δ (ppm): 123.43 (2C); 123.55 (2C); 126.28 (2C); 126.95 (2C); 134.11 (2C); 146.83 (2C); 147.48 (2C); 152.75 (2C); 154.16 (2C); 159.13 (2C); 160.40 (2C); 170.53 (2C);

170.92 (2C). **^{1}H NMR (500.12 MHz, D_2O)** δ (ppm): 7.47 (dd, 2H, 5.89 Hz, 2.00 Hz); 7.74 (d, 2H, 5.90 Hz); 8.13 (dd, 2H, 5.76 Hz, 1.66 Hz); 8.70 (s, 2H); 8.86 (s, 2H); 9.47 (d, 2H, 5.74 Hz). **^{13}C NMR (125.76 MHz, D_2O)** δ (ppm): 121.90 (2C); 122.12 (2C); 124.57 (2C); 125.59 (2C); 132.03 (2C); 143.87 (2C); 144.51 (2C); 152.35 (2C); 153.25 (2C); 157.76 (2C); 158.85 (2C); 171.43 (2C); 171.77 (2C). **^{1}H NMR (500.12 MHz, d^{6}-DMSO)** δ (ppm): 7.42 (d, 2H, 5.48 Hz); 7.45 (dd, 2H, 5.75 Hz, 1.52 Hz); 8.07 (dd, 2H, 5.62 Hz, 1.46 Hz); 8.53 (s, 2H); 8.69 (s, 2H); 9.16 (d, 2H, 5.68 Hz). **ESI-MS$^{(-)}$:** $[Ru(H\text{-}dcbpy)_2(NCS)_2]^{2-}$ - 351.97. **ATR-FTIR:** $\nu_{C\text{-}N}$ 2109 cm^{-1}. **EA (expected):** % C - 36.40, % H - 1.41, % N - 9.79; **EA (obtained):** % C 36.27, % H - 1.52, % N - 9.81.

3.8.4.3 Ru(H_2-dcbpy)(5,5`-F_2-bpy)$(NCS)_2$ synthesis

[Ru(H_2-dcbpy)(p-cymene)(NCS)][NCS] (50 mg, 83.9 μmol), 5,5`-F_2-bpy (16.1 mg, 83.9 μmol) and NH_4NCS (1.6 mg, 21.0 μmol) were dissolved in 20 ml DMF and the solution was N_2-purged for 15 minutes. The mixture was then heated in a pre-heated oil bath at 140 ^{o}C for 90 minutes, and, after cooling, the solution was filtered. The solvent was removed from the filtrate by rotary evaporation, and the crude product was dissolved in aqueous 0.1M NaOH solution (ca. 5-10 ml). The solution was filtered, and the product was precipitated from the filtrate by reducing the pH to 3.0 by addition of aqueous 0.1M HNO_3. The resulting dark red solid was isolated by centrifugation, and washed with copious volumes of water, a small quantity of isopropanol, and diethyl ether (33.4 mg, 61%). **^{1}H NMR (500.12 MHz, d^{6}-DMSO)** δ (ppm): 7.60 (t, 1H, 2.59 Hz); 7.61 (dd, 1H, 5.99 Hz, 1.70 Hz); 7.91 (td, 1H, 8.29 Hz, 2.84 Hz); 7.92 (d, 1H, 5.67 Hz); 8.28 (td, 1H 7.00 Hz, 2.71 Hz); 8.29 (dd, 1H, 7.31 Hz, 1.64 Hz); 8.66 (dd, 1H, 8.89 Hz, 5.23 Hz); 8.81 (dd, 1H, 8.89 Hz, 5.23 Hz); 8.93 (s, 1H); 9.03 (t, 1H, 2.65 Hz); 9.08 (s, 1H); 9.39 (d, 1 H, 6.12 Hz). **^{19}F NMR ^{1}H coupled (376.28 MHz, d^{6}-DMSO)** δ (ppm): -120.42 (m, 1F); -119.83 (m, 1F). **^{19}F NMR ^{1}H decoupled (376.28 MHz, d^{6}-DMSO)** δ (ppm): -120.42 (s, 1F); -119.83 (s, 1F). **ESI-MS$^{(-)}$:** $[Ru(H\text{-}dcbpy)(5,5`\text{-}F_2\text{-}bpy)(NCS)_2]^{-}$ - 652.8. **ATR-FTIR:** $\nu_{C\text{-}N}$ 2108 cm^{-1}. **EA (expected):** % C – 44.10, % H – 2.16, % N – 12.86; **EA (obtained):** % C – 43.89, % H – 2.06, % N – 12.74.

3.8.4.4 Ru(H_2-dcbpy)(4,4'-Cl_2-bpy)$(NCS)_2$ synthesis

The reaction was carried out as described in 3.8.4.3, with addition of 4,4`-$Cl_2$-bpy (18.9 mg, 83.9 μmol) instead of 5,5`-F_2-bpy, yielding a dark red solid (34.5 mg, 60%). **^{1}H NMR (500.12 MHz, d^6-DMSO)** δ (ppm): 7.39 (dd, 1H, 6.24 Hz, 2.27 Hz); 7.52 (d, 1H, 6.24 Hz); 7.62 (dd, 1H, 5.86 Hz, 1.70 Hz); 7.92 (d, 1H, 5.86 Hz); 8.19 (dd, 1H, 6.18 Hz, 2.21 Hz); 8.33 (dd, 1H, 5.86 Hz, 1.58 Hz); 8.96 (s, 1H); 8.97 (s, 1H); 9.12 (s, 1H); 9.13 (s, 1H); 9.15 (d, 1H, 6.18 Hz); 9.42 (d, 1H, 5.93 Hz). **ESI-MS$^{(-)}$:** $[Ru(H\text{-}dcbpy)(4,4`\text{-}Cl_2\text{-}bpy)(NCS)_2]^-$ - 684.8. **ATR-FTIR:** $\nu_{C\text{-}N}$ 2101 cm^{-1}. **EA (expected):** % C – 41.99, % H – 2.06, % N – 12.24; **EA (obtained):** % C 41.86, % H – 1.98, % N – 12.16.

3.8.4.5 Ru(H_2-dcbpy)(5,5`-Cl_2-bpy)$(NCS)_2$ synthesis

The reaction was carried out as described in 3.8.4.3, with addition of 5,5`-$Cl_2$-bpy (18.9 mg, 83.9 μmol) instead of 5,5`-F_2-bpy, yielding a dark red solid (40.4 mg, 70%). **^{1}H NMR (500.12 MHz, d^6-DMSO)** δ (ppm): 7.58 (d, 1H, 2.21 Hz); 7.63 (dd, 1H, 5.91 Hz, 1.73 Hz); 7.94 (d, 5.91 Hz); 8.09 (dd, 1H, 8.75 Hz, 2.21 Hz); 8.30 (dd, 1H, 5.75 Hz, 1.73 Hz); 8.44 (dd, 1H, 8.75 Hz, 2.29 Hz); 8.63 (d, 1H, 8.75 Hz); 8.78 (d, 1H, 8.75 Hz); 8.96 (s, 1H); 9.10 (s, 1H); 9.10 (d, 1H, 2.21 Hz); 9.39 (d, 1H, 5.91 Hz). **ESI-MS$^{(-)}$:** $[Ru(H\text{-}dcbpy)(5,5`\text{-}Cl_2\text{-}bpy)(NCS)_2]^-$ - 684.8. **ATR-FTIR:** $\nu_{C\text{-}N}$ 2102 cm^{-1}, 2109 cm^{-1}. **EA (expected):** % C – 41.99, % H – 2.06, % N – 12.24; **EA (obtained):** % C – 41.85, % H – 1.95, % N – 12.15.

3.8.4.6 Ru(H_2-dcbpy)(4,4`-Br_2-bpy)$(NCS)_2$ synthesis

The reaction was carried out as described in 3.8.4.3, with addition of 4,4`-$Br_2$-bpy (26.4 mg, 83.9 μmol) instead of 5,5`-F_2-bpy, yielding a dark red solid (49.0 mg, 75%). **^{1}H NMR (500.12 MHz, d^6-DMSO)** δ (ppm): 7.40 (d, 1H, 6.23 Hz); 7.46 (dd, 1H, 6.23 Hz, 2.05 Hz); 7.61 (dd, 1H, 5.99 Hz, 1.73 Hz); 7.91 (d, 1H, 5.99 Hz); 8.22 (dd, 1H, 6.07 Hz, 1.89 Hz); 8.27 (dd, 1H, 5.99 Hz, 1.50 Hz); 8.91 (s, 1H); 9.00 (s, 1H); 9.03 (d, 1H, 6.07 Hz); 9.06 (s, 1H); 9.15 (s, 1H); 9.39 (d, 1H, 5.83 Hz). **ESI-**

MS$^{(-)}$: [Ru(H-dcbpy)(4,4`-Br_2-bpy)$(NCS)_2$]$^-$ - 774.7. **ATR-FTIR:** ν_{C-N} 2100 cm^{-1}. **EA (expected):** % C – 37.17, % H – 1.82, % N – 10.84; **EA (obtained):** % C 37.05, % H – 1.85, % N – 10.94.

3.8.4.7 Ru(H_2-dcbpy)(5,5`-Br_2-bpy)$(NCS)_2$ synthesis

The reaction was carried out as described in 3.8.4.3, with addition of 5,5`-$Br_2$-bpy (26.4 mg, 83.9 μmol) instead of 5,5`-F_2-bpy, yielding a dark red solid (52.7 mg, 81%). **^{1}H NMR (500.12 MHz, d^6-DMSO)** δ (ppm): 7.61 (d, 1H, 2.08 Hz); 7.63 (dd, 1H, 5.93 Hz, 1.70 Hz); 7.93 (d, 1H, 5.93 Hz); 8.22 (dd, 1H, 8.70 Hz, 2.08 Hz); 8.32 (dd, 1H, 5.86 Hz, 1.70 Hz); 8.56 (dd, 1H, 8.70 Hz, 2.14 Hz); 8.58 (d, 1H, 8.70 Hz); 8.73 (d, 1H, 8.70 Hz); 8.97 (s, 1H); 9.11 (s, 1H); 9.20 (d, 1H, 2.14 Hz); 9.39 (d, 1H, 9.39 Hz). **ESI-MS$^{(-)}$:** [Ru(H-dcbpy)(5,5`-Br_2-bpy)$(NCS)_2$]$^-$ - 774.7. **ATR-FTIR:** ν_{C-N} 2112 cm^{-1}. **EA (expected):** % C – 37.17, % H – 1.82, % N – 10.84; **EA (obtained):** % C 37.25, % H – 1.89, % N – 10.76.

Chapter 4: The Chalcogen Series

4.1 Introduction

There has been considerable interest in the mechanism of dye regeneration by I^- but there is still limited understanding of this process due to the complex nature of the I^-/I_3^- redox couple (1.3.3.5). The enhanced regeneration kinetics of $Ru(H_2\text{-dcbpy})_2(NCS)_2$ compared to $Ru(H_2\text{-dcbpy})_2(CN)_2$[22] and *in silico* studies on the potential intermediates of dye regeneration[62] have led to postulation of an interaction between the sulfur atom of the $^-$NCS ligand and I^-. Experiments have also shown that substituting two sulfur atoms for oxygen atoms within a dye causes a reduction in dye recombination[83], probably because of a weaker interaction between the dye and I_2. This led to a small increase in the open circuit voltage of the cell. It is therefore somewhat surprising that, despite the considerable volume of research into ruthenium dyes for DSSCs, there have been no studies on the effect of changing the group 16 atom of the chalcogenocyanate ligand on dye regeneration and recombination in DSSCs. Although a number of patents[88,212-214] have been granted which consider the other chalcogenocyanate ligands (namely $^-$NCO and $^-$NCSe), ruthenium dyes containing these ligands have not been synthesised. In fact, since the 1980s there have been few investigations into the effect of the group 16 atom in a chalcogenocyanate ligand on the electronic and spectroscopic properties of transition metal complexes.

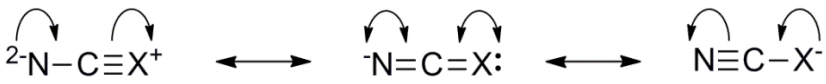

Fig. 4.1: *The possible resonance structures of the $^-$NCX ligand.*

Chalcogenocyanate ligands ($^-$NCX where X = O, S, Se, Te) are σ-donor, π-donor ligands with three possible resonance structures (Fig. 4.1)[119]. They are ambidentate; thus they can act as both terminal and bridging ligands. Although $^-$NCS is the most

commonly used ligand, ¯NCO and ¯NCSe have also been studied as bridging ligands for incorporation into large metal frameworks[215,216] and for use in catalysis[217]. As a terminal ligand, ¯NCO is predominantly found as the N-bound isomer[119]. Whether the ¯NCS and ¯NCSe ligands bind to a metal through the N or the X atom can depend on steric effects because a linear M-N-C bond is formed, whereas the M-X-C bond is bent[218]. However, the ancillary ligands in the complex can also affect the binding mode of ¯NCS. For example the N-bound isomer of the ¯NCS ligand is more thermodynamically stable for complexes with ancillary σ-donor, π-acceptor ligands, such as polypyridyl ligands[219]; thus this is the more stable isomer in ruthenium dyes. Similar electronic effects are not yet known for the ¯NCSe ligand[220,221].

4.2 Theoretical properties of $Ru(H_2\text{-dcbpy})_2(NCX)_2$ dyes

ZZ`	% occupancy of HOMO per atom				Total % occupancy on $Ru(NCX)_2$ or $Ru(CN)_2$ fragment
	Ru	N	C	X	
$(CN)_2$	74.30	1.74	6.25	-	90.3
$(NCO)_2$	51.71	8.31	1.42	6.10	83.4
$(NCS)_2$	24.40	8.03	0.46	24.76	90.9
$(NCSe)_2$	14.25	6.43	0.19	32.56	92.6

Table 4.1: *Calculated percentage occupancy, in vacuo, of the HOMO of $Ru(H_2\text{-dcbpy})_2(Z)$ dyes where Z= $(CN)_2$, $(NCO)_2$, $(NCS)_2$, $(NCSe)_2$,.*

DFT calculations (2.2.4) showed the locations of the HOMO and LUMO to be consistent with what would be expected[222] for each of the three dyes (Figure 4.2). The percentage contributions of the Ru atom and ¯NCX ligand to the HOMO (Table 4.1) were calculated; demonstrating that going down group 16 the contribution of the chalcogen atom to the HOMO increases; resulting in a reduced contribution from the ruthenium metal centre. There is also decreased delocalisation of the HOMO onto the pyridine rings *trans* to the ¯NCX ligands going down group 16 (Fig. 4.2), which causes an increase in the total percentage occupancy of the HOMO on the Ru and ¯NCX parts of the molecule (Table 4.1). Therefore, to promote charge separation within a DSSC, the ¯NCSe ligand would be the preferred ligand.

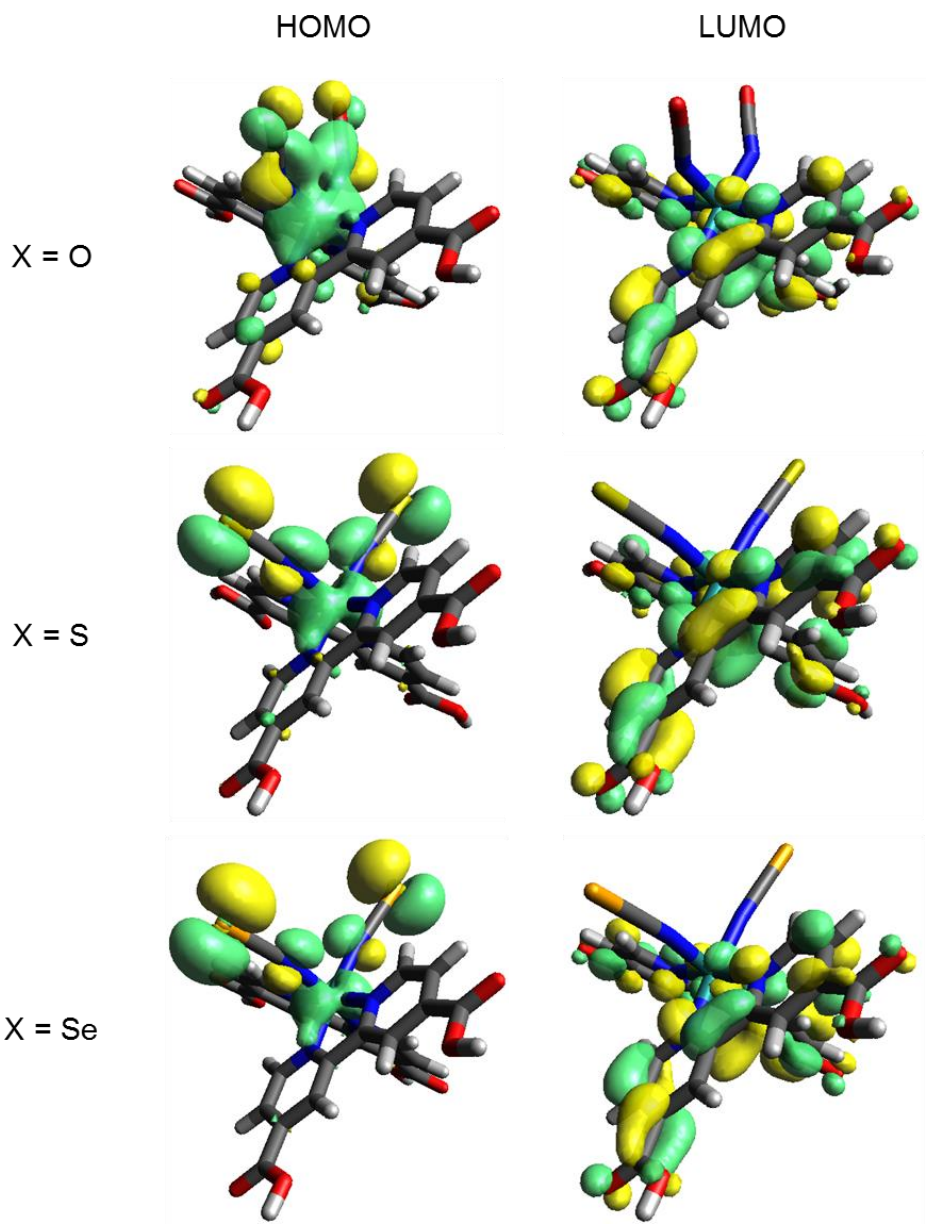

Fig. 4.2: *The distribution of the HOMO and LUMO orbitals of $Ru(H_2\text{-dcbpy})_2(NCX)_2$ where X = O, S, Se in vacuo. Calculations performed with dye solvation by methanol, ethanol, water, DMSO gave similar orbital distributions.*

These effects can be justified by considering the contribution of each of the possible resonance forms of the $^{-}$NCX ligand when X = O, S, Se (Table 4.2). The increased contribution of structure C when X = Se results in increased electron density on the Se atom; whereas the increased contribution of structure A when X = O explains the decrease in electron density on the O atom. The increased σ-donor character of

structure A compared to structures B and C is also likely to explain the increase in electron density on the pyridine rings trans to the ¯NCO ligand in Ru(H_2-dcbpy)$_2$(NCO)$_2$. Despite some of the HOMO of the Ru(H_2-dcbpy)$_2$(NCO)$_2$ dye being delocalised onto the O atom of the ¯NCX ligand, this results in reduced charge separation within this dye compared to Ru(H_2-dcbpy)$_2$(CN)$_2$ (Table 4.1).

Structure	X	O / %	S / %	Se / %
A	$^{2-}N-C\equiv X^{+}$	24	19 (17*)	12
B	$^{-}N=C=X$	1	5 (12*)	0
C	$N\equiv C-X^{-}$	75	76 (71*)	88

Table 4.2: *The percentage contributions of each resonance form of the ¯NCX ligand. Values were calculated by Norbury[119] (and *Jones[223]) using methods developed by Pauling[224] and bond lengths calculated from IR data by Wagner[225].*

ZZ`	Ru-NC or Ru-CN angle / ^{o}				
	In vacuo	In DMSO	In EtOH	In H_2O	In MeOH
$(CN)_2$	174.6	178.4	178.3	178.5	178.4
$(NCO)_2$	146.0	165.1	164.3	165.5	164.7
$(NCS)_2$	172.7	178.9	178.8	178.9	178.9
$(NCSe)_2$	172.2	178.6	178.7	178.3	178.5

Table 4.3: *The Ru-NCX angle for Ru(H_2-dcbpy)$_2$(ZZ`) where Z=Z`= $(CN)_2$, $(NCO)_2$, $(NCS)_2$, $(NCSe)_2$, in vacuo and solvated.*

Comparison of the Ru-NC or Ru-CN angle of the dyes (Table 4.3) showed the Ru-ligand bond to be significantly more bent in Ru(H_2-dcbpy)$_2$(NCO)$_2$ than in the other dyes. This suggests an alternative binding mode for the ¯NCO ligand compared to the ¯NCS and ¯NCSe ligands *in vacuo*, with less π-bonding in the Ru-N bond for the ¯NCO ligand compared to the ¯NCS ligand. This would be consistent with different resonance forms of the ¯NCX ligand binding to ruthenium depending on whether the X atom is O or S (Fig. 4.3). This suggestion is substantiated by the higher energy CN-stretching vibration for the O dye compared to the S dye (Fig. 4.4, 4.3). Solvating each of the dyes by use of a polarisable continuum model (2.2.4) caused an increase in the linearity of the Ru-ligand bond; an effect which was greater for

$Ru(H_2\text{-dcbpy})_2(NCO)_2$ than for the other dyes. There was also some variation in the Ru-ligand angle with different solvents; thus solvation affects the binding mode of the ¯NCX ligand with ruthenium, which could contribute to the solvatochromic effects observed with these types of dyes[34,226].

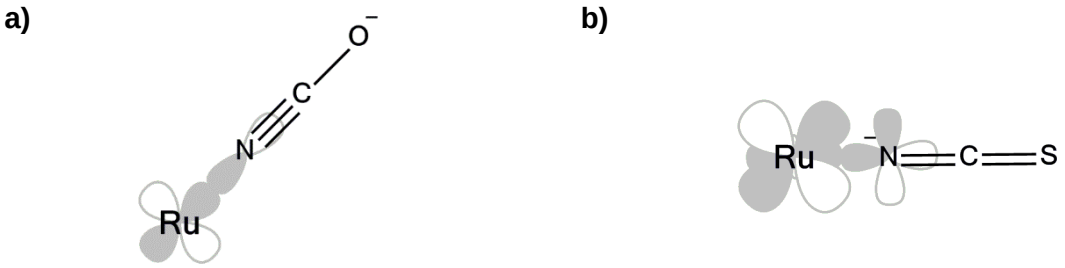

Fig. 4.3: *The possible mechanisms for binding of the ¯NCX ligand to ruthenium* in vacuo *where* ***a)*** *X = O;* ***b)*** *X = S.*

Solvent	ZZ`	% occupancy of HOMO per atom				Total % occupancy on $Ru(NCX)_2$ or $Ru(CN)_2$ fragment
		Ru	N	C	X	
In vacuo	$(CN)_2$	74.30	6.25	1.74	-	90.3
	$(NCO)_2$	51.71	8.31	1.42	6.10	83.4
	$(NCS)_2$	24.40	8.03	0.46	24.76	90.9
	$(NCSe)_2$	14.25	6.43	0.19	32.56	92.6
DMSO	$(CN)_2$	79.96	4.86	0.57	-	90.8
	$(NCO)_2$	64.87	5.48	1.41	4.72	88.0
	$(NCS)_2$	51.38	4.47	1.20	14.68	92.1
	$(NCSe)_2$	38.21	4.28	0.74	22.96	94.2
Ethanol	$(CN)_2$	79.82	4.90	0.60	-	90.8
	$(NCO)_2$	64.40	5.59	1.42	4.78	88.0
	$(NCS)_2$	50.21	4.63	1.17	15.16	92.1
	$(NCSe)_2$	36.97	4.31	0.78	23.35	93.9
Water	$(CN)_2$	80.02	4.84	0.56	-	90.8
	$(NCO)_2$	65.09	5.42	1.42	4.69	88.2
	$(NCS)_2$	51.93	4.39	1.22	14.45	92.1
	$(NCSe)_2$	38.91	4.20	0.77	22.64	94.1
Methanol	$(CN)_2$	79.89	4.88	0.59	-	90.8
	$(NCO)_2$	64.64	5.53	1.42	4.75	88.0
	$(NCS)_2$	50.80	4.55	1.19	14.92	92.1
	$(NCSe)_2$	37.51	4.34	0.72	23.29	94.2

Table 4.4: *Percentage occupancy of the HOMO of $Ru(H_2\text{-dcbpy})_2(ZZ`)$ where Z=Z`= $(CN)_2$, $(NCO)_2$, $(NCS)_2$, $(NCSe)_2$, in vacuo and solvated.*

This change in binding is likely to be the cause of the considerable change in the distribution of the HOMO of $Ru(H_2\text{-dcbpy})_2(NCO)_2$ when the dye is solvated compared to when the dye is *in vacuo* (Table 4.4). However, regardless of the conditions of the calculation, the trends in the dye characteristics remain the same; thus the calculations give a good representation of the change in dye properties across the series of dyes. The change in the distribution of the HOMO was also similar when calculations were performed on the fully deprotonated dyes (Table 4.5). Therefore, irrespective of the conditions, the chalcogen atom causes charge separation within the dye to increase going down group 16, due to an increase in the localisation of the HOMO on the chalcogen atom.

ZZ`	% occupancy of HOMO per atom				Total % occupancy on $Ru(NCX)_2$ or $Ru(CN)_2$ fragment
	Ru	N	C	X	
$(CN)_2$	80.91	4.60	0.35	-	90.8
$(NCO)_2$	71.61	3.83	1.42	3.70	89.5
$(NCS)_2$	64.10	2.68	1.62	9.42	91.5
$(NCSe)_2$	55.79	2.68	1.31	14.57	92.9

Table 4.5: *Calculated percentage occupancy, in methanol, of the HOMO of* $[Ru(dcbpy)_2(ZZ`)]^{4-}$ *dyes where Z=Z`=* $(CN)_2$, $(NCO)_2$, $(NCS)_2$, $(NCSe)_2$.

4.3 Dye characterisation

			δ / ppm					
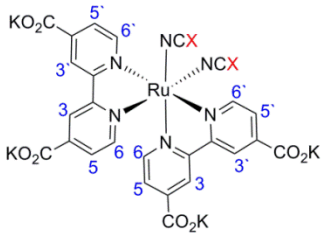	X	Solvent	6	6`	5	5`	3	3`
	O	CD_3OD	7.64	9.57	7.49	8.15	8.81	8.98
		D_2O	7.76	9.53	7.40	8.10	8.69	8.86
		d^6-DMSO	7.38	9.31	7.34	8.00	8.48	8.64
	S	CD_3OD	7.63	9.49	7.55	8.21	8.84	9.00
		D_2O	7.74	9.47	7.44	8.13	8.70	8.86
		d^6-DMSO	7.42	9.16	7.45	8.07	8.53	8.69

Table 4.6: *Assignment of* ^1H *NMR shifts for* $K_4[Ru(dcbpy)_2(NCX)_2]$ *where X = O, S.*

A dye containing the ¯NCSe ligand was not stable enough to be synthesised (3.2.4). However, the syntheses of $K_4[Ru(dcbpy)_2(NCO)_2]$ and $K_4[Ru(dcbpy)_2(NCS)_2]$

(herein referred to as the O dye and S dye respectively) were successfully achieved (3.2.5), and the *cis* conformation of the complexes was confirmed by the presence of 6 peaks in the ^{1}H NMR spectrum. The peaks have been assigned (Table 4.6) according to literature precedent[111] (2.1.1.2). There were 13 peaks in the ^{13}C NMR for the S dye but the peak representing the carbon of the ^{-}NCO ligand was only apparent in the ^{13}C NMR of the O dye in MeOD. The intensity of this peak was very small, perhaps explaining why the peak representing the ^{-}NCO carbon was not observed in D_2O. ESI-MS$^{(-)}$ showed the expected molecular ion peaks (3.8.4.1, 3.8.4.2) and the presence of N-bound ^{-}NCO and ^{-}NCS ligands was confirmed by IR spectroscopy[119,177] (Fig. 4.4, 2.1.3.1). The elemental analysis results showed good agreement with expected results (3.8.4.1, 3.8.4.2).

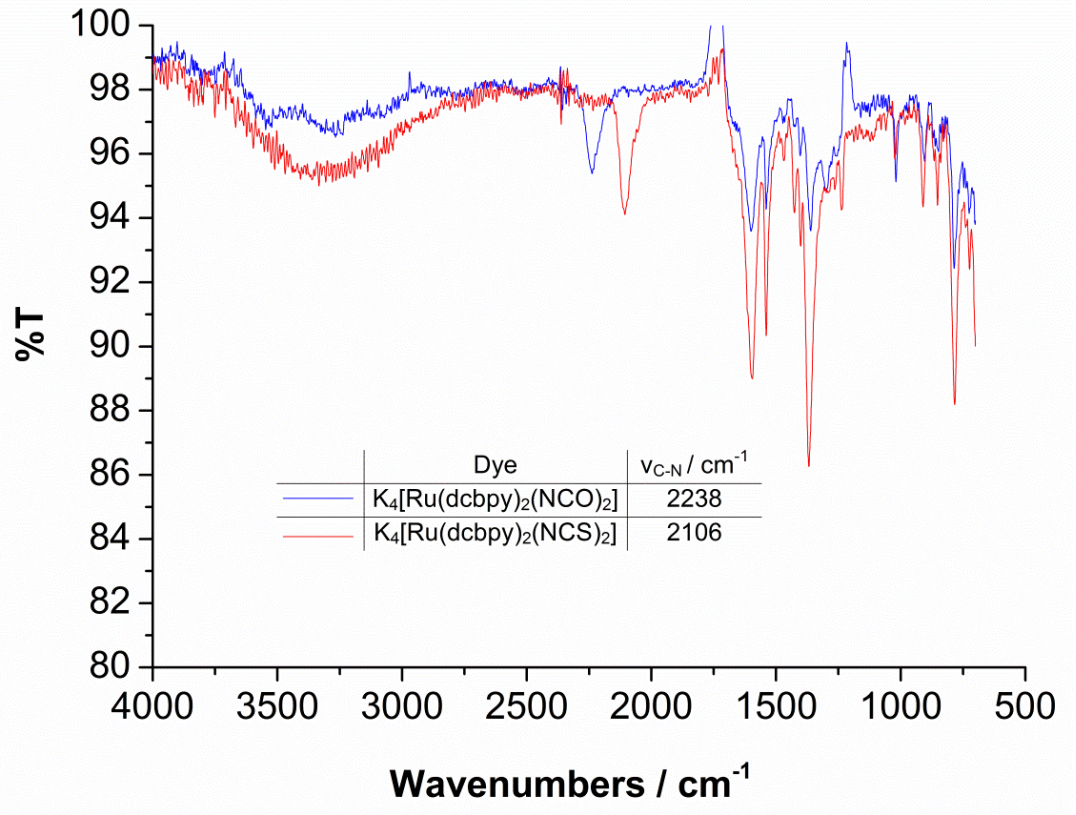

Fig. 4.4: *$\nu_{C\text{-}N}$ stretches for $K_4[Ru(dcbpy)_2(NCX)_2]$ where X = O, S.*

4.4 Dye stability

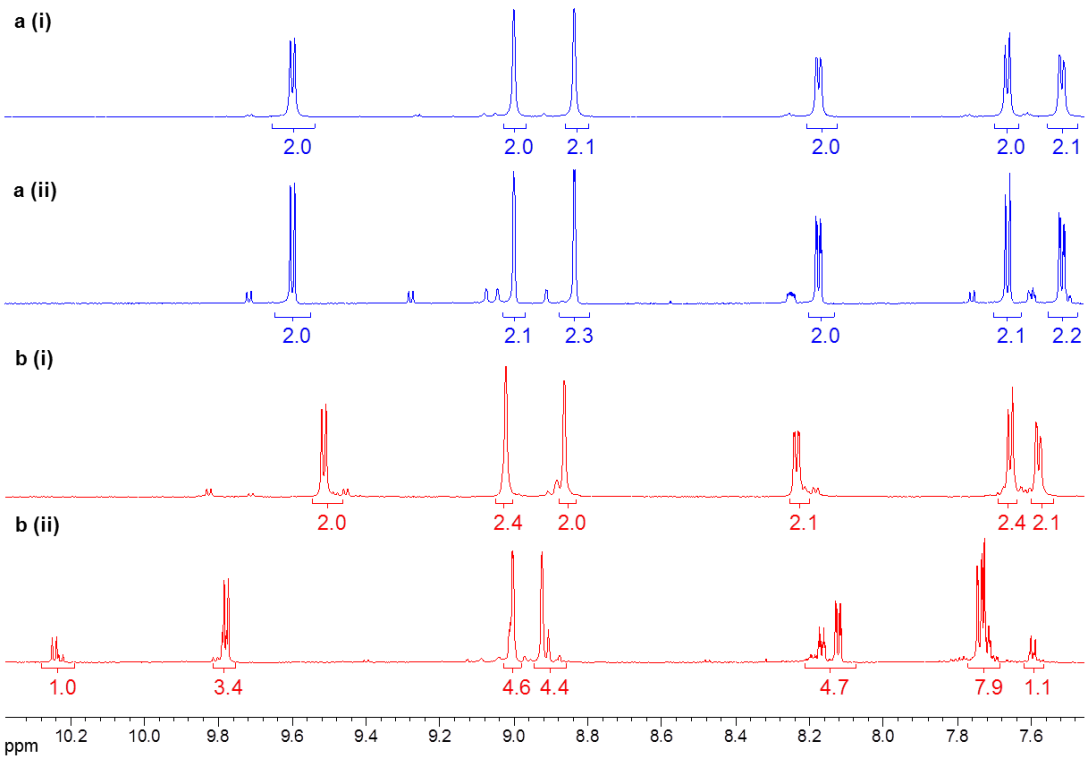

Fig. 4.5: *^{1}H NMR of the **a)** O dye; **b)** S dye in MeOD after **(i)** 0 days; **(ii)** 3 months. The solutions were exposed to air and low level lighting.*

Ruthenium isothiocyanate dyes are known to be unstable in solution when exposed to light[159]. This was confirmed when observing the change in ^{1}H NMR of the S dye in CD_3OD over time (Fig. 4.5b). Yet, by ^{1}H NMR and ^{13}C NMR, it appeared that the O dye was stable in CD_3OD (Fig. 4.5a) for more than three months. In D_2O the O dye did break down (Fig. 4.6), which was likely to be due to hydrolysis of dye. This was also the probable cause of the growth of the minor impurity peaks in CD_3OD. Therefore, in the absence of water, the O dye has a higher stability in solution than the S dye. The poor stability in solution of the dye containing the $^{-}$NCSe ligand prevented the synthesis of $K_4[Ru(dcbpy)_2(NCSe)_2]$ (3.2.4). Therefore, the nature of the X atom has a surprising impact on the stability of the ruthenium dye in solution; with the stability decreasing going down group 16.

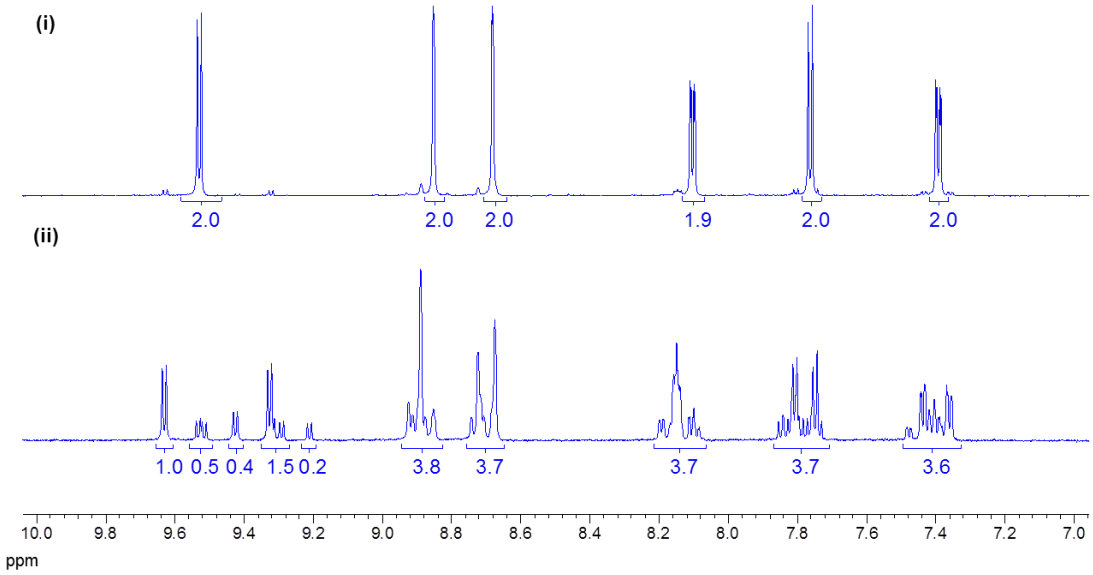

Fig. 4.6: *^{1}H NMR of the O dye in D_2O after **(i)** 0 days; **(ii)** 3 months. The solutions were exposed to air and low level lighting.*

4.5 Dye properties

4.5.1 Light absorption properties

4.5.1.1 Excitation spectroscopy

The effect of changing the X atom on light absorption by the dyes was immediately apparent as the solid dyes are dark purple and dark red when X = O and S respectively. This shift in dye absorption was verified by UV/vis spectroscopy in dry MeOH (Fig. 4.7); as you substitute S for O there is a red shift of 27 nm (970 cm^{-1}) in the lowest energy MLCT transition, and 16 nm (1080 cm^{-1}) in the higher energy MLCT transition. The molar absorption co-efficients for the MLCT transitions didn't change significantly with the X atom, and they were consistent with literature values for these types of ruthenium dyes[18,34]. Considering the solar spectrum (1.3.3.1), this change in light absorption is likely to result in enhanced light harvesting by the O dye compared to the S dye.

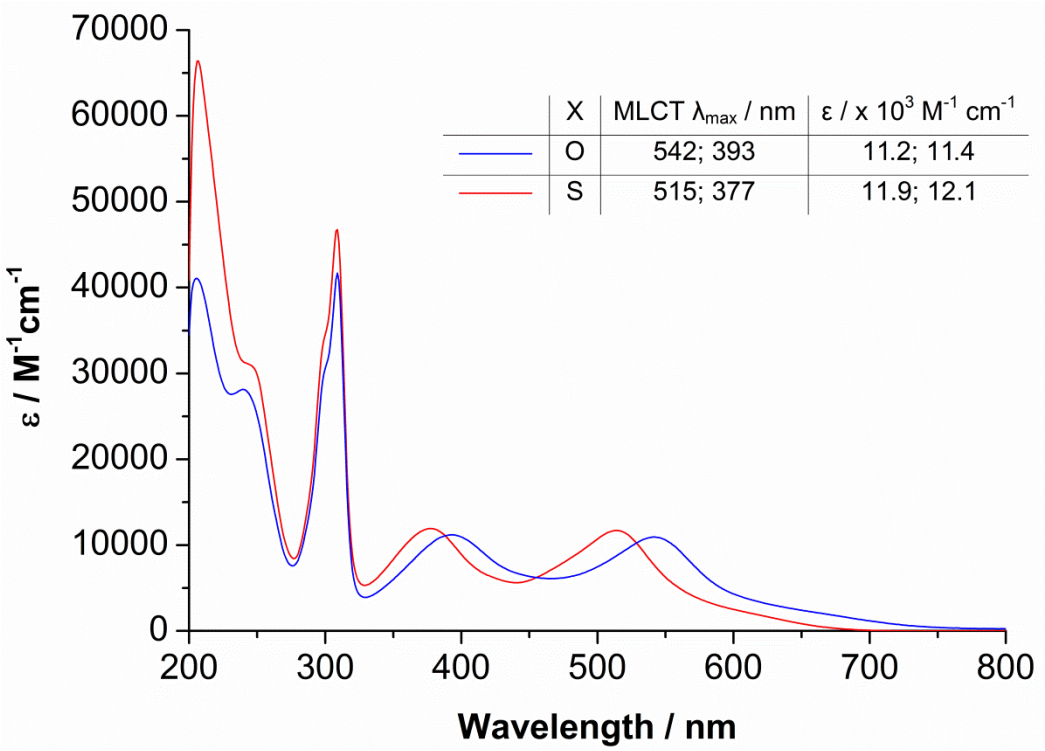

Fig. 4.7: *UV/vis spectroscopy of $K_4[Ru(dcbpy)_2(NCX)_2]$, where X O, S, in dry MeOH.*

4.5.1.2 Solvatochromic effects

	Solvent properties[227]		MLCT λ_{max} / nm		
Solvent	AN	ε	$[Ru(dcbpy)_2(NCO)_2]^{4-}$	$[Ru(dcbpy)_2(NCS)_2]^{4-}$	$*[Ru(dcbpy)_2(CN)_2]^{4-}$
DMSO	19.3	46.7	553; 397	514; 374	492; 358
EtOH	37.1	24.3	546; 393	519; 379	487; 351
MeOH	41.3	32.6	542; 393	515; 377	470; 350
H_2O	54.8	78.4	527; 388	500; 370	452; 340

Table 4.7: *The solvatochromism of $[Ru(dcbpy)_2(ZZ`)]^{4-}$ dyes where ZZ` = $(CN)_2$, $(NCO)_2$, $(NCS)_2$. *Measurements performed qualitatively by dissolving $Ru(H_2$-$dcbpy)_2(CN)_2$ (purchased from Solaronix) in 0.1 M KO^tBu / solvent. AN = acceptor number; ε = dielectric constant of the solvent.*

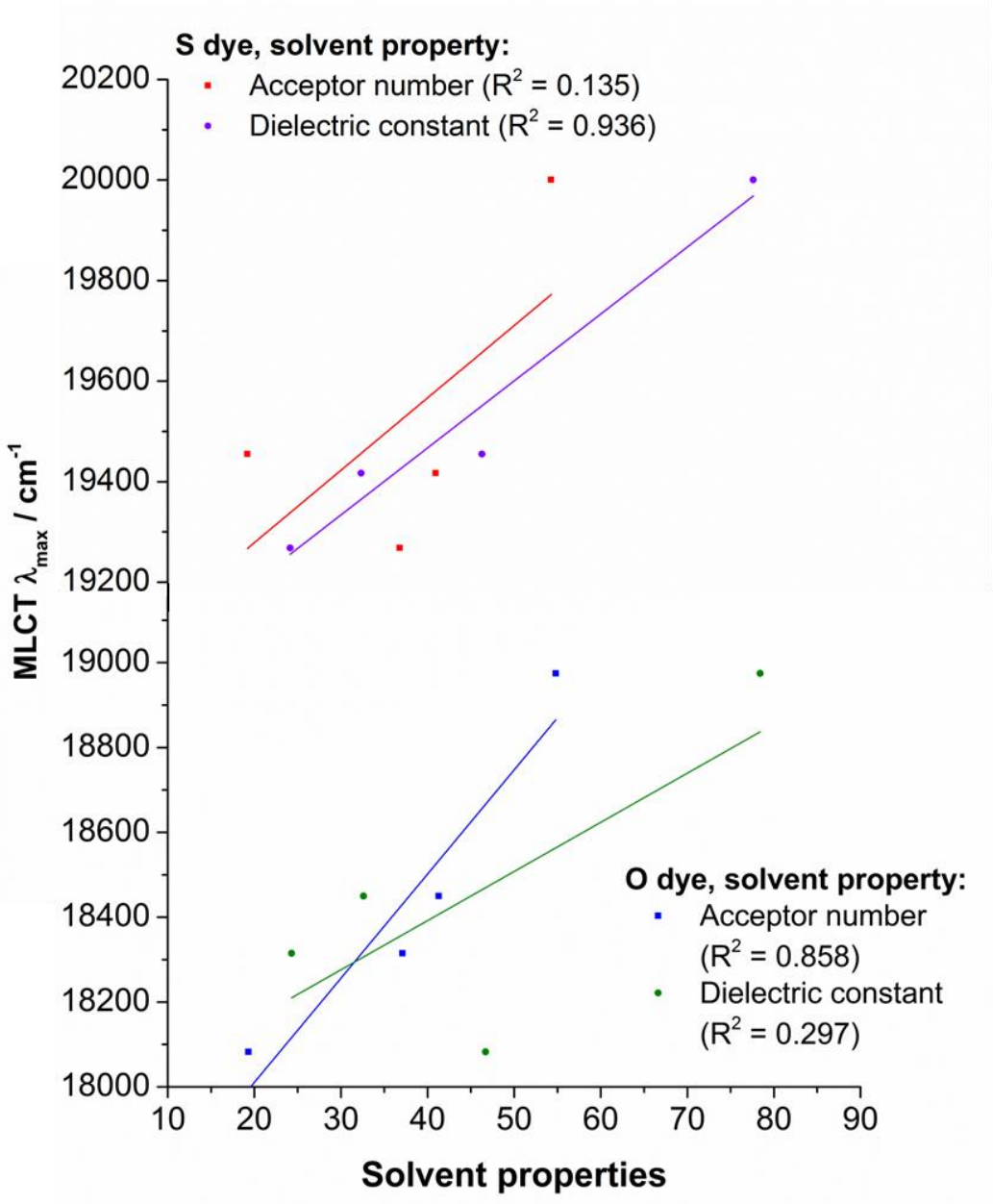

Fig 4.8: *The effect of the solvent acceptor number and solvent dielectric constant on the lowest energy MLCT transition of the O and S dyes.*

The solvatochromism of ruthenium polypyridyl isothiocyanate dyes has been previously reported[32,223], thus it is not surprising that the O and S dyes displayed solvatochromic effects (Table 4.7). For the S dye, a positive correlation between the lowest energy MLCT transition and the dielectric constant of the solvent[227] was observed (R^2 = 0.936, Fig. 4.8). A similar correlation could not be assigned to the O

dye as the R^2 value was 0.297. In fact, the O dye showed a stronger correlation (R^2 = 0.858) with the solvent acceptor number[227] (Figure 4.8); a correlation which was not observed for the S dye (R^2 = 0.135). It is interesting that a correlation with solvent acceptor number (R^2 = 0.757) but not the solvent dielectric constant (R^2 = 0.299) was also observed for $K_4[Ru(dcbpy)_2(CN)_2]$. The blue shift in the λ_{max} of both of the MLCT peaks of the O dye and $[Ru(dcbpy)(CN)_2]^{4-}$ with increasing solvent acceptor number (Table 4.7) suggests stabilisation of the HOMO by acceptance of electron density by the solvent.

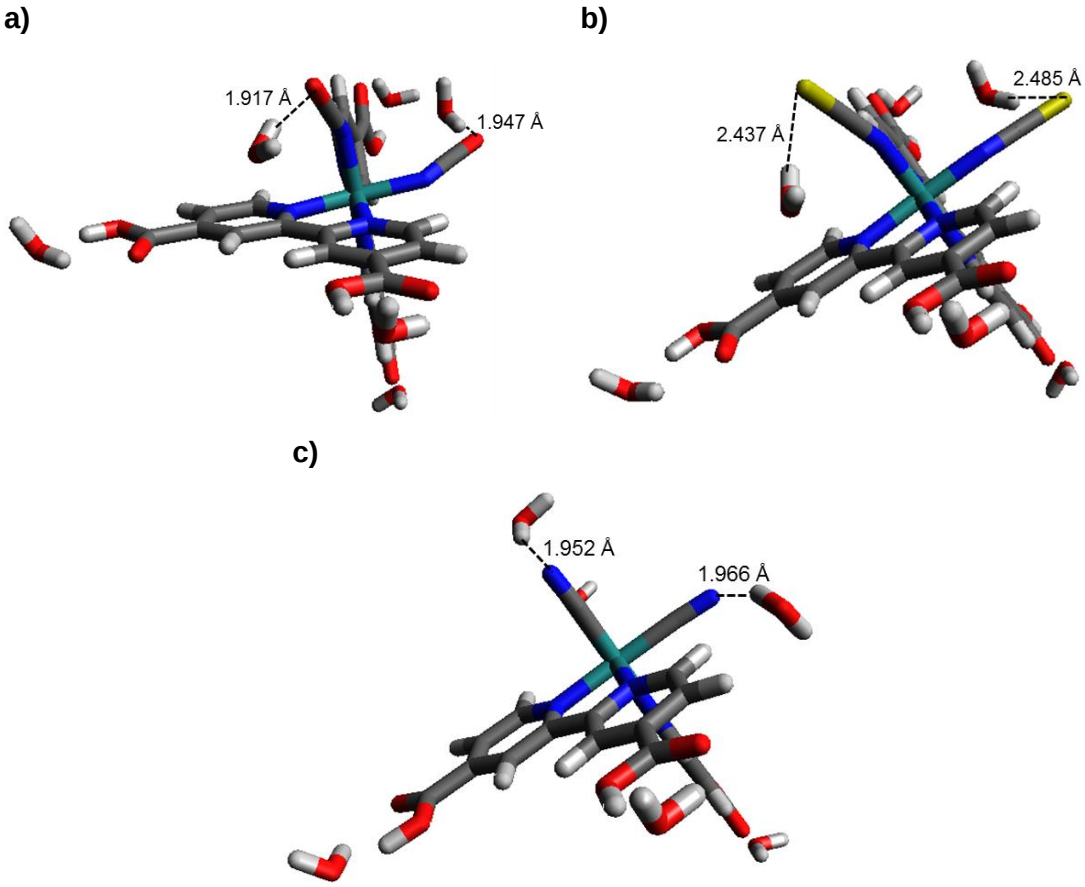

Fig 4.9: *The interaction between the ZZ` ligand and water for $K_4[Ru(dcbpy)_2(ZZ`)]$ dyes where* ***a)*** *ZZ` = $(NCO)_2$;* ***b)*** *ZZ` = $(NCS)_2$;* ***c)*** *ZZ` = $(CN)_2$.*

To probe this interaction, computational calculations were performed on the O, S and $[Ru(dcbpy)_2(CN)_2]^{4-}$ dyes with explicit solvation by six water molecules (2.2.4.3). Geometry optimisation showed that the strength of the interactions between the water

molecules and the carboxylic acid groups were little affected by the nature of the ZZ` ligand. However, significantly stronger ZZ` - water interactions were formed when ZZ` = $(NCO)_2$, $(CN)_2$ than when ZZ` = $(NCS)_2$ (Fig. 4.9). Considering the definitions for hydrogen bonds[228], when ZZ` = $(NCO)_2$, $(CN)_2$, the interaction between the HOMO and water is so strong that the bond would be defined as covalent. However, if long range solvation were modelled the interactions would be likely to be weaker. Conversely, when ZZ` = $(NCS)_2$, a partially covalent, partially electrostatic hydrogen bond between the S atom and water forms. This solvation effect is likely to be the cause of the change in the solvatochromic trends when ¯NCS is substituted by ¯NCO, and it could also explain the improved photo stability of the O dye.

Although the interaction between the dye and the water molecules did not cause the HOMO of the dye to extend onto the water molecules, it did reduce the proportion of the HOMO on the ruthenium centre and increase the localisation of the HOMO on the terminal atom (Table 4.8). Unexpectedly, this effect was particularly pronounced for $Ru(H_2\text{-dcbpy})_2(NCS)_2$ despite the weaker bonding between the HOMO of this dye and the water molecules.

ZZ`	Solvent model	% occupancy of HOMO per atom				Total % occupancy on $Ru(NCX)_2$ or $Ru(CN)_2$ fragment
		Ru	N	C	X	
$(CN)_2$	PCM	80.02	4.84	0.56	-	90.8
	Explicit	77.05	5.57	1.07	-	90.3
$(NCO)_2$	PCM	65.09	5.42	1.42	4.69	88.2
	Explicit	59.90	6.50	1.59	5.21	86.5
$(NCS)_2$	PCM	51.93	4.39	1.22	14.45	92.1
	Explicit	33.23	8.76; 4.95	0.69; 0.78	28.22; 15.17	91.8

Table 4.8: *The distribution of the HOMO of $Ru(H_2\text{-dcbpy})_2(ZZ`)$ dyes, where ZZ` = $(CN)_2$, $(NCO)_2$, $(NCS)_2$, with explicit solvation, and solvation utilising the polarisable continuum model (PCM).*

4.5.1.3 TD-DFT studies

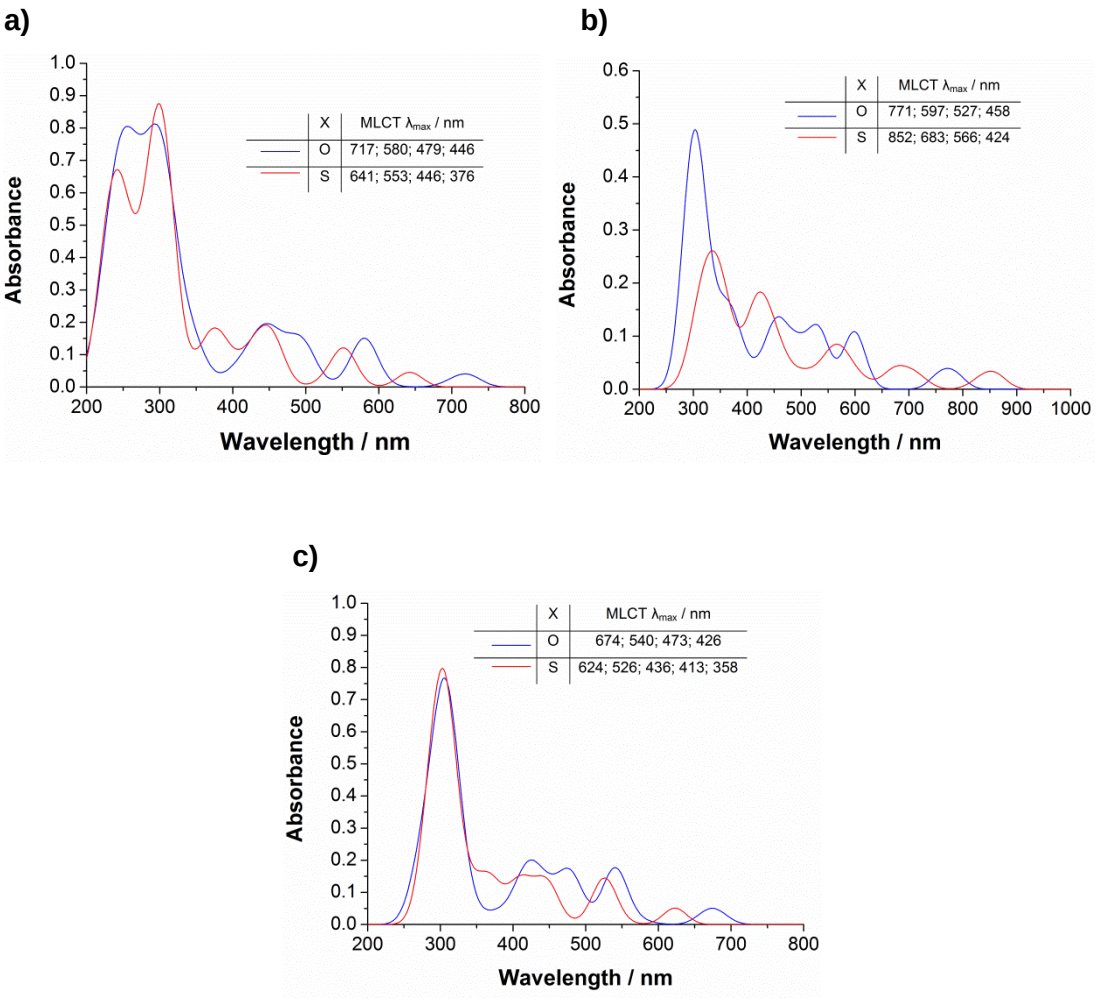

Fig 4.10: *TD-DFT calculations on $Ru(H_2\text{-dcbpy})_2(NCX)_2$ where X = O, S. The dye was solvated with water using* ***a)*** *the polarisable continuum model;* ***b)*** *explicit solvation with six water molecules;* ***c)*** *application of the polarisable continuum model to the TD-DFT calculation on the explicitly solvated dye.*

Due to the differing interactions of the O dye and the S dye with the solvent, determination of the optimal solvent model for TD-DFT calculations was required. As the introduction of charge can complicate TD-DFT calculations, a variety of solvent conditions were tested on the fully protonated O and S dyes. Geometry optimisation, and subsequent TD-DFT studies were performed on the dyes with the addition of a polarisable continuum of water (Fig. 4.10a), and with explicit solvation

by six water molecules (Fig. 4.10b). Geometry optimisation of the explicitly solvated molecule with addition of a polarisable continuum was not achieved; most likely because of the complexity of the solvent – dye interactions. However, addition of a polarisable continuum to the TD-DFT calculation on the explicitly solvated dye was performed (Fig. 4.10c).

Irrespective of the solvent model employed, direct transitions from the $^{-}$NCX ligands to the H_2-dcbpy ligands (LLCT transitions) contributed more to the absorption spectrum for $Ru(H_2\text{-dcbpy})_2(NCS)_2$ than $Ru(H_2\text{-dcbpy})_2(NCO)_2$ (Appendix A3.1, A3.2). This reflects the higher localisation of electron density on the sulfur atom of $Ru(H_2\text{-dcbpy})_2(NCS)_2$ compared to the oxygen atom of $Ru(H_2\text{-dcbpy})_2(NCO)_2$, or the higher contribution of the ruthenium metal to electronic excitations for $Ru(H_2\text{-dcbpy})_2(NCO)_2$. Using the polarisable continuum model for calculations on the dyes both with and without explicit solvation showed the expected red shift in the calculated absorption spectrum when the $^{-}$NCS ligands are exchanged with $^{-}$NCO (Fig 4.10a,c). However, the calculations on the explicitly solvated dye without a polarisable continuum showed the MLCT transitions for $Ru(H_2\text{-dcbpy})_2(NCO)_2$ to be blue shifted compared to $Ru(H_2\text{-dcbpy})_2(NCS)_2$ at wavelengths longer than 500 nm (Fig. 4.10b). Above 500 nm, LLCT transitions have a significant contribution to the absorption spectrum for $Ru(H_2\text{-dcbpy})_2(NCS)_2$ (Appendix A3.2, Table A3.2.4). A similar contribution was only observed for $Ru(H_2\text{-dcbpy})_2(NCO)_2$ at wavelengths shorter than 500nm (Appendix A3.1, Table A3.1.4). Explicit solvation of the dye had a larger effect on the distribution of the occupied frontier orbitals of $Ru(H_2\text{-dcbpy})_2(NCS)_2$ than $Ru(H_2\text{-dcbpy})_2(NCO)_2$ (Appendix A3.1, A3.2; Tables A3.1.3, A3.2.3), despite the weaker X – H_2O interactions. That this caused a considerable red shift in the absorption spectrum for $Ru(H_2\text{-dcbpy})(NCS)_2$, which was not replicated experimentally, suggests that this solvent model is inappropriate for this dye.

The addition of a polarisable continuum to the TD-DFT calculation on the explicitly solvated dyes caused LLCT transitions to be less prevalent for both dyes (Appendix A3.1, A3.2; Tables A3.1.6, A 3.2.6). Thus the polarisable continuum diluted the effect

of explicit solvation, causing the absorption spectrum of $Ru(H_2\text{-dcbpy})_2(NCS)_2$ to be blue shifted by 228 nm, 4290 cm^{-1} (Fig. 4.10b,c). The spectrum for $Ru(H_2\text{-dcbpy})_2(NCO)_2$ only shifted by 97 nm, 1870 cm^{-1}; thus the polarisable continuum had a much larger effect on $Ru(H_2\text{-dcbpy})_2(NCS)_2$ than $Ru(H_2\text{-dcbpy})_2(NCO)_2$. Without explicit solvation, both spectra were red-shifted (Fig. 4.10a,c) suggesting that the hydrogen bonding interaction between the dye molecules and the solvent causes an increase in the energies of both the MLCT and LLCT transitions.

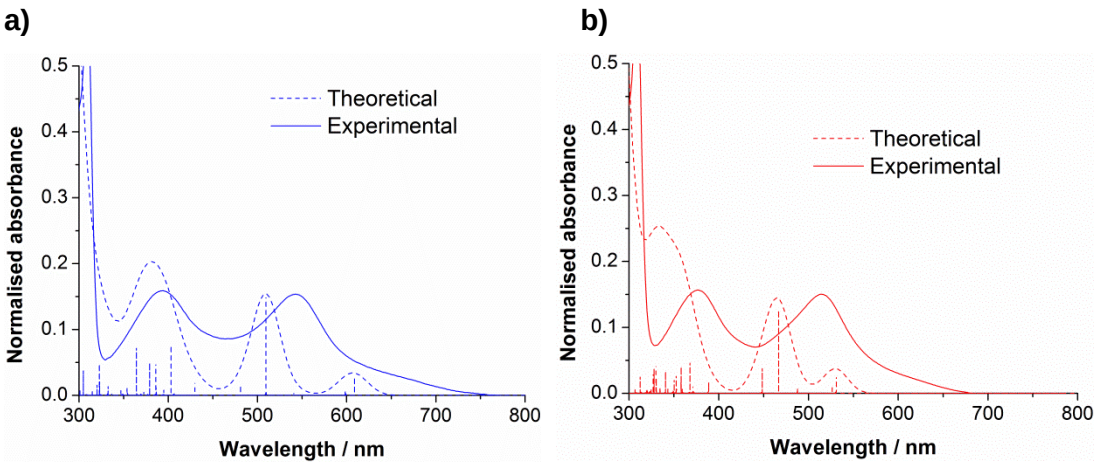

Fig 4.11: *Experimental versus theoretical UV/vis spectra of* $[Ru(dcbpy)_2(NCX)_2]^{4-}$ *where* ***a)*** *X = O;* ***b)*** *X = S.* In silico, *the dye was solvated with methanol using the polarisable continuum model.*

Experimentally, for the fully deprotonated dyes, a red shift of 1030 cm^{-1} was observed in water when the $^-$NCS ligands were substituted by $^-$NCO. *In silico*, a shift of 842 cm^{-1} was calculated when solely the polarisable continuum model was used; but using the polarisable continuum model on the explicitly solvated dye a shift of 492 cm^{-1} was calculated. As solvent molecules were localised around the carboxylic acid groups, it is possible that performing calculations on the fully protonated dye could have affected these results. However, you would expect this effect to be the same for both dyes, suggesting that, of the three models investigated, the polarisable continuum model on the unsolvated dye is the most appropriate model for these dyes.

TD-DFT calculations were therefore performed on the deprotonated dyes using the polarisable continuum model to model the solvent. Although the energies of the transitions were imperfectly calculated (Fig. 4.11), the shift in the calculated absorption spectrum due to the substitution of the chalogen atom replicated the experimental shift (Table 4.9). Analysis of the transitions (Appendix A3.3, A3.4; Tables A3.3.2, A3.4.2) showed a larger contribution of d-d transitions at longer wavelengths for the O dye compared to the S dye. The contribution of the ruthenium centre was also significantly higher for all of the MLCT transitions for the O dye compared to the S dye (Appendix A3.3, A3.4; Tables A3.3.1, A3.4.1). It is possible that the higher contribution of the metal centre, or lower contribution of the $^{-}$NCX ligands, to the electronic transitions calculated resulted in a red shift in the absorption spectrum for the O dye compared to the S dye. This could be the cause of the red-shift observed experimentally.

	MLCT λ_{max} / nm	
X	TD-DFT	Experimental
O	607; 510; 383	542; 393
S	530; 464; 333	515; 377

Table 4.9: *The energies of the experimental and calculated MLCT transitions for $K_4[Ru(dcbpy)_2(NCX)_2]$ dyes, where X = O, S.*

For both dyes, this model does not perfectly reproduce the UV/vis characteristics measured experimentally (Table 4.10, Fig. 4.11). Nor could accurate modelling of the solvatochromic effects observed for the O dye be achieved, despite the fact that these computational methods have successfully modelled solvatochromism[222] and pH dependent absorption shifts[132] of the N3 dye. This is probably because the polarisable continuum model models the solvent with respect to its dielectric constant (2.2.4.2), and there is no correlation between the solvatochromism of the O dye and the dielectric constant of the solvent (4.5.1.2). TD-DFT calculations on an explicitly solvated structure which has been geometry optimised with a polarisable continuum model could produce more accurate results. Further exploration of the number of solvent molecules used for explicit solvation, or the location of the solvent molecules

could also enable a more appropriate model to be developed for these dyes. However, it is possible that different solvent models would need to be used for the two dyes *in silico* to replicate the different interactions of the dyes with solvent observed experimentally.

4.5.2 Luminescence spectroscopy

Emission of the S dye was observed at room temperature (Fig. 4.12a) as previously reported[34], and was attributed to phosphorescence due to the pseudo-Stokes shift (5,490 cm^{-1}). Phosphorescence of the S dye was only observed from excitation to the lowest energy MLCT excited state, no luminescence from the higher energy MLCT transitions was observed. Freezing the sample (Fig. 4.12b) resulted in a small reduction in the pseudo-Stoke's shift (5,150 cm^{-1}), but the luminescence properties observed were very similar to those seen at room temperature.

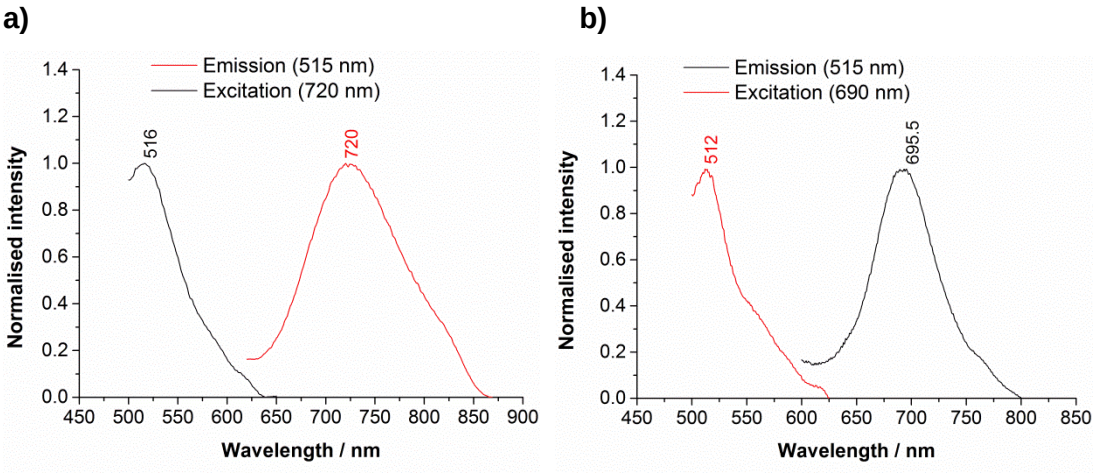

Fig 4.12: *Luminescence of $K_4[Ru(dcbpy)_2(NCS)_2]$ in N_2-purged, dry methanol. The spectra were recorded* ***a)*** *at room temperature;* ***b)*** *frozen.*

However, even frozen, no luminescence was observed for the O dye suggesting that there is a marked increase in the rate of non-radiative decay of the excited state through substitution of S for O. It is the metal centered d-d excited state of ruthenium polypyridyl complexes from which rapid non-radiative decay occurs[40] (2.2.2.2). The

absence of luminescence of the O dye thus suggests that the energy of the ^{3}d-d excited state is lower for the O dye than the S dye, thus allowing decay via the ^{3}d-d state to occur. This is supported by the lower energy of the d-d transitions calculated by TD-DFT for the O dye compared to the S dye (Appendix A3.3, A3.4). As the energy of the ^{3}d-d excited state provides an indication of the energy of the e_g orbitals of the ground state complex, this suggests that the e_g orbitals decrease in energy as you substitute S for O.

The change in e_g energy can be attributed to the change in crystal field splitting of the ligands. Considering the σ-symmetry of the e_g orbitals, this analysis suggests that by substituting S for O, the $^-$NCX ligand becomes a weaker σ-donor causing destabilisation of the e_g orbitals. This is consistent with the calculated electronegativities of the two ligands (3.05, 2.90 for $^-$NCO, $^-$NCS respectively[229]).

4.5.3 Electrochemistry

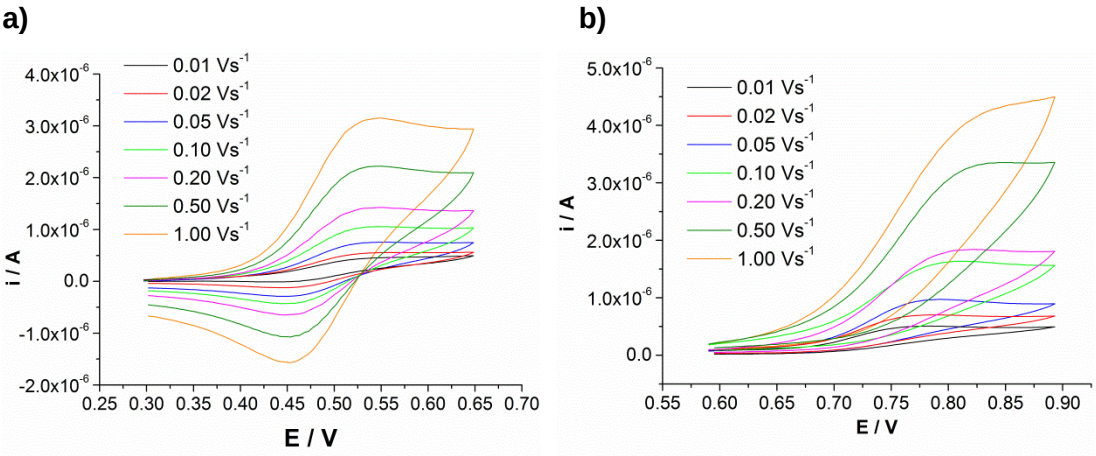

Fig. 4.13: *Cyclic voltammetry of $K_4[Ru(dcbpy)_2(NCX)_2]$ where* ***a)*** *X = O;* ***b)*** *X = S. Measurements recorded in 0.3M $TBABF_4$ / methanol vs. Ag/AgCl.*

Due to the low solubilities of the O and S dyes in most organic solvents, the implementation of electrochemical studies was limited to the use of methanol as a solvent. As methanol itself is reduced at negative potentials, only the oxidation

potential of the dyes could be determined. The oxidation of the S dye was chemically irreversible (Fig. 4.13b); a feature which has been attributed to the elimination of sulfur forming the ⁻CN analogue[111]. However, the oxidation of the O dye was proved to be fully chemically and electrochemically reversible (Fig. 4.13a). DPV studies on the ⁻CN analogue also suggested that the oxidation of this dye was electrochemically reversible, although this was difficult to confirm as the peak appeared on the edge of the solvent window for methanol. Thus, as well as being more photo stable, the O dye is more stable to electrochemical oxidation than the S dye in solution.

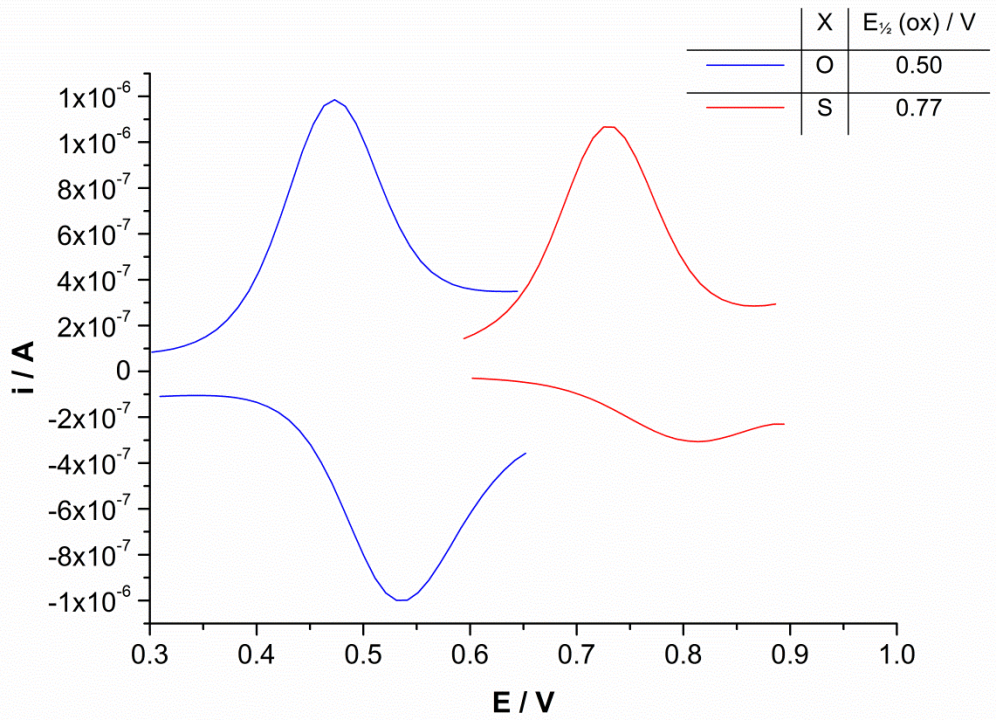

Fig. 4.14: *Differential pulse voltammetry of $K_4[Ru(dcbpy)_2(NCX)_2]$ where X = O, S. Measurements recorded in 0.3M $TBABF_4$ / methanol vs. Ag/AgCl.*

As the difference in the voltage of the oxidation and reduction peak was the same for the O dye and Fc/Fc^+ by cyclic voltammetry, the oxidation of the O dye was confirmed as a one-electron process. Due to its electrochemical irreversibility, a similar comparison could not be made for the S dye. However, the intensity of the differential pulse scan (Fig. 4.14) is relatively similar to the O dye suggesting that the oxidation of the S dye is also a one electron process. The oxidation potential of the

dye decreases as the S atoms are substituted by O (Fig. 4.14). As the oxidation potential is indicative of the HOMO energy level of the dye, the HOMO is therefore destabilised as the S atoms are substituted for O. This is consistent with the observation of a lower energy MLCT transition for the O dye than the S dye in the UV/vis spectrum, suggesting that the change in UV/vis spectrum is due to a change in the HOMO energy level of the dye.

Structure	X / %	O	S
A	$^{2-}N-C\equiv X^{+}$	24	19 (17*)
B	$^{-}N=C=X$	1	5 (12*)
C	$N\equiv C-X^{-}$	75	76 (71*)

Table 4.10: *The percentage contributions of each resonance form of the $^{-}$NCX ligand. Values were calculated by Norbury[119] (and *Jones[223]) using methods developed by Pauling[224] and bond lengths calculated from IR data by Wagner[225].*

The change in the energy of the t_{2g} orbitals (the HOMO) is consistent with the increase in the crystal field splitting energy when O is exchanged with S in other metal-NCX complexes[119,177]. The π-symmetry of the t_{2g} orbitals implies that this effect is due to a change in the π-donor strength of the ligand, which could be justified by considering the different resonance forms of the $^{-}$NCX ligand (Table 4.10). For structure A, the nitrogen atom only contains a single bond to the neighbouring carbon atom; thus the p-orbitals will be very readily available for π-bonding with the metal centre. Therefore, an increase in π-donation from the $^{-}$NCO ligand, causing a destabilisation of the t_{2g} orbitals, is consistent with the higher contribution of structure A when X = O. This implication is not supported by the IR data (4.3), nor is it consistent with the ligand binding modes implied by the TD-DFT calculations (4.2). However, these measurements were performed on the solid state dyes and *in vacuo* respectively, suggesting that the mode of ligand binding changes significantly in solution. This is entirely consistent with the changes observed when the O dye was solvated *in silico* (4.2).

4.6 Solar cell studies

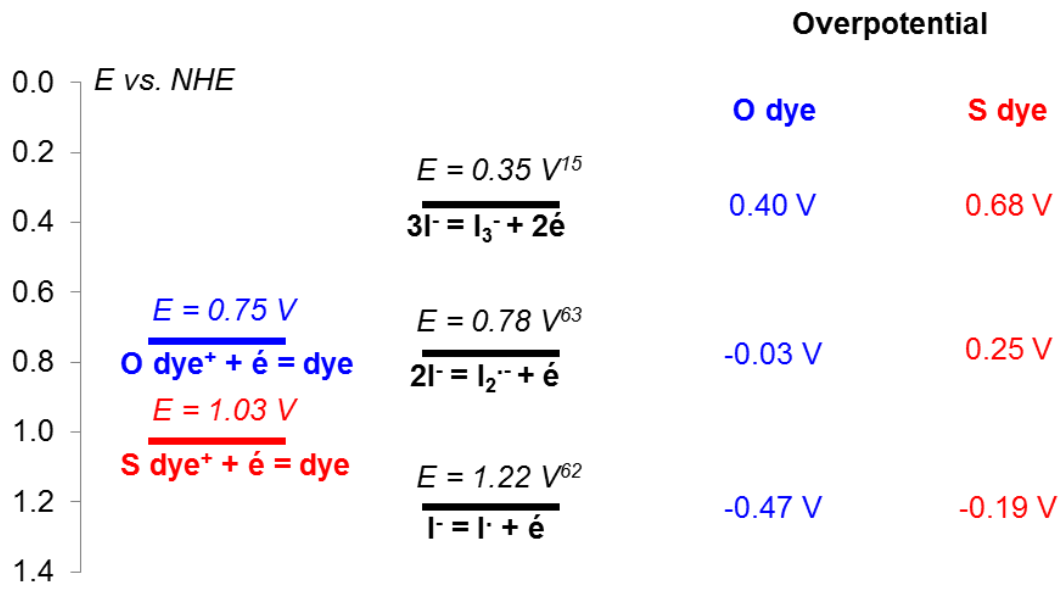

Fig. 4.15: *The reduction of $[K_4[Ru(dcbpy)_2(NCX)_2]]^+$ where X = O, S against the oxidation potential of various components of the I^-/I_3^- redox couple.*

The 0-0 transition energy (2.2.3) could not be estimated for the O dye as no emission was observed for this dye. However, as the bpy ligands were unchanged in the two dyes and the fully deprotonated S dye is known to function in a DSSC[34], it was assumed that injection into the TiO_2 surface was feasible for both dyes; although the short lifetime of the excited state of the O dye could reduce the yield of injected electrons. However, the change in the energy of the HOMO when the S atoms were substituted with O, results in a significant reduction in the overpotential of the dye for regeneration by I^-/I_3^- (Fig. 4.15). The significance of this change on the performance of the dye in a DSSC was therefore investigated.

4.6.1 Performance in DSSCs

There was some variation in the calculated efficiencies of the six cells tested for each dye (Appendix A1.2, A1.3); but the average values showed that changing the

chalcogen atom had a significant effect on the performance of the dye in a DSSC (Table 4.11, Fig. 4.16). By changing the X atom from S to O, the J_{SC} and V_{OC} are significantly reduced, resulting in a 77% decrease in solar cell efficiency. The performance of the cells sensitised by both the S dye and the O dye was poorer than the cells sensitised by N719, most likely due to reduced protonation of the dye which has been shown to cause a reduction in the cell efficiency[34].

Dye	J_{sc} / mAcm^{-2}	V_{oc} / mV	FF	η / %
N719	10.66 ± 1.01	636 ± 19	0.623 ± 0.022	4.21 ± 0.28
$K_4[Ru(dcbpy)_2(NCO)_2$	2.40 ± 0.41	576 ± 25	0.598 ± 0.024	0.829 ± 0.191
$K_4[Ru(dcbpy)_2(NCS)_2$	8.34 ± 0.52	682 ± 40	0.636 ± 0.039	3.61 ± 0.17

Table 4.11: *The performance of $K_4[Ru(dcbpy)_2(NCX)_2]$ where X = O, S in Dye-Sensitised Solar Cells. The mean values, calculated by testing six cells, are presented.*

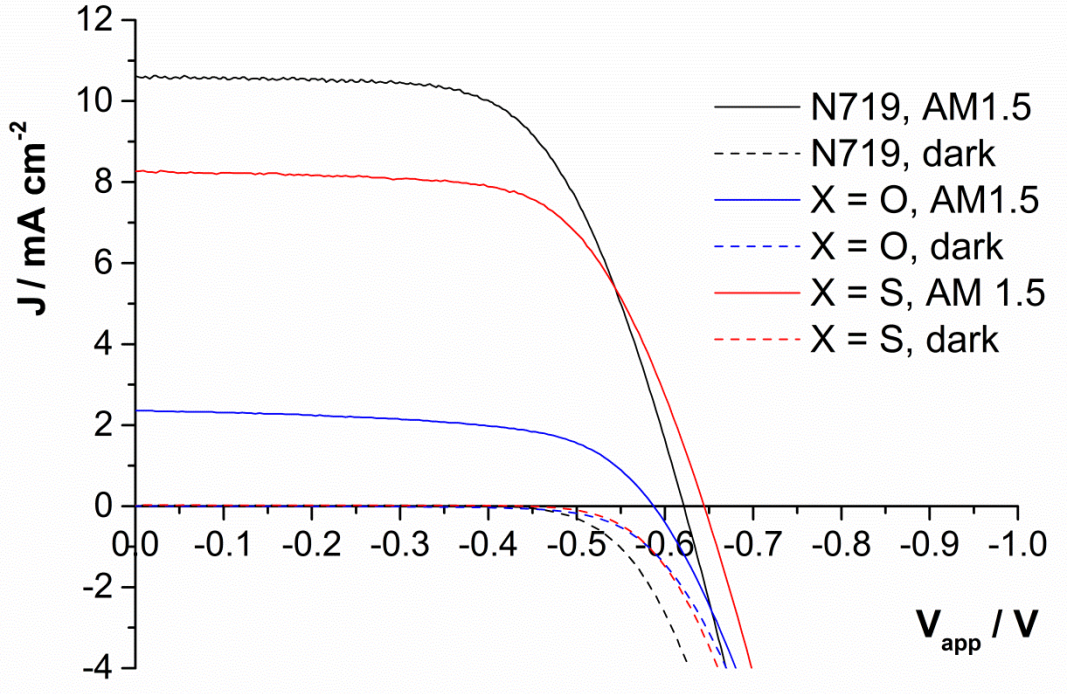

Fig. 4.16: *Representative J-V curves for Dye-Sensitised Solar Cells sensitised by $K_4[Ru(dcbpy)_2(NCX)_2]$ (where X = O, S) and N719 dyes.*

4.6.2 Impedance studies

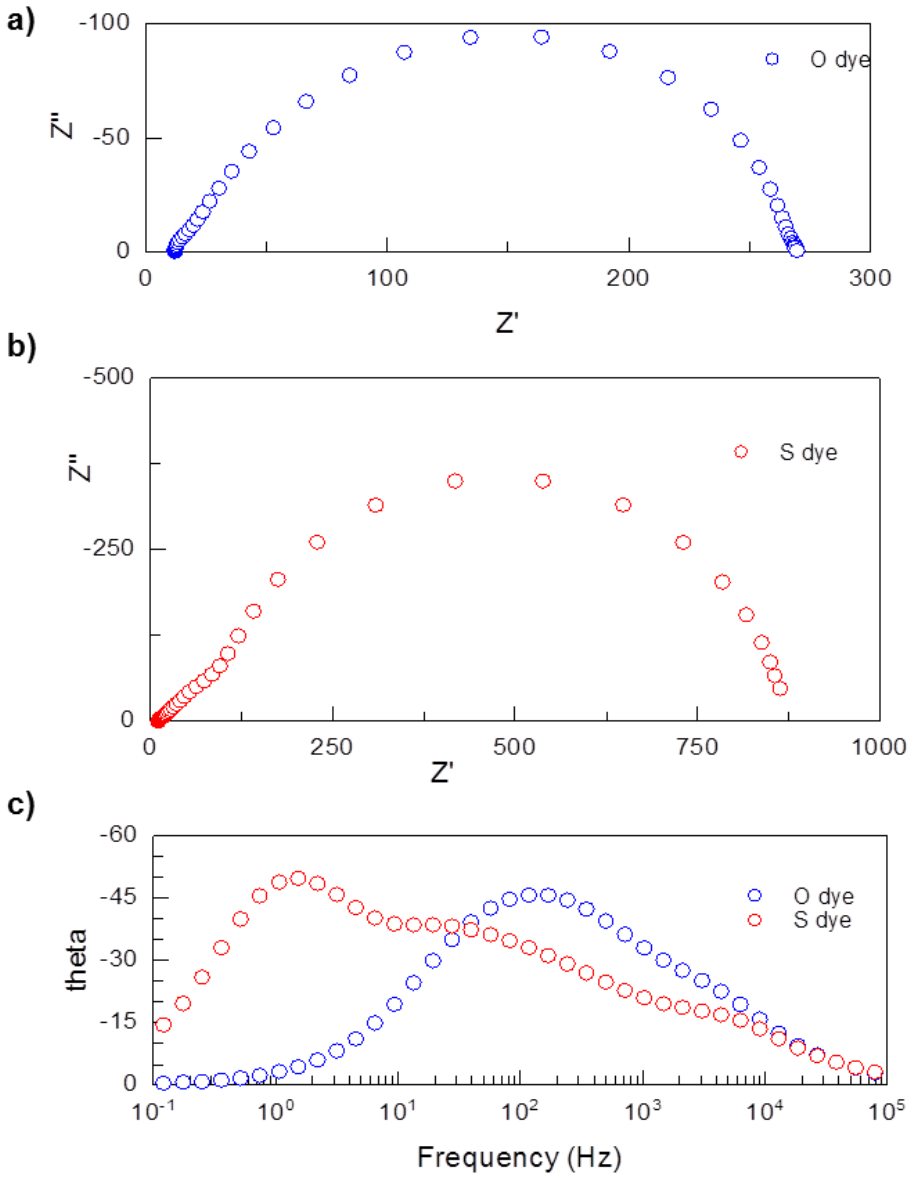

Fig. 4.17: *Electrochemical impedance spectroscopy of Dye-Sensitised Solar Cells sensitised by $K_4[Ru(dcbpy)_2(NCX)_2]$ (where X = O, S) at an applied bias of -0.5V.* ***a)*** *Nyquist plot of S dye;* ***b)*** *Nyquist plot of O dye;* ***c)*** *Bode plots of the O and S dyes.*

In order to explain the reduced cell efficiency for the O dye compared to the S dye, electrochemical impedance spectroscopy was carried out on the cells (2.3.3). For each dye, there was large variation in the fitted parameters across the six cells tested

(Appendix A2.2, A2.3), probably because each cell was doctor bladed individually. However, the differences observed between the cells sensitised by the S dye and O dye were considerable; allowing some conclusions to be drawn.

By comparing two spectra obtained at the same applied potential for cells sensitised by the S dye and the O dye, it was clear from the change in the shape of the Bode plots that the cells sensitised by the two dyes had different impedance characteristics (Fig. 4.17c). The Nyquist plots showed the more linear part of the plot at high frequencies for S dye cells (Fig. 4.17b); but this feature was not apparent at the same applied potential for the O dye cells (Fig. 4.17a). This suggested that the resistance to transport within the TiO_2 film had little contribution to the impedance within cells sensitised by the O dye; a conclusion which was verified by modelling the data (Appendix A2.2, 2.3, Table 4.12).

		TiO_2	TiO_2 – dye – I^- / I_3^- interface	
E_{app} / V	Dye	r_{trans} / Ω cm^{-3}	r_{rec} / Ω cm^3	c_{TiO2} / F cm^{-3}
-0.5	N719	78.4	208.7	7.84×10^{-4}
	X = O	-	279	6.36×10^{-5}
	X = S	370.6	826.2	5.29×10^{-4}
-0.6	N719	4.46	30.90	1.85×10^{-3}
	X = O	-	30.8	2.51×10^{-4}
	X = S	12.94	108.16	1.39×10^{-3}
-0.7	N719	-	8.13	3.08×10^{-3}
	X = O	-	7.90	5.82×10^{-4}
	X = S	-	19.45	2.62×10^{-3}
-0.8	N719	-	3.64	4.07×10^{-3}
	X = O	-	3.61	9.91×10^{-4}
	X = S	-	6.56	3.76×10^{-3}

Table 4.12: *Impedance data for Dye-Sensitised Solar Cells sensitised by N719 and $K_4[Ru(dcbpy)_2(NCX)_2]$ where X = O, S. The mean values, calculated by testing six cells, are presented.*

The O dye cells also had a considerably lower distributed capacitance at the TiO_2-dye-I^-/I_3^- interface than the cells sensitised by the S dye (Table 4.12, Fig. 4.18). This suggests that there are fewer charge traps at the TiO_2 surface, implying that the O

dye is somehow modifying the TiO_2 surface, or perhaps binding to species within the electrolyte to prevent them from modifying the TiO_2 surface.

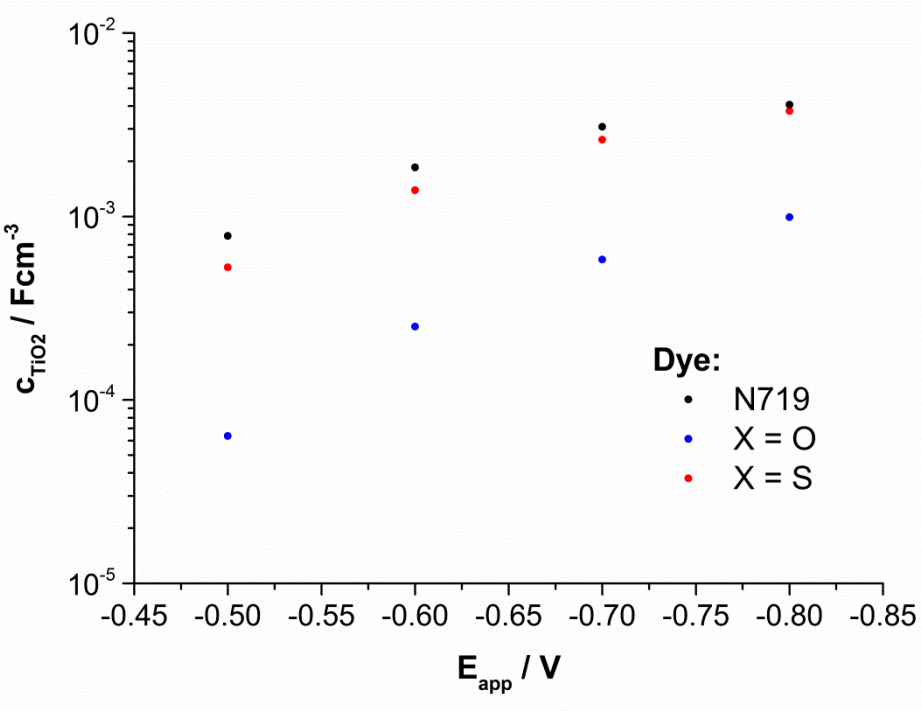

Fig. 4.18: *The change in the distributed capacitance at the TiO_2-dye-I^-/I_3^- interface for DSSCs sensitised by N719, and $K_4[Ru(dcbpy)_2(NCX)_2]$ where X = O, S.*

As well as the considerable changes in the capacitance of the TiO_2 film, the resistance to recombination across the TiO_2-dye-I^-/I_3^- interface was considerably lower for the O dye than the S dye (Table 4.12). By calculating the electron lifetime at this interface (2.3.3.2), it was seen that at all potentials there is a considerable decrease in lifetime when the $^-$NCS ligands are substituted by $^-$NCO (Fig. 4.19a). Due to significant difference in the capacitance of the TiO_2 film for cells sensitised by the O and S dyes, the lifetime was also plotted against the capacitance showing a difference of over an order of magnitude in the lifetime of the electron in the TiO_2 film at a particular capacitance (Fig. 4.19b). Therefore, recombination at the TiO_2-dye-I^-/I_3^- interface is considerably more prolific when X = O than when X = S; which is consistent with the lower V_{OC} observed for DSSCs sensitised by the O dye (4.6.1).

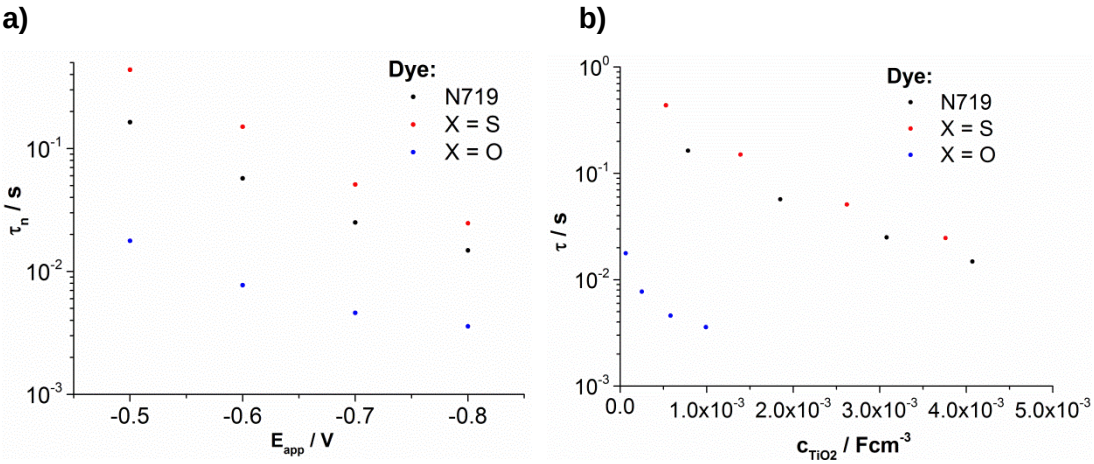

Fig. 4.19: *The electron lifetime against* ***a)*** *the applied voltage;* ***b)*** *the capacitance at the TiO_2-dye-I^-/I_3^- interface for DSSCs sensitised by N719 and $K_4[Ru(dcbpy)_2(NCX)_2]$ where X = O, S.*

The considerable decrease in the resistance to recombination from the TiO_2 to the electrolyte when the S atoms are substituted for O atoms is contrary to previous findings which suggest that the recombination rate is halved by substituting S atoms for O atoms within a dye (Fig. 4.20) used to sensitise solar cells with a variety of TiO_2 morphologies and electrolyte compositions[83]. This change was attributed to increased binding to iodine by the sulfur atom than the oxygen atom, causing an increase in the iodine concentration at the TiO_2 surface for electron recombination from the TiO_2 to the electrolyte. The higher availability of the lone pair on the chalcogen atom, and lower electron affinity of the atom have been shown to increase the strength of binding to iodine[230-233]. Considering the O and S dyes, the oxygen atom has a higher electron affinity (3.44 compared to 2.58 for S[83]), and the change in the contribution of the different resonance structures of $^-$NCX suggests that the lone pairs on the O atoms are less readily available for binding to iodine than those on the S atoms. Therefore, weaker binding between the X atom and iodine would be expected for the O dye compared to the S dye.

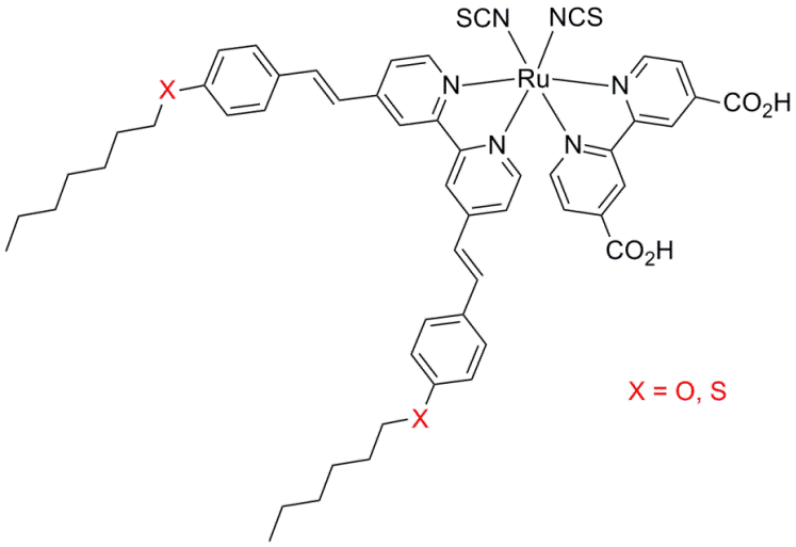

Fig. 4.20: *The structure of the TG6 (X = S) and K19 (X = O) dyes*[83].

On numerous occasions it has been shown that in ruthenium dyes for DSSCs iodine normally binds to the S atom of the ⁻NCS ligand (1.3.4.3). These results could therefore suggest that this interaction is beneficial, as it keeps the iodine away from the TiO_2 surface. It is interesting to note that for dyes containing four carboxylic acid groups, iodine binding to the carboxylic acid groups which are not bound to TiO_2 in dyes has not been considered. Data for iodine binding to a carboxylic acid group was apparently absent from the literature. However, iodine binding to carbonyl groups is reported to be only slightly weaker than iodine binding to ⁻NCS groups[234]. It is therefore possible that for the O dye, iodine binds to the free carbonyl groups, thus increasing the rate of recombination. It is also possible that an alternative recombination mechanism from the TiO_2 to the electrolyte could be causing the considerable increase in recombination across this interface when ⁻NCS is substituted with ⁻NCO. Using recently derived methods[87] to study iodine binding to the O and S dyes when they are bound to TiO_2 could therefore provide more insight into the mechanisms of recombination within a DSSC.

4.6.3 Transient absorption spectroscopy

Further exploration of the effect of the chalcogen atom was carried out by transient absorption spectroscopy on TiO_2 films sensitised by the two dyes. Studies on cells completed with an inert electrolyte showed that substituting the S atoms for O atoms caused the lifetime of the oxidised dye on the TiO_2 surface to decrease by more than an order of magnitude (Table 4.13). This suggests that there was a considerable increase in recombination of electrons in the TiO_2 surface to the oxidised O dye compared to the oxidised S dye. This could be due to the decrease in charge separation within the dye molecule when S is substituted with O. Also, the higher HOMO energy of the O dye than the S dye causes the potential drive for this process to be lower than the potential drive for electron transfer from the TiO_2 surface to the S dye. Thus, electron transfer from the TiO_2 surface to the oxidised O dye may not be in the Marcus inverted region (1.3.4.2), making this process more kinetically favourable than recombination to the oxidised S dye.

Conditions	X	A / ΔO.D	β	τ_{ww} / s
Inert electrolyte	O	2.02×10^{-5}	0.247	1.78×10^{-4}
	S	2.38×10^{-4}	0.268	6.15×10^{-3}
I^-/I_3^- electrolyte	O	3.65×10^{-5}	0.399	1.19×10^{-4}
	S	6.59×10^{-5}	0.775	8.75×10^{-6}

Table 4.13: *TAS data for Dye-Sensitised Solar Cells sensitised by $K_4[Ru(dcbpy)_2(NCX)_2]$ where X = O, S. Inert electrolyte refers to a solution of 0.5M TBP, 0.01M Gnd. NCS in acetonitrile.*

Considering the effect of adding a redox active electrolyte to the cell, it is clear that the change in dye lifetime was considerably greater for the S dye cells than the O dye cells (Table 4.13, Fig. 4.22d). In fact, the change in the lifetime of the oxidised O dye was negligible, suggesting that it is recombination from the TiO_2 film to the dye which limits the lifetime of the oxidised O dye within the solar cell. For this reason, the rate of dye regeneration could not be determined, although it cannot be faster than 1.2×10^{-4} seconds. This is two orders of magnitude slower than regeneration of the S dye under the same conditions. Therefore, regeneration of the dye by I^-/I_3^- is

considerably slower for the O dye than the S dye. This could be due to the increase in the energy of the HOMO of the O dye, reducing the overpotential for dye regeneration. It could also be the result of decreased localisation of the oxidised dye on the O atom, or a decrease in the strength of the interaction between I^- and the chalcogen atom.

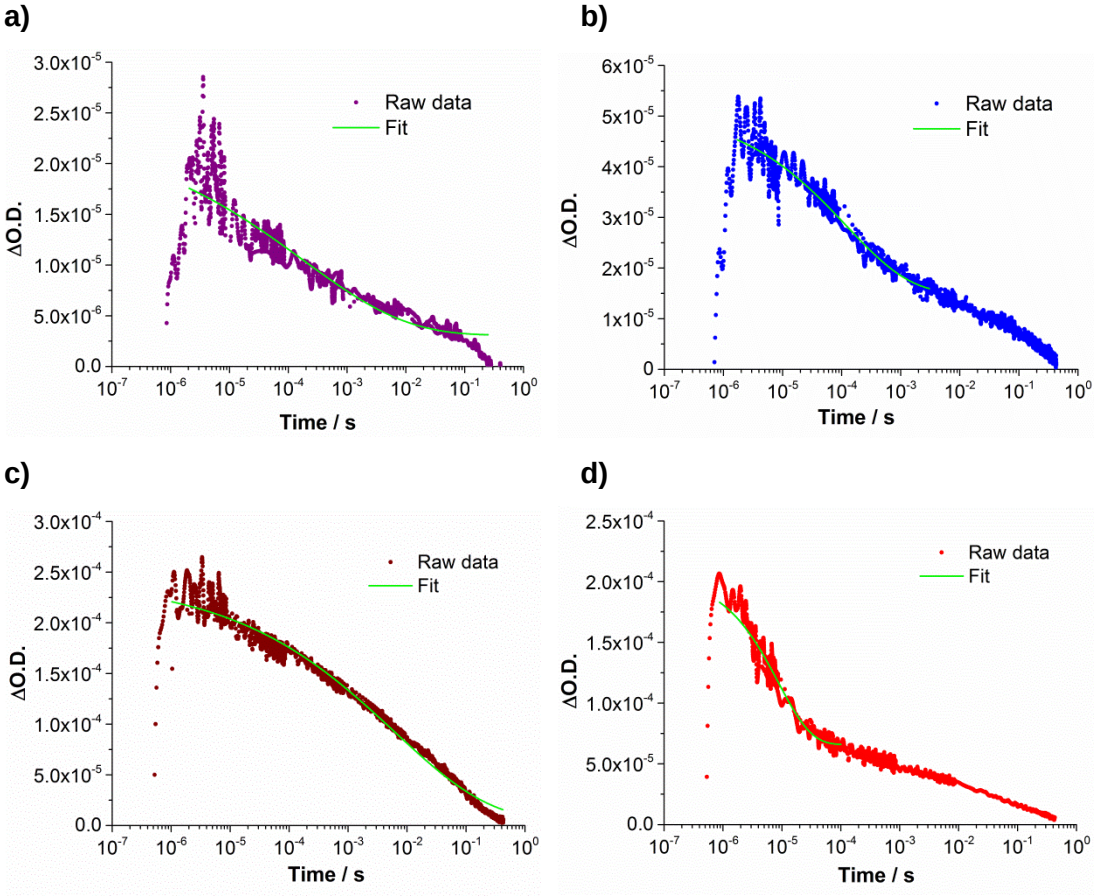

Fig. 4.21: *Fits for TAS data on the* ***a)*** *O dye with an inert electrolyte;* ***b)*** *O dye with* I^- */* I_3^-*;* ***c)*** *S dye with an inert electrolyte;* ***d)*** *S dye with* I^- */* I_3^-*.*

It is important to note that the signals obtained for TAS studies on the O dye were an order of magnitude smaller than the signals obtained for TAS studies on the S dye (Fig. 4.21). Therefore, the validity of the qualitative analysis of these spectra could be called into question. By normalising the data (Fig. 4.22), it is clear that the conclusions drawn from the fits of the plots are supported; for example the normalised plots for the O dye with an inert electrolyte and with a redox active

electrolyte are very similar, showing that the lifetime of the oxidised O dye is little affected by the electrolyte used. However, as the signals were weak and the data were noisy, comparisons between the lifetimes for these dyes and literature values have not been made.

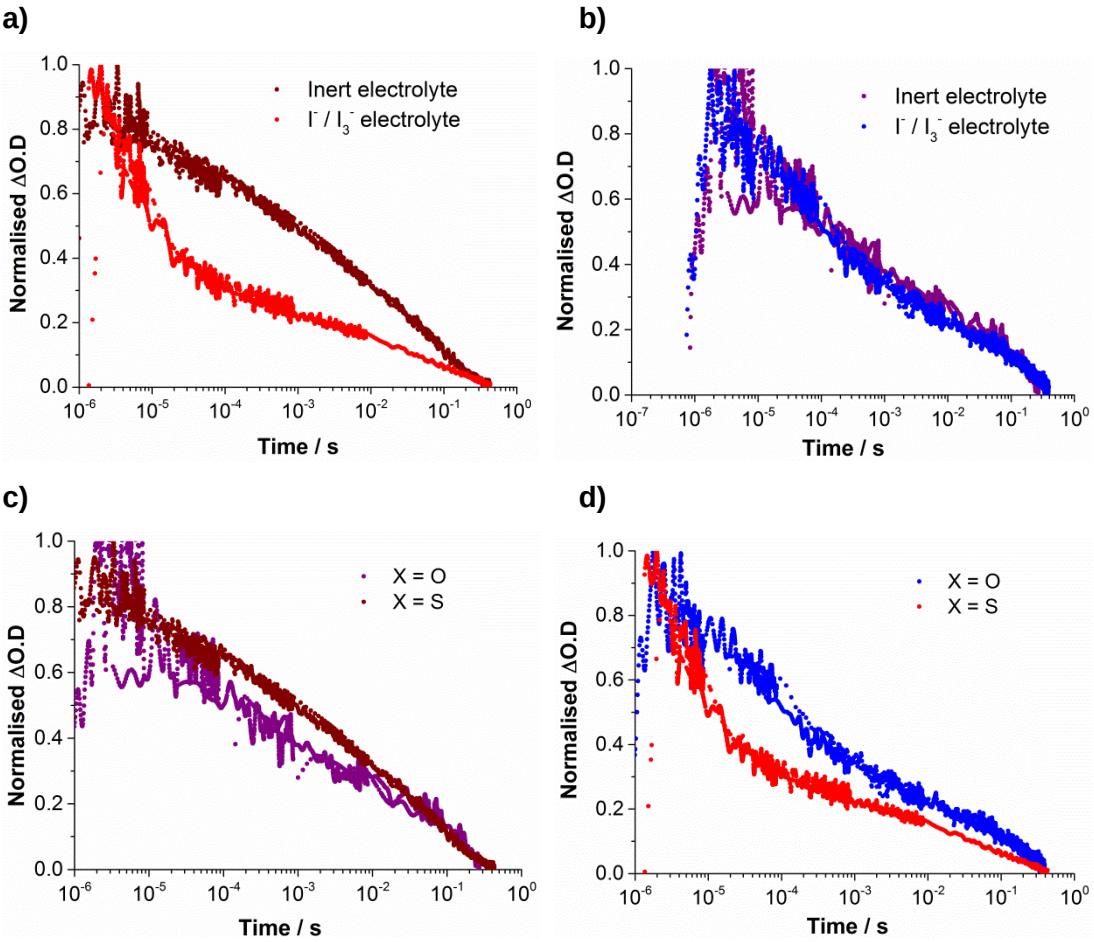

Fig. 4.22: *Normalised TAS data on the* ***a)*** *S dye cells with different electrolytes;* ***b)*** *O dye cells with different electrolytes;* ***c)*** *O and S dyes cells with an inert electrolyte;* ***d)*** *O and S dyes cells with* I^- / I_3^-.

4.6.4 High efficiency cells and cell stability

Dye	J_{sc} / mAcm^{-2}	V_{oc} / mV	FF	η / %
N719	15.8 ± 0.7	735 ± 4	0.707 ± 0.034	8.19 ± 0.08
X = O	7.10 ± 0.55	589 ± 7	0.720 ± 0.036	3.00 ± 0.09
X = S	12.2 ± 0.9	703 ± 16	0.733 ± 0.041	6.29 ± 0.21

Table 4.14: *Efficiencies of high efficiency DSSCs sensitised by N719 and $K_4[Ru(dcbpy)_2(NCX)_2]$ where X = O, S. The cells were manufactured by Benjamin Grew at Loughborough University.*

High efficiency DSSCs manufactured at Loughborough University showed the same trend in solar cell efficiency; with cells sensitised by the O dye showing a considerably poorer efficiency than those sensitised by the S dye (Table 4.14). Re-testing the cells after ten days showed that all of the cells had increased in efficiency, but the efficiency of the O dye cells had increased considerably more than the efficiency of the S dye cells or the N719 cells (Table 4.15). This change in efficiency was coupled with a change in the colour of the dye within the solar cell (Fig. 4.23), suggesting that the dye was reacting within the solar cell.

Dye	Day	J_{sc} / mAcm^{-2}	V_{oc} / mV	FF	η / %
N719	0	15.5	737	0.726	8.28
	10	17.7	778	0.699	9.64
X = O	0	5.53	594	0.777	2.56
	10	12.04	658	0.724	5.74
X = S	0	11.6	704	0.751	6.12
	10	14.1	771	0.735	8.00

Table 4.15: *The change in the efficiency of DSSCs sensitised by N719 and $K_4[Ru(dcbpy)_2(NCX)_2]$ where X = O, S. The cells were manufactured by Benjamin Grew at Lougborough University.*

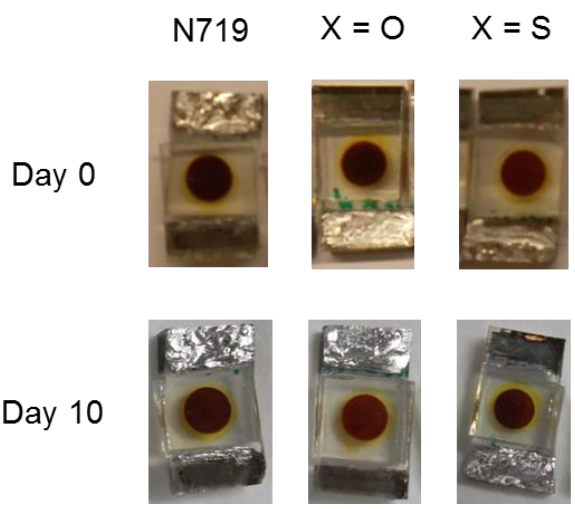

Fig. 4.23: *DSSCs sensitised by N719 and $K_4[Ru(dcbpy)_2(NCX)_2]$ where X = O, S.*

Ruthenium dyes are susceptible to photochemical ligand exchange in solution, but when bound to titania they are stabilised by electron injection into the TiO_2 surface. However, population of the ^{3}d-d excited state when the dye is bound to TiO_2 can lead to ligand exchange[45]. It has already been discussed that the O dye appears to have a lower lying ^{3}d-d excited state which can be more readily thermally populated; thus it is likely that ligand exchange between the dye and species in the electrolyte is occurring. To ensure the S dye wasn't forming *in situ* by ligand exchange between the O dye and guanidinium thiocyanate (Gnd. NCS) in the electrolyte, cells were made using electrolyte with and without Gnd. NCS and the change in their efficiency was monitored (Fig. 4.24). This showed that the absence of Gnd. NCS in the electrolyte had little effect on the change in cell properties observed, suggesting that if ligand exchange between the dye and the electrolyte is occurring, it is not necessarily the S dye which is forming.

For both cells, the change in the fill factor was negligible, with the fill factor reducing slightly over time (Fig. 4.24d). The pattern in the change in the efficiencies of the cells (Fig. 4.24a) closely matched the change in J_{SC} (Fig. 4.24b), suggesting that it is the change in J_{SC} which contributes most to the change in cell efficiency. There is some oscillation in the change of both of these parameters; however, there is an overall increase in both the efficiencies and J_{SC}s of the cells. This could be due to

an increase in the rate of dye regeneration within the cell, suggesting the *in situ* formation of a dye with a more stable HOMO than the O dye. This would be consistent with the more red colour of the dye within the solar cell (Fig. 4.23).

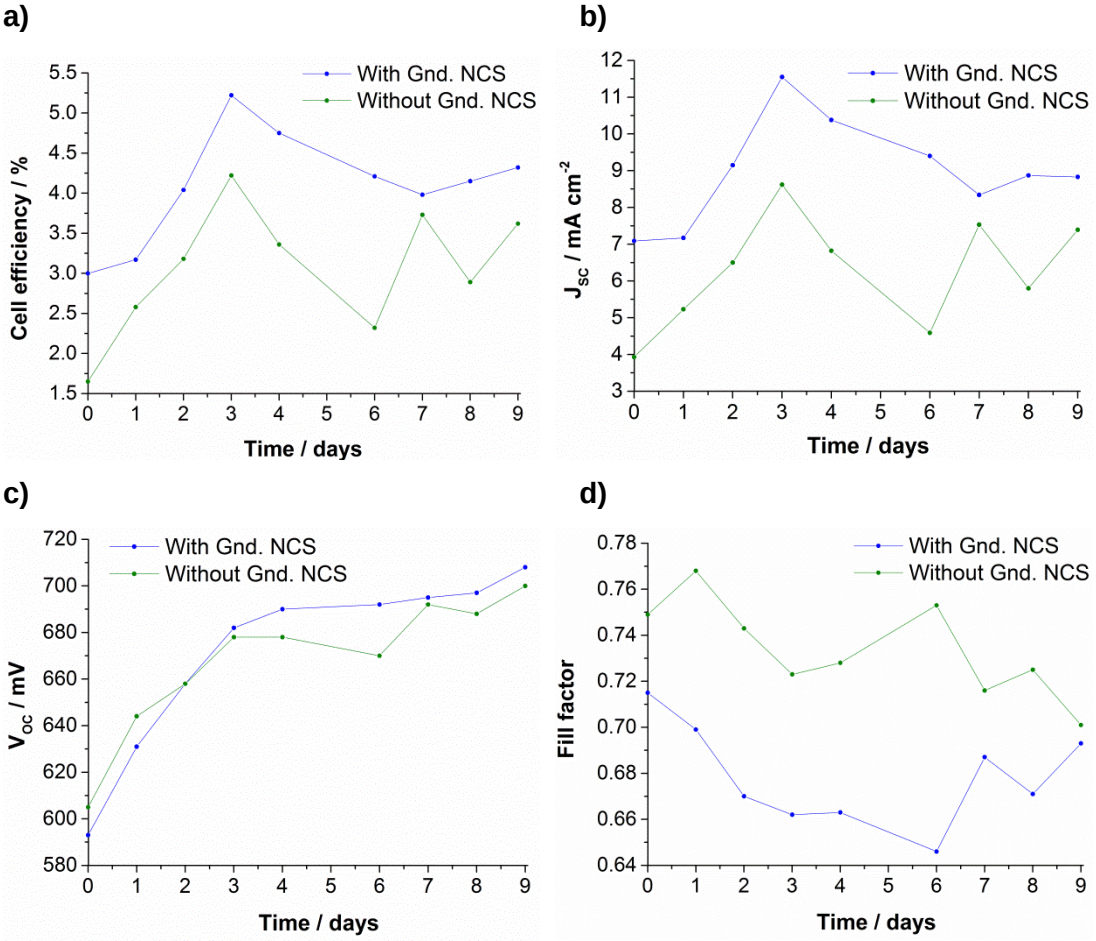

Fig. 4.24: *The change in the **a)** efficiency; **b)** J_{SC}; **c)** V_{OC}; **d)** fill factor of DSSCs sensitised by $K_4[Ru(dcbpy)_2(NCO)_2]$ with and without guanidinium thiocyanate in the electrolyte.*

The change in V_{OC} was more consistent, with a steady increase in V_{OC} observed over time (Fig. 4.24c). This implies that there is a reduction of recombination from the TiO_2 to the dye, which would be consistent with the formation of a new dye on the surface. Therefore, it appears that ligand exchange between the O dye and a species within the electrolyte, a species which isn't necessarily Gnd. NCS, causes the formation of a dye which performs favourably within a DSSC.

4.7 Conclusion

The effects of substituting the S atoms of the ⁻NCS ligands for O atoms within a ruthenium dye are numerous; therefore large changes in dye structure are not required for significant changes in the dye properties. Without the introduction of bidentate ligands, the stability of the dye in solution and under electrochemical oxidation was enhanced. Yet this effect did not translate to enhanced stability of the dye within the solar cell, as the O dye was in fact more susceptible to a change in structure than the S dye. The instability of the S dye in solution mostly arises from the oxidation of the ⁻NCS ligand to form ⁻CN. The ⁻NCO ligand is less susceptible to this process; yet it is more susceptible to ligand exchange causing a change in the properties of the solar cell. Therefore, it is important to recognise that the stability of a dye in solution does not always translate to stability within a DSSC, as different mechanisms of dye breakdown are possible under different conditions.

The substantial decrease in the resistance to recombination by substituting O for S within the dye is consistent with the change in the V_{OC} of the cell, but contrary to the expected effects if iodine binding with the dye is the main cause of recombination across this TiO_2-dye-I^-/I_3^- interface. The results therefore show that alternative mechanisms of recombination from the titania to the electrolyte must be considered to gain a more complete understanding of recombination across this interface.

The increase in the metal character of the O dye compared to the S dye caused a red-shift in the dye's absorption spectrum. However, the destabilisation of the HOMO also resulted in a reduction in the rate of dye regeneration, and an increase in the rate of recombination from the titania surface to the dye. These results question the possibility of achieving the synthesis of ruthenium dyes with higher energy HOMOs which will perform better in a DSSC – it appears that the fine balance of the energetics within the cell is not conducive to such a change in dye characteristics.

Chapter 5: The Halide Series and Structural Considerations

5.1 Introduction

To date, only electron donating substituents in the 4,4` positions of an ancillary bpy ligand have been investigated in attempts to improve the performance of asymmetric dyes in DSSCs. In order to explore the effects of using an electron withdrawing substituent on an ancillary bpy ligand, a series of dyes containing halogenated bpy ligands were synthesised (Fig. 5.1).

a) **b)**

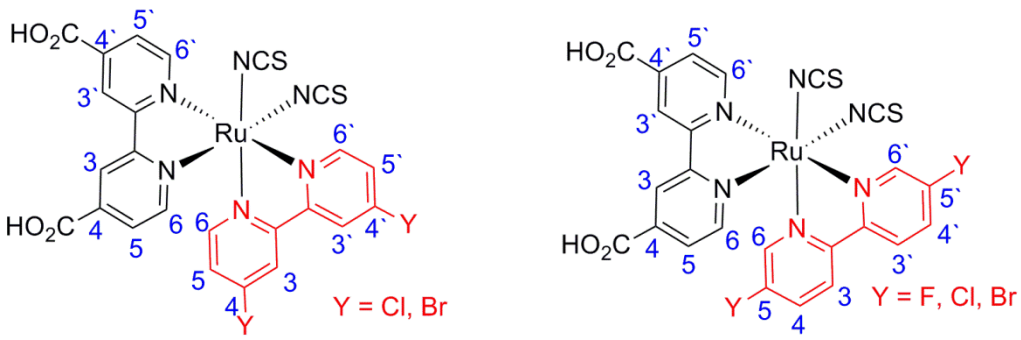

Fig. 5.1: *Numbering scheme for* ***a)*** *Ru(H_2-dcbpy)(4,4`-$Y_2$-bpy)$(NCS)_2$ and* ***b)*** *Ru($H_2$-dcbpy)(5,5`-Y_2-bpy)$(NCS)_2$ dyes where Y = F, Cl, Br.*

The spectral and electrochemical properties of halogenated bpy ligands have been investigated, and the nature of the halide atom has been shown to have a significant effect on the reduction potentials of the free ligand (Table 5.1). Due to resonance around the bpy ligand[235-239], the position of the substituent group has also been shown to affect the reduction potential of the ligand (Table 5.1). Dyes with halide substituents in both the 4,4` and 5,5` positions of the ancillary bpy ligand (Fig. 5.1) have therefore been synthesised to probe the effect of the position of the substituent on the properties of the resulting ruthenium dye. In order to identify the position and

nature of the substituent group which is being altered in this series of dyes, the dyes will subsequently be referred to as the 4F, 4Cl, 4Br, 5F, 5Cl and 5Br dyes.

	Reduction potential(s) vs. Ag/AgCl / V	
Y	N,N` = 4,4`	N,N` = 5,5`
F	-1.78[235]	-2.02[235]
Cl	-1.69[237]	-1.74[236]
Br	-	-1.72[236]

Table 5.1: *Reduction potentials of the free N,N`-Y_2-bpy ligand where N = 4, 5; Y = F, Cl, Br.*

It is possible that the effects of iodine binding to the dye (1.3.4.3) may also be probed by considering the halogen series. Iodine binding to a molecule can be quantified by observing the blue-shift in the absorption spectrum of iodine in the presence of the compound being studied[230]. Thus, iodine binding constants for a large number of molecules have been calculated, and the results have been compiled[230,234]. However, inconsistencies in the conditions used for measurement of iodine binding, particularly the solvent used, can cause difficulties in the comparison of the effects of different atoms. By careful consideration of the available data, a diiodine basicity scale has been compiled[234], and it has been determined that for iodine-bond acceptor sites the Lewis basicity is in the order N > P~Se > S > I~O > Br > Cl > F. As the strength of iodine binding increases going down the halide series, whether a single atom, such as fluorine, could be used to hinder iodine binding within a DSSC has been explored by testing these dyes in DSSCs.

5.2 Theoretical properties of Ru(H_2-dcbpy)(N,N`-Y_2-bpy)$(NCS)_2$ dyes where N = 4, 5; Y = F, Cl, Br.

In each of the dyes in this series, the distributions of the HOMO and LUMO orbitals are fairly similar. The LUMOs of the dyes are localised on the carboxylic acid substituted bpy ligand (Fig. 5.2, 5.3) which is the desired location for efficient

injection of the excited state electron. The HOMOs are localised on the ¯NCS ligands and Ru atom of the dyes. Thus the Y_2-bpy ligand is acting as an ancillary ligand as expected.

Orbital	Dye	% occupancy of orbitals			
		$(NCS)_2$	Ru	H_2-dcbpy	N,N`-Y_2-bpy
HOMO	4F	38.00	54.21	4.26	3.53
	4Cl	38.94	53.06	4.10	3.90
	4Br	38.97	52.93	4.14	3.96
	5F	39.63	52.78	4.15	3.44
	5Cl	40.08	52.33	4.11	3.48
	5Br	39.98	52.42	4.11	3.49
LUMO	4F	1.35	9.43	86.65	2.57
	4Cl	1.32	8.97	86.50	3.21
	4Br	1.32	8.96	86.45	3.27
	5F	1.33	9.11	86.96	2.60
	5Cl	1.30	8.91	86.75	3.04
	5Br	1.29	8.85	86.58	3.28

Table 5.2: *The distribution of the HOMO and LUMO orbitals of Ru(H_2-dcbpy)(N,N`-Y_2-bpy)$(NCS)_2$ dyes where N = 4,5; Y = F,Cl,Br.*

When the halide atom is in both the 4,4` and 5,5` positions, there is slightly more LUMO localised on the Y_2-bpy ligand going down group 17. This is mostly countered by a decrease in the contribution of the ruthenium metal to the LUMO. Going down the halide series there is also a slightly higher contribution from the Y_2-bpy ligand to the HOMO, although this effect appears to be more prominent for the 4,4` dyes than the 5,5` dyes. Again, this is mostly compensated for by an increase in the localisation of the HOMO on the ruthenium centre. It can be seen that the pyridyl rings which are *trans* to the ¯NCS ligand have a small contribution to the HOMO (Fig. 5.2, 5.3). This contribution resonates around the 2, 4, and 6 positions of the bpy ligand, explaining the larger effect of the halogen in the 4 position on the distribution of the HOMO. For the 4F dye, the highly electron withdrawing nature of the F atom caused a small proportion of the HOMO to be localised on this atom (Fig. 5.2). However, as the changes in orbital distribution are minor, the calculations suggest that the nature and position of the halide substituent has little effect on the HOMO and LUMO distribution of the dye.

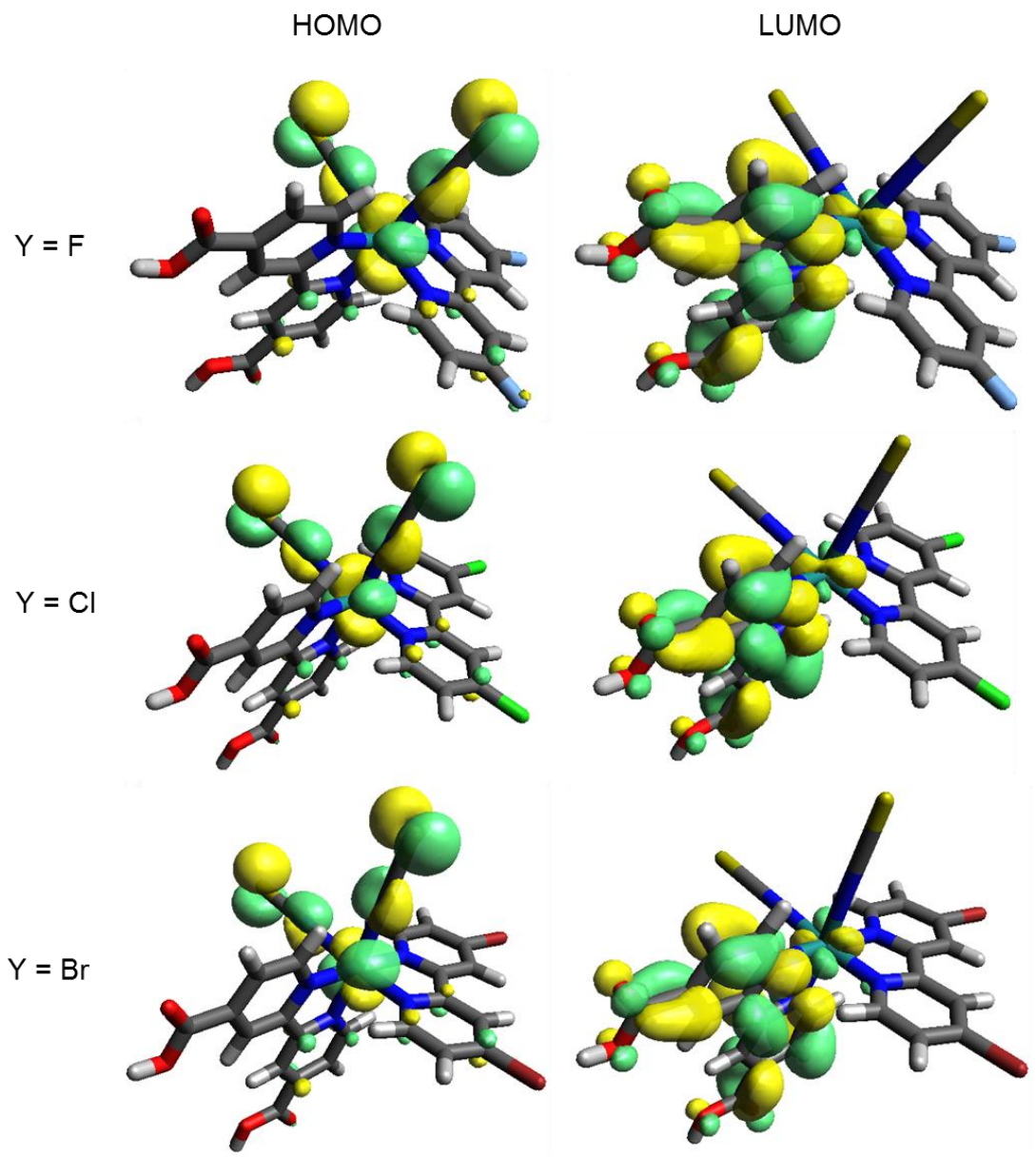

Fig. 5.2: *The distribution of the HOMOs and LUMOs of Ru(H_2-dcbpy)(4,4`-Y_2-bpy)$(NCS)_2$. The geometries of the dyes were optimised with solvation by DMF using the polarisable continuum model*

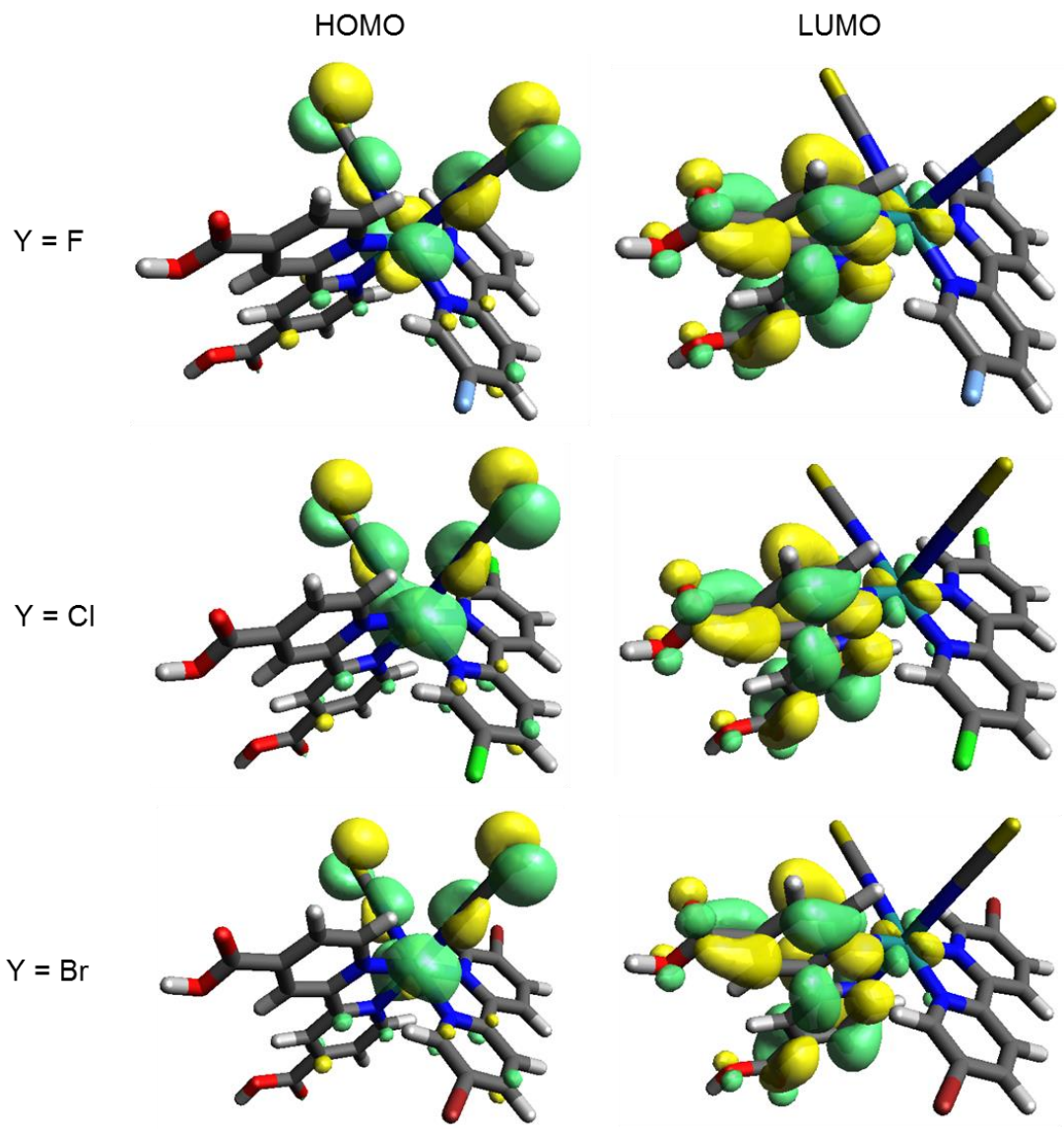

Fig. 5.3: *The distribution of the HOMOs and LUMOs of Ru(H_2-dcbpy)(5,5`-Y_2-bpy)$(NCS)_2$. The geometries of the dyes were optimised with solvation by DMF using the polarisable continuum model.*

5.3 Dye characterisation

Due to the susceptibility of the 4F dye to nucleophilic substitution of the halide atom (3.6.2), the synthesis of this dye was not achieved to a sufficient level of purity for analysis. However, the syntheses of the other five dyes in the series were achieved to

a high level of purity by elemental analysis (3.8.4.3-3.8.4.7). By ^{1}H NMR in d^{6}-DMSO, the dyes also appeared pure, but ^{1}H NMR studies in other solvents such as CD_3OD could not be carried out due to the poor solubility of the dyes. This also prevented the use of ^{13}C NMR for further characterisation. Using the chemical shifts, splitting patterns and coupling constants for the peaks observed, the ^{1}H NMR peaks of each of the dyes were assigned showing that the chemical shifts of the protons of the H_2-dcbpy ligands were little affected by the change in the nature and position of the halide atom (Fig. 5.1, Table 5.3). However, for the Y_2-bpy ligand, whether the protons in the 5,5` positions were *trans* to ¯NCS or a bpy ligand had a greater effect on the chemical shift than for the protons in the 4,4` positions. This suggests that groups in the 5,5` positions of the bpy ring are more influenced by the environment of the metal centre than those in the 4,4` positions.

Dye	H_2-dcbpy δ / ppm						N,N`-Y_2-bpy δ / ppm						ν_{CN} / cm^{-1}
	6	6`	5	5`	3	3`	6	6`	5	5`	3	3`	
4Cl	7.92	9.42	7.62	8.33	8.96	9.12	7.52	9.15	7.39	8.19	8.97	9.13	2101
4Br	7.91	9.39	7.61	8.27	8.91	9.15	7.40	9.03	7.46	8.22	9.00	9.06	2100
-	6	6`	5	5`	3	3`	6	6`	4	4`	3	3`	-
5F	7.92	9.39	7.61	8.29	8.93	9.08	7.60	9.03	7.91	8.28	8.66	8.81	2108
5Cl	7.94	9.39	7.63	8.30	8.96	9.10	7.58	9.10	8.09	8.44	8.63	8.78	2109
5Br	7.93	9.39	7.63	8.32	8.97	9.11	7.61	9.20	8.22	8.56	8.58	8.73	2112

Table 5.3: *^{1}H NMR chemical shifts in d^{6}-DMSO and ν_{CN} energies of Ru(H_2-dcbpy)(N,N`-Y_2-bpy)(NCS)$_2$ where N = 4,5; Y = F, Cl, Br.*

The structures of the dyes were confirmed by the presence of the expected mass of the singly deprotonated anion by ESI-MS$^{(-)}$, and the isotopic patterns were consistent with the presence of both chlorine and bromine where appropriate. Coupling of the protons in the bpy rings to fluorine were apparent in the ^{1}H NMR of the 5F dye, so it was proved for each of the dyes that nucleophilic substitution of the halide substituents had not occurred. The ¯NCS ligands were shown to be bound through the nitrogen atom by IR spectroscopy (Table 5.3). Considering the ν_{CN} energies of the dyes, it is interesting to note that the position of the halide substituent had a greater effect on the ¯NCS ligand than the nature of the halide ligand, although the changes observed are minor.

5.4 Dye properties

5.4.1 Light absorption properties

5.4.1.1 Absorption spectroscopy

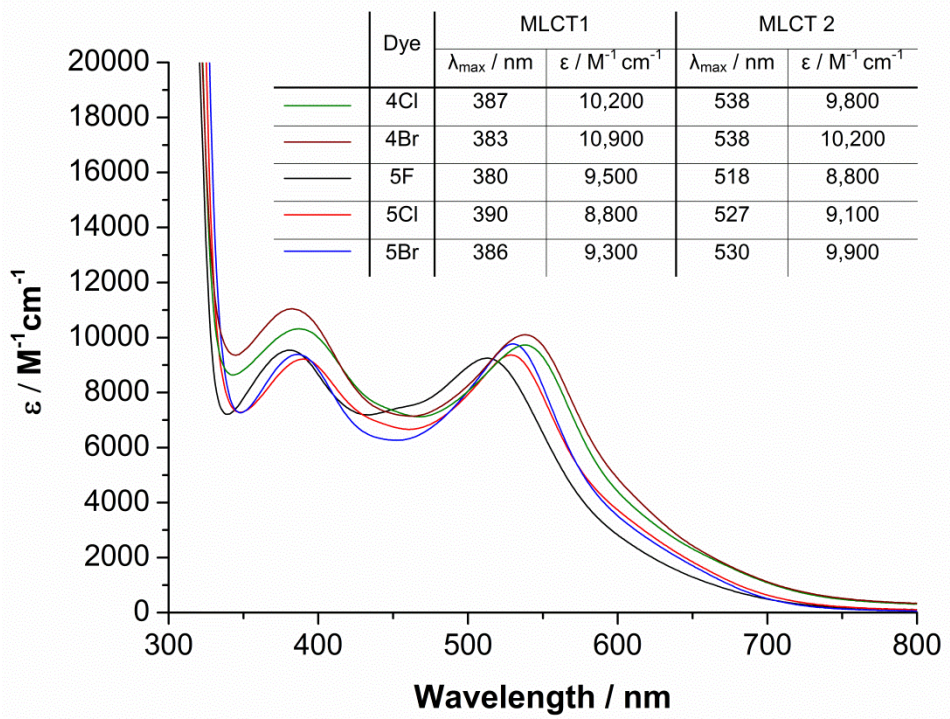

Fig. 5.4: *The UV/vis spectra of Ru(H_2-dcbpy)(N,N`-Y_2-bpy)$(NCS)_2$ dyes in dry DMF where N = 4, 5; Y = F, Cl, Br.*

Analysis of the UV/vis spectra of the dyes (Fig. 5.4) shows that when the halogen atoms are in the 4,4` positions, there is no change in the $\lambda_{max}$ of the lowest energy MLCT transition (MLCT 2, Fig. 5.4). However, when the halogens are in the 5,5` positions of the bpy ring there is a red shift in the λ_{max} of the lowest energy MLCT transition going down group 17 (MLCT 2, Fig. 5.4). The red shift seen for the 5Cl dye compared to the 5F dye amounts to a change of 330 cm^{-1}; and λ_{max} for the 5Br dye is red shifted by 110 cm^{-1} compared to the 5Cl dye. The blue shift observed by moving the bromine substituents from the 4,4` positions to the 5,5` positions of the

bpy ring is 280 cm^{-1}, and by changing the position of the chlorine substituents a shift of 390 cm^{-1} is observed. Therefore, changing the position of the substituent on the bpy ring has as much of, if not more of, an effect on the lowest energy MLCT transition than changing the nature of the halogen atom.

For the higher energy MLCT peak, the trend in the change in λ_{max} is more difficult to define. The λ_{max} values ranged from 380 to 390 nm, thus there was a variation of 675 cm^{-1} across the series of dyes. When the halogens were in the 4,4` positions, there was a blue shift of 270 $cm^{-1}$ by substituting Cl atoms with Br atoms. The same substitutions in the 5,5` positions caused a blue shift of 265 cm^{-1}, suggesting that the effect of changing the halogen on the higher energy MLCT transition is not dependent on the position of the substituent. As with the lower energy MLCT transition, the 5F dye was the most blue shifted of the series of dyes implying that the highly electron withdrawing nature of this substituent causes an overall blue shift in the absorption spectrum. The red-shift observed by changing the position of the halogen substituents from 4,4` to 5,5` is 201 cm^{-1} and 203 cm^{-1} for the Cl and Br dyes respectively. Therefore, the change in MLCT energy due to the position of the halogen is independent of the nature of the halogen in this case. This red shift also opposes the blue shift observed in the lower energy MLCT transition when the substituents were changed from the 4,4` to the 5,5` positions.

By comparing the molar extinction co-efficients of the MLCT transitions for the five dyes, it is again difficult to perceive a clear trend. The molar extinction co-efficients of the 4,4` dyes are slightly higher than those of the 5,5` dyes and the Br dyes have slightly higher molar extinction co-efficients than the Cl dyes; but the values for the 5F dye do not fit into a trend. Overall, the molar extinction co-efficients for all of the dyes are similar to those obtained for dyes where the Y substituent is an alkyl group (ε = 10,100 - 11,600 M^{-1} cm^{-1} [169]). Direct comparison of the λ_{max} values of these dyes and alkyl substituted dyes was not possible due to the use of different solvents for measuring the UV/vis spectra; therefore the effect of the use of electron withdrawing or electron donating group on light absorption by the dye could not be established.

5.4.1.2 TD-DFT studies

λ / nm (% contribution of charge transfer to H_2-dcbpy)				
4Cl	4Br	5F	5Cl	5Br
663 (100)	662 (100)	659 (100)	657 (100)	658 (100)
586 (23.1)	584 (16.8)	523 (88.4)	573 (27.2)	576 (25.9)
553 (81.3)	553 (80.7)	471 (38.0)	550 (79.5)	551 (88.7)
508 (11.7)	507 (11.7)	460 (56.5)	497 (12.8)	499 (12.4)
467 (64.8)	466 (100)	453 (70.4)	464 (100)	465 (100)
454 (24.0)	454 (100)	429 (88.8)	455 (100)	455 (100)
430 (100)	430 (100)	386 (64.2)	428 (100)	428 (100)
388 (83.8)	388 (83.3)	376 (23.8)	386 (79.6)	386 (81.0)
380 (17.2)	380 (37.0)	367 (72.1)	369 (50.9)	370 (21.6)
371 (43.7)	371 (62.8)	-	-	369 (53.2)
367 (18.5)	367 (19.6)	-	-	-

Table 5.4: *The calculated charge transfer transitions for Ru(H_2-dcbpy)(N,N`-Y_2-bpy)$(NCS)_2$ solvated with DMF using the polarisable continuum model.*

Considering the comparison between the UV /vis spectra calculated *in silico* and those obtained experimentally (Fig. 5.5), there was a reasonable agreement. However, for each of the dyes the charge transfer transition which dominated the experimentally determined lower energy MLCT transition was calculated at too low an energy. Similarly, although the experimental λ_{max} value for the first MLCT transition for the 4Br dye was blue shifted compared to the 4Cl dye, the calculated absorption spectra of these two dyes are very similar at all wavelengths (Table 5.4). The calculated absorption spectra for the 5Br and 5Cl dyes are also very similar, with only a small blue shift calculated at longer wavelengths due to the substitution of the bromine substituents with chlorine. However, the blue shift in the absorption of the 5F dye observed experimentally was clearly replicated *in silico* (Table 5.4).

By determining the nature of each of the calculated charge transfer transitions (Appendix A3.5 to A3.9), it can be seen that not all of the MLCT excitation processes transfer charge to the H_2-dcbpy ligand; some charge is transferred to the Y_2-bpy ligand (Table 5.4). However, for all of the dyes, the lowest energy charge transfer is to the H_2-dcbpy ligand. As excitations to higher energy levels are likely to

relax to the lowest energy MLCT state, charge transfer to the Y_2-bpy ligand should still result in charge injection into the TiO_2 surface (1.3.3.2).

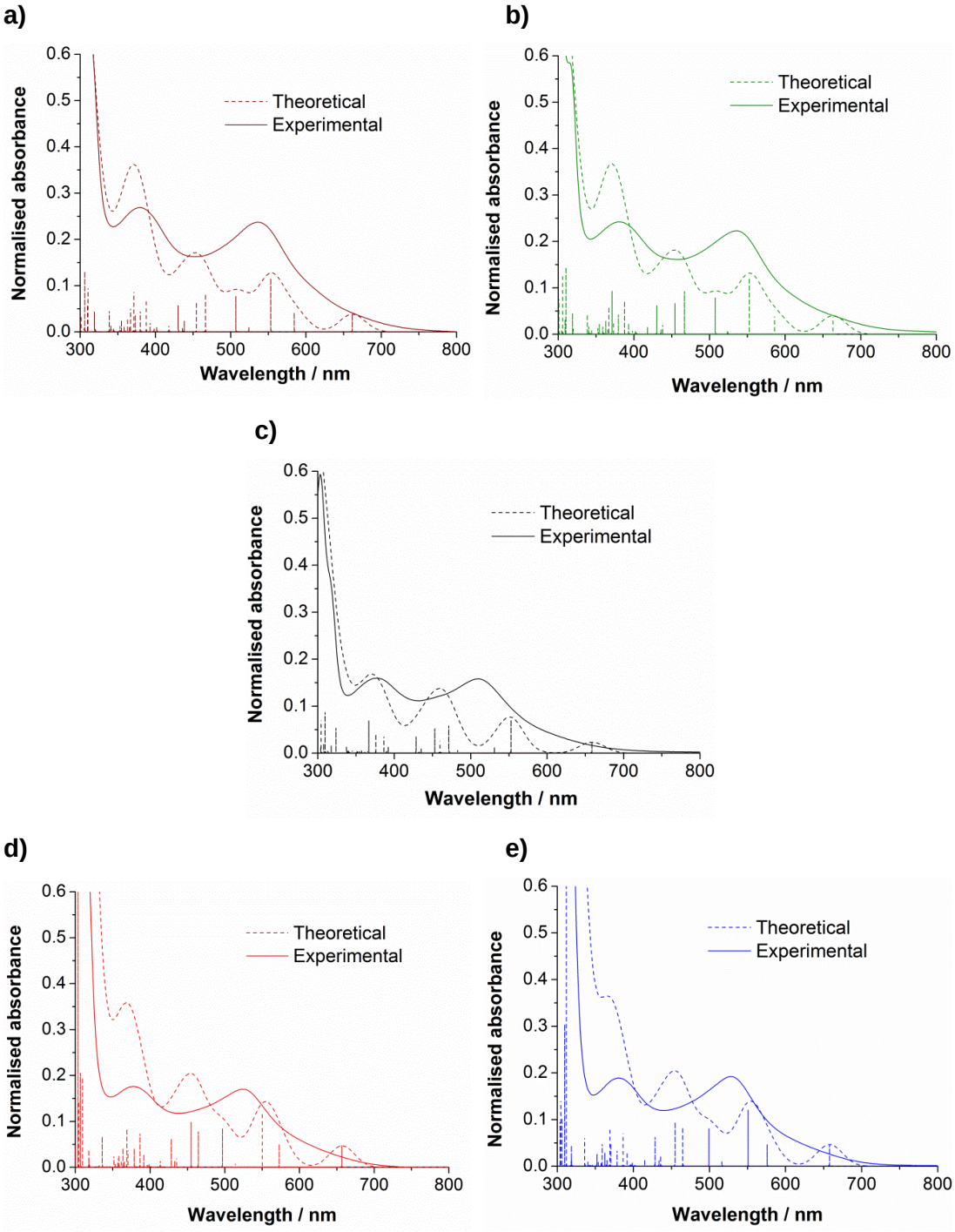

Fig. 5.5: *Theoretical versus experimental UV/vis spectra for Ru(H_2-dcbpy)(N,N`-Y_2-bpy)$(NCS)_2$ dyes where* ***a)*** *N = 4, Y = Cl;* ***b)*** *N = 4, Y = Br;* ***c)*** *N = 5, Y = F;* ***d)*** *N = 5, Y = Cl;* ***e)*** *N = 5, Y = Br.*

5.4.2 Luminescence spectroscopy

Emission from the lower energy MLCT transitions was observed for all of the dyes (Fig. 5.6, 5.7). At room temperature, phosphorescence of the 5,5` substituted dyes was observed (Fig. 5.6), whereas for the 4,4` substituted dyes only fluorescence was observed (Fig. 5.7) suggesting that inter-system crossing occurs more readily in the 5,5` dyes than the 4,4` dyes. Fluorescence of the 5Cl and 5Br dyes was not observed under any conditions, but both fluorescence and phosphorescence of the 5F dye was observed at room temperature (Fig. 5.6 a(i)). The peak representing phosphorescence for the 5,5` dyes was broader at room temperature than in the solid state, possibly because of dye - solvent interactions when the dye was in solution.

Dye	293 ^{o}K			Frozen			0-0 Transition wavelength / nm
	Excitation / nm	Emission / nm	Spectral shift / cm^{-1}	Excitation / nm	Emission / nm	Spectral shift / cm^{-1}	
4Cl	490; 526	537; 578	389	467; 515	687	4,860	630
4Br	490; 525	533; 572	287	466; 513	686	4,920	632
5F	488; 525	535; 571; 708	357; 4,570	466; 482	660	5,590	589
5Cl	467; 522	742	5,680	466; 507	682	5,060	629
5Br	468; 524	750	5,750	467; 510	681	4,920	619

Table 5.5: *The excitation and emission wavelengths of $Ru(H_2\text{-}dcbpy)(N,N`\text{-}Y_2\text{-}bpy)(NCS)_2$ dyes (where N = 4,5; Y = F, Cl, Br) in N_2-purged, dry DMF. The concentrations of the solutions ranged from 1.28 to 2.56 x 10^{-5} $moldm^{-3}$.*

By comparing the emission properties of the dyes at room temperature and frozen, it was apparent that the trends in the properties of the dyes were dependent on the physical state of the material being measured (Table 5.5). This suggests that at room temperature, solvent – dye interactions affect the energies of the frontier orbitals of the dyes. Considering the propensity of halogens to form intermolecular bonds, it is likely that dipole-dipole interactions are causing this change in properties. Due to the possible effects of these interactions, only the values determined by emission from the frozen sample will be discussed more fully.

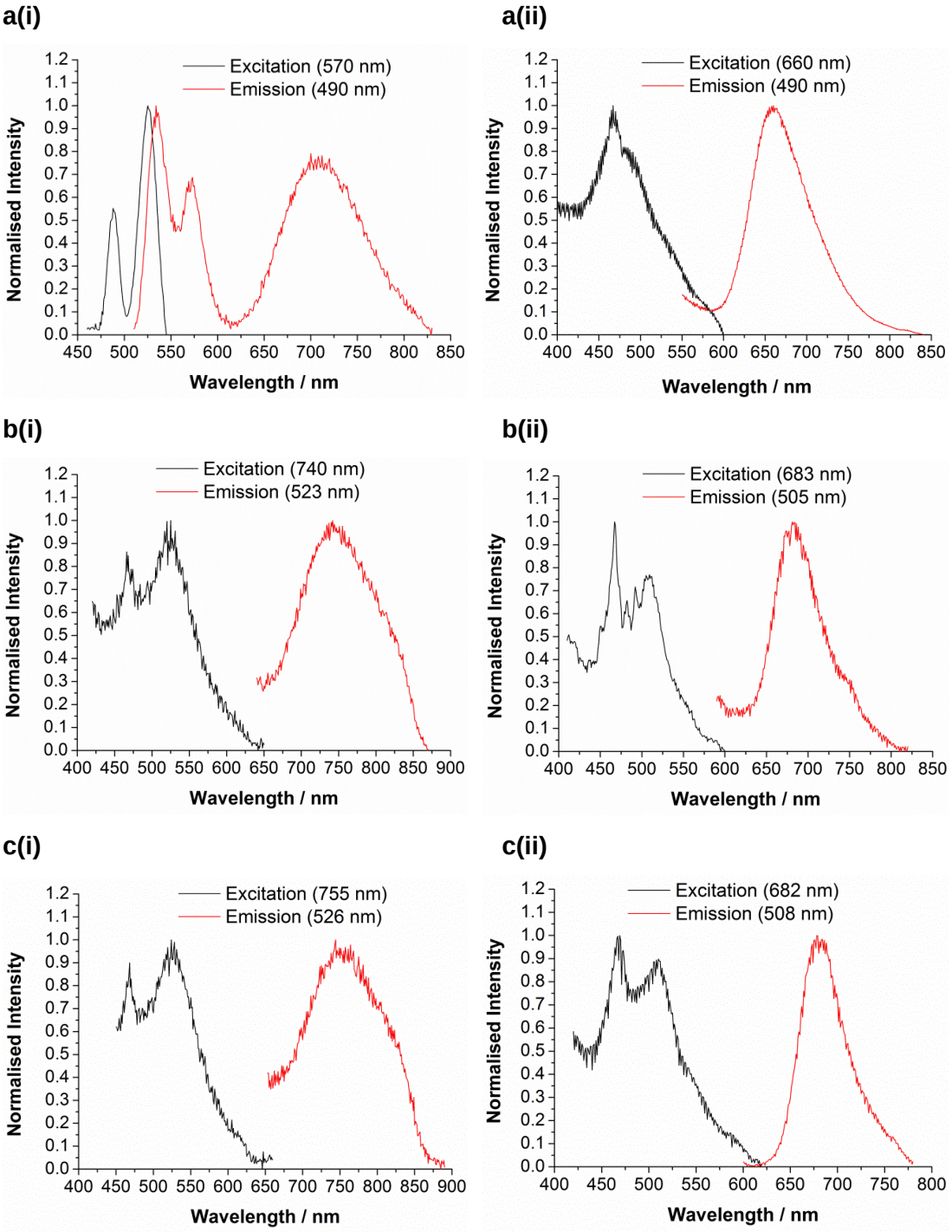

Fig. 5.6: *The emission spectra of Ru(H_2-dcbpy)(5,5`-Y_2-bpy)$(NCS)_2$ where Y =* ***a)*** *F;* ***b)*** *Cl;* ***c)*** *Br, in N_2-purged, dry DMF. Experiments were performed* ***(i)*** *at 293 ^oK;* ***(ii)*** *frozen with liquid nitrogen.*

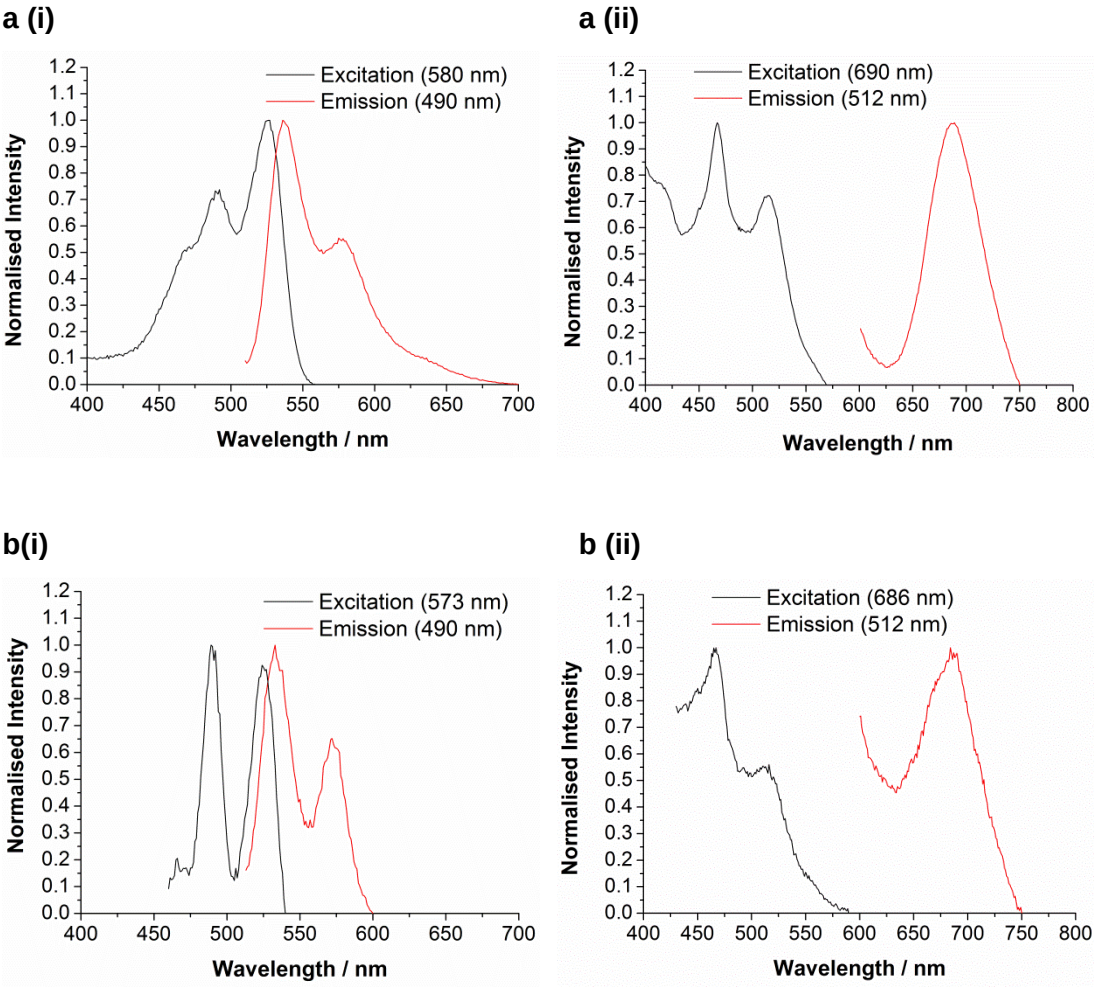

Fig. 5.7: *The emission spectra of Ru(H_2-dcbpy)(4,4`-Y_2-bpy)$(NCS)_2$ where Y =* ***a)*** *Cl;* ***b)*** *Br, in N_2-purged, dry DMF. Experiments were performed* ***(i)*** *at 293 ^oK;* ***(ii)*** *frozen with liquid nitrogen.*

Measuring the excitation spectra showed a peak at 466 or 467 nm for all of the dyes. This peak is not consistent with the λ_{max} values determined by UV/vis spectroscopy (5.4.1.1), but it is consistent with the charge transfer transitions calculated by TDDFT (5.4.1.2). The trough in the experimental absorption spectrum at around 450 nm is not large (Fig. 5.4), and it can be seen for each of the dyes, particularly the 5,5` substituted dyes, that there is an asymmetry in the shape of the trough which suggests a transition at around 470 nm (Fig. 5.5). Therefore, an electronic excitation at this wavelength is likely, although it is masked by other, more prolific, electronic transitions in the UV/vis spectrum.

The change in the lowest energy excitation wavelength matched the trends observed in the experimental absorption spectrum; although all of the transitions were blue–shifted, most likely because of the change in the physical state of the material being measured. The change in the 0-0 transition energy across the series of dyes (Table 5.5) reiterated the larger effect of the nature of the halogens when they are in the 5,5` position than when they are in the 4,4` positions.

5.4.3 Electrochemistry

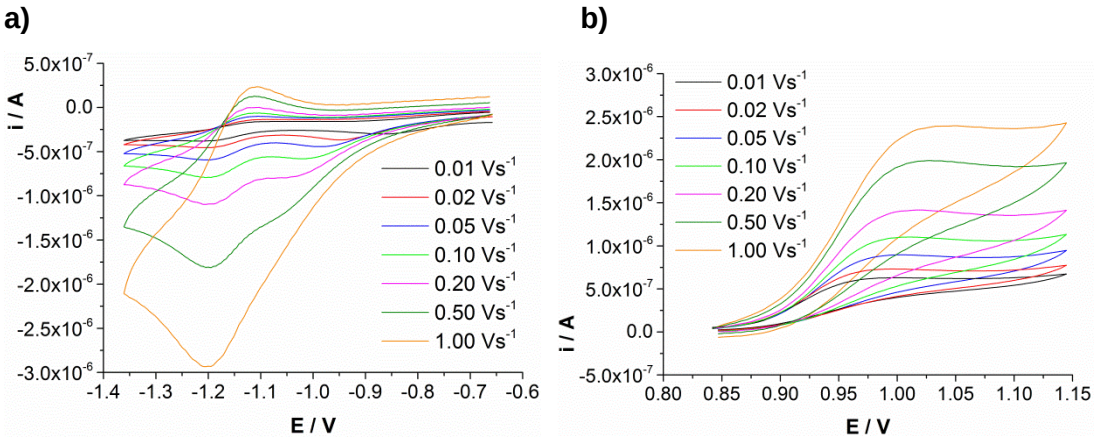

Fig. 5.8: *Scan rate studies on a) the reductions and b) the oxidation of Ru(H_2-dcbpy)(4,4`-$Cl_2$-bpy)$(NCS)_2$. These graphs are also representative of the features observed for Ru($H_2$-dcbpy)(4,4`-Br_2-bpy)$(NCS)_2$ and Ru(H_2-dcbpy)(5,5`-Y_2-bpy)$(NCS)_2$ where Y = F, Cl, Br. Studies were performed in 0.1M $TBABF_4$/ DMF using an Ag/AgCl (sat. LiCl in EtOH) reference. The potentials were calibrated against ferrocene.*

Electrochemical studies on the series of five dyes showed an oxidation process assigned to $Ru^{2+/3+}$ which was chemically irreversible for all of the dyes (Fig. 5.8b). For each of the dyes, two reduction processes were apparent by CV (Fig. 5.8a), but the first reduction was electrochemically irreversible with the E_{red} shifting to more negative potentials with increasing scan rates (Fig. 5.8a). As this peak masked the second reduction process at more negative potentials, the reversibility of the second reduction process could not be conclusively affirmed from the scan rate studies.

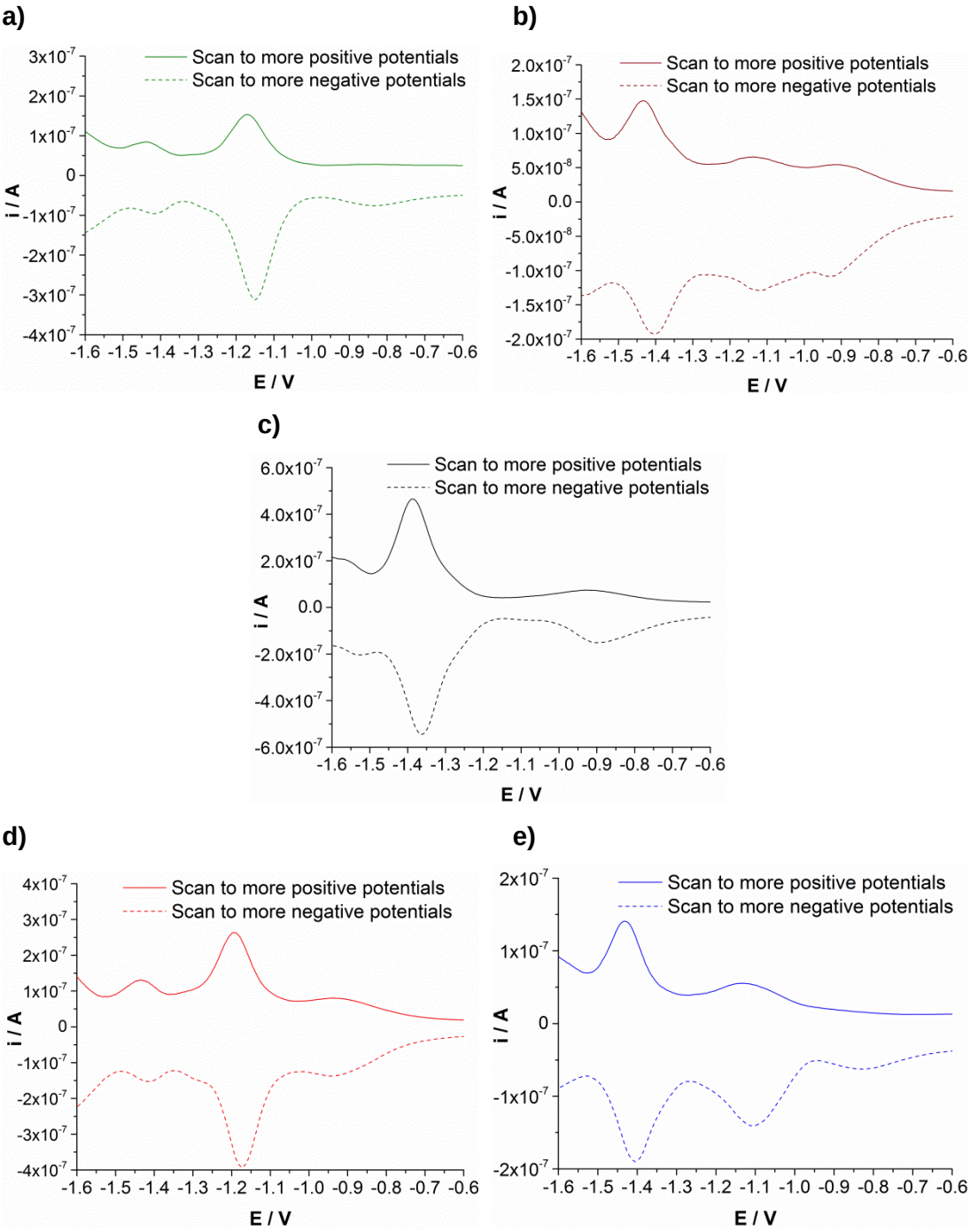

Fig. 5.9: *Differential pulse scans at negative potentials for Ru(H_2-dcbpy)(N,N`-Y_2-bpy)$(NCS)_2$ where a) N = 4, Y = Cl; b) N = 4, Y = Br; c) N = 5, Y = F; d) N = 5, Y = Cl; e) N = 5, Y = Br. Studies were performed in 0.1M $TBABF_4$/ DMF using an Ag/AgCl (sat. LiCl in EtOH) reference. The potentials were calibrated against ferrocene.*

By differential pulse voltammetry, more detailed analysis of the reduction processes was possible. For each dye, three main features were observed in the spectra (Fig. 5.9), but one of the three features appeared to represent a multiple electron process as both the oxidation and reduction peak were considerably larger than the other peaks. It is therefore possible that four reduction processes were observed for the dyes, which would be consistent with the one-electron reduction of each pyridyl ring on the dye.

For all of the dyes, the least negative reduction process was chemically and electrochemically irreversible. This is consistent with the reduction of the H_2-dcbpy ligand which has been previously shown to be chemically irreversible due to the loss of protons from the ligand[125]. That the lowest energy reduction process was due to the reduction of the H_2-dcbpy ligand is consistent with the DFT calculations performed on these dyes (5.2) which suggest that the LUMO is localised on this ligand. Due to the numerous reduction processes observed, further assignment of the peaks observed could not be reliably carried out. However, the $E_{½}$ values for each of the processes were determined (Table 5.6).

Dye	E_{ox} / V	E_{red} / V	$E_{½}$ (red) / V	$E_{½}$ (red) / V
4Cl	0.93	-0.84[#]	-1.16	-1.43
4Br	0.92	-0.93[#]	-1.13	-1.42
5F	0.95	-0.91[#]	-1.37	-1.55
5Cl	0.95	-0.94[#]	-1.18	-1.42
5Br	0.95	-0.82[#]	-1.13	-1.42

Table 5.6: *The electrochemical features of Ru(H_2-dcbpy)(N,N`-Y_2-bpy)$(NCS)_2$ dyes where N = 4, 5; Y = F, Cl, Br. Studies were performed in 0.1M $TBABF_4$ / DMF and referenced to Ag./AgCl (sat. LiCl in EtOH). The potentials were calibrated against ferrocene. [#]The electrochemical irreversibility of these reduction processes causes the potentials obtained to be unreliable. Values in red represent multiple electron reduction processes.*

From these data it can be seen that there is little change in the energy level of the HOMO of these dyes. The potential of the first reduction varies slightly amongst the five dyes, but due to the electrochemical irreversibility of this reduction, the values

obtained could not be deemed reliable. Considering the second reduction process, the effect of changing the position of the Br and Cl substituents on the electrochemical properties of the dyes was apparently negligible for Br and minor for Cl. Irrespective of the position of the substituent; substituting Br atoms for Cl atoms caused the second reduction potential to become more negative. In line with the halide series, substituting Cl atoms for F atoms also caused a shift of the second reduction process to more negative potentials.

5.4.4 Discussion - trends in dye properties

The properties of the 4,4` dyes were little affected by the nature of the halogen substituent; whereas there were significant changes in the 5,5` dyes. This suggests that substituents in the 5,5` positions have a larger effect on the spectroscopic and electrochemical properties of $Ru(H_2\text{-dcbpy})(Y_2\text{-bpy})(NCS)_2$ dyes than substituents in the 4,4` positions. Thus, investigations into the use of different substituents in the 5,5` positions of these dyes could allow fine tuning of the dye properties, without the need to change the H_2-dcbpy or $^-$NCS ligands.

For all of the dyes, the oxidation potential was very similar, suggesting that the nature and position of the substituent of the Y_2-bpy ligand has little effect on the energy of the HOMO. This is consistent with the DFT calculations which show little contribution of the Y_2-bpy ligand to the HOMO, or the other occupied frontier orbitals of the dye (Appendix A3.5 to A3.9). Therefore, the change in UV/vis absorption by the dyes is likely to be due to changes in the unoccupied orbitals of the dyes. For the 5,5` dyes, the energy of the lowest energy MLCT transitions linearly correlates with the second reduction potential of the dye (R^2 = 0.98, Fig. 5.10a); confirming that it is the change in the energies of the unoccupied orbitals which caused the change in UV/vis properties.

When the halogens are in the 5,5` positions, the change in the energy of the lowest energy MLCT transition correlates with the electronegativities (F, 4.0; Cl, 3.0; Br, 2.8[229]) of the halide substituents (R^2 = 0.99, Fig. 5.10a). The second reduction

potential correlates with the change in the lowest energy MLCT transition, thus the second reduction potential of the dye also correlates with the electronegativity of the halide substituent (R^2 = 0.99, Fig. 5.10b). There is also a correlation between the meta Hammett parameter (F, σ_m = 0.34; Cl, σ_m = 0.37; Br, σ_m = 0.39[193]) of the substituent and the lowest energy MLCT and second reduction potential of the dye (R^2 = 0.97, 0.95 respectively). This is consistent with the correlations observed between the Hammett parameters and the reduction potentials of free bpy ligands[235-239], and the oxidation potentials of bpy substituted copper complexes[240]. These correlations suggest that for Ru(H_2-dcbpy)(5,5`-$Y_2$-bpy)$(NCS)_2$ dyes, both the electronegativity and meta Hammett parameter of the Y substituent could be used to predict the dye properties; for example, the use of less electronegative atoms or groups in the 5,5` positions should result in a red shift in the absorption spectrum. However, the 0-0 transition energies of the 5,5` dyes (5.4.2) don't follow the same trend, possibly because the Hammett parameter is measured in solution and the 0-0 transition energy is determined from solid state measurements.

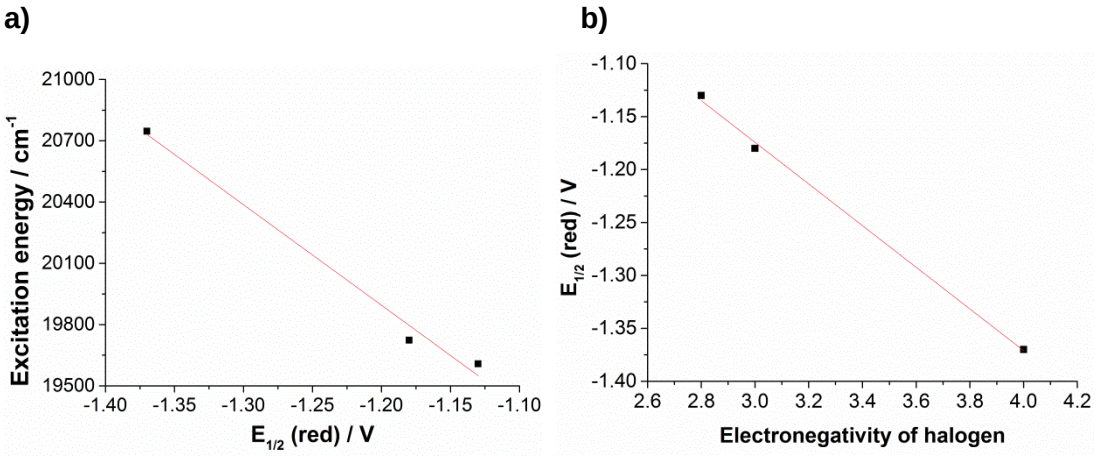

***Fig. 5.10**: The correlation between the second reduction potential of Ru(H_2-dcbpy)(5,5`-Y_2-bpy)$(NCS)_2$ and **a)** the lowest energy excitation wavelength of the dye; **b)** the electronegativity of the halogen substituent.*

5.5 Solar cell studies

From the electrochemical and luminescence studies on the dyes in solution, the reduction potential of the oxidised dye and the oxidation potential of the excited state dye were calculated. This analysis showed small differences in the energy levels of the dyes, particularly the potential of the excited state dye (Fig. 5.11). However, there should be sufficient overpotential for electron injection and dye regeneration for each of the five dyes, so these changes should not have a large effect on the efficiencies of the dyes in a DSSC. It is therefore likely that any significant changes in solar cell efficiency will be due to chemical interactions within the solar cell. The effects of changing the nature and position of the halide substituent on the ancillary bpy ring on the performance of the dyes in DSSCs were therefore explored.

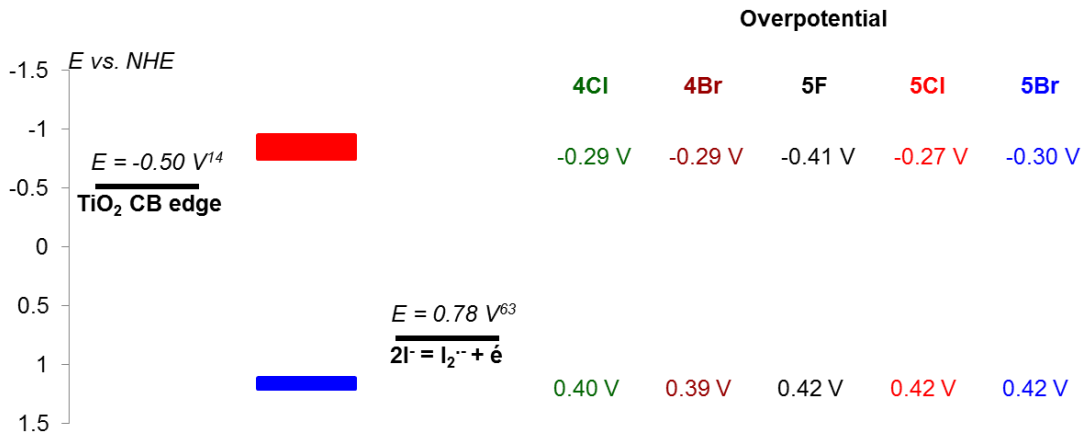

Fig. 5.11: *The overpotential for electron injection and dye regeneration in DSSCs sensitised by Ru(H_2-dcbpy)(N,N`-Y_2-bpy)$(NCS)_2$, where N = 4, 5; Y = F, Cl, Br.*

5.5.1 J-V characteristics

By measuring DSSCs sensitised by these dyes (Appendix A1.5 to A1.9), it was apparent that all five dyes were inferior to N719 in terms of solar cell performance (Table 5.7, Fig 5.12). This is due to the smaller J_{SC} and V_{OC} of the cells sensitised by

the asymmetric dyes. Within the series of halide substituted dyes, the J_{SC}s of cells sensitised by the 4,4` dyes are higher than those for cells sensitised by the 5,5` dyes; which could be due to the higher molar extinction co-efficients of the 4,4` dyes than the 5,5` dyes. Cells sensitised by the 4,4` dyes also had higher V_{OC}s, which could be due to a reduction in recombination within the solar cell.

Dye	J_{sc} / mAcm^{-2}	V_{oc} / mV	FF	η / %
N719	10.66 ± 1.01	636 ± 19	0.623 ± 0.022	4.21 ± 0.28
4Cl	5.59 ± 0.23	524 ± 5	0.664 ± 0.016	1.95 ± 0.05
4Br	5.11 ± 0.14	539 ± 12	0.659 ± 0.037	1.82 ± 0.11
5F	5.29 ± 0.46	536 ± 15	0.672 ± 0.007	1.90 ± 0.18
5Cl	4.05 ± 0.39	499 ± 8	0.677 ± 0.031	1.37 ± 0.15
5Br	4.56 ± 0.50	516 ± 20	0.629 ± 0.034	1.48 ± 0.11

Table 5.7: *The J-V characteristics of DSSCs sensitised by Ru(H_2-dcbpy)(N,N`-Y_2-bpy)(NCS)$_2$ dyes, where N = 4, 5; Y = F, Cl, Br, and N719.The mean values, calculated by measuring six cells, are reported.*

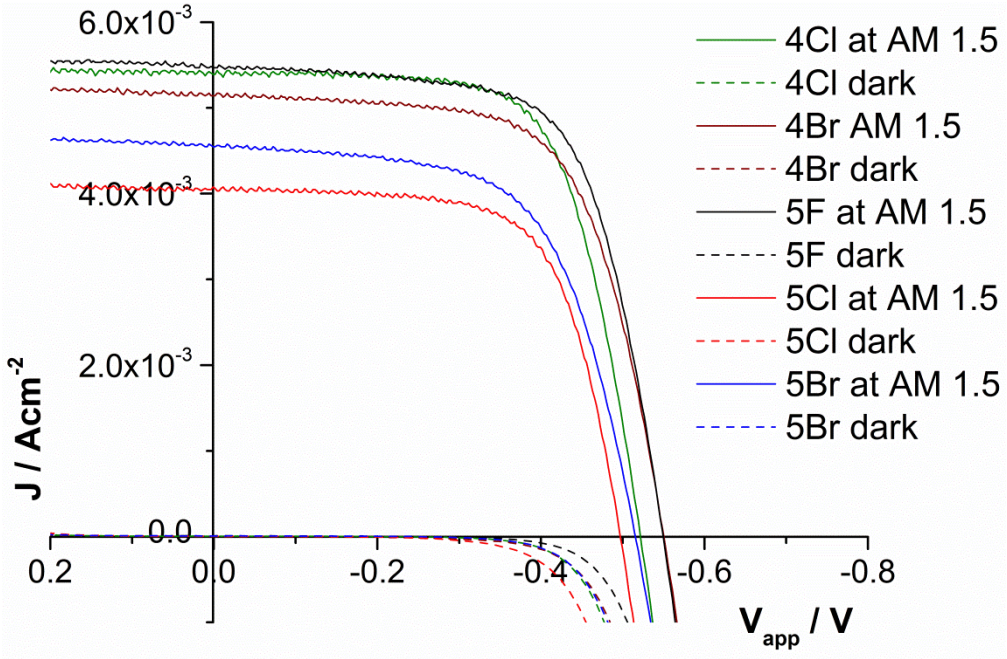

Fig. 5.12: *Representative J-V curves of DSSCs sensitised by Ru(H_2-dcbpy)(N,N`-Y_2-bpy)(NCS)$_2$ dyes, where N = 4, 5; Y = F, Cl, Br.*

With respect to the nature of the halogen substituent, cells sensitised by dyes where Y = Cl had lower V_{OC}s than those sensitised by dyes where Y = Br (Table 5.7, Fig 5.12). For the 5,5` series, the cells sensitised by Ru($H_2$-dcbpy)(5,5`-F_2-bpy)$(NCS)_2$ had the highest V_{OC}s and J_{SC}s (Appendix A1.5 to A1.9), suggesting that of the halides, the use of fluorine atoms is most beneficial in a DSSC. Across the 4,4` and 5,5` series, there was no trend in the change in the J_{SC}s of the cells when Br was substituted by Cl. For further understanding of these changes in solar cell performance, electrochemical impedance spectroscopy of the dyes was carried out.

5.5.2 Impedance studies

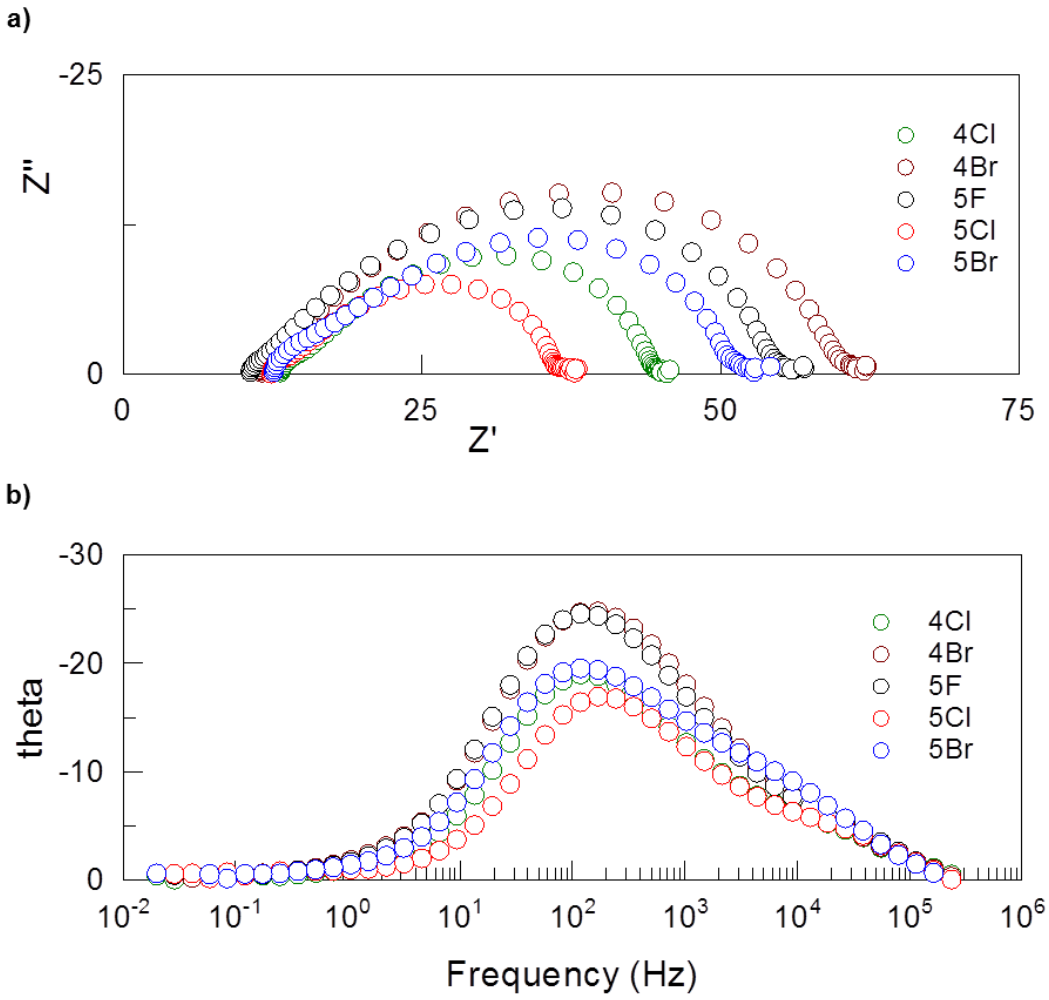

Fig. 5.13: *Representative* ***a)*** *Nyquist and* ***b)*** *Bode plots for DSSCs at -0.5 V sensitised by Ru(H_2-dcbpy)(N,N`-Y_2-bpy)$(NCS)_2$ dyes, where N = 4, 5; Y = F, Cl, Br.*

		TiO_2	TiO_2 – dye – I^- / I_3^-interface	
E_{app} / V	Dye	r_{trans} / Ω cm^{-3}	r_{rec} / Ω cm^3	c_{TiO2} / F cm^{-3}
-0.5	N719	78.40	208.70	7.84×10^{-4}
	4Cl	60.10	14.29	5.05×10^{-4}
	4Br	83.90	20.19	2.51×10^{-4}
	5F	78.58	23.01	2.15×10^{-4}
	5Cl	45.93	11.24	2.68×10^{-4}
	5Br	62.38	17.15	2.37×10^{-4}
-0.6	N719	4.46	30.90	1.85×10^{-3}
	4Cl	14.24	3.79	1.42×10^{-3}
	4Br	18.87	4.79	1.17×10^{-3}
	5F	17.96	3.81	1.27×10^{-3}
	5Cl	13.40	3.16	8.29×10^{-4}
	5Br	16.98	4.06	1.01×10^{-3}
-0.7	N719	-	8.13	3.08×10^{-3}
	4Cl	3.78	2.81	1.80×10^{-3}
	4Br	4.60	3.16	2.01×10^{-3}
	5F	3.53	2.83	1.61×10^{-3}
	5Cl	3.88	2.31	1.18×10^{-3}
	5Br	5.84	2.41	1.47×10^{-3}
-0.8	N719	-	3.64	4.07×10^{-3}
	4Cl	2.59	1.76	2.24×10^{-3}
	4Br	3.27	1.43	2.89×10^{-3}
	5F	3.09	1.24	2.31×10^{-3}
	5Cl	2.72	1.40	1.59×10^{-3}
	5Br	4.18	1.28	2.11×10^{-3}

Table 5.8: *The impedance characteristics of DSSCs sensitised by Ru(H_2-dcbpy)(N,N`-Y_2-bpy)$(NCS)_2$ dyes, where N = 4, 5; Y = F, Cl, Br, and N719.The mean values, calculated by measuring six cells, are reported.*

Considering the Nyquist and Bode plots for the solar cells sensitised by Ru(H_2-dcbpy)(N,N`-Y_2-bpy)$(NCS)_2$ dyes where N = 4, 5; Y = F, Cl, Br (Fig. 5.13); there were no significant changes in the shapes of the plots, showing that the solar cells all have similar characteristics. By modelling the data and considering the capacitance at the TiO_2 surface of the cells, it was clear that there weren't considerable differences in the values calculated for the five dyes (Table 5.8, Appendix, A2.4 to A2.8). The trends across the dye series also changed with the applied voltage (Fig. 5.14). The capacitances at the TiO_2 surface of solar cells sensitised by N719 were slightly higher, but not too dissimilar to the capacitances of solar cells sensitised by the

halogenated dyes. Therefore, it is unlikely that these dyes affect the electronic characteristics of the TiO_2 surface.

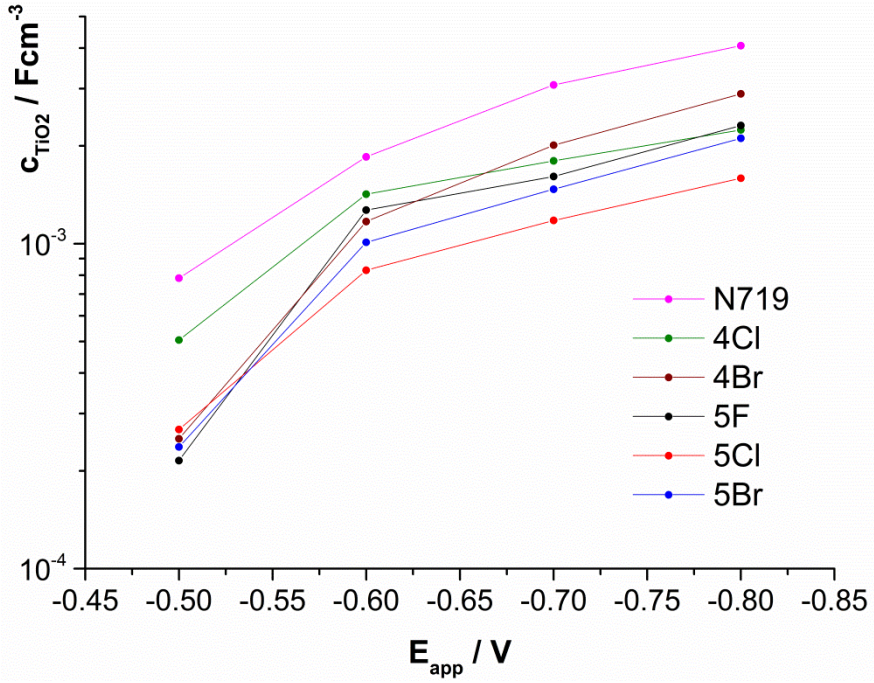

Fig. 5.14: *The variation of the mean capacitance at the TiO_2-dye-I^-/I_3^- interface with the applied forward bias for DSSCs sensitised by Ru(H_2-dcbpy)(N,N`-Y_2-bpy)$(NCS)_2$ dyes, where N = 4, 5; Y = F, Cl, Br.*

However, there were clear trends in the change in the resistance to recombination across this dye series. By plotting the r_{rec} at -0.5 V against the V_{OC} of the cell; there was a reasonable correlation (R^2 = 0.90, Fig. 5.15); showing that decreases in the V_{OC}s of the cells are most likely due to decreases in the resistance to recombination. The higher resistance to recombination across this interface for cells sensitised by N719 is also consistent with the higher V_{OC}s for the N719 cells. Similar relationships between the V_{OC} and the resistance to recombination have also been observed for other series of dyes[84,85].

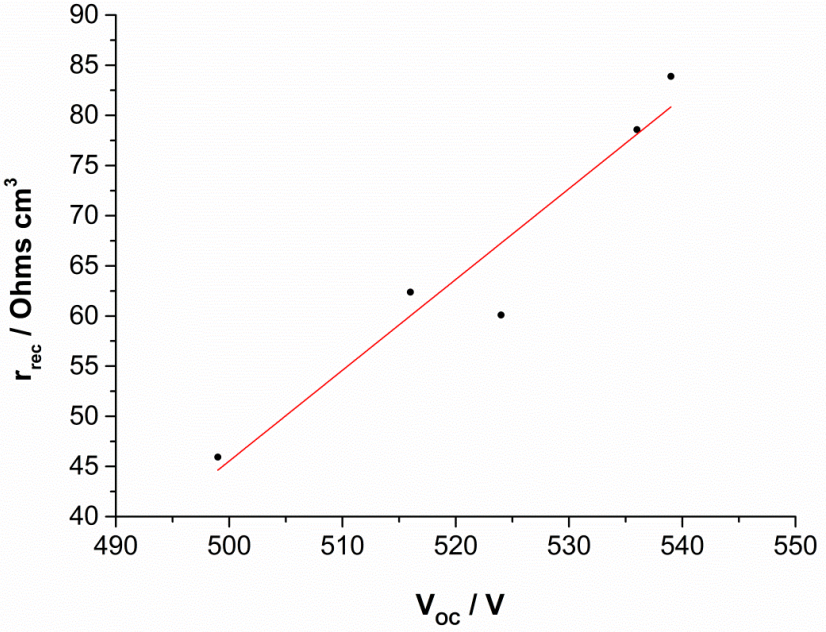

Fig. 5.15: *The correlation between the mean r_{rec} and the mean V_{OC} for DSSCs at -0.5 V sensitised by Ru(H_2-dcbpy)(N,N`-Y_2-bpy)(NCS)$_2$ dyes, where N = 4, 5; Y = F, Cl, Br.*

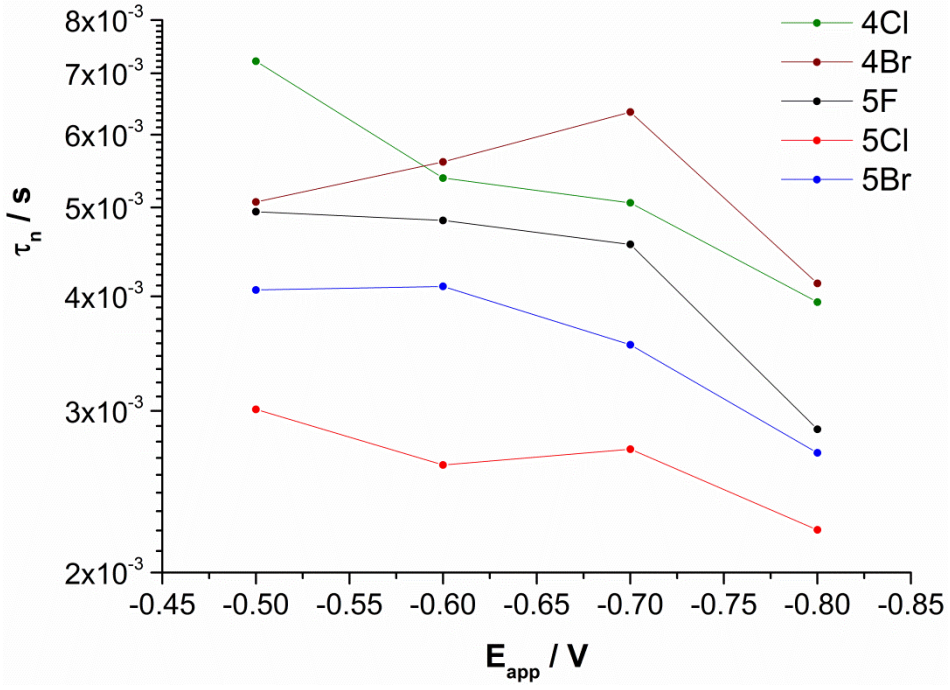

Fig. 5.16: *The variation of the mean electron lifetime at the TiO_2-dye-I^-/I_3^- interface with the applied forward biases for DSSCs sensitised by Ru(H_2-dcbpy)(N,N`-Y_2-bpy)(NCS)$_2$ dyes, where N = 4, 5; Y = F, Cl, Br.*

The electron lifetimes at the TiO_2-dye-I^-/I_3^- interface for solar cells sensitised by $Ru(H_2\text{-dcbpy})(N,N`\text{-}Y_2\text{-bpy})(NCS)_2$ were considerably shorter than the lifetimes of the cells sensitised by N719 – most likely because of the large increase in recombination across this interface. As the distribution of charge in the TiO_2 film was similar across this series of cells, the electron lifetimes were plotted against the applied voltage (Fig. 5.16) showing that the trends were mostly similar to the trends observed for the change in the resistance to recombination of the cells. Thus the change in electron lifetime is also likely to be due to an increase in the rate of recombination across the TiO_2-dye-I^-/I_3^- interface.

The considerable change in cell performance due to the change in the position of the substituent has no precedent in the literature. Due to the position of the substituent, there was also a change in the electronic and spectroscopic properties of the analogous 4,4` and 5,5` dyes. However, all of the dyes still had the required parameters to function in a solar cell, so this should not have effected a considerable change in solar cell performance (5.5). It is possible that the halogen atom in the 5 position (on the pyridyl ring *trans* to ^-NCS) would be closer to the TiO_2 surface than the halogen atom in the 4 position. Therefore, any binding between the halogen and iodine would bring the iodine closer to the surface for the 5,5` dyes than the 4,4` dyes, which could explain this effect.

That the Cl substituted dyes performed more poorly than both the F and Br substituted dyes is not in keeping with the di-iodine basicity scale (5.1). However, if you consider the contribution of resonance or π-effects to the Hammett parameters for these dyes (Br = -0.22, Cl = -0.19, F = -0.39); an increase in the rate of recombination correlates to a decrease in donation of the lone pairs of the halogen atom into the bpy ring. It is feasible that increased resonance into the bpy ring will reduce the availability of the lone pairs for binding to iodine; thus explaining the trends observed. However, determination of the strength of iodine binding to these dyes when they are bound to TiO_2 would be required to verify such a conclusion.

5.6 Conclusion

The effects of changing the positions of the substituents on an ancillary bpy ligand have not been previously studied. However, this investigation showed that the effects were similar to, if not greater than, the effects of changing the nature of the substituent on the bpy ligand. This was found to be true in terms of the electronic and spectroscopic properties of the dyes, as well as the performance of the dye in DSSCs and the rate of recombination at the TiO_2-dye-I^-/I_3^- interface.

The nature of the halogen substituent in the 5,5` positions of the bpy ring also had more of an effect on the spectroscopic and electronic properties of the dye than the nature of the halogens in the 4,4` positions. As the use of halogens led to a poor solar cell performance, and the 5,5` dyes behaved more poorly than the 4,4` dyes, it is possible that the use of substituents which improve solar cell performance could be more beneficial if they are in the 5,5` positions than the 4,4` positions. Therefore, these studies show that careful consideration of the position of substituents, in conjunction with the nature of substituents, on a bpy ring must be considered in order to optimise solar cell performance. Further studies of these effects could therefore enable a more systematic approach to the design of $Ru(H_2\text{-dcbpy})(N,N`\text{-}Y_2\text{-bpy})(NCS)_2$ dyes.

With respect to the halide series, the trends in the V_{OC}s did not follow the recently derived diiodine basicity scale[234]. This scale was derived using the binding constants of iodine to halogens within a variety of environments. However, binding constants for halogenated pyridyl and bpy molecules were not available. There could also be effects due to the bond between the ligand and the metal centre which must be considered. Therefore, to enable consideration of iodine binding to ruthenium dyes; binding constants should be calculated on the dye itself when it is bound to TiO_2. If a number of dyes were thus investigated, it is possible that a scale showing the suitability of substituents to include in dyes for DSSCs could be derived.

Conclusion

In making minor changes to the structures of well-researched ruthenium dyes for DSSCs, significant effects have been observed. By simply substituting the S atoms of the $^{-}$NCS ligands for O in $[Ru(dcbpy)_2(NCX)_2]^{4-}$ dyes, changes in the electronic properties of the TiO_2 surface and a considerable decrease in the resistance to recombination was observed. And even changing substituents from the 4,4` positions to the 5,5` positions on an ancillary bpy ligand in $Ru(H_2\text{-dcbpy})(N,N`\text{-}Y_2\text{-bpy})(NCS)_2$ caused changes in the electronic and spectroscopic properties of the dyes, as well affecting the rate of recombination from the TiO_2 to the electrolyte within the solar cell. These studies have therefore provided new insight into the role of the dye structure on the mechanisms of electron transfer in the TiO_2-ruthenium dye-I^-/I_3^- solar cell.

To perform these studies, the synthesis of the dyes was required. During the course of the study, a large number of previously unreported factors which could prevent successful dye synthesis were discovered; for example, the importance of the order of ligand addition in the synthesis of asymmetric $Ru(H_2\text{-dcbpy})(N,N`\text{-}Y_2\text{-bpy})(NCS)_2$ dyes. Thus two novel synthetic procedures have been developed; and the implementation of reaction monitoring by UV/vis has proved to be valuable in the optimisation of a synthetic procedure. By broadening the tools available for dye synthesis, the synthesis of novel, possibly more unusual, dyes for further exploration of the effects described is likely to be more easily achieved.

References

(1) Arrhenius, S. *Philosophical Magazine and Journal of Science* **1896**, *41*, 237.
(2) Eisenberg, R.; Nocera, D. G. *Inorganic Chemistry* **2005**, *44*, 6799.
(3) Anonymous *New Scientist* **2012**, *214*, 4.
(4) International Energy Agency: http://www.worldenergyoutlook.org/media/weowebsite/2012/factsheets.pdf.
(5) Lewis, N. S.; Nocera, D. G. *Proceedings of the National Academy of Sciences* **2006**, *103*, 15729.
(6) International Energy Agency: http://www.iea.org/publications/freepublications/publication/kwes.pdf.
(7) W. N.; World Nuclear Association: http://www.world-nuclear.org/info/inf75.html.
(8) BBC News: http://www.bbc.co.uk/news/world-europe-13592208, 2011.
(9) The Economist: http://www.economist.com/node/18441163, 2011.
(10) Osterloh, F. E. *Chemical Society Reviews* **2013**, *42*, 2294.
(11) Becquerel, M. E. *Comptes Rendus de l'Academie des Sciences* **1839**, *9*, 561.
(12) Fritts, C. E. *American Journal of Science* **1883**, *26*, 465.
(13) European Photovoltaic Industry Association: http://www.epia.org/home/.
(14) National Renewable Energy Laboratory: http://www.nrel.gov/ncpv/images/efficiency_chart.jpg.
(15) Argazzi, R.; Murakami Iha, N. Y.; Zabri, H.; Odobel, F.; Bignozzi, C. A. *Coordination Chemistry Reviews* **2004**, *248*, 1299.
(16) Angelis, F. D.; Fantacci, S.; Selloni, A. *Nanotechnology* **2008**, *19*, 424002.
(17) Boschloo, G.; Hagfeldt, A. *Accounts of Chemical Research* **2009**, *42*, 1819.
(18) Nazeeruddin, M. K.; Kay, A.; Rodicio, I.; Humphry-Baker, R.; Mueller, E.; Liska, P.; Vlachopoulos, N.; Grätzel, M. *Journal of the American Chemical Society* **1993**, *115*, 6382.
(19) Zakeeruddin, S. M.; Nazeeruddin, M. K.; Humphry-Baker, R.; Péchy, P.; Quagliotto, P.; Barolo, C.; Viscardi, G.; Grätzel, M. *Langmuir* **2002**, *18*, 952.
(20) Peter, L. *Accounts of Chemical Research* **2009**, *42*, 1839.
(21) Anderson, A. Y.; Barnes, P. R. F.; Durrant, J. R.; O'Regan, B. C. *The Journal of Physical Chemistry C* **2011**, *115*, 2439.
(22) Clifford, J. N.; Palomares, E.; Nazeeruddin, M. K.; Grätzel, M.; Durrant, J. R. *The Journal of Physical Chemistry C* **2007**, *111*, 6561.
(23) Wang, P.; Zakeeruddin, S. M.; Moser, J. E.; Nazeeruddin, M. K.; Sekiguchi, T.; Grätzel, M. *Nature Materials* **2003**, *2*, 402.
(24) Fujishima, A.; Honda, K. *Nature* **1972**, *238*, 37.
(25) Tributsch, H. *Photochemistry and Photobiology* **1972**, *16*, 261.
(26) O'Regan, B.; Grätzel, M. *Nature* **1991**, *353*, 737.

(27) Furlong, D. N.; Wells, D.; Sasse, W. H. F. *The Journal of Physical Chemistry* **1986**, *90*, 1107.
(28) Gerischer, H.; Willig, F. In *Physical and Chemical Applications of Dyestuffs*; Schäfer, F. P., Gerischer, H., Willig, F., Meier, H., Jahnke, H., Schönborn, M., Zimmermann, G., Eds.; Springer Berlin Heidelberg: 1976; Vol. 61, p 31.
(29) Vlachopoulos, N.; Liska, P.; Augustynski, J.; Graetzel, M. *Journal of the American Chemical Society* **1988**, *110*, 1216.
(30) Amadelli, R.; Argazzi, R.; Bignozzi, C. A.; Scandola, F. *Journal of the American Chemical Society* **1990**, *112*, 7099.
(31) Kalyanasundaram, K.; Grätzel, M. *Coordination Chemistry Reviews* **1998**, *177*, 347.
(32) Gillaizeau-Gauthier, I.; Odobel, F.; Alebbi, M.; Argazzi, R.; Costa, E.; Bignozzi, C. A.; Qu, P.; Meyer, G. J. *Inorganic Chemistry* **2001**, *40*, 6073.
(33) Galoppini, E. *Coordination Chemistry Reviews* **2004**, *248*, 1283.
(34) Nazeeruddin, M. K.; Zakeeruddin, S. M.; Humphry-Baker, R.; Jirousek, M.; Liska, P.; Vlachopoulos, N.; Shklover, V.; Fischer, C.-H.; Grätzel, M. *Inorganic Chemistry* **1999**, *38*, 6298.
(35) K. Nazeeruddin, M.; Pechy, P.; Gratzel, M. *Chemical Communications* **1997**, *0*, 1705.
(36) Han, L.; Islam, A.; Chen, H.; Malapaka, C.; Chiranjeevi, B.; Zhang, S.; Yang, X.; Yanagida, M. *Energy & Environmental Science* **2012**, *5*, 6057.
(37) Garcia-Iglesias, M.; Pelleja, L.; Yum, J.-H.; Gonzalez-Rodriguez, D.; Nazeeruddin, M. K.; Grätzel, M.; Clifford, J. N.; Palomares, E.; Vazquez, P.; Torres, T. *Chemical Science* **2012**, *3*, 1177.
(38) Gao, F.; Wang, Y.; Shi, D.; Zhang, J.; Wang, M.; Jing, X.; Humphry-Baker, R.; Wang, P.; Zakeeruddin, S. M.; Grätzel, M. *Journal of the American Chemical Society* **2008**, *130*, 10720.
(39) National Renewable Energy Laboratory: http://rredc.nrel.gov/solar/spectra/am1.5/.
(40) Campagna, S.; Puntoriero, F.; Nastasi, F.; Bergamini, G.; Balzani, V.; Balzani, V., Campagna, S., Eds.; Springer Berlin / Heidelberg: 2007; Vol. 280, p 117.
(41) Pastore, M.; Fantacci, S.; De Angelis, F. *The Journal of Physical Chemistry C* **2013**, *117*, 3685.
(42) Caspar, J. V.; Meyer, T. J. *Inorganic Chemistry* **1983**, *22*, 2444.
(43) Robertson, N. *Angewandte Chemie International Edition* **2006**, *45*, 2338.
(44) Nazeeruddin, M. K.; De Angelis, F.; Fantacci, S.; Selloni, A.; Viscardi, G.; Liska, P.; Ito, S.; Takeru, B.; Grätzel, M. *Journal of the American Chemical Society* **2005**, *127*, 16835.
(45) Vos, J. G.; Kelly, J. M. *Dalton Transactions* **2006**, *0*, 4869.

(46) Hoertz, P. G.; Staniszewski, A.; Marton, A.; Higgins, G. T.; Incarvito, C. D.; Rheingold, A. L.; Meyer, G. J. *Journal of the American Chemical Society* **2006**, *128*, 8234.
(47) Benkö, G.; Kallioinen, J.; Korppi-Tommola, J. E. I.; Yartsev, A. P.; Sundström, V. *Journal of the American Chemical Society* **2001**, *124*, 489.
(48) Wenger, B.; Grätzel, M.; Moser, J.-E. *Journal of the American Chemical Society* **2005**, *127*, 12150.
(49) Das, S.; Kamat, P. V. *The Journal of Physical Chemistry B* **1998**, *102*, 8954.
(50) Tachibana, Y.; Moser, J. E.; Grätzel, M.; Klug, D. R.; Durrant, J. R. *The Journal of Physical Chemistry* **1996**, *100*, 20056.
(51) Bell, T. D. M.; Pagba, C.; Myahkostupov, M.; Hofkens, J.; Piotrowiak, P. *The Journal of Physical Chemistry B* **2006**, *110*, 25314.
(52) Grätzel, M. *Inorganic Chemistry* **2005**, *44*, 6841.
(53) Peter, L. M. *The Journal of Physical Chemistry C* **2007**, *111*, 6601.
(54) Papageorgiou, N.; Maier, W. F.; Grätzel, M. *Journal of The Electrochemical Society* **1997**, *144*, 876.
(55) Wang, H.; Nicholson, P. G.; Peter, L.; Zakeeruddin, S. M.; Grätzel, M. *The Journal of Physical Chemistry C* **2010**, *114*, 14300.
(56) Zistler, M.; Wachter, P.; Wasserscheid, P.; Gerhard, D.; Hinsch, A.; Sastrawan, R.; Gores, H. J. *Electrochimica Acta* **2006**, *52*, 161.
(57) Pelet, S.; Moser, J.-E.; Grätzel, M. *The Journal of Physical Chemistry B* **2000**, *104*, 1791.
(58) Montanari, I.; Nelson, J.; Durrant, J. R. *The Journal of Physical Chemistry B* **2002**, *106*, 12203.
(59) Anderson, A. Y.; Barnes, P. R. F.; Durrant, J. R.; O'Regan, B. C. *The Journal of Physical Chemistry C* **2010**, *114*, 1953.
(60) Wu, K.-L.; Li, C.-H.; Chi, Y.; Clifford, J. N.; Cabau, L.; Palomares, E.; Cheng, Y.-M.; Pan, H.-A.; Chou, P.-T. *Journal of the American Chemical Society* **2012**, *134*, 7488.
(61) Schiffmann, F.; VandeVondele, J.; Hutter, J.; Urakawa, A.; Wirz, R.; Baiker, A. *Proceedings of the National Academy of Sciences* **2010**, *107*, 4830.
(62) Privalov, T.; Boschloo, G.; Hagfeldt, A.; Svensson, P. H.; Kloo, L. *The Journal of Physical Chemistry C* **2008**, *113*, 783.
(63) Asaduzzaman, A. M.; Schreckenbach, G. *Physical Chemistry Chemical Physics* **2011**, *13*, 15148.
(64) Gardner, J. M.; Giaimuccio, J. M.; Meyer, G. J. *Journal of the American Chemical Society* **2008**, *130*, 17252.
(65) Jeon, J.; Goddard, W. A.; Kim, H. *Journal of the American Chemical Society* **2013**, *135*, 2431.
(66) Suryanarayanan, V.; Lee, K.-M.; Chen, J.-G.; Ho, K.-C. *Journal of Electroanalytical Chemistry* **2009**, *633*, 146.

(67) Boschloo, G.; Gibson, E. A.; Hagfeldt, A. *The Journal of Physical Chemistry Letters* **2011**, *2*, 3016.
(68) O'Regan, B. C.; Durrant, J. R. *Accounts of Chemical Research* **2009**, *42*, 1799.
(69) Grampp, G. *Angewandte Chemie International Edition in English* **1993**, *32*, 691.
(70) Marcus, R. A. *The Journal of Chemical Physics* **1956**, *24*, 966.
(71) Marcus, R. A. *Discussions of the Faraday Society* **1960**, *29*, 21.
(72) Ramakrishna, G.; Ghosh, H. N. *The Journal of Physical Chemistry B* **2001**, *105*, 7000.
(73) Gaal, D. A.; Hupp, J. T. *Journal of the American Chemical Society* **2000**, *122*, 10956.
(74) Martini, I.; Hodak, J. H.; Hartland, G. V. *The Journal of Physical Chemistry B* **1998**, *102*, 607.
(75) Kuciauskas, D.; Freund, M. S.; Gray, H. B.; Winkler, J. R.; Lewis, N. S. *The Journal of Physical Chemistry B* **2000**, *105*, 392.
(76) Clifford, J. N.; Palomares, E.; Nazeeruddin, M. K.; Grätzel, M.; Nelson, J.; Li, X.; Long, N. J.; Durrant, J. R. *Journal of the American Chemical Society* **2004**, *126*, 5225.
(77) Zhang, C.; Huang, Y.; Huo, Z.; Chen, S.; Dai, S. *The Journal of Physical Chemistry C* **2009**, *113*, 21779.
(78) Yu, Q.; Wang, Y.; Yi, Z.; Zu, N.; Zhang, J.; Zhang, M.; Wang, P. *ACS Nano* **2010**, *4*, 6032.
(79) Reynal, A.; Forneli, A.; Palomares, E. *Energy & Environmental Science* **2010**, *3*, 805.
(80) Sae-Kung, C.; Hatha, A.; Sichanugrist, P.; Pungwiwut, N.; Laosooksathit, S. In *Organic Photovoltaics VIII* 2007; Vol. 6656, p 665617/1
(81) Murakami, T. N.; Koumura, N.; Uchiyama, T.; Uemura, Y.; Obuchi, K.; Masaki, N.; Kimura, M.; Mori, S. *Journal of Materials Chemistry A* **2013**, *1*, 792.
(82) Reynal, A.; Forneli, A.; Martinez-Ferrero, E.; Sánchez-Díaz, A.; Vidal-Ferran, A. n.; O'Regan, B. C.; Palomares, E. *Journal of the American Chemical Society* **2008**, *130*, 13558.
(83) O'Regan, B. C.; Walley, K.; Juozapavicius, M.; Anderson, A.; Matar, F.; Ghaddar, T.; Zakeeruddin, S. M.; Klein, C. d.; Durrant, J. R. *Journal of the American Chemical Society* **2009**, *131*, 3541.
(84) Wu, K.-L.; Hsu, H.-C.; Chen, K.; Chi, Y.; Chung, M.-W.; Liu, W.-H.; Chou, P.-T. *Chemical Communications* **2010**, *46*, 5124.
(85) Liu, B.; Zhu, W.; Wang, Y.; Wu, W.; Li, X.; Chen, B.; Long, Y.-T.; Xie, Y. *Journal of Materials Chemistry* **2012**, *22*, 7434.

(86) Tuikka, M.; Hirva, P.; Rissanen, K.; Korppi-Tommola, J.; Haukka, M. *Chemical Communications* **2011**, *47*, 4499.
(87) Li, X.; Reynal, A.; Barnes, P.; Humphry-Baker, R.; Zakeeruddin, S. M.; De Angelis, F.; O'Regan, B. C. *Physical Chemistry Chemical Physics* **2012**, *14*, 15421.
(88) Jennings, J. R.; Liu, Y.; Wang, Q.; Zakeeruddin, S. M.; Gratzel, M. *Physical Chemistry Chemical Physics* **2011**, *13*, 6637.
(89) Yanagida, S.; Yu, Y.; Manseki, K. *Accounts of Chemical Research* **2009**, *42*, 1827.
(90) Hamann, T. W. *Dalton Transactions* **2012**, *41*, 3111.
(91) Feldt, S. M.; Gibson, E. A.; Gabrielsson, E.; Sun, L.; Boschloo, G.; Hagfeldt, A. *Journal of the American Chemical Society* **2010**, *132*, 16714.
(92) Yella, A.; Lee, H.-W.; Tsao, H. N.; Yi, C.; Chandiran, A. K.; Nazeeruddin, M. K.; Diau, E. W.-G.; Yeh, C.-Y.; Zakeeruddin, S. M.; Grätzel, M. *Science* **2011**, *334*, 629.
(93) Hardin, B. E.; Snaith, H. J.; McGehee, M. D. *Nat Photon* **2012**, *6*, 162.
(94) Burschka, J.; Dualeh, A.; Kessler, F.; Baranoff, E.; Cevey-Ha, N.-L.; Yi, C.; Nazeeruddin, M. K.; Grätzel, M. *Journal of the American Chemical Society* **2011**, *133*, 18042.
(95) Burschka, J.; Pellet, N.; Moon, S.-J.; Humphry-Baker, R.; Gao, P.; Nazeeruddin, M. K.; Gratzel, M. *Nature* **2013**, *499*, 316.
(96) Bessho, T.; Yoneda, E.; Yum, J.-H.; Guglielmi, M.; Tavernelli, I.; Imai, H.; Rothlisberger, U.; Nazeeruddin, M. K.; Grätzel, M. *Journal of the American Chemical Society* **2009**, *131*, 5930.
(97) Greijer Agrell, H.; Lindgren, J.; Hagfeldt, A. *Solar Energy* **2003**, *75*, 169.
(98) Tuyet Nguyen, P.; Degn, R.; Thai Nguyen, H.; Lund, T. *Solar Energy Materials and Solar Cells* **2009**, *93*, 1939.
(99) Hinsch, A.; Kroon, J. M.; Kern, R.; Uhlendorf, I.; Holzbock, J.; Meyer, A.; Ferber, J. *Progress in Photovoltaics: Research and Applications* **2001**, *9*, 425.
(100) Thomalla, M.; Tributsch, H. *Comptes Rendus Chimie* **2006**, *9*, 659.
(101) Robson, K. C. D.; Koivisto, B. D.; Yella, A.; Sporinova, B.; Nazeeruddin, M. K.; Baumgartner, T.; Grätzel, M.; Berlinguette, C. P. *Inorganic Chemistry* **2011**, *50*, 5494.
(102) Shockley, W.; Queisser, H. J. *Journal of Applied Physics* **1961**, *32*, 510.
(103) Péchy, P.; Renouard, T.; Zakeeruddin, S. M.; Humphry-Baker, R.; Comte, P.; Liska, P.; Cevey, L.; Costa, E.; Shklover, V.; Spiccia, L.; Deacon, G. B.; Bignozzi, C. A.; Grätzel, M. *Journal of the American Chemical Society* **2001**, *123*, 1613.
(104) Onozawa-Komatsuzaki, N.; Funaki, T.; Kasuga, K.; Nakazawa, Y.; Sayama, K.; Sugihara, H. *Japanese Journal of Applied Physics* **2012**, *51*, 10NE11.

(105) Hsu, Y.-C.; Zheng, H.; T'Suen Lin, J.; Ho, K.-C. *Solar Energy Materials and Solar Cells* **2005**, *87*, 357.
(106) Funaki, T.; Funakoshi, H.; Kitao, O.; Onozawa-Komatsuzaki, N.; Kasuga, K.; Sayama, K.; Sugihara, H. *Angewandte Chemie International Edition* **2012**, *51*, 7528.
(107) McCall, K. L.; Jennings, J. R.; Wang, H.; Morandeira, A.; Peter, L. M.; Durrant, J. R.; Yellowlees, L. J.; Woollins, J. D.; Robertson, N. *Journal of Photochemistry and Photobiology A: Chemistry* **2009**, *202*, 196.
(108) Shklover, V.; Nazeeruddin, M. K.; Grätzel, M.; Ovchinnikov, Y. E. *Applied Organometallic Chemistry* **2002**, *16*, 635.
(109) Shklover, V.; Ovchinnikov, Y. E.; Braginsky, L. S.; Zakeeruddin, S. M.; Grätzel, M. *Chemistry of Materials* **1998**, *10*, 2533.
(110) Polo, A. S.; Itokazu, M. K.; Murakami Iha, N. Y. *Coordination Chemistry Reviews* **2004**, *248*, 1343.
(111) Wolfbauer, G.; Bond, A. M.; MacFarlane, D. R. *Inorganic Chemistry* **1999**, *38*, 3836.
(112) Gottlieb, H. E.; Kotlyar, V.; Nudelman, A. *The Journal of Organic Chemistry* **1997**, *62*, 7512.
(113) Fulmer, G. R.; Miller, A. J. M.; Sherden, N. H.; Gottlieb, H. E.; Nudelman, A.; Stoltz, B. M.; Bercaw, J. E.; Goldberg, K. I. *Organometallics* **2010**, *29*, 2176.
(114) Tuyet Nguyen, P.; Rand Andersen, A.; Morten Skou, E.; Lund, T. *Solar Energy Materials and Solar Cells* **2010**, *94*, 1582.
(115) Nour-Mohammadi, F.; Nguyen, H. T.; Boschloo, G.; Lund, T. *Journal of Photochemistry and Photobiology A: Chemistry* **2007**, *187*, 348.
(116) Hansen, G.; Gervang, B.; Lund, T. *Inorganic Chemistry* **2003**, *42*, 5545.
(117) Jänis, J.; Jakonen, M.; Oresmaa, L.; Hirva, P.; Laurila, E.; Vlasova, L.; Vainiotalo, P.; Haukka, M. *Organometallics* **2010**, *29*, 1070.
(118) Hori, H.; Ishihara, J.; Koike, K.; Takeuchi, K.; Ibusuki, T.; Tanabe, J.; Ishitani, O. *Analytical Sciences* **1998**, *14*, 287.
(119) Norbury, A. H. In *Advances in Inorganic Chemistry and Radiochemistry*; Emeléus, H. J., Sharpe, A. G., Eds.; Academic Press: 1975; Vol. Volume 17, p 231.
(120) Caspar, J. V.; Meyer, T. J. *Journal of the American Chemical Society* **1983**, *105*, 5583.
(121) Lin, S. H. *The Journal of Chemical Physics* **1970**, *53*, 3766.
(122) Adelt, M.; Devenney, M.; Meyer, T. J.; Thompson, D. W.; Treadway, J. A. *Inorganic Chemistry* **1998**, *37*, 2616.
(123) Noviandri, I.; Brown, K. N.; Fleming, D. S.; Gulyas, P. T.; Lay, P. A.; Masters, A. F.; Phillips, L. *The Journal of Physical Chemistry B* **1999**, *103*, 6713.

(124) Wolfbauer, G.; M. Bond, A.; R. MacFarlane, D. *Journal of the Chemical Society, Dalton Transactions* **1999**, *0*, 4363.
(125) Eskelinen, E.; Luukkanen, S.; Haukka, M.; Ahlgren, M.; Pakkanen, T. A. *Journal of the Chemical Society, Dalton Transactions* **2000**, *0*, 2745.
(126) Bates, R. G.; Macaskill, J. B. *Pure and Applied Chemistry* **1978**, *50*, 1701.
(127) Pizzoli, G.; Lobello, M. G.; Carlotti, B.; Elisei, F.; Nazeeruddin, M. K.; Vitillaro, G.; De Angelis, F. *Dalton Transactions* **2012**, *41*, 11841.
(128) Becke, A. D. *Journal of Chemical Physics* **1993**, *98*, 5648.
(129) Stephens, P. J.; Devlin, F. J.; Chabalowski, C. F.; Frisch, M. J. *The Journal of Physical Chemistry* **1994**, *98*, 11623.
(130) Lee, C.; Yang, W.; Parr, R. G. *Physical Review B* **1988**, *37*, 785.
(131) Lobello, M. G.; Fantacci, S.; De Angelis, F. *The Journal of Physical Chemistry C* **2011**, *115*, 18863.
(132) De Angelis, F.; Fantacci, S.; Selloni, A. *Chemical Physics Letters* **2004**, *389*, 204.
(133) Escudero, D.; González, L. *Journal of Chemical Theory and Computation* **2011**, *8*, 203.
(134) Feller, D. *Journal of Computational Chemistry* **1996**, *17*, 1571.
(135) Schuchardt, K. L.; Didier, B. T.; Elsethagen, T.; Sun, L.; Gurumoorthi, V.; Chase, J.; Li, J.; Windus, T. L. *Journal of Chemical Information and Modeling* **2007**, *47*, 1045.
(136) Hay, P. J.; Wadt, W. R. *Journal of Chemical Physics* **1985**, *82*, 270.
(137) Krishnan, R.; Binkley, J. S.; Seeger, R.; Pople, J. A. *The Journal of Chemical Physics* **1980**, *72*, 650.
(138) McLean, A. D.; Chandler, G. S. *The Journal of Chemical Physics* **1980**, *72*, 5639.
(139) Blaudeau, J.-P.; McGrath, M. P. *Journal of Chemical Physics* **1997**, *107*, 5016.
(140) Zhang, X.; Zhang, W.; Meng, F. *Journal of Theoretical and Computational Chemistry* **2012**, *11*, 421.
(141) Miertuš, S.; Scrocco, E.; Tomasi, J. *Chemical Physics* **1981**, *55*, 117.
(142) Cossi, M.; Barone, V.; Cammi, R.; Tomasi, J. *Chemical Physics Letters* **1996**, *255*, 327.
(143) Kalyanasundaram, K. *Dye-Sensitized Solar Cells*; CRC PressINC, 2010.
(144) Lasia, A. In *Modern Aspects of Electrochemistry*; Conway, B. E., Bockris, J. O. M., White, R., Eds.; Springer US: 2002; Vol. 32, p 143.
(145) Kern, R.; Sastrawan, R.; Ferber, J.; Stangl, R.; Luther, J. *Electrochimica Acta* **2002**, *47*, 4213.
(146) Wang, Q.; Moser, J.-E.; Grätzel, M. *The Journal of Physical Chemistry B* **2005**, *109*, 14945.
(147) Bisquert, J. *Physical Chemistry Chemical Physics* **2000**, *2*, 4185.

(148) Bisquert, J. *The Journal of Physical Chemistry B* **2001**, *106*, 325.
(149) Wang, Q.; Ito, S.; Grätzel, M.; Fabregat-Santiago, F.; Mora-Seró, I.; Bisquert, J.; Bessho, T.; Imai, H. *The Journal of Physical Chemistry B* **2006**, *110*, 25210.
(150) Sánchez, M.; Rincón, M. E.; Guirado-López, R. A. *The Journal of Physical Chemistry C* **2009**, *113*, 21635.
(151) Fabregat-Santiago, F.; Bisquert, J.; Garcia-Belmonte, G.; Boschloo, G.; Hagfeldt, A. *Solar Energy Materials and Solar Cells* **2005**, *87*, 117.
(152) Barnes, P. R. F.; Miettunen, K.; Li, X.; Anderson, A. Y.; Bessho, T.; Gratzel, M.; O'Regan, B. C. *Advanced Materials* **2013**, *25*, 1881.
(153) Wang, M.; Chen, P.; Humphry-Baker, R.; Zakeeruddin, S. M.; Grätzel, M. *ChemPhysChem* **2009**, *10*, 290.
(154) Adachi, M.; Sakamoto, M.; Jiu, J.; Ogata, Y.; Isoda, S. *The Journal of Physical Chemistry B* **2006**, *110*, 13872.
(155) Adachi, M.; Noda, K.; Tanino, R.; Adachi, J.; Tsuchiya, K.; Mori, Y.; Uchida, F. *Chemistry Letters* **2011**, *40*, 890.
(156) Reynal, A.; Palomares, E. *European Journal of Inorganic Chemistry* **2011**, *2011*, 4509.
(157) Griffith, W. P. *Ruthenium Oxidation Complexes: Their Uses As Homogenous Organic Catalysts*; Springer Netherlands, 2011.
(158) Takeuchi, K. J.; Samuels, G. J.; Gersten, S. W.; Gilbert, J. A.; Meyer, T. J. *Inorganic Chemistry* **1983**, *22*, 1407.
(159) Kohle, O.; Grätzel, M.; Meyer, A. F.; Meyer, T. B. *Advanced Materials* **1997**, *9*, 904.
(160) Wadman, S. H.; Kroon, J. M.; Bakker, K.; Havenith, R. W. A.; van Klink, G. P. M.; van Koten, G. *Organometallics* **2010**, *29*, 1569.
(161) Nazeeruddin, M. K.; Grätzel, M. *Inorganic Syntheses* **2002**, *33*, 185.
(162) Wu, X.-H.; Wang, S.; Guo, Y.; Xie, Z.-Y.; Han, L.; Jiang, Z.-H. *Chinese Journal of Chemistry* **2008**, *26*, 1939.
(163) Freys, J. C.; Gardner, J. M.; D'Amario, L.; Brown, A. M.; Hammarstrom, L. *Dalton Transactions* **2012**, *41*, 13105.
(164) Kristensen, S. H.; Toster, J.; Iyer, K. S.; Raston, C. L. *New Journal of Chemistry* **2011**, *35*, 2752.
(165) Xie, P.-H.; Hou, Y.-J.; Wei, T.-X.; Zhang, B.-W.; Cao, Y.; Huang, C.-H. *Inorganica Chimica Acta* **2000**, *308*, 73.
(166) Mahalingam, V.; Chitrapriya, N.; Fronczek, F. R.; Natarajan, K. *Polyhedron* **2008**, *27*, 2743.
(167) Kohle, O.; Ruile, S.; Grätzel, M. *Inorganic Chemistry* **1996**, *35*, 4779.
(168) Bennett, M. A.; Huang, T. N.; Matheson, T. W.; Smith, A. K.; Ittel, S.; Nickerson, W. In *Inorganic Syntheses*; John Wiley & Sons, Inc.: 2007, p 74.

(169) Nazeeruddin, M. K.; Zakeeruddin, S. M.; Lagref, J. J.; Liska, P.; Comte, P.; Barolo, C.; Viscardi, G.; Schenk, K.; Graetzel, M. *Coordination Chemistry Reviews* **2004**, *248*, 1317.
(170) Sosa, J. M. *Analytical Chemistry* **1980**, *52*, 910.
(171) Hallett, A. J.; Jones, J. E. *Dalton Transactions* **2011**, *40*, 3871.
(172) Rau, S.; Schäfer, B.; Grüßing, A.; Schebesta, S.; Lamm, K.; Vieth, J.; Görls, H.; Walther, D.; Rudolph, M.; Grummt, U. W.; Birkner, E. *Inorganica Chimica Acta* **2004**, *357*, 4496.
(173) Sun, Y.; Machala, M. L.; Castellano, F. N. *Inorganica Chimica Acta* **2010**, *363*, 283.
(174) Anderson, T. J.; Scott, J. R.; Millett, F.; Durham, B. *Inorganic Chemistry* **2006**, *45*, 3843.
(175) Baghurst, D. R.; Mingos, D. M. P. *Journal of Organometallic Chemistry* **1990**, *384*, C57.
(176) Nazeeruddin, M. K.; Kalyanasundaram, K. *Inorganic Chemistry* **1989**, *28*, 4251.
(177) Nagao, H.; Ooyama, D.; Hirano, T.; Naoi, H.; Shimada, M.; Sasaki, S.; Nagao, N.; Mukaida, M.; Oi, T. *Inorganica Chimica Acta* **2001**, *320*, 60.
(178) Schalke, P. M. In *Ullmann's Encyclopedia of Industrial Chemistry*; Wiley-VCH Verlag GmbH & Co. KGaA: 2000.
(179) Hála, J. *Journal of Physical and Chemical Reference Data* **2004**, *33*, 176.
(180) Pearson, D. E.; Buehler, C. A. *Chemical Reviews* **1974**, *74*, 45.
(181) Waitkins, G. R.; Shutt, R.; McReynolds, J. P.; McFadden, R. L. In *Inorganic Syntheses*; John Wiley & Sons, Inc.: 2007, p 186.
(182) Ryan, P. E.; Guénée, L.; Canard, G.; Gumy, F. d. r.; Bünzli, J.-C. G.; Piguet, C. *Inorganic Chemistry* **2009**, *48*, 2549.
(183) Canard, G.; Koeller, S.; Bernardinelli, G.; Piguet, C. *Journal of the American Chemical Society* **2007**, *130*, 1025.
(184) Freire, M. G.; Neves, C. M. S. S.; Marrucho, I. M.; Coutinho, J. o. A. P.; Fernandes, A. M. *The Journal of Physical Chemistry A* **2009**, *114*, 3744.
(185) Shimidzu, T.; Iyoda, T.; Izaki, K. *The Journal of Physical Chemistry* **1985**, *89*, 642.
(186) Ruile, S.; Kohle, O.; Pettersson, H.; Michael Gratzel, a. *New Journal of Chemistry* **1998**, *22*, 25.
(187) Shan, B. Z.; Zhao, Q.; Goswami, N.; Eichhorn*, D. M.; Rillema*, D. P. *Coordination Chemistry Reviews* **2001**, *211*, 117.
(188) Uyguner, C. S.; Bekbolet, M. *Desalination* **2005**, *176*, 47.
(189) Uyguner, C. S.; Bekbolet, M. *Catalysis Today* **2005**, *101*, 267.
(190) Kumke, M. U.; Specht, C. H.; Brinkmann, T.; Frimmel, F. H. *Chemosphere* **2001**, *45*, 1023.

(191) Valencia, S.; Marín, J. M.; Restrepo, G.; Frimmel, F. H. *Science of The Total Environment* **2013**, *442*, 207.
(192) Freedman, D. A.; Evju, J. K.; Pomije, M. K.; Mann, K. R. *Inorganic Chemistry* **2001**, *40*, 5711.
(193) Hansch, C.; Leo, A.; Taft, R. W. *Chemical Reviews* **1991**, *91*, 165.
(194) Vratny, F. *Appl. Spectrosc.* **1959**, *13*, 59.
(195) Kremer, C.; Lützen, A. *Synthesis* **2011**, *2011*, 210.
(196) Janiak, C.; Deblon, S.; Wu, H.-P. *Synthetic Communications* **1999**, *29*, 3341.
(197) Miller, J.; Parker, A. J. *Journal of the American Chemical Society* **1961**, *83*, 117.
(198) Kiplinger, J. L.; Richmond, T. G.; Osterberg, C. E. *Chemical Reviews* **1994**, *94*, 373.
(199) Otsuka, M.; Endo, K.; Shibata, T. *Chemical Communications* **2010**, *46*, 336.
(200) Piglosiewicz, I. M.; Kraft, S.; Beckhaus, R.; Haase, D.; Saak, W. *European Journal of Inorganic Chemistry* **2005**, *2005*, 938.
(201) Clot, E.; Eisenstein, O.; Jasim, N.; Macgregor, S. A.; McGrady, J. E.; Perutz, R. N. *Accounts of Chemical Research* **2011**, *44*, 333.
(202) Reade, S. P.; Mahon, M. F.; Whittlesey, M. K. *Journal of the American Chemical Society* **2009**, *131*, 1847.
(203) Macgregor, S. A.; McKay, D.; Panetier, J. A.; Whittlesey, M. K. *Dalton Transactions* **2013**, *42*, 7386.
(204) Panetier, J. A.; Macgregor, S. A.; Whittlesey, M. K. *Angewandte Chemie International Edition* **2011**, *50*, 2783.
(205) Frost-Pennington, E. Masters Dissertation, University of Edinburgh, 2013.
(206) Renard, P.-Y.; Schwebel, H.; Vayron, P.; Leclerc, E.; Dias, S.; Mioskowski, C. *Tetrahedron Letters* **2001**, *42*, 8479.
(207) Rai, C.; Braunwarth, J. B. *The Journal of Organic Chemistry* **1961**, *26*, 3434.
(208) Lee, K.; Lee, P. H. *Tetrahedron Letters* **2008**, *49*, 4302.
(209) García-Lago, R.; Alonso-Gómez, J.-L.; Sicre, C.; Cid, M.-M. *Heterocycles* **2008**, *75*, 57.
(210) Hassan, J.; Penalva, V.; Lavenot, L.; Gozzi, C.; Lemaire, M. *Tetrahedron* **1998**, *54*, 13793.
(211) Ayme, J.-F.; Beves, J. E.; Leigh, D. A.; McBurney, R. T.; Rissanen, K.; Schultz, D. *Nat Chem* **2012**, *4*, 15.
(212) Masuda, H.; Ozawa, T.; Funabashi, Y.; Inomata, T.; Yamamoto, K. 2012; Vol. JP 2012007083.
(213) Noda, S.; Imawaka, N.; Matsubayashi, K.; Tanaka, K.; Furukawa, M. 2011; Vol. JP 2011157449.
(214) Je, J. T.; Jung, S. O.; Lee, S. H.; Lim, J. G.; A2 ed. 2011; Vol. KR 2011063336.

(215) Handa, M.; Ishida, H.; Ito, K.; Adachi, T.; Ikeue, T.; Hiromitsu, I.; Mikuriya, M.; Kasuga, K. *Chemical Papers* **2008**, *62*, 410.
(216) Wriedt, M.; Nather, C. *Chemical Communications* **2010**, *46*, 4707.
(217) Naumann, S.; Unold, J.; Frey, W.; Buchmeiser, M. R. *Macromolecules* **2011**, *44*, 8380.
(218) Norbury, A. H.; Sinha, A. I. P. *Journal of the Chemical Society A: Inorganic, Physical, Theoretical* **1968**, 1598.
(219) Turco, A.; Pecile, C. *Nature* **1961**, *191*, 66.
(220) Palaniappan, V.; Agarwala, U. C. *Inorganic Chemistry* **1986**, *25*, 4064.
(221) Burmeister, J. L.; Gysling, H. J. *Inorganica Chimica Acta* **1967**, *1*, 100.
(222) Fantacci, S.; De Angelis, F.; Selloni, A. *Journal of the American Chemical Society* **2003**, *125*, 4381.
(223) Jones, L. H. *The Journal of Chemical Physics* **1956**, *25*, 1069.
(224) Pauling, L.; Sherman, J. *The Journal of Chemical Physics* **1933**, *1*, 606.
(225) Wagner, E. L. *The Journal of Chemical Physics* **1965**, *43*, 2728.
(226) Argazzi, R.; Bignozzi, C. A.; Yang, M.; Hasselmann, G. M.; Meyer, G. J. *Nano Letters* **2002**, *2*, 625.
(227) Schmid, R. *Journal of Solution Chemistry* **1983**, *12*, 135.
(228) Jeffrey, G. A. *An Introduction to Hydrogen Bonding*; Oxford University Press on Demand, 1997.
(229) Clifford, A. F. *The Journal of Physical Chemistry* **1959**, *63*, 1227.
(230) Rao, C. N. R.; Bhat, S. N.; Dwedi, P. C. *Applied Spectroscopy Reviews* **1972**, *5*, 1.
(231) Tamres, M.; Brandon, O. P. M. *Journal of the American Chemical Society* **1960**, *82*, 2134.
(232) Tsubomura, H.; Lang, R. P. *Journal of the American Chemical Society* **1961**, *83*, 2085.
(233) Wayland, B. B.; Drago, R. S. *Journal of the American Chemical Society* **1964**, *86*, 5240.
(234) Laurence, C.; Graton, J.; Berthelot, M.; El Ghomari, M. J. *Chemistry – A European Journal* **2011**, *17*, 10431.
(235) Holliday, S. Masters Dissertation, University of Edinburgh, 2011.
(236) Al-Musharafi, S. K. Ph.D Thesis, University of Edinburgh, 2007.
(237) McInnes, E. J. Ph.D Thesis, University of Edinburgh, 1995.
(238) Delf, A. R. L. Ph.D Thesis, University of Edinburgh, 2011.
(239) Murray, P. R. Ph.D Thesis, University of Edinburgh, 2006.
(240) Magenau, A. J. D.; Kwak, Y.; Schröder, K.; Matyjaszewski, K. *ACS Macro Letters* **2012**, *1*, 508.

Appendix

A1: J-V data

A1.1: N719

Cell	J_{sc} / mAcm^{-2}	V_{oc} / mV	FF	η / %
A	11.67 (11.61)	617 (629)	0.607 (0.620)	4.37 (4.52)
B	10.63 (10.34)	622 (634)	0.627 (0.635)	4.14 (4.16)
C	10.28 (10.06)	634 (641)	0.629 (0.646)	4.10 (4.17)
D	10.94 (10.70)	644 (644)	0.620 (0.626)	4.36 (4.31)
E	9.45 (9.42)	644 (653)	0.645 (0.649)	3.93 (4.00)
F	10.97 (10.95)	653 (658)	0.611 (0.626)	4.38 (4.52)

Table A1.1: *The J-V characteristics of DSSCs sensitised with N719. Values after impedance measurement on the cells are shown in parentheses.*

A1.2: $K_4[Ru(dcbpy)_2(NCO)_2$

Cell	J_{sc} / mAcm^{-2}	V_{oc} / mV	FF	η / %
A	2.81 (2.89)	600 (609)	0.583 (0.566)	0.980 (0.998)
B	2.09 (2.48)	551 (561)	0.575 (0.573)	0.661 (0.795)
C	2.05 (2.59)	556 (565)	0.592 (0.620)	0.672 (0.911)
D	2.31 (2.36)	561 (580)	0.622 (0.616)	0.804 (0.845)
E	2.80 (3.27)	595 (605)	0.614 (0.617)	1.02 (1.22)
F	2.36 (2.50)	590 (595)	0.599 (0.585)	0.836 (0.877)

Table A1.2: *The J-V characteristics of DSSCs sensitised with $K_4[Ru(dcbpy)_2(NCO)_2$. Values after impedance measurement on the cells are shown in parentheses.*

A1.3: $K_4[Ru(dcbpy)_2(NCS)_2$

Cell	J_{sc} / $mAcm^{-2}$	V_{oc} / mV	FF	η / %
A	8.06 (7.94)	722 (732)	0.632 (0.652)	3.67 (3.79)
B	8.65 (8.56)	722 (736)	0.600 (0.627)	3.76 (3.96)
C	7.98 (7.92)	688 (702)	0.641 (0.661)	3.51 (3.68)
D	8.27 (8.42)	649 (663)	0.642 (0.652)	3.44 (3.65)
E	8.19 (8.42)	653 (673)	0.675 (0.673)	3.61 (3.81)
F	8.86 (8.86)	658 (658)	0.628 (0.635)	3.66 (3.70)

Table A1.3: *The J-V characteristics of DSSCs sensitised with $K_4[Ru(dcbpy)_2(NCS)_2$. Values after impedance measurement on the cells are shown in parentheses.*

A1.4 High efficiency cells data

Dye	Cell	J_{sc} / $mAcm^{-2}$	V_{oc} / mV	FF	η / %
N719	A	15.3	738	0.723	8.19
	B	15.5	737	0.726	8.28
	C	16.5	731	0.673	8.11
X = O	A	7.09	593	0.715	3.00
	B	6.57	588	0.756	2.92
	C	7.64	586	0.690	3.09
X = S	A	12.0	717	0.756	6.50
	B	11.6	704	0.751	6.12
	C	13.1	687	0.692	6.24

Table A1.4: *The J-V characteristics of high efficiency DSSCs sensitised with a variety of dyes. The cells were manufactured at Loughborough Univeristy by Benjamin Grew.*

A1.5: Ru(H_2-dcbpy)(4,4`-Cl_2-bpy)$(NCS)_2$

Cell	J_{sc} / mAcm^{-2}	V_{oc} / mV	FF	η / %
A	5.39 (6.20)	524 (536)	0.679 (0.673)	1.92 (2.24)
B	5.78 (6.02)	529 (539)	0.650 (0.650)	1.98 (2.11)
C	5.64 (6.09)	526 (541)	0.674 (0.678)	2.00 (2.23)
D	5.66 (6.20)	522 (531)	0.648 (0.652)	1.91 (2.15)
E	5.73 (5.31)	526 (517)	0.652 (0.662)	1.97 (1.82)
F	5.36 (5.65)	519 (529)	0.682 (0.668)	1.90 (2.00)

Table A1.5: *The J-V characteristics of DSSCs sensitised with Ru(H_2-dcbpy)(4,4`-Cl_2-bpy)$(NCS)_2$. Values after impedance measurement on the cells are shown in parentheses.*

A1.6: Ru(H_2-dcbpy)(4,4`-Br_2-bpy)$(NCS)_2$

Cell	J_{sc} / mAcm^{-2}	V_{oc} / mV	FF	η / %
A	5.05 (5.13)	539 (556)	0.676 (0.664)	1.84 (1.89)
B	5.14 (5.56)	551 (561)	0.658 (0.652)	1.86 (2.03)
C	5.25 (5.19)	541 (548)	0.665 (0.652)	1.89 (1.86)
D	5.03 (5.20)	539 (546)	0.666 (0.657)	1.81 (1.87)
E	5.03 (5.25)	531 (544)	0.667 (0.658)	1.78 (1.88)
F	5.17 (5.94)	531 (546)	0.622 (0.569)	1.71 (1.84)

Table A1.6: *The J-V characteristics of DSSCs sensitised with Ru(H_2-dcbpy)(4,4`-Br_2-bpy)$(NCS)_2$. Values after impedance measurement on the cells are shown in parentheses.*

A1.7: Ru(H_2-dcbpy)(5,5`-F_2-bpy)$(NCS)_2$

Cell	J_{sc} / mAcm^{-2}	V_{oc} / mV	FF	η / %
A	5.63 (5.61)	542 (546)	0.669 (0.668)	2.04 (2.05)
B	5.55 (5.73)	534 (544)	0.669 (0.665)	1.98 (2.07)
C	4.83 (5.03)	529 (536)	0.675 (0.673)	1.72 (1.82)
D	5.47 (5.63)	551 (556)	0.665 (0.646)	2.01 (2.02)
E	5.17 (5.20)	526 (544)	0.676 (0.663)	1.81 (1.87)
F	5.08 (5.42)	534 (536)	0.679 (0.677)	1.84 (1.97)

Table A1.7: *The J-V characteristics of DSSCs sensitised with Ru(H_2-dcbpy)(5,5`-F_2-bpy)$(NCS)_2$. Values after impedance measurement on the cells are shown in parentheses.*

A1.8: Ru(H_2-dcbpy)(5,5`-Cl_2-bpy)$(NCS)_2$

Cell	J_{sc} / mAcm^{-2}	V_{oc} / mV	FF	η / %
A	4.00 (4.22)	507 (519)	0.646 (0.651)	1.31 (1.43)
B	4.09 (4.58)	495 (502)	0.686 (0.673)	1.39 (1.55)
C	4.23 (4.72)	495 (502)	0.701 (0.689)	1.47 (1.63)
D	3.66 (4.02)	492 (504)	0.677 (0.675)	1.22 (1.37)
E	4.22 (4.84)	507 (519)	0.680 (0.672)	1.46 (1.69)
F	4.08 (4.59)	497 (512)	0.672 (0.678)	1.36 (1.59)

Table A1.8: *The J-V characteristics of DSSCs sensitised with Ru(H_2-dcbpy)(5,5`-Cl_2-bpy)$(NCS)_2$. Values after impedance measurement on the cells are shown in parentheses.*

A1.9: Ru(H_2-dcbpy)(5,5`-Br_2-bpy)$(NCS)_2$

Cell	J_{sc} / mAcm^{-2}	V_{oc} / mV	FF	η / %
A	4.52 (4.42)	536 (534)	0.646 (0.653)	1.57 (1.54)
B	4.23 (4.25)	504 (509)	0.639 (0.639)	1.37 (1.38)
C	4.52 (4.67)	509 (514)	0.640 (0.626)	1.47 (1.50)
D	5.06 (5.03)	517 (522)	0.630 (0.630)	1.65 (1.65)
E	4.48 (4.48)	514 (522)	0.595 (0.610)	1.37 (1.43)
F	4.55 (4.50)	517 (524)	0.622 (0.608)	1.46 (1.43)

Table A1.9: *The J-V characteristics of DSSCs sensitised with Ru(H_2-dcbpy)(5,5`-Br_2-bpy)$(NCS)_2$. Values after impedance measurement on the cells are shown in parentheses.*

A2: Impedance data

A2.1: N719

		TiO_2	TiO_2 – dye – I^- / I_3^- interface		Pt – I^- / I_3^- interface	
E_{app} / V	Cell	r_{trans} / Ωcm^{-3}	r_{rec} / Ωcm^3	c_{TiO2} / Fcm^{-3}	R_{Pt} / Ω	C_{Pt} / F
-0.5	A	57.45	96.69	8.22×10^{-4}	0.66	5.66×10^{-7}
	B	54.42	193.3	8.46×10^{-4}	0.79	7.17×10^{-7}
	C	62.36	160.6	9.01×10^{-4}	0.49	2.81×10^{-7}
	D	80.65	299.8	7.30×10^{-4}	1.20	1.39×10^{-6}
	E	99.12	248.8	6.82×10^{-4}	0.26	9.76×10^{-8}
	F	116.6	252.9	7.23×10^{-4}	1.11	1.81×10^{-6}
-0.6	A	4.58	19.06	1.82×10^{-3}	1.03	2.19×10^{-6}
	B	3.94	27.95	1.80×10^{-3}	1.31	2.83×10^{-6}
	C	3.65	29.26	2.09×10^{-3}	0.99	2.20×10^{-6}
	D	3.75	33.57	1.86×10^{-3}	2.16	6.76×10^{-6}
	E	4.93	36.34	1.81×10^{-3}	1.19	5.89×10^{-6}
	F	5.88	39.21	1.73×10^{-3}	2.32	9.00×10^{-6}
-0.7	A	-	6.74	2.87×10^{-3}	0.97	2.53×10^{-6}
	B	-	7.22	2.98×10^{-3}	1.21	3.68×10^{-6}
	C	-	8.28	3.39×10^{-3}	0.98	3.10×10^{-6}
	D	-	7.56	3.12×10^{-3}	1.99	8.91×10^{-6}
	E	-	9.40	3.25×10^{-3}	1.20	7.89×10^{-6}
	F	-	9.56	2.87×10^{-3}	2.03	8.82×10^{-6}
-0.8	A	-	3.40	3.81×10^{-3}	1.01	5.55×10^{-6}
	B	-	3.26	3.61×10^{-3}	1.03	2.96×10^{-6}
	C	-	3.71	4.36×10^{-3}	0.85	2.52×10^{-6}
	D	-	3.31	4.20×10^{-3}	1.66	8.69×10^{-6}
	E	-	4.22	4.55×10^{-3}	1.22	1.19×10^{-5}
	F	-	3.96	3.89×10^{-3}	1.68	8.69×10^{-6}

Table A2.1: *Impedance data for DSSCs sensitised with N719.*

A2.2: $K_4[Ru(dcbpy)_2(NCO)_2]$

		TiO_2	TiO_2 – dye – I^- / I_3^- interface		Pt – I^- / I_3^- interface	
E_{app} / V	Cell	r_{trans} / Ωcm^{-3}	r_{rec} / Ωcm^3	c_{TiO2} / Fcm^{-3}	R_{Pt} / Ω	C_{Pt} / F
-0.5	A	-	427.60	5.31×10^{-5}	17.73	1.29×10^{-5}
	B	-	162.50	8.01×10^{-5}	6.05	3.36×10^{-5}
	C	-	172.90	6.30×10^{-5}	4.67	5.14×10^{-5}
	D	-	251.2	6.57×10^{-5}	7.76	2.90×10^{-5}
	E	-	321.1	6.62×10^{-5}	5.60	2.72×10^{-5}
	F	-	338.1	5.37×10^{-5}	8.80	2.52×10^{-5}
-0.6	A	-	44.26	1.89×10^{-4}	18.42	1.51×10^{-5}
	B	-	21.71	3.03×10^{-4}	7.62	2.94×10^{-5}
	C	-	20.77	2.44×10^{-4}	6.82	3.31×10^{-5}
	D	-	29.07	2.52×10^{-4}	8.98	2.09×10^{-5}
	E	-	32.84	2.94×10^{-4}	7.92	2.51×10^{-5}
	F	-	35.87	2.24×10^{-4}	9.30	1.73×10^{-5}
-0.7	A	-	10.22	5.13×10^{-4}	10.07	1.82×10^{-5}
	B	-	6.22	6.28×10^{-4}	5.57	4.26×10^{-5}
	C	-	5.63	5.24×10^{-4}	4.65	3.62×10^{-5}
	D	-	8.06	5.70×10^{-4}	6.12	1.97×10^{-5}
	E	-	8.35	7.09×10^{-4}	5.46	2.37×10^{-5}
	F	-	8.92	5.50×10^{-4}	6.32	1.78×10^{-5}
-0.8	A	-	4.13	8.17×10^{-4}	6.36	2.08×10^{-5}
	B	-	2.97	9.21×10^{-4}	4.05	5.22×10^{-5}
	C	-	2.73	8.44×10^{-4}	3.19	3.33×10^{-5}
	D	-	3.88	9.94×10^{-4}	4.20	1.67×10^{-5}
	E	-	3.81	1.29×10^{-3}	3.79	2.11×10^{-5}
	F	-	4.12	1.08×10^{-3}	4.33	1.67×10^{-5}

Table A2.2: *Impedance data for DSSCs sensitised with $K_4[Ru(dcbpy)_2(NCO)_2$.*

A2.3: $K_4[Ru(dcbpy)_2(NCS)_2]$

		TiO_2	TiO_2 – dye – I^- / I_3^- interface		Pt – I^- / I_3^- interface	
E_{app} / V	Cell	r_{trans} / Ωcm^{-3}	r_{rec} / Ωcm^3	c_{TiO2} / Fcm^{-3}	R_{Pt} / Ω	C_{Pt} / F
-0.5	A	648.9	1913	3.80×10^{-4}	-	-
	B	409.7	1574	4.50×10^{-4}	-	-
	C	285.8	743	4.96×10^{-4}	-	-
	D	244.7	239.3	6.29×10^{-4}	-	-
	E	331.5	250.8	5.85×10^{-4}	-	-
	F	302.8	236.9	6.36×10^{-4}	-	-
-0.6	A	19.56	216.5	1.22×10^{-3}	3.38	1.34×10^{-5}
	B	15.47	207.0	1.40×10^{-3}	4.72	1.46×10^{-5}
	C	10.61	92.24	1.41×10^{-3}	4.14	1.59×10^{-5}
	D	9.71	40.11	1.55×10^{-3}	2.13	1.03×10^{-5}
	E	11.04	41.95	1.58×10^{-3}	1.16	7.25×10^{-6}
	F	11.26	51.16	1.20×10^{-3}	1.74	1.03×10^{-5}
-0.7	A	-	31.49	2.38×10^{-3}	3.54	2.29×10^{-5}
	B	-	33.93	2.70×10^{-3}	4.66	1.91×10^{-5}
	C	-	18.35	2.61×10^{-3}	3.94	2.09×10^{-5}
	D	-	10.32	2.64×10^{-3}	2.06	1.36×10^{-5}
	E	-	10.16	2.71×10^{-3}	1.23	1.21×10^{-5}
	F	-	12.44	2.67×10^{-3}	1.68	1.27×10^{-5}
-0.8	A	-	8.94	3.54×10^{-3}	2.65	1.44×10^{-5}
	B	-	9.92	4.29×10^{-3}	3.48	1.61×10^{-5}
	C	-	6.63	3.95×10^{-3}	2.98	1.73×10^{-5}
	D	-	4.41	3.34×10^{-3}	1.86	1.47×10^{-5}
	E	-	4.40	3.70×10^{-3}	1.26	1.93×10^{-5}
	F	-	5.07	3.75×10^{-3}	1.55	1.59×10^{-5}

Table A2.3: *Impedance data for DSSCs sensitised with $K_4[Ru(dcbpy)_2(NCS)_2$.*

A2.4: Ru(H_2-dcbpy)(4,4`-Cl_2-bpy)$(NCS)_2$

		TiO_2	TiO_2 – dye – I^- / I_3^-interface		Pt – I^- / I_3^- interface	
E_{app} / V	Cell	r_{trans} / Ωcm^{-3}	r_{rec} / Ωcm^3	c_{TiO2} / Fcm^{-3}	R_{Pt} / Ω	C_{Pt} / F
-0.5	A	65.55	15.39	2.99×10^{-4}	0.26	1.61×10^{-7}
	B	58.36	15.92	2.98×10^{-4}	0.37	6.67×10^{-5}
	C	66.42	14.53	4.71×10^{-4}	0.17	4.16×10^{-5}
	D	59.13	14.34	3.43×10^{-4}	0.41	1.28×10^{-6}
	E	58.14	12.42	8.11×10^{-4}	-	-
	F	53.02	13.16	8.09×10^{-4}	0.25	1.94×10^{-7}
-0.6	A	16.91	3.44	1.05×10^{-3}	0.96	5.35×10^{-6}
	B	12.88	3.91	8.02×10^{-4}	0.76	4.40×10^{-6}
	C	16.31	3.51	1.66×10^{-3}	0.65	5.16×10^{-6}
	D	15.78	3.56	9.95×10^{-4}	1.23	9.37×10^{-6}
	E	13.04	4.16	1.99×10^{-3}	-	-
	F	10.50	4.17	2.01×10^{-3}	0.72	3.62×10^{-6}
-0.7	A	4.18	2.76	1.29×10^{-3}	0.79	2.73×10^{-6}
	B	3.95	2.43	1.14×10^{-3}	0.56	1.68×10^{-6}
	C	3.77	2.89	2.20×10^{-3}	0.50	1.89×10^{-6}
	D	3.95	2.91	1.29×10^{-3}	0.91	4.03×10^{-6}
	E	3.72	3.04	2.11×10^{-3}	-	-
	F	3.11	2.80	2.76×10^{-3}	0.61	1.81×10^{-6}
-0.8	A	3.28	1.58	1.91×10^{-3}	0.80	3.65×10^{-6}
	B	2.85	1.38	1.50×10^{-3}	0.54	1.98×10^{-6}
	C	3.02	1.64	2.73×10^{-3}	0.55	2.91×10^{-6}
	D	3.06	1.66	1.70×10^{-3}	0.89	4.60×10^{-6}
	E	1.69	2.36	2.60×10^{-3}	-	-
	F	1.63	1.93	2.99×10^{-3}	0.58	1.63×10^{-6}

Table A2.4: *Impedance data for DSSCs sensitised with Ru(H_2-dcbpy)(4,4`-Cl_2-bpy)$(NCS)_2$.*

A2.5: Ru(H_2-dcbpy)(4,4`-Br_2-bpy)$(NCS)_2$

		TiO_2	TiO_2 – dye – I^- / I_3^-interface		Pt – I^- / I_3^- interface	
E_{app} / V	Cell	r_{trans} / Ωcm^{-3}	r_{rec} / Ωcm^3	c_{TiO2} / Fcm^{-3}	R_{Pt} / Ω	C_{Pt} / F
-0.5	A	86.94	22.06	2.35×10^{-4}	-	-
	B	114.2	29.95	2.47×10^{-4}	-	-
	C	80.34	23.69	2.17×10^{-4}	-	-
	D	76.75	23.94	2.47×10^{-4}	-	-
	E	71.31	19.21	3.15×10^{-4}	-	-
	F	73.89	26.24	2.45×10^{-4}	-	-
-0.6	A	21.50	4.97	1.32×10^{-3}	0.92	7.69×10^{-6}
	B	21.97	5.47	1.09×10^{-3}	1.62	2.19×10^{-5}
	C	18.01	4.68	1.10×10^{-3}	0.85	1.72×10^{-5}
	D	16.81	4.54	1.11×10^{-3}	1.12	2.76×10^{-5}
	E	15.86	4.10	1.24×10^{-3}	0.92	5.87×10^{-6}
	F	19.04	4.96	1.13×10^{-3}	1.80	1.89×10^{-5}
-0.7	A	4.37	3.06	1.83×10^{-3}	0.69	2.95×10^{-6}
	B	5.44	3.31	1.66×10^{-3}	1.28	1.14×10^{-5}
	C	4.41	3.19	1.83×10^{-3}	0.49	2.33×10^{-6}
	D	4.51	3.02	2.12×10^{-3}	0.72	4.94×10^{-6}
	E	3.56	3.01	2.21×10^{-3}	0.61	1.67×10^{-6}
	F	5.33	3.36	2.41×10^{-3}	1.25	6.67×10^{-6}
-0.8	A	3.90	1.43	2.81×10^{-3}	0.80	5.37×10^{-6}
	B	4.70	1.43	2.97×10^{-3}	1.29	1.31×10^{-5}
	C	3.75	1.51	2.53×10^{-3}	0.53	3.76×10^{-6}
	D	3.62	1.46	2.91×10^{-3}	0.77	7.15×10^{-6}
	E	3.62	1.27	2.82×10^{-3}	0.65	2.59×10^{-6}
	F	4.30	1.50	3.29×10^{-3}	1.33	9.36×10^{-6}

Table A2.5: *Impedance data for DSSCs sensitised with Ru(H_2-dcbpy)(4,4`-Br_2-bpy)$(NCS)_2$.*

A2.6: Ru(H_2-dcbpy)(5,5`-F_2-bpy)$(NCS)_2$

		TiO_2	TiO_2 – dye – I^- / I_3^-interface		Pt – I^- / I_3^- interface	
E_{app} / V	Cell	r_{trans} / Ωcm^{-3}	r_{rec} / Ωcm^3	c_{TiO2} / Fcm^{-3}	R_{Pt} / Ω	C_{Pt} / F
-0.5	A	74.25	21.57	2.34 x 10^{-4}	-	-
	B	75.79	21.24	2.80 x 10^{-4}	-	-
	C	68.66	19.93	1.76 x 10^{-4}	-	-
	D	119.10	36.78	1.79 x 10^{-4}	-	-
	E	68.90	19.85	2.15 x 10^{-4}	-	-
	F	64.78	18.66	2.07 x 10^{-4}	-	-
-0.6	A	17.13	3.99	1.31 x 10^{-3}	0.35	9.29 x 10^{-7}
	B	16.37	3.93	1.20 x 10^{-3}	0.77	2.80 x 10^{-6}
	C	17.25	3.44	1.19 x 10^{-3}	0.16	3.52 x 10^{-7}
	D	22.42	4.51	1.38 x 10^{-3}	0.72	3.27 x 10^{-6}
	E	19.77	3.59	1.40 x 10^{-3}	0.21	5.28 x 10^{-7}
	F	14.79	3.42	1.15 x 10^{-3}	0.35	7.47 x 10^{-7}
-0.7	A	3.11	3.06	1.84 x 10^{-3}	0.24	2.18 X 10^{-7}
	B	3.23	2.91	1.79 x 10^{-3}	0.54	8.88 x 10^{-7}
	C	3.67	2.49	1.32 x 10^{-3}	0.13	1.19 x 10^{-7}
	D	4.53	3.20	1.68 x 10^{-3}	0.56	1.34 x 10^{-6}
	E	3.25	2.93	1.46 x 10^{-3}	0.15	1.48 x 10^{-5}
	F	3.40	2.40	1.56 x 10^{-3}	0.27	2.34 x 10^{-7}
-0.8	A	3.53	1.31	2.40 x 10^{-3}	0.32	6.10 x 10^{-7}
	B	3.41	1.25	2.34 x 10^{-3}	0.61	1.50 x 10^{-6}
	C	3.84	1.09	2.26 x 10^{-3}	0.18	4.39 x 10^{-7}
	D	3.81	1.50	2.38 x 10^{-3}	0.65	2.57 x 10^{-6}
	E	3.97	1.18	2.20 x 10^{-3}	0.23	5.23 x 10^{-7}
	F	3.30	1.08	2.28 x 10^{-3}	0.33	5.61 x 10^{-7}

Table A2.6: *Impedance data for DSSCs sensitised with Ru(H_2-dcbpy)(5,5`-F_2-bpy)$(NCS)_2$.*

A2.7: Ru(H_2-dcbpy)(5,5`-Cl_2-bpy)(NCS)

		TiO_2	TiO_2 – dye – I^- / I_3^-interface		Pt – I^- / I_3^- interface	
E_{app} / V	Cell	r_{trans} / Ωcm^{-3}	r_{rec} / Ωcm^3	c_{TiO2} / Fcm^{-3}	R_{Pt} / Ω	C_{Pt} / F
-0.5	A	54.77	13.94	2.13 x 10^{-4}	0.07	2.72 x 10^{-8}
	B	40.41	10.13	2.65 x 10^{-4}	-	-
	C	46.83	8.50	4.75 x 10^{-4}	-	-
	D	43.59	11.11	2.72 x 10^{-4}	0.51	1.32 x 10^{-6}
	E	47.50	12.82	2.09 x 10^{-4}	0.38	2.36 x 10^{-6}
	F	42.50	10.92	1.74 x 10^{-4}	-	-
-0.6	A	14.91	3.52	7.62 x 10^{-4}	0.57	1.35 x 10^{-6}
	B	14.31	2.84	9.61 x 10^{-4}	0.19	9.05 x 10^{-7}
	C	13.53	2.71	1.09 x 10^{-3}	0.51	1.34 x 10^{-6}
	D	12.39	3.43	7.39 x 10^{-4}	0.92	2.62 x 10^{-6}
	E	12.59	3.55	6.70 x 10^{-4}	0.78	2.54 x 10^{-6}
	F	12.66	2.90	7.53 x 10^{-4}	0.18	3.24 x 10^{-7}
-0.7	A	3.26	2.88	1.08 x 10^{-3}	0.41	5.00 x 10^{-7}
	B	3.48	2.21	1.27 x 10^{-3}	0.43	7.61 x 10^{-7}
	C	3.77	2.11	1.28 x 10^{-3}	0.44	8.35 x 10^{-7}
	D	3.83	2.49	1.18 x 10^{-3}	0.70	1.19 x 10^{-6}
	E	3.54	2.55	1.10 x 10^{-3}	0.59	1.12 x 10^{-6}
	F	5.41	1.63	1.15 x 10^{-3}	0.20	3.47 x 10^{-7}
-0.8	A	3.66	1.27	1.42 x 10^{-3}	0.50	1.19 x 10^{-6}
	B	1.94	1.68	1.57 x 10^{-3}	0.15	5.08 x 10^{-7}
	C	1.56	1.60	1.81 x 10^{-3}	0.40	9.29 x 10^{-7}
	D	2.47	1.56	1.56 x 10^{-3}	0.68	1.42 x 10^{-6}
	E	3.32	1.22	1.71 x 10^{-3}	0.64	1.75 x 10^{-6}
	F	3.35	1.05	1.49 x 10^{-3}	0.19	3.74 x 10^{-7}

Table A2.7: *Impedance data for DSSCs sensitised with Ru(H_2-dcbpy)(5,5`-Cl_2-bpy)$(NCS)_2$.*

A2.8: Ru(H_2-dcbpy)(5,5`-Br_2-bpy)(NCS)

		TiO_2	TiO_2 – dye – I^- / I_3^-interface		Pt – I^- / I_3^- interface	
E_{app} / V	Cell	r_{trans} / Ωcm^{-3}	r_{rec} / Ωcm^3	c_{TiO2} / Fcm^{-3}	R_{Pt} / Ω	C_{Pt} / F
-0.5	A	85.45	23.94	1.74×10^{-4}	-	-
	B	49.84	12.50	1.41×10^{-4}	-	-
	C	49.96	13.93	2.20×10^{-4}	0.76	4.14×10^{-6}
	D	59.37	16.18	3.01×10^{-4}	0.99	1.23×10^{-5}
	E	66.71	19.09	2.86×10^{-4}	2.63	1.76×10^{-5}
	F	62.93	17.27	2.97×10^{-4}	2.57	5.06×10^{-5}
-0.6	A	20.80	4.14	1.39×10^{-3}	1.01	1.29×10^{-5}
	B	17.04	2.78	9.63×10^{-4}	0.24	7.26×10^{-7}
	C	13.48	3.68	7.35×10^{-4}	1.19	7.11×10^{-6}
	D	15.93	3.91	1.14×10^{-3}	1.29	7.37×10^{-6}
	E	17.86	4.82	1.02×10^{-3}	2.57	9.66×10^{-6}
	F	16.74	5.09	8.27×10^{-4}	1.87	1.14×10^{-5}
-0.7	A	4.10	3.03	1.73×10^{-3}	0.80	6.13×10^{-6}
	B	6.03	1.79	1.17×10^{-3}	0.26	8.41×10^{-7}
	C	6.45	1.77	1.31×10^{-3}	0.99	4.08×10^{-6}
	D	5.61	2.40	1.53×10^{-3}	1.05	4.39×10^{-6}
	E	5.40	3.25	1.62×10^{-3}	1.81	5.13×10^{-6}
	F	7.42	2.20	1.48×10^{-3}	1.50	5.66×10^{-6}
-0.8	A	4.38	1.20	2.95×10^{-3}	0.85	8.03×10^{-6}
	B	3.97	1.09	1.43×10^{-3}	0.27	9.95×10^{-7}
	C	3.72	1.15	1.61×10^{-3}	0.84	2.93×10^{-6}
	D	4.18	1.32	2.34×10^{-3}	0.94	4.03×10^{-6}
	E	4.37	1.54	2.19×10^{-3}	1.68	5.99×10^{-6}
	F	4.43	1.37	2.11×10^{-3}	1.24	4.09×10^{-6}

Table A2.8: *Impedance data for DSSCs sensitised with Ru(H_2-dcbpy)(5,5`-Br_2-bpy)$(NCS)_2$.*

A3: DFT and TD-DFT data

A3.1: $Ru(H_2\text{-}dcbpy)_2(NCO)_2$

Orbital	% occupancy of orbital					
	Ru	N	C	O	$Ru(NCO)_2$	$(dcbpy)_2$
HOMO-5	28.06	13.19	0.58	12.75	81.1	18.9
HOMO-4	32.72	12.71	0.56	11.65	82.6	17.4
HOMO-3	1.02	24.44	2.33	20.57	95.7	4.3
HOMO-2	62.28	6.08	1.20	5.18	87.2	12.8
HOMO-1	66.89	4.86	1.09	4.24	87.3	12.7
HOMO	65.09	5.42	1.42	4.69	88.2	11.8
LUMO	7.91	0.29	0.06	0.05	8.7	91.3
LUMO+1	12.78	0.36	0.13	0.17	14.1	85.9
LUMO+2	1.43	0.02	0.03	0.01	1.6	98.4
LUMO+3	4.74	0.04	0.06	0.04	5.0	95.0
LUMO+4	1.05	0.03	0.11	0.00	1.3	98.7
LUMO+5	1.68	0.04	0.03	0.01	1.8	98.2
LUMO+9	39.12	1.21	0.49	0.10	42.7	57.3

Table A3.1.1: *The location of the frontier orbitals of $Ru(H_2\text{-}dcbpy)_2(NCO)_2$ solvated with water using the polarisable continuum model.*

Wavelength / nm	Transition	% Contribution	Nature of transition
722.47	HOMO-2 to LUMO	14.7	MLCT
	HOMO to LUMO	85.3	MLCT
580.47	HOMO-2 to LUMO	38.0	MLCT
	HOMO-1 to LUMO	8.4	MLCT
	HOMO-1 to LUMO+1	33.9	MLCT
	HOMO to LUMO	10.9	MLCT
	HOMO to LUMO+2	8.8	MLCT
496.64	HOMO to LUMO+2	100.0	MLCT
470.70	HOMO-2 to LUMO+1	9.4	MLCT
	HOMO-1 to LUMO	10.1	MLCT
	HOMO-1 to LUMO+2	18.9	MLCT
	HOMO to LUMO+3	32.6	MLCT
	HOMO to LUMO+4	18.9	MLCT
	HOMO to LUMO+5	10.0	MLCT
450.40	HOMO-2 to LUMO+2	25.5	MLCT
	HOMO-1 to LUMO+2	14.3	MLCT
	HOMO-1 to LUMO+3	60.1	MLCT
442.69	HOMO-2 to LUMO+2	64.0	MLCT
	HOMO-1 to LUMO+2	14.1	MLCT
	HOMO-1 to LUMO+3	21.9	MLCT
432.94	HOMO-3 to LUMO	6.8	MLCT
	HOMO-2 to LUMO+2	7.4	MLCT
	HOMO-2 to LUMO+5	6.7	MLCT
	HOMO-1 to LUMO+2	16.1	MLCT
	HOMO-1 to LUMO+4	13.7	MLCT
	HOMO to LUMO+3	13.1	MLCT
	HOMO to LUMO+5	36.2	MLCT
350.82	HOMO-5 to LUMO+1	11.2	MLCT
	HOMO-4 to LUMO	54.8	MLCT
	HOMO-4 to LUMO+1	11.4	MLCT
	HOMO-2 to LUMO+9	12.4	d-d / MLCT
	HOMO to LUMO+9	10.2	d-d / MLCT

Table A3.1.2: *The electronic transitions of $Ru(H_2\text{-dcbpy})_2(NCO)_2$ at longer wavelengths than 350 nm with an oscillator strength greater than 0.025. The dye was solvated using the polarisable continuum model.*

Orbital	% occupancy of orbital					
	Ru	N	C	O	$Ru(NCO)_2$	$(dcbpy)_2$
HOMO-5	33.76	1.77; 21.55	0.04; 1.01	1.33; 20.09	79.6	20.4
HOMO-4	28.86	23.14; 1.90	1.29; 0.12	20.25; 1.71	77.3	22.7
HOMO-3	3.98	22.89	2.64	18.62	88.3	11.7
HOMO-2	65.71	3.73; 6.42	0.77; 1.30	2.64; 5.04	85.6	14.4
HOMO-1	59.89	8.73; 4.71	1.75; 0.91	6.55; 3.53	86.1	13.9
HOMO	59.90	6.50	1.59	5.21	86.5	13.5
LUMO	8.71	0.32	0.09	0.06	9.7	90.3
LUMO+1	13.37	0.46	0.20	0.18	15.1	84.9
LUMO+2	2.08	0.05	0.04	0.01	2.3	97.7
LUMO+3	5.00	0.04	0.06	0.04	5.3	94.7
LUMO+4	1.51	0.10	0.14	0.01	2.0	98.0
LUMO+5	1.90	0.07	0.04	0.01	2.1	97.9
LUMO+8	45.89	5.07	2.25	1.06	62.7	37.3

Table A3.1.3: *The location of the frontier orbitals of $Ru(H_2\text{-}dcbpy)_2(NCO)_2$ with explicit solvation by six water molecules.*

Wavelength / nm	Transition	% Contribution	Nature of transition
785.53	HOMO-2 to LUMO+1	12.0	MLCT
	HOMO to LUMO	52.7	MLCT
	HOMO to LUMO+1	35.4	MLCT
756.93	HOMO-2 to LUMO	9.2	MLCT
	HOMO-1 to LUMO	8.8	MLCT
	HOMO-1 to LUMO+1	16.3	MLCT
	HOMO to LUMO	26.3	MLCT
	HOMO to LUMO+1	39.4	MLCT
599.66	HOMO-2 to LUMO	7.4	MLCT
	HOMO-2 to LUMO+1	31.1	MLCT
	HOMO-1 to LUMO	27.5	MLCT
	HOMO-1 to LUMO+1	12.1	MLCT
	HOMO to LUMO	10.9	MLCT
	HOMO to LUMO+2	11.0	MLCT
532.17	HOMO-2 to LUMO+1	12.1	MLCT
	HOMO to LUMO	16.7	MLCT
	HOMO to LUMO+2	71.2	MLCT
494.25	HOMO-2 to LUMO	14.9	MLCT
	HOMO-2 to LUMO+2	11.1	MLCT
	HOMO-1 to LUMO+1	8.9	MLCT
	HOMO to LUMO+1	7.8	MLCT
	HOMO to LUMO+3	31.1	MLCT
	HOMO to LUMO+4	18.8	MLCT
	HOMO to LUMO+5	7.5	MLCT
455.68	HOMO-3 to LUMO	18.2	$^{\#}$LLCT
	HOMO-2 to LUMO+2	13.0	MLCT
	HOMO-2 to LUMO+3	32.8	MLCT
	HOMO-1 to LUMO+2	20.9	MLCT
	HOMO to LUMO+5	15.1	MLCT
451.85	HOMO-3 to LUMO	48.4	$^{\#}$LLCT
	HOMO-2 to LUMO+2	11.6	MLCT
	HOMO-2 to LUMO+3	18.4	MLCT
	HOMO-1 to LUMO+2	9.5	MLCT
	HOMO-1 to LUMO+3	12.1	MLCT
375.02	HOMO-5 to LUMO	28.6	MLCT / $^{\#}$LLCT
	HOMO-4 to LUMO	25.1	MLCT / $^{\#}$LLCT
	HOMO-4 to LUMO+1	25.9	MLCT / $^{\#}$LLCT
	HOMO to LUMO+8	20.3	d-d / MLCT
359.63	HOMO-5 to LUMO+1	11.9	MLCT / $^{\#}$LLCT
	HOMO-3 to LUMO+2	12.6	$^{\#}$LLCT
	HOMO-3 to LUMO+3	75.5	$^{\#}$LLCT

Table A3.1.4: *The electronic transitions of $Ru(H_2\text{-dcbpy})_2(NCO)_2$ at longer wavelengths than 350 nm with an oscillator strength greater than 0.025. The dye was explicitly solvated with six water molecules. $^{\#}$LLCT represents charge transfer from the $^{-}$NCO ligands to the $(dcbpy)^{2-}$ ligands.*

Orbital	% occupancy of orbital					
	Ru	N	C	O	$Ru(NCO)_2$	$(dcbpy)_2$
HOMO-2	65.71	3.73; 6.42	0.77; 1.30	2.64; 5.04	85.6	14.4
HOMO-1	59.89	8.73; 4.71	1.75; 0.91	6.55; 3.53	86.1	13.9
HOMO	59.90	6.50	1.59	5.21	86.5	13.5
LUMO	8.71	0.32	0.09	0.06	9.7	90.3
LUMO+1	13.37	0.46	0.20	0.18	15.1	84.9
LUMO+2	2.08	0.05	0.04	0.01	2.3	97.7
LUMO+3	5.00	0.04	0.06	0.04	5.3	94.7
LUMO+4	1.51	0.10	0.14	0.01	2.0	98.0
LUMO+5	1.90	0.07	0.04	0.01	2.1	97.9

Table A3.1.5: *The location of the frontier orbitals of $Ru(H_2\text{-}dcbpy)_2(NCO)_2$ with explicit solvation by six water molecules.*

Wavelength / nm	Transition	% Contribution	Nature of transition
680.53	HOMO to LUMO	66.0	MLCT
	HOMO to LUMO+1	44.0	MLCT
667.7	HOMO-2 to LUMO+1	16.2	MLCT
	HOMO-1 to LUMO	8.8	MLCT
	HOMO to LUMO	26.1	MLCT
	HOMO to LUMO+1	48.9	MLCT
540.40	HOMO-2 to LUMO	42.0	MLCT
	HOMO-1 to LUMO+1	35.7	MLCT
	HOMO to LUMO	10.5	MLCT
	HOMO to LUMO+2	11.7	MLCT
478.77	HOMO to LUMO	14.8	MLCT
	HOMO to LUMO+2	85.2	MLCT
446.77	HOMO-2 to LUMO+1	11.0	MLCT
	HOMO-1 to LUMO	15.9	MLCT
	HOMO-1 to LUMO+2	23.0	MLCT
	HOMO to LUMO+1	7.2	MLCT
	HOMO to LUMO+3	32.3	MLCT
	HOMO to LUMO+5	10.6	MLCT
427.70	HOMO-2 to LUMO+2	23.7	MLCT
	HOMO-1 to LUMO+3	65.6	MLCT
	HOMO to LUMO+4	10.7	MLCT
418.80	HOMO-2 to LUMO+2	75.6	MLCT
	HOMO-1 to LUMO+3	24.4	MLCT
416.21	HOMO-2 to LUMO+2	10.6	MLCT
	HOMO-2 to LUMO+3	34.0	MLCT
	HOMO to LUMO+5	55.4	MLCT
385.15	HOMO-2 to LUMO+4	100.0	MLCT

Table A3.1.6: *The electronic transitions of $Ru(H_2\text{-}dcbpy)_2(NCO)_2$ at longer wavelengths than 350 nm with an oscillator strength greater than 0.025. The dye was explicitly solvated with six water molecules and the solvation was extended for the TD-DFT calculation using the polarisable continuum model.*

A3.2: $Ru(H_2\text{-}dcbpy)_2(NCS)_2$

Orbital	% occupancy of orbital					
	Ru	N	C	S	$Ru(NCS)_2$	$(dcbpy)_2$
HOMO-6	45.42	2.70	1.24	17.65	88.6	11.4
HOMO-5	49.96	2.81	0.78	15.85	88.8	11.2
HOMO-4	51.72	2.76	0.71	15.16	89.0	11.0
HOMO-3	0.66	10.40	0.37	38.20	98.6	1.4
HOMO-2	43.02	5.44	0.69	18.18	91.6	8.4
HOMO-1	47.91	4.64	0.67	16.27	91.1	8.9
HOMO	51.93	4.39	1.22	14.45	92.1	7.9
LUMO	6.63	0.33	0.09	0.09	7.7	92.3
LUMO+1	10.92	0.35	0.20	0.23	12.5	87.5
LUMO+2	1.12	0.00	0.02	0.01	1.2	98.8
LUMO+3	3.62	0.01	0.09	0.06	3.9	96.1
LUMO+4	1.02	0.13	0.20	0.06	1.8	98.2

Table A3.2.1: *The location of the frontier orbitals of $Ru(H_2\text{-}dcbpy)_2(NCS)_2$ solvated with water using the polarisable continuum model.*

Wavelength / nm	Transition	% Contribution	Nature of transition
645.75	HOMO to LUMO	100.0	MLCT / $^{\#}$LLCT
553.30	HOMO-2 to LUMO	49.2	MLCT / $^{\#}$LLCT
	HOMO-1 to LUMO+1	39.1	MLCT / $^{\#}$LLCT
	HOMO to LUMO	11.8	MLCT / $^{\#}$LLCT
530.45	HOMO-2 to LUMO+1	42.7	MLCT / $^{\#}$LLCT
	HOMO-1 to LUMO	25.8	MLCT / $^{\#}$LLCT
	HOMO to LUMO+1	16.8	MLCT / $^{\#}$LLCT
	HOMO to LUMO+3	14.8	MLCT / $^{\#}$LLCT
461.15	HOMO-3 to LUMO+1	16.4	$^{\#}$LLCT
	HOMO to LUMO+2	83.6	MLCT / $^{\#}$LLCT
447.39	HOMO-3 to LUMO	27.3	$^{\#}$LLCT
	HOMO-2 to LUMO+1	8.7	MLCT / $^{\#}$LLCT
	HOMO-1 to LUMO	8.1	MLCT / $^{\#}$LLCT
	HOMO-1 to LUMO+2	12.0	MLCT / $^{\#}$LLCT
	HOMO to LUMO+3	43.9	MLCT / $^{\#}$LLCT
445.87	HOMO-3 to LUMO+1	84.4	$^{\#}$LLCT
	HOMO to LUMO+2	15.6	MLCT / $^{\#}$LLCT
427.63	HOMO-1 to LUMO+3	73.3	MLCT / $^{\#}$LLCT
	HOMO to LUMO+4	26.7	MLCT / $^{\#}$LLCT
421.94	HOMO-2 to LUMO+2	86.1	MLCT / $^{\#}$LLCT
	HOMO-2 to LUMO+3	13.9	MLCT / $^{\#}$LLCT
389.19	HOMO-4 to LUMO	100.0	MLCT / $^{\#}$LLCT
381.66	HOMO-6 to LUMO	12.9	MLCT / $^{\#}$LLCT
	HOMO-5 to LUMO+1	74.3	MLCT / $^{\#}$LLCT
	HOMO-1 to LUMO+1	12.8	MLCT / $^{\#}$LLCT
369.05	HOMO-6 to LUMO	74.0	MLCT / $^{\#}$LLCT
	HOMO-5 to LUMO+1	11.6	MLCT / $^{\#}$LLCT
	HOMO-3 to LUMO+3	14.4	$^{\#}$LLCT

Table A3.2.2: *The electronic transitions of Ru(H_2-dcbpy)$_2$($NCS)_2$ at longer wavelengths than 350 nm with an oscillator strength greater than 0.025. The dye was solvated using the polarisable continuum model. $^{\#}$LLCT represents charge transfer from the $^{-}$NCS ligands to the $(dcbpy)^{2-}$ ligands.*

Orbital	% occupancy of orbital					
	Ru	N	C	S	$Ru(NCS)_2$	$(dcbpy)_2$
HOMO-6	65.34	0.49; 1.00	1.45; 1.57	6.35; 9.59	85.8	14.2
HOMO-5	65.06	0.39; 1.59	0.78; 2.01	4.11; 13.32	87.3	12.7
HOMO-4	66.04	1.35; 0.38	1.97; 0.29	12.18; 2.54	84.8	15.2
HOMO-3	7.95	5.63; 13.55	0.39; 0.74	20.49; 45.95	94.7	5.3
HOMO-2	23.34	3.08; 12.04	0.15; 0.51	10.98; 41.56	91.7	8.3
HOMO-1	24.42	13.80; 1.33	0.68; 0.09	45.69; 4.00	90.0	10.0
HOMO	33.23	8.76; 4.95	0.69; 0.78	28.22; 15.17	91.8	8.2
LUMO	7.90	0.34	0.13	0.20	9.2	90.8
LUMO+1	11.48	0.50	0.26	0.32	13.6	86.4
LUMO+2	1.89	0.01	0.02	0.02	2.0	98.0
LUMO+3	3.77	0.02	0.06	0.05	4.0	96.0
LUMO+8	42.75	3.23; 6.95	1.30; 3.71	0.86; 1.98	60.8	39.2

Table A3.2.3: *The location of the frontier orbitals of $Ru(H_2\text{-}dcbpy)_2(NCS)_2$ with explicit solvation by six water molecules.*

Wavelength / nm	Transition	% Contribution	Nature of transition
859.36	HOMO-1 to LUMO	16.0	MLCT / #LLCT
	HOMO to LUMO	84.0	MLCT / #LLCT
670.38	HOMO-3 to LUMO+1	8.4	#LLCT
	HOMO-2 to LUMO	18.7	MLCT / #LLCT
	HOMO-2 to LUMO+1	41.4	MLCT / #LLCT
	HOMO-1 to LUMO+1	8.1	MLCT / #LLCT
	HOMO to LUMO+1	13.2	MLCT / #LLCT
	HOMO to LUMO+2	10.2	MLCT / #LLCT
574.99	HOMO-3 to LUMO	12.8	#LLCT
	HOMO-3 to LUMO+1	14.8	#LLCT
	HOMO to LUMO+2	72.4	MLCT / #LLCT
446.87	HOMO-6 to LUMO	12.6	MLCT
	HOMO-6 to LUMO+1	6.4	MLCT
	HOMO-5 to LUMO	12.1	MLCT
	HOMO-5 to LUMO+1	30.4	MLCT
	HOMO-4 to LUMO	12.7	MLCT
	HOMO-4 to LUMO+1	13.9	MLCT
	HOMO-3 to LUMO+3	12.0	#LLCT
419.14	HOMO-6 to LUMO	56.8	MLCT
	HOMO-6 to LUMO+1	14.9	MLCT
	HOMO-5 to LUMO	14.2	MLCT
	HOMO-4 to LUMO+1	14.0	MLCT
358.92	HOMO-5 to LUMO+2	20.0	MLCT
	HOMO-5 to LUMO+3	24.5	MLCT
	HOMO-4 to LUMO+2	43.6	MLCT
	HOMO-4 to LUMO+3	11.9	MLCT
354.28	HOMO-6 to LUMO+2	11.9	MLCT
	HOMO-5 to LUMO+2	41.4	MLCT
	HOMO-4 to LUMO+2	23.4	MLCT
	HOMO-4 to LUMO+3	15.7	MLCT
	HOMO to LUMO+8	7.7	d-d / MLCT

Table A3.2.4: *The electronic transitions of $Ru(H_2\text{-}dcbpy)_2(NCS)_2$ at longer wavelengths than 350 nm with an oscillator strength greater than 0.025. The dye was explicitly solvated with six water molecules. #LLCT represents charge transfer from the ^-NCS ligands to the $(dcbpy)^{2-}$ ligands.*

Orbital	% occupancy of orbital					
	Ru	N	C	S	$Ru(NCS)_2$	$(dcbpy)_2$
HOMO-6	65.34	0.49; 1.00	1.45; 1.57	6.35; 9.59	85.8	14.2
HOMO-5	65.06	0.39; 1.59	0.78; 2.01	4.11; 13.32	87.3	12.7
HOMO-4	66.04	1.35; 0.38	1.97; 0.29	12.18; 2.54	84.8	15.2
HOMO-3	7.95	5.63; 13.55	0.39; 0.74	20.49; 45.95	94.7	5.3
HOMO-2	23.34	3.08; 12.04	0.15; 0.51	10.98; 41.56	91.7	8.3
HOMO-1	24.42	13.80; 1.33	0.68; 0.09	45.69; 4.00	90.0	10.0
HOMO	33.23	8.76; 4.95	0.69; 0.78	28.22; 15.17	91.8	8.2
LUMO	7.90	0.34	0.13	0.20	9.2	90.8
LUMO+1	11.48	0.50	0.26	0.32	13.6	86.4
LUMO+2	1.89	0.01	0.02	0.02	2.0	98.0
LUMO+3	3.77	0.02	0.06	0.05	4.0	96.0
LUMO+4	1.57	0.12	0.16	0.06	2.3	97.7

Table A3.2.5: *The location of the frontier orbitals of $Ru(H_2\text{-}dcbpy)_2(NCS)_2$ with explicit solvation by six water molecules.*

Wavelength / nm	Transition	% Contribution	Nature of transition
624.26	HOMO to LUMO	100.0	MLCT / #LLCT
526.54	HOMO-2 to LUMO	35.2	MLCT / #LLCT
	HOMO-2 to LUMO+1	11.9	MLCT / #LLCT
	HOMO-1 to LUMO	17.4	MLCT / #LLCT
	HOMO-1 to LUMO+1	26.7	MLCT / #LLCT
	HOMO to LUMO	8.7	MLCT / #LLCT
450.54	HOMO to LUMO+2	86.4	MLCT / #LLCT
	HOMO to LUMO+3	13.6	MLCT / #LLCT
436.71	HOMO-3 to LUMO	8.8	MLCT / #LLCT
	HOMO-2 to LUMO+1	11.3	MLCT / #LLCT
	HOMO-1 to LUMO	12.9	MLCT / #LLCT
	HOMO-1 to LUMO+2	12.6	MLCT / #LLCT
	HOMO to LUMO+3	54.3	MLCT / #LLCT
410.92	HOMO-2 to LUMO+3	11.2	MLCT / #LLCT
	HOMO-2 to LUMO+2	16.0	MLCT / #LLCT
	HOMO-2 to LUMO+3	56.7	MLCT / #LLCT
	HOMO to LUMO+4	16.0	MLCT / #LLCT
370.70	HOMO-5 to LUMO	39.6	MLCT
	HOMO-5 to LUMO+1	11.8	MLCT
	HOMO-4 to LUMO	11.7	MLCT
	HOMO-4 to LUMO+1	36.8	MLCT
350.09	HOMO-6 to LUMO	78.9	MLCT
	HOMO-6 to LUMO+1	21.1	MLCT

Table A3.2.6: *The electronic transitions of $Ru(H_2\text{-}dcbpy)_2(NCS)_2$ at longer wavelengths than 350 nm with an oscillator strength greater than 0.025. The dye was explicitly solvated with six water molecules and the solvation was extended using the polarisable continuum model. #LLCT represents charge transfer from the $^-$NCS ligands to the $(dcbpy)^{2-}$ ligands.*

A3.3: $K_4[Ru(dcbpy)_2(NCO)_2]$

Orbital	% occupancy of orbital					
	Ru	N	C	O	$Ru(NCO)_2$	$(dcbpy)_2$
HOMO-2	70.97	3.77	1.05	3.49	87.6	12.4
HOMO-1	73.67	3.04	0.97	2.96	87.6	12.4
HOMO	71.61	3.83	1.42	3.70	89.5	10.5
LUMO	6.22	0.23	0.05	0.04	6.9	93.1
LUMO+1	10.10	0.30	0.10	0.11	11.1	88.9
LUMO+2	2.50	0.06	0.20	0.01	3.0	97.0
LUMO+3	3.02	0.02	0.04	0.01	3.2	96.8
LUMO+4	1.60	0.02	0.05	0.01	1.8	98.2
LUMO+5	5.33	0.07	0.04	0.03	5.6	94.4
LUMO+8	50.27	4.23	1.76	0.97	64.2	35.8
LUMO+9	44.86	0.77	0.48	0.13	47.6	52.4

Table A3.3.1: *The location of the frontier orbitals of $[Ru(dcbpy)_2(NCO)_2]^{4-}$ solvated with methanol.*

Wavelength / nm	Transition	% Contribution	Nature of transition
608.94	HOMO to LUMO	100.0	MLCT
509.50	HOMO-2 to LUMO	53.9	MLCT
	HOMO-1 to LUMO+1	34.3	MLCT
	HOMO to LUMO	11.8	MLCT
403.08	HOMO to LUMO+2	11.4	MLCT
	HOMO to LUMO+4	76.3	MLCT
	HOMO to LUMO+8	12.3	d-d / MLCT
386.07	HOMO-2 to LUMO+1	6.9	MLCT
	HOMO-2 to LUMO+5	9.4	MLCT
	HOMO-1 to LUMO+2	20.4	MLCT
	HOMO-1 to LUMO+4	19.0	MLCT
	HOMO to LUMO+3	11.7	MLCT
	HOMO to LUMO+5	32.5	MLCT
379.05	HOMO-1 to LUMO+3	52.1	MLCT
	HOMO-1 to LUMO+5	17.8	MLCT
	HOMO-1 to LUMO+9	13.9	d-d / MLCT
	HOMO to LUMO+8	16.2	d-d / MLCT
364.36	HOMO-2 to LUMO+4	67.7	MLCT
	HOMO-1 to LUMO+3	17.6	MLCT
	HOMO-1 to LUMO+5	14.7	MLCT

Table A3.3.2: *The electronic transitions of $[Ru(dcbpy)_2(NCO)_2]^{4-}$ at longer wavelengths than 350 nm with an oscillator strength greater than 0.025.The dye was solvated with methanol using the polarisable continuum model.*

A3.4: $K_4[Ru(dcbpy)_2(NCS)_2]$

Orbital	% occupancy of orbital					
	Ru	N	C	S	$Ru(NCS)_2$	$(dcbpy)_2$
HOMO-13	0.28	0.14	0.01	0.60	1.8	98.2
HOMO-12	0.09	0.05	0.00	0.23	0.7	99.3
HOMO-7	0.56	10.20	0.42	38.42	98.6	1.4
HOMO-2	62.00	2.97	0.97	10.12	90.1	9.9
HOMO-1	64.79	2.48	0.96	8.92	89.5	10.5
HOMO	64.10	2.68	1.62	9.42	91.5	8.5
LUMO	5.31	0.29	0.09	0.07	6.2	93.8
LUMO+1	8.34	0.32	0.21	0.17	9.7	90.3
LUMO+2	2.43	0.26	0.36	0.13	3.9	96.1
LUMO+3	2.53	0.01	0.08	0.04	2.8	97.2
LUMO+4	1.26	0.03	0.07	0.02	1.5	98.5
LUMO+5	4.60	0.14	0.08	0.07	5.2	94.8
LUMO+7	44.43	5.61	3.76	2.45	68.1	31.9
LUMO+9	41.52	1.07	1.07	0.42	46.6	53.4

Table A3.4.1: *The location of the frontier orbitals of $[Ru(dcbpy)_2(NCS)_2]^{4-}$ solvated with methanol.*

Wavelength / nm	Transition	% Contribution	Nature of transition
531.16	HOMO to LUMO	100.0	MLCT
466.74	HOMO-2 to LUMO	58.4	MLCT
	HOMO-1 to LUMO+1	30.1	MLCT
	HOMO to LUMO	11.5	MLCT
448.32	HOMO-2 to LUMO+1	50.0	MLCT
	HOMO-1 to LUMO	30.8	MLCT
	HOMO to LUMO+1	19.2	MLCT
367.85	HOMO to LUMO+4	72.1	MLCT
	HOMO to LUMO+7	27.9	d-d / MLCT
357.99	HOMO-7 to LUMO	9.3	$LLCT^{\#}$
	HOMO-2 to LUMO+5	8.3	MLCT
	HOMO-1 to LUMO+2	18.3	MLCT
	HOMO-1 to LUMO+4	13.0	MLCT
	HOMO to LUMO+3	9.6	MLCT
	HOMO to LUMO+5	41.5	MLCT
352.65	HOMO-1 to LUMO+3	51.8	MLCT
	HOMO-1 to LUMO+5	15.6	MLCT
	HOMO-1 to LUMO+9	17.0	d-d / MLCT
	HOMO to LUMO+7	15.6	d-d / MLCT

Table A3.4.2: *The electronic transitions of $[Ru(dcbpy)_2(NCS)_2]^{4-}$ at longer wavelengths than 350 nm with an oscillator strength greater than 0.025. The dye was solvated with methanol using the polarisable continuum model. $^{\#}$LLCT represents charge transfer from the $^{-}$NCS ligands to the $(dcbpy)^{2-}$ ligands.*

A3.5: $Ru(H_2\text{-dcbpy})(4,4`\text{-}Cl_2\text{-bpy})(NCS)_2$

Orbital	% occupancy of orbitals			
	$(NCS)_2$	Ru	H_2-dcbpy	4,4`-Cl_2-bpy
HOMO-6	44.75	42.87	5.40	6.98
HOMO-5	40.33	48.91	6.42	4.34
HOMO-4	38.6	48.90	4.46	8.04
HOMO-3	98.01	0.66	0.66	0.67
HOMO-2	46.66	44.72	4.43	4.19
HOMO-1	41.63	49.33	4.77	4.27
HOMO	38.94	53.06	4.10	3.90
LUMO	1.32	8.97	86.50	3.21
LUMO+1	0.95	5.83	2.48	90.74
LUMO+2	0.18	2.33	95.78	1.71
LUMO+3	0.78	1.25	82.49	15.48
LUMO+4	13.65	4.01	0.64	81.70
LUMO+5	0.21	1.57	1.62	96.60

Table A3.5.1: *The distribution of the frontier orbitals of $Ru(H_2\text{-dcbpy})(4,4`\text{-}Cl_2\text{-bpy})(NCS)_2$.*

Wavelength / nm	Transition	% Contribution	Nature of transition
663.25	HOMO-2 to LUMO	19.7	MLCT
	HOMO to LUMO	80.3	MLCT
586.00	HOMO-1 to LUMO	23.1	MLCT
	HOMO to LUMO+1	76.9	MLCT
552.64	HOMO-2 to LUMO	45.0	MLCT
	HOMO-1 to LUMO	15.3	MLCT
	HOMO-1 to LUMO+1	10.7	MLCT
	HOMO to LUMO	11.5	MLCT
	HOMO to LUMO+1	8.1	MLCT
	HOMO to LUMO+2	9.5	MLCT
507.46	HOMO-2 to LUMO+1	41.4	MLCT
	HOMO-1 to LUMO+1	33.3	MLCT
	HOMO to LUMO+1	13.6	MLCT
	HOMO to LUMO+2	11.7	MLCT
466.73	HOMO-3 to LUMO+1	24.4	$^{\#}$LLCT
	HOMO-2 to LUMO+1	10.8	MLCT
	HOMO to LUMO+3	64.8	MLCT
454.25	HOMO-3 to LUMO+1	76.0	$^{\#}$LLCT
	HOMO to LUMO+3	24.0	MLCT
430.15	HOMO-2 to LUMO+2	78.9	MLCT
	HOMO to LUMO+3	21.1	MLCT
387.62	HOMO-6 to LUMO	12.6	MLCT
	HOMO-5 to LUMO	58.0	MLCT
	HOMO-4 to LUMO	13.2	MLCT
	HOMO to LUMO+5	16.2	MLCT
379.38	HOMO-6 to LUMO	8.8	MLCT
	HOMO-5 to LUMO	8.4	MLCT
	HOMO-4 to LUMO+1	14.8	MLCT
	HOMO-1 to LUMO+4	18.7	MLCT
	HOMO to LUMO+5	49.3	MLCT
371.09	HOMO-6 to LUMO	34.3	MLCT
	HOMO-4 to LUMO+1	12.9	MLCT
	HOMO-3 to LUMO+2	9.4	$^{\#}$LLCT
	HOMO-2 to LUMO+4	34.8	MLCT
	HOMO-1 to LUMO+4	8.6	MLCT
366.95	HOMO-6 to LUMO	18.5	MLCT
	HOMO-5 to LUMO+1	9.3	MLCT
	HOMO-4 to LUMO+1	32.7	MLCT
	HOMO-2 to LUMO+4	27.5	MLCT
	HOMO-1 to LUMO+4	12.0	MLCT

Table A3.5.2: *The electronic transitions of Ru(H_2-dcbpy)(4,4`-$Cl_2$-bpy)$(NCS)_2$ at longer wavelengths than 350 nm with an oscillator strength greater than 0.025. The dye was solvated with DMF using the polarisable continuum model. Values in red represent charge transfer to the 4,4`-Cl_2-bpy ligand and $^{\#}$LLCT represents charge transfer from the $^{-}$NCS ligands to one of the bpy ligand.*

A3.6: Ru(H_2-dcbpy)(4,4`-Br_2-bpy)$(NCS)_2$

Orbital	% occupancy of orbitals			
	$(NCS)_2$	Ru	H_2-dcbpy	4,4`-Br_2-bpy
HOMO-6	44.56	41.77	5.32	8.35
HOMO-5	40.25	49.02	6.54	4.19
HOMO-4	38.42	47.82	4.27	9.49
HOMO-3	97.97	0.66	0.22	1.15
HOMO-2	46.74	44.65	4.39	4.22
HOMO-1	41.33	49.42	4.82	4.43
HOMO	38.97	52.93	4.14	3.96
LUMO	1.32	8.96	86.45	3.27
LUMO+1	0.98	6.00	2.66	90.36
LUMO+2	0.20	2.36	95.63	1.81
LUMO+3	0.76	1.20	82.65	15.39
LUMO+4	0.63	3.95	13.81	81.61
LUMO+5	0.22	1.63	1.68	96.47

Table A3.6.1: *The distribution of the frontier orbitals of Ru(H_2-dcbpy)(4,4`-Br_2-bpy)$(NCS)_2$.*

Wavelength / nm	Transition	% Contribution	Nature of transition
661.63	HOMO-2 to LUMO	19.7	MLCT
	HOMO to LUMO	80.3	MLCT
584.35	HOMO-2 to LUMO+1	11.1	MLCT
	HOMO-1 to LUMO	16.8	MLCT
	HOMO to LUMO+1	72.1	MLCT
553.03	HOMO-2 to LUMO	44.1	MLCT
	HOMO-1 to LUMO	15.9	MLCT
	HOMO-1 to LUMO+1	10.6	MLCT
	HOMO to LUMO	11.6	MLCT
	HOMO to LUMO+1	8.7	MLCT
	HOMO to LUMO+2	9.1	MLCT
506.78	HOMO-2 to LUMO+1	43.1	MLCT
	HOMO-1 to LUMO+1	31.3	MLCT
	HOMO to LUMO+1	13.9	MLCT
	HOMO to LUMO+2	11.7	MLCT
466.38	HOMO-3 to LUMO	74.7	$^{\#}$LLCT
	HOMO to LUMO+2	25.3	MLCT
454.47	HOMO-1 to LUMO+2	60.8	MLCT
	HOMO to LUMO+3	39.2	MLCT
430.21	HOMO-2 to LUMO+2	77.8	MLCT
	HOMO to LUMO+3	22.2	MLCT
387.75	HOMO-6 to LUMO	11.7	MLCT
	HOMO-5 to LUMO	54.1	MLCT
	HOMO-4 to LUMO	17.5	MLCT
	HOMO to LUMO+5	16.7	MLCT
379.79	HOMO-6 to LUMO	9.7	MLCT
	HOMO-5 to LUMO	9.5	MLCT
	HOMO-4 to LUMO+1	14.3	MLCT
	HOMO-1 to LUMO+4	17.8	MLCT
	HOMO to LUMO+5	48.8	MLCT
371.28	HOMO-6 to LUMO	37.7	MLCT
	HOMO-4 to LUMO+1	15.6	MLCT
	HOMO-3 to LUMO+2	9.5	MLCT
	HOMO-2 to LUMO+4	37.2	MLCT
366.89	HOMO-6 to LUMO	19.6	MLCT
	HOMO-4 to LUMO+1	34.2	MLCT
	HOMO-2 to LUMO+4	33.5	MLCT
	HOMO-1 to LUMO+4	12.8	MLCT

Table A3.6.2: *The electronic transitions of Ru(H_2-dcbpy)(4,4`-$Br_2$-bpy)$(NCS)_2$ at longer wavelengths than 350 nm with an oscillator strength greater than 0.025. The dye was solvated with DMF using the polarisable continuum model.Values in red represent charge transfer to the 4,4`-Br_2-bpy ligand and $^{\#}$LLCT represents charge transfer from the $^{-}$NCS ligands to the H_2-dcbpy ligand.*

A3.7: Ru(H_2-dcbpy)(5,5`-F_2-bpy)$(NCS)_2$

Orbital	% occupancy of orbitals			
	$(NCS)_2$	Ru	H_2-dcbpy	5,5`-F_2-bpy
HOMO-6	42.93	44.45	5.44	7.18
HOMO-5	39.47	49.60	5.39	4.54
HOMO-4	38.25	49.07	4.50	8.18
HOMO-3	98.01	0.67	0.67	0.65
HOMO-2	47.55	44.02	4.39	4.04
HOMO-1	42.46	48.86	4.68	4.00
HOMO	39.63	52.78	4.15	3.44
LUMO	1.33	9.11	86.96	2.60
LUMO+1	1.03	6.78	5.97	86.22
LUMO+2	0.28	3.04	92.07	4.61
LUMO+3	0.67	1.06	88.73	9.54
LUMO+4	0.67	3.27	8.79	87.27
LUMO+5	0.24	1.78	1.80	96.18

Table A3.7.1: *The distribution of the frontier orbitals of Ru(H_2-dcbpy)(5,5`-F_2-bpy)$(NCS)_2$.*

Wavelength / nm	Transition	% Contribution	Nature of transition
658.65	HOMO-2 to LUMO	19.7	MLCT
	HOMO to LUMO	80.3	MLCT
522.74	HOMO-2 to LUMO	44.1	MLCT
	HOMO-1 to LUMO	20.3	MLCT
	HOMO to LUMO	12.9	MLCT
	HOMO to LUMO+1	11.6	MLCT
	HOMO to LUMO+2	11.1	MLCT
471.43	HOMO-2 to LUMO+1	31.3	MLCT
	HOMO-1 to LUMO+1	18.0	MLCT
	HOMO to LUMO+1	12.7	MLCT
	HOMO to LUMO+2	38.0	MLCT
459.73	HOMO-3 to LUMO	32.6	$^{\#}$LLCT
	HOMO-2 to LUMO+1	22.0	MLCT
	HOMO-1 to LUMO+1	21.5	MLCT
	HOMO to LUMO+2	23.9	MLCT
453.03	HOMO-3 to LUMO	44.0	$^{\#}$LLCT
	HOMO-2 to LUMO+1	14.5	MLCT
	HOMO-1 to LUMO+1	15.1	MLCT
	HOMO to LUMO+2	26.4	MLCT
428.69	HOMO-2 to LUMO+1	11.2	MLCT
	HOMO-2 to LUMO+2	63.2	MLCT
	HOMO to LUMO+3	25.6	MLCT
386.29	HOMO-6 to LUMO	15.0	MLCT
	HOMO-5 to LUMO	49.2	MLCT
	HOMO-3 to LUMO+1	10.3	$^{\#}$LLCT
	HOMO to LUMO+4	10.3	MLCT
	HOMO to LUMO+5	15.1	MLCT
375.90	HOMO-6 to LUMO	23.8	MLCT
	HOMO to LUMO+4	13.2	MLCT
	HOMO to LUMO+5	63.1	MLCT
366.75	HOMO-6 to LUMO	37.5	MLCT
	HOMO-5 to LUMO	11.0	MLCT
	HOMO-3 to LUMO+2	23.6	$^{\#}$LLCT
	HOMO-2 to LUMO+4	10.7	MLCT
	HOMO-1 to LUMO+4	17.3	MLCT

Table A3.7.2: *The electronic transitions of Ru(H_2-dcbpy)(5,5`-$F_2$-bpy)$(NCS)_2$ at longer wavelengths than 350 nm with an oscillator strength greater than 0.025. The dye was solvated with DMF using the polarisable continuum model. Values in red represent charge transfer to the 5,5`-F_2-bpy ligand and $^{\#}$LLCT represents charge transfer from the $^{-}$NCS ligands to one of the bpy ligands.*

A3.8: Ru(H_2-dcbpy)(5,5`-Cl_2-bpy)$(NCS)_2$

Orbital	% occupancy of orbitals			
	$(NCS)_2$	Ru	H_2-dcbpy	5,5`-Cl_2-bpy
HOMO-6	42.13	44.87	5.54	7.46
HOMO-5	38.66	49.95	6.40	4.99
HOMO-4	37.24	49.67	4.56	8.53
HOMO-3	98.04	0.67	0.65	0.64
HOMO-2	48.26	43.31	4.30	4.13
HOMO-1	43.13	48.25	4.64	3.98
HOMO	40.08	52.33	4.11	3.48
LUMO	1.30	8.91	86.75	3.04
LUMO+1	0.90	5.82	97.48	90.76
LUMO+2	0.21	2.38	95.27	2.14
LUMO+3	0.75	1.19	83.56	14.50
LUMO+4	0.64	4.20	13.50	81.66
LUMO+5	0.25	1.76	1.82	96.17

Table A3.8.1: *The distribution of the frontier orbitals of Ru(H_2-dcbpy)(5,5`-Cl_2-bpy)$(NCS)_2$.*

Wavelength / nm	Transition	% Contribution	Nature of transition
656.90	HOMO-2 to LUMO	18.8	MLCT
	HOMO to LUMO	81.2	MLCT
572.86	HOMO-2 to LUMO	12.7	MLCT
	HOMO-2 to LUMO+1	10.1	MLCT
	HOMO-1 to LUMO	14.5	MLCT
	HOMO to LUMO+1	62.8	MLCT
550.30	HOMO-2 to LUMO	40.9	MLCT
	HOMO-1 to LUMO	19.1	MLCT
	HOMO-1 to LUMO+1	8.3	MLCT
	HOMO to LUMO	11.0	MLCT
	HOMO to LUMO+1	12.2	MLCT
	HOMO to LUMO+2	8.5	MLCT
496.90	HOMO-2 to LUMO+1	43.8	MLCT
	HOMO-1 to LUMO+1	29.8	MLCT
	HOMO to LUMO+1	13.5	MLCT
	HOMO to LUMO+2	12.8	MLCT
464.46	HOMO-3 to LUMO	35.3	$^{\#}$LLCT
	HOMO to LUMO+2	64.7	MLCT
454.81	HOMO-3 to LUMO	68.2	$^{\#}$LLCT
	HOMO to LUMO+2	31.8	MLCT
428.33	HOMO-2 to LUMO+2	78.9	MLCT
	HOMO to LUMO+3	21.1	MLCT
386.26	HOMO-6 to LUMO	16.4	MLCT
	HOMO-5 to LUMO	63.1	MLCT
	HOMO to LUMO+5	20.4	MLCT
368.82	HOMO-6 to LUMO	35.3	MLCT
	HOMO-4 to LUMO+1	12.6	MLCT
	HOMO-3 to LUMO+2	15.6	$^{\#}$LLCT
	HOMO-2 to LUMO+4	36.5	MLCT

Table A3.8.2: *The electronic transitions of Ru(H_2-dcbpy)(5,5`-$Cl_2$-bpy)$(NCS)_2$ at longer wavelengths than 350 nm with an oscillator strength greater than 0.025. The dye was solvated with DMF using the polarisable continuum model. Values in red represent charge transfer to the 5,5`-F_2-bpy ligand and $^{\#}$LLCT represents charge transfer from the $^{-}$NCS ligands to one of the bpy ligands.*

A3.9: Ru(H_2-dcbpy)(5,5`-Br_2-bpy)$(NCS)_2$

Orbital	% occupancy of orbitals			
	$(NCS)_2$	Ru	H_2-dcbpy	5,5`-Br_2-bpy
HOMO-6	41.05	43.56	5.29	10.10
HOMO-5	38.68	49.84	6.27	5.21
HOMO-4	37.02	48.15	4.54	10.29
HOMO-3	98.03	0.67	0.68	0.62
HOMO-2	47.98	43.54	4.37	4.11
HOMO-1	43.00	48.33	4.74	3.93
HOMO	39.98	52.42	4.11	3.49
LUMO	1.29	8.85	86.58	3.28
LUMO+1	0.90	5.81	2.54	90.75
LUMO+2	0.20	2.33	95.52	1.95
LUMO+3	0.71	1.21	83.94	14.14
LUMO+4	0.65	4.29	13.26	81.80
LUMO+5	0.25	1.76	1.83	96.16

Table A3.9.1: *The distribution of the frontier orbitals of Ru(H_2-dcbpy)(5,5`-Br_2-bpy)$(NCS)_2$.*

Wavelength / nm	Transition	% Contribution	Nature of transition
657.89	HOMO-2 to LUMO	19.4	MLCT
	HOMO to LUMO	80.6	MLCT
575.79	HOMO-2 to LUMO	12.4	MLCT
	HOMO-2 to LUMO+1	9.9	MLCT
	HOMO-1 to LUMO	13.5	MLCT
	HOMO to LUMO+1	64.1	MLCT
550.76	HOMO-2 to LUMO	43.2	MLCT
	HOMO-1 to LUMO	16.6	MLCT
	HOMO-1 to LUMO+2	9.0	MLCT
	HOMO to LUMO	11.2	MLCT
	HOMO to LUMO+1	11.3	MLCT
	HOMO to LUMO+2	8.7	MLCT
499.33	HOMO-2 to LUMO+1	42.8	MLCT
	HOMO-1 to LUMO+1	31.4	MLCT
	HOMO to LUMO+1	13.4	MLCT
	HOMO to LUMO+2	12.4	MLCT
464.71	HOMO-3 to LUMO	33.9	$^{\#}$LLCT
	HOMO to LUMO+2	66.1	MLCT
454.84	HOMO-3 to LUMO	69.5	$^{\#}$LLCT
	HOMO to LUMO+2	30.5	MLCT
428.46	HOMO-2 to LUMO+2	79.0	MLCT
	HOMO to LUMO+3	21.0	MLCT
386.40	HOMO-6 to LUMO	17.4	MLCT
	HOMO-5 to LUMO	63.5	MLCT
	HOMO to LUMO+5	19.0	MLCT
370.33	HOMO-6 to LUMO	21.6	MLCT
	HOMO-2 to LUMO+4	13.3	MLCT
	HOMO-1 to LUMO+4	52.3	MLCT
	HOMO to LUMO+5	12.7	MLCT
369.08	HOMO-6 to LUMO	33.2	MLCT
	HOMO-5 to LUMO	7.6	MLCT
	HOMO-4 to LUMO+1	14.0	MLCT
	HOMO-3 to LUMO+2	12.4	$^{\#}$LLCT
	HOMO-2 to LUMO+4	32.7	MLCT

Table A3.9.2: *The electronic transitions of Ru(H_2-dcbpy)(5,5`-$Br_2$-bpy)$(NCS)_2$ at longer wavelengths than 350 nm with an oscillator strength greater than 0.025. The dye was solvated with DMF using the polarisable continuum model. Values in red represent charge transfer to the 5,5`-F_2-bpy ligand and $^{\#}$LLCT represents charge transfer from the $^{-}$NCS ligands to one of the bpy ligands.*